# Classical mechanisms of recollision and high harmonic generation

Simon A. Berman

# CLASSICAL MECHANISMS OF RECOLLISION AND HIGH HARMONIC GENERATION

A Dissertation
Presented to
The Academic Faculty

By

Simon A. Berman

In Partial Fulfillment
of the Requirements for the Degree
Doctor of Philosophy in the
School of Physics

Georgia Institute of Technology

May 2019

**CLASSICAL MECHANISMS OF RECOLLISION AND HIGH HARMONIC GENERATION**

Approved by:

Dr. Claire Berger
Néel Institute
*French National Center for Scientific Research (CNRS)*

Dr. Cristel Chandre, Advisor
Institut de Mathématiques de Marseille
*French National Center for Scientific Research (CNRS)*

Dr. Emmanuel Lorin
School of Mathematics and Statistics
*Carleton University*

Dr. Bradley Shadwick
Department of Physics and Astronomy
*University of Nebraska-Lincoln*

Dr. Turgay Uzer, Advisor
School of Physics
*Georgia Institute of Technology*

Date Approved: December 3, 2018

Finally, some progress has been made in the reduction of electromagnetism to a dynamical science, by shewing that no electromagnetic phenomenon is contradictory to the supposition that it depends on purely dynamical action.

*James Clerk Maxwell*

To my sister, Emma.

## ACKNOWLEDGEMENTS

The lone name on the byline belies the many people who contributed to my success and made this dissertation a reality. First, I would like to thank my committee and rapporteurs for their careful reading of my thesis manuscript and their feedback. I am grateful that my work was met with their earnest interest and engagement in the subject.

I would also like to extend my gratitude to the staff of the IT, financial, and maintenance departments, both at Georgia Tech and Aix-Marseille Université. I appreciate their efforts in maintaining a proper work environment on a daily basis.

I must also thank my advisors, Cristel Chandre and Turgay Uzer, for their guidance, encouragement, and unflagging support throughout my PhD. They struck the right balance between oversight and laissez-faire and worked to create a collegial atmosphere in which I was able to flourish. It was truly a pleasure to work alongside them.

I acknowledge François Mauger for poring over every manuscript I sent him and providing keen insights that helped me advance my work.

Turning now to my peers, I would first like to acknowledge my group members Jonathan Dubois and Maxime Perin. Besides being collaborators, I am happy to call them my friends. I am also grateful for their efforts in making me feel at home during my many trips to their native France, for example by providing me ample opportunities to practice my French and by guiding me through the oft-inscrutable French bureaucracy on multiple occasions.

Next, I acknowledge my friends and fellow graduate students in Atlanta and Marseille. I am grateful for their companionship over the years, and I am glad to say I could count on them whenever I was in need. In particular, I would like to acknowledge Chris Crowley, Evan Mistur, Jean-Philippe Turmaud, Jeremy Yang, Jonathan Michel, Matt Conrad, Oliver Pierson, Shane Jacobeen, Stephen Spitz, and Travis Tune in Atlanta, and Carlos Alvarez, Catarina Santos, Joan Romeu, Luca Crevatin, Lucrezia Rinaldi, Saif Shaikh, and Serena Corti in Marseille.

Lastly, I would like to thank my family. The thousands of miles separating us did not diminish the support provided by my loving parents. I have also been continuously inspired by my sister Emma, not only by her passion for science and the arts, but by the discipline and work ethic she brings to everything she does. I am grateful also for the constant support of my grandparents on both sides.

## TABLE OF CONTENTS

## LIST OF TABLES

## LIST OF FIGURES

## SUMMARY

Thirty years after the demonstration of the production of high laser harmonics through nonlinear laser-gas interaction, high harmonic generation (HHG) is being used to probe molecular dynamics in real time and is realizing its technological potential as a table-top source of attosecond pulses in the XUV to soft X-ray range. Despite experimental progress, theoretical efforts have been stymied by the excessive computational cost of first-principles simulations and the difficulty of systematically deriving reduced models for the non-perturbative, multiscale interaction of an intense laser pulse with a macroscopic gas of atoms. In this thesis, we investigate first-principles reduced models for HHG using classical mechanics. On the microscopic level, we examine the recollision process—the laser-driven collision of an ionized electron with its parent ion—that drives HHG. Using nonlinear dynamics, we elucidate the indispensable role played by the ionic potential during recollisions in the strong-field limit. On the macroscopic level, we show that the intense laser-gas interaction can be cast as a classical field theory. Borrowing a technique from plasma physics, we systematically derive a hierarchy of reduced Hamiltonian models for the self-consistent interaction between the laser and the atoms during pulse propagation. The reduced models can accommodate either classical or quantum electron dynamics, and in both cases, simulations over experimentally-relevant propagation distances are feasible. We build a classical model based on these simulations which agrees quantitatively with the quantum model for the propagation of the dominant components of the laser field. Subsequently, we use the classical model to trace the coherent buildup of harmonic radiation to its origin in phase space. In a simplified geometry, we show that the anomalously high frequency radiation seen in simulations results from the delicate interplay between electron trapping and higher energy recollisions brought on by propagation effects.

# CHAPTER 1
# INTRODUCTION

The electrons of an isolated atom are organized in a complex pattern, known as the ground-state wave function. Loosely speaking, this pattern is a standing wave: a stationary solution to the Schrödinger equation, describing the motion of the electrons. Nevertheless, experimental measurements and quantum theory tell us that electrons exhibit wave-particle duality: sometimes they behave like waves, other times they behave like particles, and, most interestingly, they can even behave like both waves and particles. A striking manifestation of this behavior occurs when an atom is subjected to an intense laser pulse. In this situation, the atom may ionize: one of the atomic electrons can be detached from the atom's ionic core, and subsequently accelerated away by the electric field of the laser. However, the direction of the laser field oscillates periodically, meaning it does not take long before it has reversed direction, and the electron is now accelerated back towards the ionic core. With the right kind of laser, there is a significant probability that the electron subsequently collides with the core, an event known as a *recollision* [1–3]. The electron may bring with it significant kinetic energy that it acquired from the laser, triggering complex microscopic processes within the ion.

So far, the description of the electron's motion has been based on its particle nature, and indeed, the electron can interact with the ion in particle-like ways. For example, it may scatter off the ion while the other electrons remain undisturbed, leading to a change in direction and possibly energy. This outcome typically leads to above-threshold ionization (ATI). On the other hand, it may collide with one of the other electrons, leading to the ionization of a second or even third electron. In this phenomenon, termed non-sequential multiple ionization (NSMI), each electron clearly behaves like a classical particle. However, it is in the last possible scenario that the intricacies of the electron's wave-particle nature emerge.

If the laser is not too strong, then the probability of single ionization is significantly less than one, meaning that only part of the electron's wave packet ionizes—the rest remains in the standing-wave configuration around the ionic core. When this ionized, particle-like part of the electron's wave packet returns to the core, it typically has a different (smaller) wavelength than the bounded part of the wave packet, because it has gained energy from the laser field. Hence, the electron wave *interferes with itself*, through the beating between the recolliding wave packet and the bounded wave packet. The beating during recollisions translates into high frequency oscillations of the atomic dipole moment, and is therefore a source of high frequency radiation.

This last phenomenon, termed high harmonic generation (HHG), has tremendous implications for the dynamical imaging of atoms and molecules and the generation of attosecond pulses of high-frequency light ($1\ \mathrm{as} = 10^{-18}\ \mathrm{s}$). The motion of the ionized electrons and the subsequent reorganization of the ionic core unfold over a subfemtosecond time scale ($1\ \mathrm{fs} = 10^{-15}\ \mathrm{s}$). It turns out that the structure of the ionic core at the time of the recollision is encoded in the spectrum of emitted radiation. This opens the possibility of imaging the structure of the ion with subfemtosecond resolution through high-harmonic spectroscopy [4–6]. On the other hand, HHG may be harnessed as a source of high-frequency attosecond pulses, suitable for performing spectroscopic measurements with attosecond-to-femtosecond resolution [7, 8]. The light produced by HHG is naturally coherent—that is, phase-locked to the incident laser pulse—and has an attosecond time structure due to the attosecond dynamics of the recolliding electrons. By taking advantage of macroscopic effects, the high-harmonic light may emerge from the gas as a train of attosecond pulses [9, 10] or an isolated attosecond pulse [11]. Indeed, macroscopic effects play a paramount role in HHG: the radiation generated by a single atom is feeble, but the sum of the radiation produced by a macroscopic gas of atoms is intense enough to be measured and used in applications.

Why should we use classical mechanics to understand this fundamentally quantum phe-

nomenon? There are many compelling reasons to do so. First and foremost, the predictions of classical theories are in agreement with experimental measurements. Classical theories successfully predict the high-harmonic cutoff, i.e. the maximum radiated frequency [2, 3], the ocurrence and atomic-species dependence of NSMI in circularly-polarized fields [12–14], and the critical laser ellipticity at which a bifurcation is observed in photoelectron momentum distributions [15, 16]. Second, the classical picture is conceptually correct and much more intuitive than the quantum picture, as it is based on electron trajectories rather than wave functions. This allows for the design of effective control strategies, for example for HHG, based on manipulating the trajectories of ionized electrons [10, 17]. Third, the computational complexity of classical models typically scales linearly with the system dimension, whereas it scales exponentially for quantum models. Indeed, within the confines of today's computational resources, classical models are sometimes the only feasible option for the first-principles simulation of a laser-particle or laser-gas system. Lastly, using a classical theory as the underlying description of the laser-particle interaction allows one to tap into the vast arsenal of mathematical techniques for studying classical dynamical systems. The classical equations describing the motion of an atomic electron driven by a laser field are chaotic, therefore they can be analyzed using nonlinear dynamics [14, 18–20]. Meanwhile, the atoms interact with each other indirectly via the self-consistent electromagnetic field, much like charged particles in a plasma [21, 22]. Hence, specialized model-reduction methods rooted in the Hamiltonian properties of collisionless plasma equations [23] are also germane to laser-gas interaction.

In this thesis, we investigate the mechanisms of recollisions and HHG using techniques from nonlinear dynamics and theoretical plasma physics. First, we study the microscopic dynamics of a single atom in a very intense laser field, so intense that the atom is certain to ionize. Surprisingly, we find that delayed, high-energy recollisions persist in this regime, and we explain this behavior using the invariant manifolds of an unstable periodic orbit of the system. Then, we study the macroscopic buildup of high-harmonic radiation during the

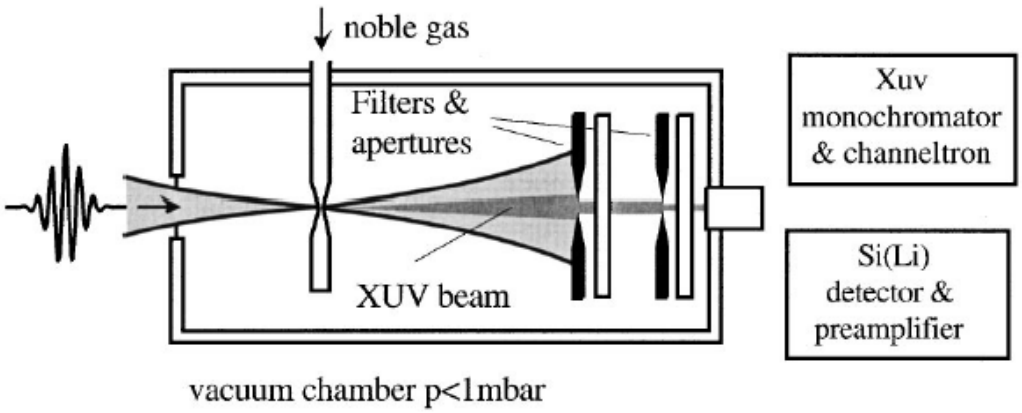


Figure 1.1: Reproduced from Ref. [24]. Schematic of a typical HHG experiment.

propagation of an intense laser pulse through an atomic gas. We derive both quantum and fully classical reduced models for the self-consistent laser-gas interaction in a Lagrangian framework on the one hand, and a Hamiltonian framework on the other. Through simulations of the models in a simplified setting, we find that the high-harmonic cutoff may be extended due to propagation effects. Phase-space analysis of the classical model reveals the emergence of higher-energy recollisions driven by the reshaping of the laser-pulse during propagation as the mechanism for this extension.

## 1.1 State of the art

Early observations of high harmonic generation (HHG) came from experiments in which intense near-infrared linearly-polarized laser pulses of tens of picoseconds in duration were focused onto rare gas jets of a few millimeters length in the pulse propagation direction. Spectrometers on the other side of the gas measure the intensity of the transmitted light as a function of frequency, as illustrated in Fig. 1.1. HHG was first reported in 1987 [25], and the first plateau in the high harmonic part of the spectrum from such an experiment followed in 1988 [26]. In the early experiments, spectra from atomic gases consisted of odd harmonics of the laser, along with resonance lines at excited states of the neutral atoms and ions. Typical spectra for three different gas species showing only the odd harmonic in-

tensities are shown in Fig. 1.2. One observes an exponential decrease in harmonic intensity until the 5th or 7th harmonic, followed by a region in which the intensity falls much more slowly on average—this is referred to as the plateau region. The plateau extends for several high harmonics up until a frequency called the high harmonic cutoff, where the harmonic intensity again drops rapidly until no more harmonics are observed. This ubiquitous feature of high-harmonic spectra is a signature of the non-perturbative nature of HHG. Indeed, perturbative calculations predict a rapid drop-off in harmonic intensity with harmonic order, in stark contrast to the plateaus which are observed [27]. In Fig. 1.2, one also readily observes a generic feature of HHG experiments: atomic gas species with smaller first ionization potentials, or $I_p$, like Xe, have a lower cutoff but higher conversion efficiency per harmonic. On the other hand, species with larger $I_p$, like Ar, have larger cutoffs but lower conversion efficiency per harmonic [27].

Advances in laser technology and the desire to harness HHG for imaging applications and attosecond pulse production have led to modifications to the HHG experiments described above. On the laser side, two notable trends have been the reduction of pulse duration and the increase in driving laser wavelength. Pulse durations first shrank to hundreds or tens of femtoseconds [28–30] and eventually hit the sub-10-fs regime [31]. The optical cycle of the oft-utilized $800\ \mathrm{nm}$ Ti:sapphire lasers is $2.7\ \mathrm{fs}$, making this the few-cycle regime. Shortening the pulse duration generally increases the maximum harmonic order that is observed, though this may happen by an extension of the plateau, an extension of the falloff region following the high harmonic cutoff, or some combination of the two, depending on other experimental parameters. More recently, HHG has been investigated with mid-infrared lasers [32–34], which has dramatically increased in the highest observed harmonics to the thousands. This effect of increasing the wavelength of the driving laser is illustrated by Fig. 1.3. On the gas side, certain experiments have replaced the millimeters-long gas jet medium with a centimeters-long hollow-core optical fiber filled with gas [33, 35, 36]. These kinds of experimental modifications, along with increased driving laser in-

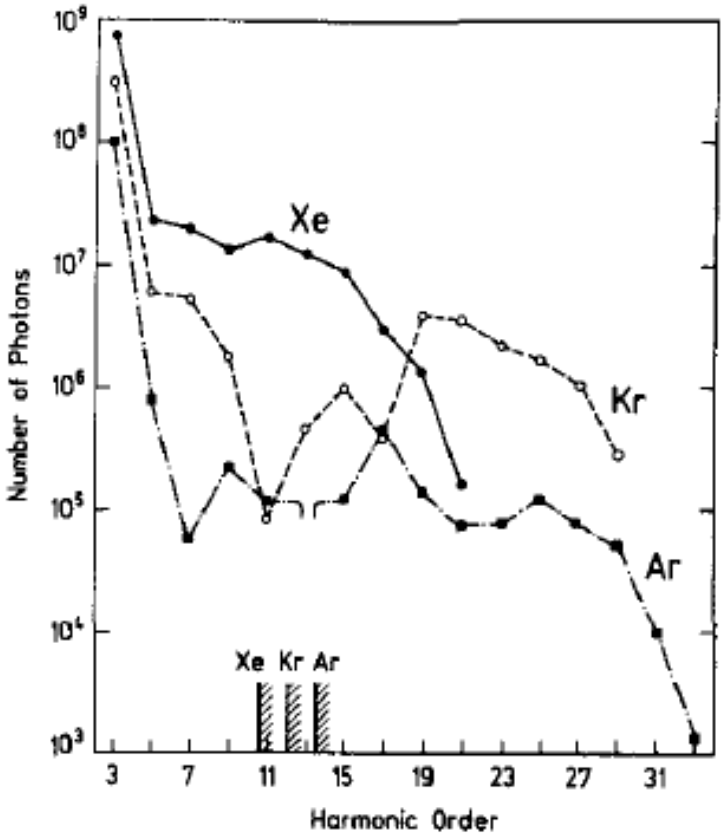


Figure 1.2: Reproduced from Ref. [27]. Typical experimental HHG spectra from Xe, Kr, and Ar with a peak laser intensity of $I = 3 \times 10^{13}$ W $\cdot$ cm$^{-2}$, a wavelength of $1064$ nm, and a pulse duration of $40$ ps. The first ionization potential $I_p$ of each atom is indicated on the horizontal axis. Only intensities of the odd harmonics are shown.

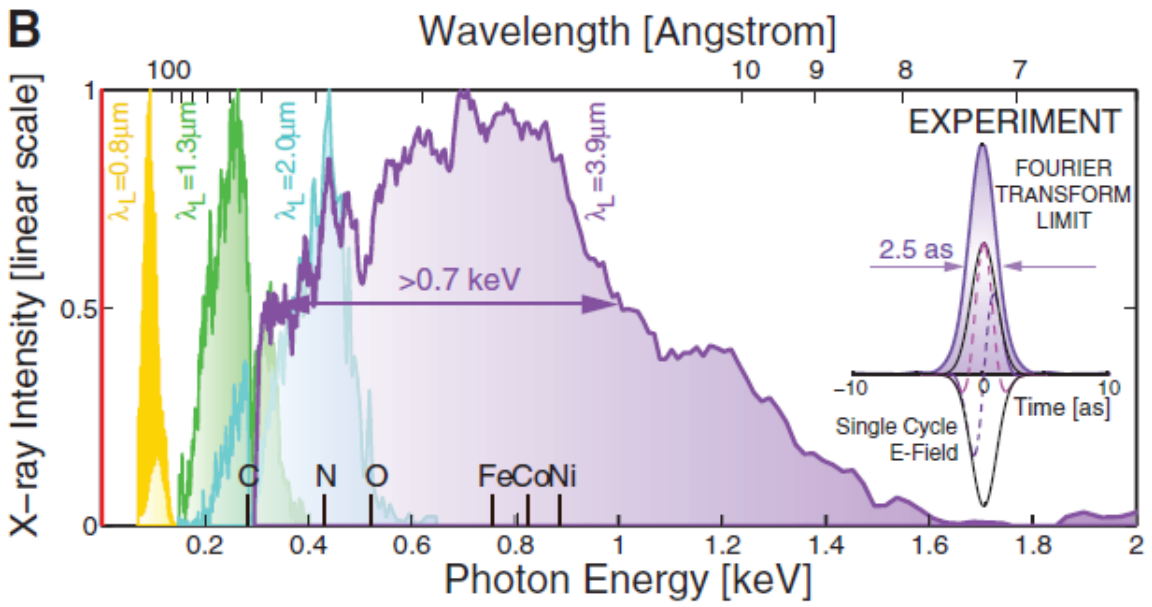


Figure 1.3: Reproduced from Ref. [33]. High-frequency part of the spectrum from HHG experiments in He with different wavelength lasers. In each case, the laser intensity and gas pressure were selected to optimize the HHG signal.

tensity [37], gas length [38], or gas density [33, 35, 39, 40], can increase the efficiency of the harmonic-conversion process and produce more intense attosecond pulses.

As the experimental parameters are pushed to further extremes, the shape of the high-harmonic spectrum inevitably undergoes dramatic changes due to the increasing importance of propagation effects. The rapid falloff following the plateau and the discrete odd-harmonic lines turn into a complicated, continuous signal over many harmonic orders, as shown in Fig. 1.3. Under conditions of high free electron density, the driving laser field undergoes tremendous reshaping while propagating through the gas due to the radiation emitted by the ionizing atoms, leading for example to a blueshift and intensity reduction [29, 41–43] throughout propagation. In this case, the high harmonic spectrum measured after propagation crucially depends on which high harmonic frequencies were produced at sufficient intensity all along the gas with just the right phase such that the radiation produced by the many atoms making up the gas adds up coherently, a collective effect referred to as phase-matching [44, 45]. One can see phase-matching unfold along the length of

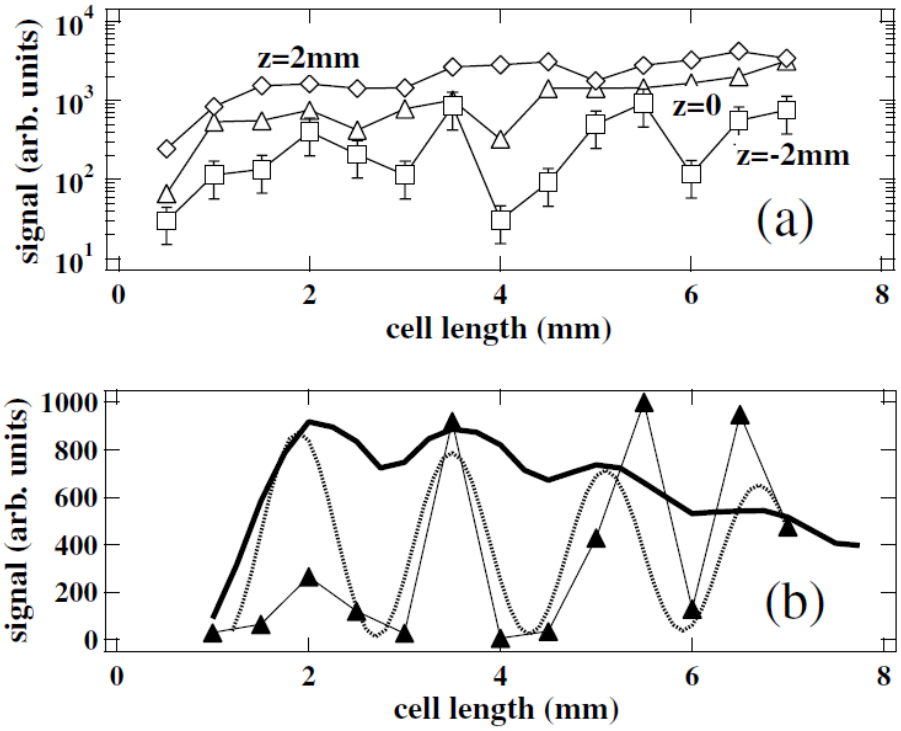


Figure 1.4: Reproduced from Ref. [38]. High harmonic yield in Ar as a function of gas-cell length. (a) Yield of harmonic 23 for different positions $z$ of the gas-cell entrance relative to the laser focus. (b) Yield of harmonic 25 at $z = -2$ mm (triangles), along with various theoretical calculations.

the gas in the experimental measurements shown in Fig. 1.4. As the total length of the gas is varied, the transmitted high-harmonic intensity, i.e. the yield, can exhibit large oscillations. This indicates alternating periods of constructive and destructive interference, or phase-matched and phase-mismatched emission, respectively, along the gas. Thus, the self-consistent interaction between the ionizing atoms and the laser field plays a decisive role in shaping the high harmonic spectrum [33, 35, 45].

Initial theoretical explanations for the structure of the high-harmonic spectrum drew on atomic physics, nonlinear optics, and plasma physics. Ideally, a theoretical or numerical treatment of HHG must bridge the gap between the microscopic response of the atoms to the electromagnetic field and the macroscopic propagation of the field through a gas of billions of atoms [27]. Atomic physicists focused on obtaining the single-atom response in the framework of the single-active-electron (SAE) approximation, studying the dynamics

of a valence electron in the combined laser and static parent ion fields. Some early approaches included numerical integration of the corresponding time-dependent Schrödinger equation (TDSE) [46, 47] and numerical integration of ensembles of classical trajectories [48, 49]. Both approaches reproduced odd harmonic generation and qualitatively reproduced the high harmonic plateau and cutoff surprisingly well, despite only being single-atom radiation spectra. On the other hand, plasma physicists were initially focused on obtaining the macroscopic electromagnetic field after propagation through the gas. Early works computed the spectra of a laser pulse propagating through a plasma with a time-dependent electron density obtained from the single-atom tunneling ionization rates [50, 51]. While odd harmonic generation was clearly captured, the high harmonic plateau was only obtained with mixed success.

Shortly thereafter, the widely-successful recollision model for the single-atom response was introduced [2, 3], and it remains the most common departure point for theories in strong field physics [53]. The recollision model follows a three-step scenario, as illustrated in Fig. 1.5: the electron is first ionized, absorbs energy while following the laser, and then is propelled back to the ionic core after the laser reverses direction, about one half laser cycle after ionization. Ionization takes place via multiphoton absorption or tunneling, depending on the intensity and frequency of the laser [54]. Once ionized, the motion of the electron may be described using classical mechanics [2, 3]. When the electron returns to the core, it exhibits quantum interference with the remaining bound state wave packet, radiating at a frequency $\omega$ such that the photon energy $\hbar\omega$ is equal to the energy difference between the bound and recolliding states [55, 56]. This step is often described more intuitively as recombination into the ground state, with the electron's excess kinetic energy released as a high-frequency photon. The high-harmonic cutoff, or maximum photon energy $\hbar\omega_{\max}$, may be determined from a purely classical calculation of the trajectory with the maximum-energy recollision [2, 3]. This results in the $\hbar\omega_{\max} = 3.17U_p + I_p$ high-harmonic cutoff law, where $U_p = e^2E_0^2/(4m_e^2\omega_L^2)$ is the pondermotive energy of an electron in an oscillating

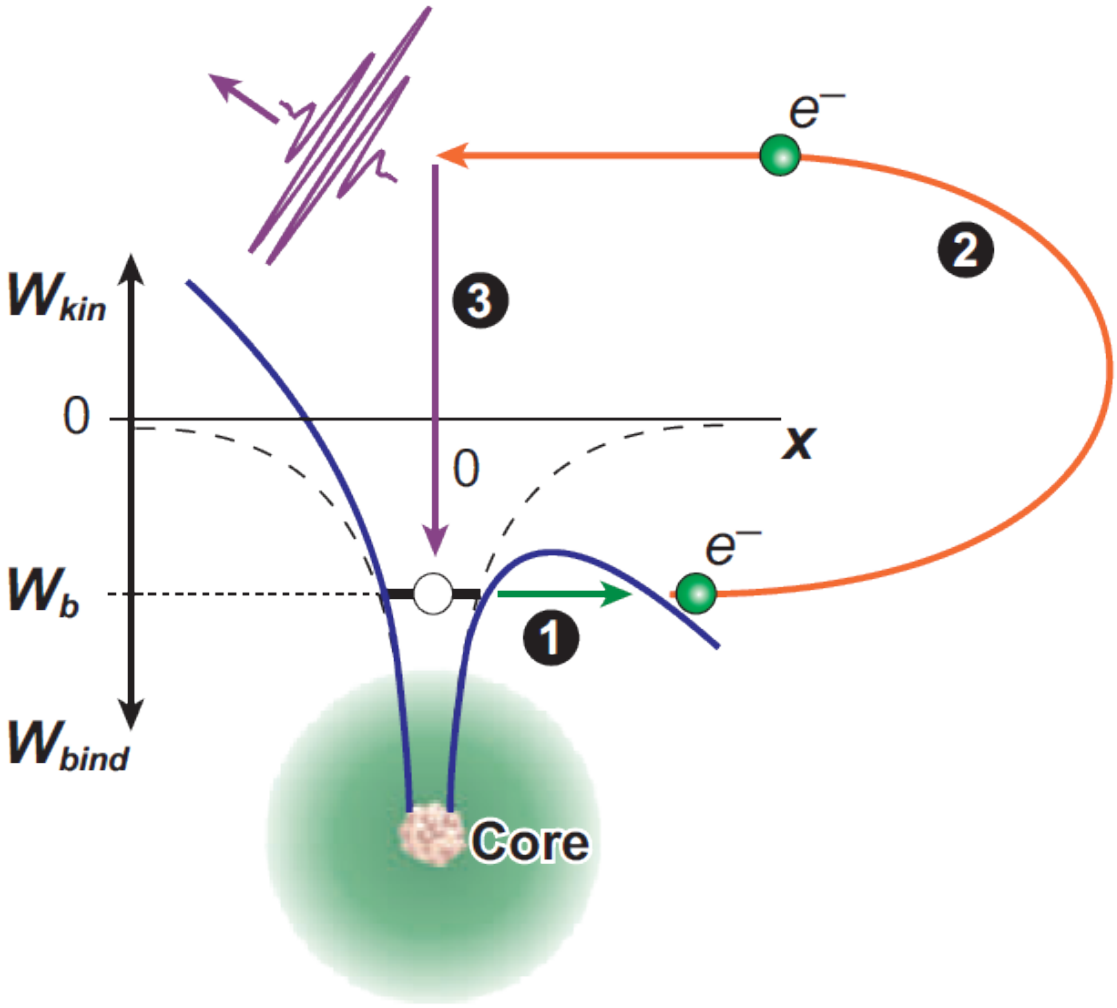


Figure 1.5: Reproduced from Ref. [52]. Schematic of the recollision model for the laser-atom interaction. An electron (1) ionizes by tunneling, (2) follows the oscillating laser field away and then back towards its parent ion, and (3) collides with its parent ion, radiating an attosecond pulse with a frequency approximately given by the electron kinetic energy.

electric field of amplitude $E_0$ and frequency $\omega_L$. This prediction is in agreement with numerical simulations of the single-atom radiation spectrum [47], but for agreement with experiments, macroscopic effects need to be taken into account [57].

For calculating the macroscopic HHG signal, the most rigorous calculation would require the self-consistent solution of Maxwell's equations in three dimensions coupled to TDSEs for the atoms [58–60]. Even today, the computational cost associated with this approach can be prohibitive, precluding the simulation of experimentally relevant sample lengths on the order of millimeters. Further, solutions of the TDSE provide limited intuition into the electron dynamics behind the single-atom response to the laser field. Thus, a common alternative consists of simplifying the description of the atomic response, splitting it into a low-frequency part dominated by ionization [42] and a high-frequency part [24, 61] comprised of the radiation of recolliding electrons. A quasistatic tunneling approximation is used to obtain the ionization rate [62], while the strong-field approximation (SFA) [63] is used to efficiently calculate the high-frequency part of the dipole radiation spectrum [44]. In the spirit of the three-step model, the SFA describes the classical motion of ionized electrons in the oscillating electric field of the laser while neglecting the Coulomb field, and the contributions of different trajectories are added coherently using a semiclassical, path-integral approach [55, 64]. This framework allows the simulation of experimental gas lengths, and the semiclassical description of the atomic response in terms of trajectories facilitates the development of control strategies based on the trajectories of electrons after ionization [17, 37, 65].

However, both the splitting of the atomic response and the SFA have some serious drawbacks. The SFA and the tunneling approximation are known to give misleading results for the ionization probability [43, 54]. Moreover, by neglecting the Coulomb field for ionized electrons, the SFA manifestly misses Coulomb focusing, i.e. the inhibited spread of the electronic wave packet due to the ion's long-range Coulomb attraction [54, 66–69]. This implies that the SFA underestimates the probability of recollision [66], and in fact

it also underestimates the energy of the recollisions [70]. Furthermore, the simplifications underlying the tunneling approximation and the SFA are inappropriate for the description of the harmonics near and below the atomic ionization threshold $I_p$ [71–74], which in certain situations can strongly influence the yield of higher harmonics [65, 75, 76]. Additionally, they leave out key elements of HHG in elliptically and circularly polarized fields [67, 77].

In addition to the aforementioned deficiencies, existing models of HHG do not provide a clear picture of the mechanisms of phase-matched buildup of high-harmonic radiation in the regime of strong mutual coupling between the atoms and the laser pulse. As a consequence, proposals for optimizing HHG (e.g. by increasing the yield) are either based on calculations of the response of a single atom to an external field [17, 78] or calculations of the macroscopic response in the limit of weak mutual coupling between the atoms and the laser [44]. The continued effectiveness of these strategies in the presence of strong macroscopic effects needs to be checked *a posteriori* [37, 79]. A more robust approach would explicitly exploit macroscopic effects, such as the ionization-driven reshaping of the laser pulse throughout propagation, to enhance phase matching [80]. To realize this, the reshaping of the electron trajectories during propagation needs to be understood [81], ideally in a way that goes beyond the SFA. Therefore, a theoretical formulation is needed which simultaneously accounts for the full complexity of the self-consistent atom-field interaction, includes the influence of the core potential on the ionized electrons, and allows for the understanding of the electron dynamics in phase space as the pulse propagates through the gas.

In this thesis, we provide such a theoretical formulation that is completely based on classical mechanics. Besides providing a representation of the electron dynamics in terms of trajectories, a completely classical framework is advantageous because it lends itself to analysis using the theory of nonlinear dynamics [82]. This theory is ideally suited to uncovering the physical mechanisms underlying both large-scale Monte Carlo simulations [48, 49, 83] and particular trajectories of relevance to HHG [2, 3, 70]. Nonlinear dynamics

allows one to describe the qualitative behavior of ensembles of trajectories and predict how these behaviors change as physical parameters are varied. This is accomplished through an identification of the invariant solutions of a system (e.g. fixed points, periodic orbits) and their invariant manifolds, when possible. In strong-field physics, this approach has proven very effective, for example by providing the first theoretical explanation of recollision and correlated double ionization in a circularly-polarized laser field [13, 14, 84]. Furthermore, when the self-consistent interaction between a gas of atoms and the electromagnetic field is cast as a classical field theory, it becomes immediately apparent that it bears many structural similarities to the theory of the self-consistent interaction of plasmas with the electromagnetic field [23]. Problems in plasma physics have spurred the development of a wide-ranging set of tools for the systematic derivation of reduced models which preserve the variational structure of the parent model, whether it be the action principle or the Hamiltonian structure [85–88]. Here, we exploit some of these tools to derive reduced classical models of the intense laser-gas interaction in a variational framework, and we use these models to identify classical mechanisms behind the coherent buildup of high-harmonic radiation.

## 1.2 Thesis work

In Ch. 2, we give brief overview of the mathematics and physics background relevant to this work. We discuss elements of the nonlinear dynamics of low-dimensional systems. Then, we describe a class of dynamical systems whose equations of motion can be obtained from variations of a single functional. Namely, we discuss systems satisfying an action principle on the one hand, and Hamiltonian systems on the other. We also cover some of the basic assumptions relying most models of strong-field physics, which are used throughout the thesis. Lastly, we give the definition of atomic units.

In Ch. 3, we investigate the electron dynamics behind HHG on a single-atom level, in the high-intensity regime. The simplest model for this is a 1.5 degree-of-freedom Hamil-

tonian system, describing one-dimensional (1D) electron motion in the potential of the ion with an external, periodic laser forcing. Though the electron motion is nearly integrable in the strong-field limit, the non-integrability has a dramatic effect on the long-time dynamics, due in part to the unbounded configuration space of the electron. We show that the non-integrability manifests itself through delayed, high-energy recollisions. Furthermore, we compute the invariant manifolds of an unstable periodic orbit of this system and show that they regulate this delayed-collision process [89]. This study lays the groundwork for our analysis of HHG in the case where the laser field is determined self-consistently from the electron dynamics.

In Ch. 4, we derive a hierarchy of reduced models from first principles which describe the self-consistent interaction occurring during the pulse propagation through the gas [90]. The derivations are rooted in variational formulations of two parent models. On the one hand, we use the Maxwell-Schrödinger equations as the parent model for a reduced quantum model. On the other hand, we use an analog of the Maxwell-Vlasov equations as the parent model for a reduced classical model. The latter constitutes the first purely classical reduced model for laser pulse propagation in atomic gases. In both cases, the systems are reduced to 1D-1D models: one dimension for the laser field, and one dimension for the motion of the electrons, as described previously. We show how the derivations could be performed in either Lagrangian or Hamiltonian formulations. The latter allows for the identification of Casimir invariants of the reduced models, which have hitherto gone unnoticed.

In Ch. 5, we carry out numerical simulations of some of the reduced models derived in the previous chapter in order to shed light on the coherent buildup of high-harmonic radiation. Our simulations show a high level of quantitative agreement between the classical and quantum models for the evolution of the laser field during propagation through a singly-ionized gas. This opens the door to understanding the high-harmonic buildup seen in the quantum calculation through a phase-space analysis of the classical model. Rather

than computing invariant manifolds, which is complicated by the aperiodicity of the self-consistent electric field, we employ a statistical trajectory analysis. We show for the first time that propagation effects can lead to an increase in maximum recollision energy, along with the concomitant increase of the high-harmonic cutoff. Our analysis highlights the interplay between Coulomb effects and the reshaping of the laser field as the mechanism for this cutoff extension [91]. We also investigate whether the classical model can be used to describe harmonic generation occurring during the ionization process itself. We find that the classical model can be optimized to match the quantum ionization rate, leading to accurate classical propagation calculations, even with ground-state atoms (as opposed to pre-ionized atoms). Based on this result, we use the classical model to trace the coherent radiation observed in certain parts of the spectrum to its origin in phase space, by separating the contributions of bound electrons from ionized electrons.

# CHAPTER 2

# BACKGROUND

In this chapter, we give an overview of mathematical techniques and physical assumptions used throughout the thesis. In Sec. 2.1, we review nonlinear dynamics for low-dimensional systems [82]. In Sec. 2.2, we review the variational formulation of mechanical systems, including discrete (finite-dimensional) and continuous (infinite-dimensional) systems. In Sec. 2.3, we state some of the basic physical assumptions of strong-field physics that we rely on in this thesis. Lastly, in Sec. 2.3, we define atomic units, which are used throughout the rest of the thesis.

## 2.1 Nonlinear dynamics

A dynamical system is a set of variables $\mathbf{z}$ describing the state of the system, and an evolution law that specifies how the state changes with time $t$. We take $d$ to be the dimension of the system, i.e. the number of variables. The space of all possible states is referred to as state space, and here we assume $\mathbf{z} \in \mathbb{R}^n$. The evolution law is specified as

$$\dot{\mathbf{z}} = F(\mathbf{z}), \tag{2.1}$$

where the over-dot signifies the time derivative $d/dt$ and $F : \mathbb{R}^n \to \mathbb{R}^n$ is a function giving the present velocity of the state. Here, we assume $F$ has no explicit time-dependence, because systems with time-dependence $F(\mathbf{z}, t)$ may be autonomized, i.e. brought into the form of Eq. (2.1), by extending the state-space dimension to accommodate time as an additional dynamical variable.

When $d \geq 3$ and $F$ is a nonlinear function, the solutions $\mathbf{z}(t)$ of Eq. (2.1) can be chaotic. By chaotic, we mean these solutions are (i) extremely sensitive to the initial con-

ditions $\mathbf{z}_0 \equiv \mathbf{z}(0)$, and (ii) recurrent, meaning that solutions can be found which return near the vicinity of $\mathbf{z}_0$ an arbitrarily large number of times. It is possible to gain insight into this complicated dynamical behavior by analyzing the system's compact, invariant sets of solutions. Examples include equilibria: solutions of $F(\mathbf{z}_0) = 0$ such that $\mathbf{z}(t) = \mathbf{z}_0$; and periodic orbits: solutions with a period $T > 0$ such that $\mathbf{z}(t + T) = \mathbf{z}(t)$. If $\mathbf{z}_0^*$ is an initial condition along a periodic orbit of period $T$, then one can study the behavior of infinitesimally-close initial conditions $\mathbf{z}_0^* + \delta\mathbf{z}_0$ by linearizing the flow around $\mathbf{z}^*(t)$. With this procedure, the initial displacement evolves to $\delta\mathbf{z}(t) = \mathbf{J}(t)\delta\mathbf{z}_0$, where $\mathbf{J}(t)$ is the tangent-flow matrix corresponding to the periodic orbit $\mathbf{z}^*(t)$. It satisfies the differential equation

$$\dot{\mathbf{J}} = \partial_{\mathbf{z}} F(\mathbf{z}^*(t)) \cdot \mathbf{J}, \tag{2.2}$$

where the initial condition of $\mathbf{J}$ is the identity matrix, i.e. $\mathbf{J}(0) = I_d$. The eigenvalues $\{\lambda_i\}_{i=1}^d$ of $\mathbf{J}(T)$ are uniquely determined by the chosen periodic orbit; in particular, they are the same for any $\mathbf{z}_0^*$ chosen along the same orbit and in any coordinate system. Besides the trivial marginal eigenvalue $\lambda_1 = 1$ (for the eigenvector $F(\mathbf{z}_0^*)$), the rest of the eigenvalues give information on the linear stability of the orbit.

Here, we concentrate on the $d = 3$ case, considering the situation where one of the remaining eigenvalues is unstable, $|\lambda_u| > 1$, and the other is stable, $|\lambda_s| < 1$. At $t = 0$, a displacement in the direction of the stable eigenvector would approach the periodic orbit exponentially quickly as $t \to \infty$, while a displacement in the direction of the unstable eigenvector would approach the periodic exponentially quickly as $t \to -\infty$. Conversely, for short positive times, the unstably-displaced trajectory escapes from the periodic orbit exponentially quickly. Hence, an arbitrary displacement may evolve closer to the periodic orbit along the stable direction, but eventually leaves the orbit by following the unstable direction. The eigenvectors can be continued far away from the periodic orbit by defining

the orbits' stable and unstable manifolds,

$$\mathcal{W}^s = \{\mathbf{z}_0 \mid \mathbf{z}(t) \to \mathbf{z}^*(t) \text{ as } t \to \infty\}, \tag{2.3a}$$

$$\mathcal{W}^u = \{\mathbf{z}_0 \mid \mathbf{z}(t) \to \mathbf{z}^*(t) \text{ as } t \to -\infty\}. \tag{2.3b}$$

The stable and unstable manifolds are the sets of initial conditions that asymptotically approach the periodic orbit in forwards and backwards in time, respectively. Due to their asymptotic definition, they are invariant under the flow. Furthermore, for $d = 3$, these manifolds are co-dimension $1$. Therefore, they form time-independent barriers in state space. The different regions which they carve out tend to exhibit qualitatively different dynamical behavior. When these manifolds intersect transversely, the system exhibits chaotic behavior. By computing these manifolds and examining the different regions of state space which they enclose, one can identify the mechanisms underlying features of interest of the chaotic motion.

It is most straightforward to calculate the manifolds on the Poincaré surface of section. The Poincaré section is a co-dimension $1$ surface in state space which is selected such that the orbits in a particular region of interest intersect the surface transversely. An example is schematically illustrated in Fig. 2.1. The surface $\Sigma$ is defined by a constraint on the state space $g(\mathbf{z}) = 0$, for a scalar function $g$, and an orientation, e.g. $dg/dt > 0$. A map on the surface $\mathcal{P} : \Sigma \to \Sigma$ can be defined which takes a point on the surface $\mathbf{z}_0$ to the point $\mathbf{z}(T_\mathcal{P})$, where $T_\mathcal{P}$ is the next time the trajectory with initial condition $\mathbf{z}_0$ pierces the surface of section. Thus, $\mathcal{P}(\mathbf{z}_0) = \mathbf{z}(T_\mathcal{P})$, as illustrated by the blue dots in Fig. 2.1. Here, we also show that periodic orbits are fixed points of the Poincaré map, i.e. $\mathcal{P}(\mathbf{z}_0^*) = \mathbf{z}_0^*$, illustrated by the red dot. Hence, the problem of studying the flow of Eq. (2.1) in the 3D state space (in this case) is reduced to studying a map $\mathcal{P}$ on a 2D surface $\Sigma$. The 2D invariant manifolds of Eqs. (2.3) of the periodic orbit become 1D invariant manifolds of the fixed point of $\mathcal{P}$—they are equivalent to the intersection of the full state-space manifolds with $\Sigma$. Significantly, no

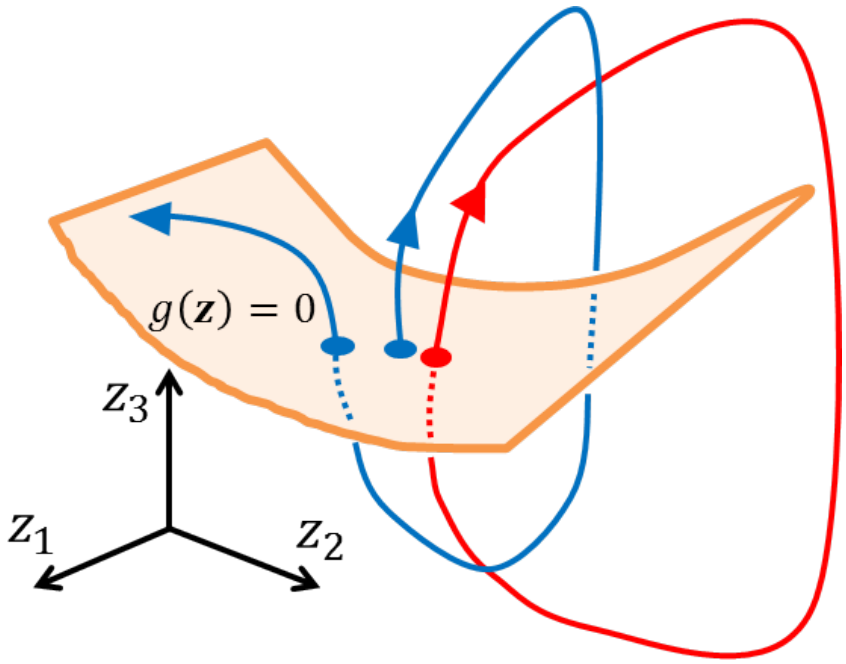


Figure 2.1: Illustration of the Poincaré section $g(\mathbf{z}) = 0$ for some scalar function of the dynamical variables $g$. The red curve depicts a periodic orbit, while the blue curve a typical, aperiodic trajectory. The points where the trajectories intersect the surface of section constitute iterates of the Poincaré map.

dynamical information is lost by this apparent reduction, yet the analysis is simplified.

## 2.2 Dynamical systems with a variational formulation

A general dynamical system such as Eq. (2.1) can in principle be specified by $d$ independent scalar functions—the components of $F$—but certain dynamical systems may be obtained by variations of a single scalar function (or functional) with respect to the $d$ dynamical variables [92, 93]. This is the case for the fundamental laws of physics. They can be formulated either in terms of a principle of least action or as a Hamiltonian system, and there is often a direct link between the two formulations. We do not review this link here, focusing instead on practical aspects of each formulation separately.

### 2.2.1 Action principles

*Finite-dimensional systems*

We consider a finite dimensional system with a configuration space $\mathbb{R}^d$, whose configuration at time $t$ is specified by $\mathbf{x}(t) \in \mathbb{R}^d$. Here, configuration space has a different meaning from state space, which we explain shortly. We assume that the evolution of the system's configuration $\mathbf{x}(t)$ obeys the principle of least action. That is, there is a scalar function $\mathcal{L}(\mathbf{x}, \dot{\mathbf{x}})$ and an action functional

$$\mathcal{A}[\mathbf{x}(t)] = \int_{t_1}^{t_2} \mathcal{L}(\mathbf{x}, \dot{\mathbf{x}}) \mathrm{d}t \tag{2.4}$$

such that the trajectories $\mathbf{x}(t)$ satisfy $\delta\mathcal{A} = 0$: they are extrema of the action functional. $\mathcal{L}$ is called the Lagrangian of the system, and in general it may also depend on $t$, though we do not consider this here for simplicity.

More precisely, the principle of least action means that, for small, arbitrary variations of the trajectories $\mathbf{x}(t) \to \mathbf{x}(t) + \varepsilon\delta\mathbf{x}(t)$ that vanish at the boundaries ($\delta\mathbf{x}(t_1) = \delta\mathbf{x}(t_2) = 0$), the change in the action $\delta\mathcal{A} = \mathcal{A}[\mathbf{x}(t) + \varepsilon\delta\mathbf{x}(t)] - \mathcal{A}[\mathbf{x}(t)]$ is of order $\varepsilon^2$. This implies that $\mathcal{A}_{x_i} = 0$ for each $i$, where $\mathcal{A}_{x_i}$ is the functional derivative of $\mathcal{A}$ with respect to $x_i(t)$, defined by

$$\mathcal{A}[\mathbf{x}(t) + \varepsilon\delta x_i(t)\hat{\mathbf{x}}_i] - \mathcal{A}[\mathbf{x}(t)] = \varepsilon \int_{t_1}^{t_2} \mathcal{A}_{x_i}(t)\delta x_i(t)\mathrm{d}t + \mathcal{O}(\varepsilon^2). \tag{2.5}$$

By substituting Eq. (2.4) into Eq. (2.5), we can apply the principle of least action to obtain the Euler-Lagrange equations,

$$\frac{d}{dt}\left(\frac{\partial\mathcal{L}}{\partial\dot{x}_i}\right) - \frac{\partial\mathcal{L}}{\partial x_i} = 0, \tag{2.6}$$

for each $i$. To obtain these equations, in particular the explicit time derivative, integration

by parts has been used. Additional work is required to identify the state space underlying Eq. (2.6) in order to transform it into the dynamical system form of Eq. (2.1). For example, if $\mathcal{L}$ contains quadratic terms of $\dot{\mathbf{x}}$, its Euler-Lagrange equations are a system of second-order differential equations. This situation is common for many mechanical systems, and often the solution consists of defining the dynamical variables as $(\mathbf{x}, \mathbf{v}) = (\mathbf{x}, \dot{\mathbf{x}})$, allowing the $d$ second-order equations (2.6) to be transformed into $2d$ first-order equations, like Eq. (2.1). However, when this cannot be done, the procedure may be more involved [94]. In any event, the existence of an underlying action principle of a given dynamical system is a fundamental property of that system. Namely, it is independent of the coordinates chosen to parametrize the configuration space. While one always has the flexibility of choosing the coordinates most suitable for a particular problem, it is considerably easier to implement the coordinate transformation on the action (2.4), rather than the $d$ or $2d$ dynamical evolution equations.

*Infinite-dimensional systems*

Going beyond finite-dimensional dynamical systems, one can consider infinite-dimensional dynamical systems, i.e. systems of coupled partial differential equations with a privileged evolution parameter $t$. Some of these systems have evolution laws that also can be obtained from an action principle. We consider a set of $n$ fields $\{\phi_i(\mathbf{z}, t)\}$, where $\phi_i : \mathbb{R}^{d+1} \to \mathbb{R}$ for each $i$ and $\mathbf{z} \in \mathbb{R}^d$ is a continuous label for each field. The action generally takes the form

$$\mathcal{A}[\{\phi_i(\mathbf{z}, t)\}] = \int_{t_1}^{t_2} L(\{\phi_i\}, \{\partial_{\mathbf{z}}\phi_i\}, \{\dot{\phi}_i\}) \mathrm{d}^d\mathbf{z}\mathrm{d}t, \tag{2.7}$$

where $L$ is referred to as the Lagrangian density. In this case, the principle of least action $\delta\mathcal{A} = 0$ implies $\mathcal{A}_{\phi_i} = 0$ for every $i$. This yields the Euler-Lagrange equations in the continuous case,

$$\frac{d}{dt}\frac{\partial L}{\partial \dot{\phi}_i} + \partial_{\mathbf{z}} \cdot \frac{\partial L}{\partial(\partial_{\mathbf{z}}\phi_i)} - \frac{\partial L}{\partial \phi_i} = 0. \tag{2.8}$$

Here, we have also used integration by parts, and we have assumed that the boundary terms associated with the $\mathbf{z}$ domain vanish. Like in in the finite-dimensional case, the system of equations above is not in the dynamical system form (Eq. (2.1) generalized for fields) in general, so an additional effort needs to be made to bring them to this form.

### 2.2.2 The link with Hamiltonian systems

Here, we consider an action principle which is linear in the time derivatives of the configuration space variables, which motivates the definition of a Hamiltonian system to follow. We focus on the finite-dimensional case, for simplicity. In this case, the action principle takes the general form

$$\mathcal{A}[\mathbf{x}(t)] = \int_{t_1}^{t_2} \left[\gamma_j(\mathbf{x})\dot{x}_j - H(\mathbf{x})\right] \mathrm{d}t, \tag{2.9}$$

where the Einstein summation convention has been used. Here, $\boldsymbol{\gamma} : \mathbb{R}^d \to \mathbb{R}^d$ is a vector of functions of the configuration space variables $\mathbf{x}$ and $H : \mathbb{R}^d \to \mathbb{R}$ is a scalar function. The Euler-Lagrange equations $\mathcal{A}_{\mathbf{x}_i} = 0$ become

$$\left(\partial_i\gamma_j - \partial_j\gamma_i\right)\dot{x}_j - \partial_i H = 0, \tag{2.10}$$

where we have used the shorthand notation $\partial_i F \equiv \partial_{x_i} F$ for a function $F$. Because the Lagrangian of the action (2.9) is linear in $\dot{\mathbf{x}}$, Eq. (2.10) constitutes a set of first-order differential equations for $\mathbf{x}$. If these equations can be brought to the form of Eq. (2.1), then $\mathbf{x}$ would actually represent a proper set of dynamical variables—the configuration space would be equivalent to the state space.

To investigate when this happens, we introduce the Lagrange matrix $\boldsymbol{\omega}$, whose elements are $\omega_{ij}(\mathbf{x}) = \partial_i\gamma_j(\mathbf{x}) - \partial_j\gamma_i(\mathbf{x})$. Thus, the Lagrange matrix is antisymmetric. Then,

Eq. (2.10) can be rewritten in matrix form as

$$\boldsymbol{\omega}(\mathbf{x})\dot{\mathbf{x}} = \partial_{\mathbf{x}} H,$$

Hence, if $\boldsymbol{\omega}$ is invertible, then the above equation can be written in the form of Eq. (2.1). We denote the inverse of $\boldsymbol{\omega}$ as $\boldsymbol{\Pi}$, and thus the equation above can be rewritten as

$$\dot{\mathbf{x}} = \boldsymbol{\Pi}(\mathbf{x})\partial_{\mathbf{x}} H. \tag{2.11}$$

This equation motivates the definition of Hamiltonian systems.

### 2.2.3 Hamiltonian systems

Hamiltonian systems are dynamical systems whose equations of motion may be obtained from a Hamiltonian $H$ and a Poisson bracket $\{\cdot,\cdot\}$. The Hamiltonian is an observable, meaning it is a scalar function of the dynamical variables and possibly the time $t$. Meanwhile, the Poisson bracket is a binary operation which takes two observables, $F$ and $G$, and produces a third observable $\{F, G\}$. The evolution equations for an arbitrary observable $F$ are obtained by $\dot{F} = \{F, H\} + \partial_t F$. The evolution equations for the dynamical system are obtained by substituting the dynamical variables into this equation. For arbitrary observables $F$, $G$, and $H$, the Poisson bracket satisfies the following properties:

$$\{F, G\} = -\{G, F\} \qquad \text{(antisymmetry)}$$

$$\{F + G, H\} = \{F, H\} + \{G, H\},\ \{F, G + H\} = \{F, G\} + \{F, H\} \qquad \text{(bilinearity)}$$

$$\{FG, H\} = F\{G, H\} + G\{F, H\} \qquad \text{(Leibniz rule)}$$

$$\{F, \{G, H\}\} + \{G, \{H, F\}\} + \{H, \{F, G\}\} = 0 \qquad \text{(Jacobi identity)}$$

An immediate consequence of the antisymmetry of the bracket is that a Hamiltonian $H$ which does not depend explicitly on time is conserved by the flow, i.e. $\dot{H} = \{H, H\} =$

$-\{H, H\} = 0$.

*Finite-dimensional systems*

For a finite-dimensional system of dimension $d$, an arbitrary observable $F$ is a scalar function of $d$ variables, $F = F(\mathbf{z})$, and the Poisson bracket reads

$$\{F(\mathbf{z}), G(\mathbf{z})\} = \Pi_{ij}(\mathbf{z})\partial_i F(\mathbf{z})\partial_j G(\mathbf{z}), \tag{2.12}$$

where again the Einstein summation convention is used, and $\mathbf{\Pi}(\mathbf{z})$ is the $d \times d$ Poisson matrix. The equations of motion for a system with Hamiltonian $H(\mathbf{z})$ are obtained by $\dot{\mathbf{z}} = \{\mathbf{z}, H\}$, giving

$$\dot{\mathbf{z}} = \mathbf{\Pi}(\mathbf{z})\partial_{\mathbf{z}} H. \tag{2.13}$$

This equation is exactly the same form as Eq. (2.11), which hints at the connection between systems with an action principle of the form (2.9) and Hamiltonian systems. To make this connection clearer, we now discuss how the conditions on the Poisson bracket, in particular the Jacobi identity, are automatically satisfied when $\mathbf{\Pi}$ is obtained as the inverse of the Lagrange matrix.

With the form of Eq. (2.12), it is clear that the Poisson bracket satisfies bilinearity and the Leibniz rule. For antisymmetry, $\mathbf{\Pi}$ must be an antisymmetric matrix. This property is automatically satisfied if $\mathbf{\Pi}$ is the inverse of $\boldsymbol{\omega}$, because $\boldsymbol{\omega}$ is also antisymmetric. The Jacobi identity imposes additional requirements on $\mathbf{\Pi}$. We calculate explicitly the first term of the Jacobi identity, for arbitrary observables $F$, $G$, and $H$:

$$\{F, \{G, H\}\} = \Pi_{in}\partial_n \Pi_{jk}\partial_i F \partial_j G \partial_k H + \Pi_{in}\Pi_{jk}\partial_i F \left(\partial^2_{nj} G \partial_k H + \partial_j G \partial^2_{nk} H\right). \tag{2.14}$$

Now, the Jacobi identity is calculated by summing the right-hand side of the above expression over all three cyclic permutations of $FGH$. By the antisymmetry of $\mathbf{\Pi}$, the second-

derivative terms in the second term of Eq. (2.14) sum to zero; this is sometimes referred to as Morrison's lemma [95], and a proof is given in App. A. Hence, the Jacobi identity is reduced to

$$\Pi_{in}\partial_n\Pi_{jk} + \Pi_{jn}\partial_n\Pi_{ki} + \Pi_{kn}\partial_n\Pi_{ij} = 0, \tag{2.15}$$

for all $i$, $j$, and $k$. One sees immediately that if $\mathbf{\Pi}$ is antisymmetric and does not depend on the dynamical variables, then the Jacobi identity is automatically satisfied. It is also satisfied when $\mathbf{\Pi}$ is the inverse of the Lagrange matrix $\boldsymbol{\omega}$. To prove this, one uses the following additional properties:

$$\partial_k\omega_{ij} + \partial_i\omega_{jk} + \partial_j\omega_{ki} = 0, \tag{2.16}$$

for all $i$, $j$, and $k$, and

$$\partial_i\mathbf{\Pi} = -\mathbf{\Pi}\partial_i\boldsymbol{\omega}\mathbf{\Pi}. \tag{2.17}$$

The former is obtained from the definition of the Lagrange matrix and the commutativity of derivatives with respect to the dynamical variables. The latter is obtained by differentiating $\boldsymbol{\omega}\mathbf{\Pi} = I_{2d}$. Equations (2.15) and (2.16) are each implied by the other. Therefore, the Jacobi identity and the existence of an action principle are inextricably linked.

A time-independent Hamiltonian system is referred to as a canonical Hamiltonian system when it is expressed in the following form. The dimension $d = 2n$ must be even, and $n$ is called the number of degrees-of-freedom (dof). The dynamical variables of such systems are divided up as $\mathbf{z} = (\mathbf{q}, \mathbf{p})$, where $\mathbf{q} \in \mathbb{R}^n$ is the set of generalized position variables and $\mathbf{p} \in \mathbb{R}^n$ is the set of canonical momenta. For Hamiltonian systems, state space is also referred to as phase space, and together, $(\mathbf{q}, \mathbf{p})$ are the so-called canonical coordinates of phase space. They are such that the Poisson matrix $\mathbf{\Pi}_c$ is expressed in block-diagonal form as

$$\mathbf{\Pi}_c = \begin{pmatrix} 0 & I_n \\ -I_n & 0 \end{pmatrix}. \tag{2.18}$$

This matrix is antisymmetric and, because it does not depend on the dynamical variables, the Poisson bracket satisfies the Jacobi identity. Meanwhile, the canonical Lagrange matrix is $\boldsymbol{\omega}_c = -\boldsymbol{\Pi}_c$, with the vector $\boldsymbol{\gamma} = (\mathbf{p}, \mathbf{0})$. Hence, the corresponding action has the form

$$\mathcal{A}[(\mathbf{q}(t), \mathbf{p}(t)] = \int_{t_1}^{t_2} [\mathbf{p} \cdot \dot{\mathbf{q}} - H(\mathbf{q}, \mathbf{p})] \, \mathrm{d}t,$$

which is referred to as the phase space action principle. Because canonical Hamiltonian systems satisfy $\dot{\mathbf{q}} = \partial_{\mathbf{p}} H$, the integrand of the action above is recognized as the Legendre transform of the Hamiltonian $H(\mathbf{q}, \mathbf{p})$, exchanging the variables $\mathbf{p}$ for $\dot{\mathbf{q}}$. This is the typical relationship between the Hamiltonian and the Lagrangian $\mathcal{L}(\mathbf{q}, \dot{\mathbf{q}})$. However, this action functional is distinct from one which depends only on $\mathbf{q}(t)$, because in the functional above, $\mathbf{p}(t)$ can be varied independently of $\mathbf{q}(t)$.

Canonical Hamiltonian systems, i.e. dynamical systems obeying Eq. (2.13) with $\boldsymbol{\Pi} = \boldsymbol{\Pi}_c$, have constrained stability properties of their orbits. In particular, if $\lambda$ is an eigenvalue of the tangent flow matrix $\mathbf{J}(t)$ of an arbitrary orbit, then so is $1/\lambda$. This is a consequence of the fact that $\mathbf{J}(t)$ is a symplectic matrix, i.e. it verifies

$$\mathbf{J}^T \boldsymbol{\Pi}_c \mathbf{J} = \boldsymbol{\Pi}_c. \tag{2.19}$$

This can be shown by observing that $\mathbf{J}(0) = I_{2n}$ is a symplectic matrix, and then taking the time derivative of Eq. (2.19) and using Eqs. (2.2), (2.13) and the fact that $\boldsymbol{\Pi}^2 = -I_{2n}$. As a consequence, there are no strictly attracting or strictly repelling orbits—that is, orbits with all eigenvalues $|\lambda| < 1$ or $|\lambda| > 1$, respectively. This is the content of Liouville's theorem, which states that phase space volume is conserved ($\det \mathbf{J} = 1$).

In fact, these constraints hold for noncanonical Hamiltonian systems as well. Noncanonical Hamiltonian systems are systems whose Poisson matrix $\boldsymbol{\Pi}(\mathbf{z})$ has a form other than Eq. (2.18); in particular, it may explicitly depend on the dynamical variables. When $\boldsymbol{\Pi}(\mathbf{z})$ is nondegenerate (implying the system is even-dimensional), Darboux's theorem

guarantees that one can always construct local canonical coordinates in any Hamiltonian system [85], thus implying the same stability constraints as in the canonical case. Non-canonical systems are also allowed to have degenerate Poisson matrices, i.e. Poisson matrices with a nontrivial null space. An observable $C$ whose gradient (with respect to the dynamical variables) is in the null space of $\mathbf{\Pi}$, i.e. $\mathbf{\Pi}(\mathbf{z})\partial_{\mathbf{z}}C(\mathbf{z}) = 0$, is called a Casimir invariant. Because of this property, Casimir invariants satisfy $\{C, F\} = 0$ for arbitrary observables $F$. Hence, Casimirs, and any function of them, are conserved for any Hamiltonian $H$. One typical example of a Hamiltonian system with a Casimir invariant is any odd-dimensional Hamiltonian system. Such a system must have at least one Casimir invariant, due to the antisymmetry of $\mathbf{\Pi}$.

When one starts with a canonical $n$ dof Hamiltonian system, one may modify the Hamiltonian such that it has an explicit time-dependence, meaning the Hamiltonian is of the form $H(\mathbf{z}, t)$. Here, the equations of motion are obtained in the same way, but the system is said to have $n + 1/2$ degrees of freedom. Significantly, $H$ is no longer a conserved quantity when it depends explicitly on time. The phase space of a $n + 1/2$ dof system is $2n + 1$-dimensional. In particular, for $n = 1$, dimension of phase space is $d = 3$. Hence, the considerations of Sec. 2.1 for $d = 3$ dynamical systems are directly relevant. Any $n + 1/2$ dof system can be autonomized: it can be transformed into an $n + 1$ dof, time-independent Hamiltonian system. To accomplish this, the dimension of phase space is extended by adding the variables $(\tau, k)$, where $\tau$ is akin to time and $k$ is akin to energy. The Hamiltonian $H_{\text{aut}}$ of the new system and the Poisson bracket $\{F, G\}_{\text{aut}}$ become

$$H_{\text{aut}}(\mathbf{z}, \tau, k) = H(\mathbf{z}, \tau) + k, \tag{2.20a}$$

$$\{F, G\}_{\text{aut}} = \{F, G\} + \partial_\tau F \partial_k G - \partial_k F \partial_\tau G. \tag{2.20b}$$

In the autonomous system, $\dot{\tau} = 1$, making the evolution of $\tau$ identical to time evolution, while the equations for the $\mathbf{z}$ variables are the same as they were before. The additional

equation for $k$, $\dot{k} = -\partial_\tau H$, serves to make $H_{\mathrm{aut}}$ a conserved quantity.

*Infinite-dimensional systems*

Certain infinite-dimensional systems, i.e. dynamical systems involving fields, may also have a Hamiltonian form. We consider a system of $n$ fields $\{\phi_i(\mathbf{z})\}$, where $\phi_i : \mathbb{R}^d \to \mathbb{R}$ for each $i$ and $\mathbf{z} \in \mathbb{R}^d$ is a continuous label for each field. Here, we have neglected to write the time-dependence of the fields explicitly. For this system, observables are functionals of the fields, $\mathcal{F}[\{\phi_i\}]$. The equations of motion for this system of fields are said to be Hamiltonian if one can find a Hamiltonian $\mathcal{H}[\{\phi_i\}]$ and a Poisson bracket between observables, $\{\mathcal{F}, \mathcal{G}\}$,

$$\mathcal{H}[\{\phi_i\}] = \int H\left(\{\phi_i\}, \{\partial_{\mathbf{z}}\phi_i\}\right) \mathrm{d}^d\mathbf{z}, \tag{2.21a}$$

$$\{\mathcal{F}, \mathcal{G}\} = \int \mathcal{F}_{\phi_i} \hat{\Pi}_{ij}\left(\{\phi_k\}, \{\partial_{\mathbf{z}}\phi_k\}, \mathbf{z}\right) \mathcal{G}_{\phi_j} \mathrm{d}^d\mathbf{z}, \tag{2.21b}$$

such that the field equations may be obtained using the evolution law $\dot{\phi}_k = \{\phi_k, \mathcal{H}\}$. In Eq. (2.21a), $H$ is a scalar function called the Hamiltonian density, while in Eq. (2.21b), $\hat{\mathbf{\Pi}}\left(\{\phi_k\}, \{\partial_{\mathbf{z}}\phi_k\}, \mathbf{z}\right)$ is a matrix of operators, which is allowed to have an explicit dependence on the dynamical variables. The implicit sums in the bracket run from 1 to $n$.

For Eq. (2.21b) to be a Poisson bracket, it must satisfy all the properties stated at the beginning of this section. Again, bilinearity and the Leibniz rule are inherent in the form of the bracket. Antisymmetry requires that $\hat{\Pi}_{ij}$ be anti-self-adjoint for all $i$ and $j$. The Jacobi identity allows one to derive a more restrictive constraint on the operator matrix $\hat{\mathbf{\Pi}}$, in the spirit of Eq. (2.15), though the general expression in the continuous case is more cumbersome [95]. In practice, it may be more straightforward to verify the Jacobi identity of a given bracket directly. We remark that Casimir invariants, $\mathcal{C}[\{\phi_i\}, \{\partial_{\mathbf{z}}\phi_i\}]$, defined $\{\mathcal{C}, \mathcal{F}\} = 0$ for arbitrary observables $\mathcal{F}$ as in the finite-dimensional case, are very common in infinite-dimensional Hamiltonian systems.

## 2.3 Basic assumptions in strong-field physics

This thesis concerns the interaction of atoms with strong electromagnetic waves. Frequently, the following assumptions are made before even writing down an interaction Hamiltonian:

- single-active-electron (SAE) approximation,
- non-relativistic electrons,
- static ions,
- dipole approximation.

We explain and justify these assumptions in the following. The first assumption is that the interaction of the electron of interest—usually described as the most loosely-bound valence electron—with the rest of the atom's electrons and nucleus can be described by a time-independent potential $V(\mathbf{x})$, where $\mathbf{x} \in \mathbb{R}^3$ is the position of the privileged electron relative to the ion. This is of course only sensible for single-electron processes, which are the only kind we consider in this thesis. Of particular interest will be the motion of the electron after ionization, when it is far away from the ionic core and thus primarily driven by the laser. The ranges of interest for the laser parameters are peak intensities $I \sim 10^{13}$–$10^{16}$ $\mathrm{W{\cdot}cm^{-2}}$ and wavelengths $\lambda_L \sim 0.8$–$2$ $\mu\mathrm{m}$. Thus, the importance of relativistic effects may be judged by comparing the speed of light $c$ to the quiver velocity of a non-relativistic free electron,

$$v_{\mathrm{quiver}} = \frac{eE_0\lambda_L}{2\pi m_e c}, \tag{2.22}$$

where $E_0 = \sqrt{2I/\epsilon_0 c}$ is the peak electric field amplitude of a wave with intensity $I$. The largest value of $v_{\mathrm{quiver}}/c$ encountered in this thesis, for $I = 10^{16}$ $\mathrm{W \cdot cm^{-2}}$ and $\lambda_L = 0.8$ $\mu\mathrm{m}$, is $v_{\mathrm{quiver}}/c \approx 0.07$. Hence, we neglect relativisitc effects in the thesis, as is routinely done by the strong-field community [24]. The motion of the ionic part of

the atom can also be safely neglected. Indeed, already in the case of hydrogen, the quiver velocity of the proton would already be $m_p/m_e \approx 1836$ times smaller than that of the electron.

Under these three assumptions, the motion of the atomic electron in the potential of the ion and an external electromagnetic field with vector potential $\mathbf{A}(\mathbf{x}, t)$ is described by the Hamiltonian

$$H(\mathbf{x}, \mathbf{p}, t) = \frac{1}{2m_e}|\mathbf{p} + e\mathbf{A}(\mathbf{x}, t)|^2 + V(\mathbf{x}), \tag{2.23}$$

where $\mathbf{p}$ is the canonically-conjugate momentum of the electron. The Poisson matrix is the canonical one, Eq. (2.18). When the excursions of the electron $\mathbf{x}$ are small compared to the length scale of spatial variations of $\mathbf{A}$, then the dipole approximation, $\mathbf{A}(\mathbf{x}, t) \approx \mathbf{A}(t)$ can be made. The smallest scale of large-amplitude spatial variations of $\mathbf{A}$ is the laser wavelength, $\lambda_L$. Meanwhile, the length scale of the excursions of an ionized (free) electron is given by the quiver radius, $x_{\text{quiver}} = v_{\text{quiver}}\lambda_L/2\pi c$. We see that $x_{\text{quiver}}/\lambda_L = v_{\text{quiver}}/2\pi c$. Hence, the dipole approximation can be justified in the non-relativistic regime.

We also autonomize the system, so that the Hamiltonian reads

$$H(\mathbf{x}, \mathbf{p}, \tau, k) = \frac{1}{2m_e}|\mathbf{p} + e\mathbf{A}(\tau)|^2 + V(\mathbf{x}) + k. \tag{2.24}$$

This is referred to as the velocity-gauge formulation of the Hamiltonian [96]. One can obtain the length-gauge formulation by making the following change of coordinates:

$$\mathbf{v} = \mathbf{p} + e\mathbf{A}(\tau), \tag{2.25a}$$

$$\widetilde{k} = k + e\partial_\tau \mathbf{A} \cdot \mathbf{x}. \tag{2.25b}$$

With this change of coordinates, the Hamiltonian becomes

$$\widetilde{H}(\mathbf{x}, \mathbf{v}, \tau, \widetilde{k}) = \frac{1}{2m_e}|\mathbf{v}|^2 + V(\mathbf{x}) + e\mathbf{E}(\tau) \cdot \mathbf{x} + \widetilde{k}, \tag{2.26}$$

where $\mathbf{E}(\tau) = -\partial_\tau \mathbf{A}(\tau)$ is the electric field associated with the vector potential. Furthermore, this change of coordinates is a canonical one: the expression of the Poisson matrix remains unchanged with these new variables.

Some additional assumptions are usually made to study this Hamiltonian. It is clear that the potential $V$ should approach the Coulomb potential far from the core, meaning $V(\mathbf{x}) \to -1/|\mathbf{x}|$ as $|\mathbf{x}| \to \infty$. However, because it is generally the potential of an ion, instead of a singly charged nucleus, it should have a different shape near the core. We thus typically use the soft-Coulomb potential, $V(\mathbf{x}) = -1/\sqrt{|\mathbf{x}|^2 + a^2}$, where $a$ is the softening-parameter, which is routinely used in strong-field physics [84, 97]. This potential has the correct behavior far from the core, and the parameter $a$ can be adjusted in order to model different kinds of atoms. In addition, the lack of a divergence at $|\mathbf{x}| = 0$ compared to the true Coulomb potential makes this potential convenient for classical numerical simulations.

This is particularly useful when the motion of an electron in a linearly-polarized laser field, $\mathbf{E}(\tau) = E(\tau)\hat{\mathbf{x}}$, is considered. Here, it is common to reduce the system to the motion of the electron along the polarization axis, so that the Hamiltonian becomes

$$H(x, v, t) = \frac{v^2}{2m_e} - \frac{1}{\sqrt{x^2 + a^2}} + eE(t)x, \tag{2.27}$$

where we have removed the $k$ variable from the Hamiltonian. This 1.5 dof system constitutes the simplest model of the interaction of an atom with an external laser field. The case of linear polarization is of interest not only because it is simpler, but also because it maximizes the probability of electron recollision after ionization [3]. Because recollisions drive HHG, the high-harmonic yield is maximized when the incident laser polarization is linear, and it decreases rapidly as the polarization is varied continuously towards circular-polarization [29]. Hence, we focus exclusively on linearly-polarized light in this thesis.

The self-consistent interaction between a macroscopic collection of atoms, i.e. a gas, with the electromagnetic field is treated in detail in Ch. 4. Here, we mention an underlying

Table 2.1: Atomic units of various quantities in terms of SI units.

| unit | expression | SI |
|---|---|---|
| length | $\hbar/(m_e c\alpha)$ | $5.291772109217 \times 10^{-11}$ m |
| time | $\hbar/(\alpha^2 m_e c^2)$ | $2.41888432650516 \times 10^{-17}$ s |
| velocity | $\alpha c$ | $2.187691263373 \times 10^{6}$ m $\cdot$ s$^{-1}$ |
| energy | $\alpha^2 m_e c^2$ | $4.3597441775 \times 10^{-18}$ J |
| electric field | $\alpha^3 m_e^2 c^3/(e\hbar)$ | $5.1422065211 \times 10^{11}$ V $\cdot$ m$^{-1}$ |

assumption of the models discussed in that chapter: neighboring atoms do not interact other than through the macroscopic electromagnetic field. In other words, we assume Coulombic interactions between neighboring atoms are negligible. This is justified when the atomic gas density is low enough, specifically when $x_{\mathrm{quiver}}$ is small compared to the typical interatomic distance. If $\rho$ is the number density of the atomic gas, a typical interatomic distance may be estimated as $\rho^{-1/3}$. The largest value of the ratio of the two distances encountered in this thesis is $x_{\mathrm{quiver}}/\rho^{-1/3} \approx 0.38$, for $I = 5 \times 10^{13}$ W $\cdot$ cm$^{-2}$, $\lambda_L = 1.2$ $\mu$m, and $\rho = 2 \times 10^{19}$ cm$^{-3}$ While this is smaller than one, it is possible that collisions between ionized electrons and neighboring atoms begin to play a role at this stage. Nevertheless, we have not explored this possibility.

## 2.4 Atomic units

Throughout the rest of the manuscript, we use atomic units instead of SI units. Atomic units are defined by setting the physical constants $\hbar = m_e = e = 1/4\pi\epsilon_0 = 1$. Conversions between atomic units and SI units are given in Table 2.1. Here, $\alpha = e^2/(4\pi\epsilon_0\hbar c)$ is the fine-structure constant. Useful formulas for converting between atomic units of $E_0$ and $\omega_L$ and laser parameters in typical units are

$$E_0 \text{ [a.u.]} = (5.338027006147334 \times 10^{-9})\sqrt{I \text{ [W} \cdot \text{cm}^{-2}]},$$
$$\omega_L \text{ [a.u.]} = (45.563352527599626)(\lambda_L \text{ [nm]})^{-1}.$$

# CHAPTER 3

# PERSISTENCE OF COULOMB FOCUSING IN THE STRONG-FIELD REGIME

## 3.1 Introduction

The theoretical framework for ionization processes in matter exposed to intense linearly polarized laser fields was established about twenty five years ago and remains the state-of-the-art in strong field physics [1, 3, 98]. It centers on the "recollision" model, which follows a three-step scenario: Electrons are first ionized, absorb energy while following the laser, and then are propelled back to the ionic core after the laser reverses direction, about half a laser cycle after ionization. The kinetic energy transfer in the core region causes ionization of more electrons (nonsequential multiple ionizations - NSMI) [84] or generates very high harmonics of the driving laser by high harmonic generation (HHG) [55]. This model applies when the target matter consists of either atoms or small molecules [53]. Despite the wide-spread use of the three-step model, it is not widely appreciated that it usually takes more than one recollision for the ionized electron to transfer its energy to set the processes of multiple ionization or high-harmonic generation into motion. It is reasonable to expect that the spreading of the electronic wave packet would make these delayed collisions much less effective. Surprisingly, the opposite is the case, and it is due to a process called Coulomb focusing [66]. The effectiveness of Coulomb focusing was demonstrated convincingly in the pioneering work of Brabec *et al.* [66], who showed that the nonsequential double ionization rate is enhanced by an order of magnitude by Coulomb focusing.

Research in the last two decades has confirmed that Coulomb focusing (and the Coulomb field in general) is a key player in the recollision process [54, 67–69, 83]. But it seems that the opposite question –namely, when the Coulomb focusing does not matter– has not

received the same attention. Perhaps the reason is that the answer seems obvious: the Coulomb field can be ignored when the laser field is strong. After all, this is one of the tenets of the Strong Field Approximation (SFA) [3, 53, 63] which ignores the Coulomb field when the electron is moving in the laser field. But how strong is "strong" for the laser field, and how weak does the Coulomb field have to be for us to neglect it altogether –i.e., is it possible to turn it off completely, as the three-step model would have us do?

In fact, the focusing effect of the Coulomb field persists well beyond what would be expected based on the comparison of field strengths, and well beyond field strengths where there is no potential barrier to trigger tunneling ionization at peak field. The consequences of the persistence of Coulomb focusing go beyond a reduced spread of the electronic wave packet. In this range of intensity, contrary to SFA predictions, delayed recollisions, i.e. recollisions occurring after the first laser cycle, continue to manifest themselves and bring back energy slightly above the $3.17U_p$ high-harmonic cutoff. The kinetic energy brought back by delayed recollisions is compatible with the value provided in the SFA for immediate recollision (occurring half a laser cycle after ionization), but those energetic delayed recollisions do not exist in the SFA. Thus, even in the strong field regime, the SFA does not accurately describe the electronic dynamics on time scales longer than one laser cycle.

This chapter is structured as follows: In Sec. 3.2 we begin by reviewing how the return energy is maximized in the SFA, and characterize the trajectories bringing maximum energy to the core. In Sec. 3.3 we investigate how the energy-maximizing classical recollision trajectories change when the Coulomb field is included. We show that delayed energy-maximizing trajectories, which are not present in the SFA, emerge. We provide a characterization of the delayed recollisions in phase space, and show that they are related to the invariant manifolds of particular periodic orbits.

## 3.2 Maximizing the Return Energy in the Strong Field Approximation

We begin with the derivation of some results on recollisions in the Strong Field Approximation. These results will form the basis for understanding the distinct effect of the Coulomb field on recollision trajectories. In a linearly polarized field, the SFA may be described by the one-dimensional classical Hamiltonian (in atomic units)

$$H(x,p,t) = \frac{1}{2}\Big(p + \frac{E_0}{\omega}\cos(\omega t + \phi)\Big)^2, \tag{3.1}$$

where $p$ is the canonical momentum, $E_0$ is the electric field amplitude, $\omega$ is the laser frequency, and the dipole approximation for the laser field is used. In the context of the three-step model, this Hamiltonian describes the motion of the electron after its ionization, which we define as occurring at $t = 0$ without loss of generality (up to a change of phase $\phi$). The three-step model does not specify the exact phase of the laser at the instant of ionization, so we allow this phase $\phi$ to be a free parameter of the model.

We write Hamiltonian (3.1) in the velocity gauge as opposed to the more common length gauge to make the translational invariance of the SFA apparent (i.e., independence of Hamiltonian (3.1) with respect to $x$). Thus, it is clear that the momentum $p$ is conserved, and as a consequence, the resulting system is integrable. It is convenient to rescale the variables so that $x$ is in units of the quiver radius $E_0/\omega^2$, $p$ is in units of $E_0/\omega$, and $t$ is in radians, so Hamiltonian (3.1) now looks like

$$\mathcal{H}(x,p,t) = \frac{1}{2}\Big(p + \cos(t + \phi)\Big)^2. \tag{3.2}$$

We also note that this Hamiltonian has the symmetry

$$(x,p,\phi) \to (-x,-p,\pi+\phi), \tag{3.3}$$

which allows us to narrow our focus to initial conditions with $\phi \in [0, \pi)$.

From Eq. (3.2) we write down the solution for $x(t)$,

$$x(t) = x_0 - \sin\phi + p_0 t + \sin(t + \phi), \tag{3.4}$$

and $p(t) = p_0$. Just as the three-step model does not exactly specify the laser phase $\phi$ at ionization, it also does not specify the position of the electron $x_0$ at ionization. Thus, we allow $x_0$ to be a free parameter as well. Also, we note that Eq. (3.4) shows that $p_0$ is the constant drift momentum of the electron.

Equation (3.4) is used to compute the maximum return energy of the electron, which provides an estimate of the high-harmonic cutoff [3, 55, 70]. First, it is assumed that the electron reaches the ionic core at time $t_r$, i.e. $x(t_r) = 0$. By substituting this into Eq. (3.4), one obtains

$$p_0(t_r, \phi) = \frac{\sin\phi - \sin(t_r + \phi) - x_0}{t_r}. \tag{3.5}$$

Now, one may fix $x_0$ and maximize the energy at return,

$$\varepsilon(t_r, \phi) = \frac{1}{2}\Big(p_0 + \cos(t_r + \phi)\Big)^2, \tag{3.6}$$

with respect to $t_r$ and $\phi$. Setting the derivatives equal to zero gives

$$\partial_{t_r}\varepsilon = \Big(p_0 + \cos(t_r + \phi)\Big)\Big(\partial_{t_r} p_0 - \sin(t_r + \phi)\Big) = 0, \tag{3.7}$$

$$\partial_{\phi}\varepsilon = \Big(p_0 + \cos(t_r + \phi)\Big)\Big(\partial_{\phi} p_0 - \sin(t_r + \phi)\Big) = 0. \tag{3.8}$$

We discard the solution $p_0 + \cos(t_r + \phi) = 0$ which corresponds to the zero-energy minima of Eq. (3.6). Thus, we get $\partial_{t_r} p_0 = \partial_{\phi} p_0$, and carrying out these derivatives using Eq. (3.5) immediately gives

$$\dot{x}(t = 0) = p_0 + \cos\phi = 0, \tag{3.9}$$

which corresponds to zero initial momentum in the length gauge. Though this result has been known for $x_0 = 0$, we have shown that it is independent of this condition and is valid for any $x_0 \neq 0$.

In addition, Eq. (3.9) tells us that when the return energy is maximized, the initial energy is zero and thus minimized, implying that the change in the energy

$$\Delta\varepsilon = \frac{1}{2}\left[\Big(p_0 + \cos(t_r + \phi)\Big)^2 - \Big(p_0 + \cos\phi\Big)^2\right],$$

is at a maximum as well. By rewriting $\Delta\varepsilon$ as

$$\Delta\varepsilon = \Big(p_0 + \frac{1}{2}\cos(t_r + \phi) + \frac{1}{2}\cos\phi\Big)\Big(\cos(t_r + \phi) - \cos\phi\Big), \tag{3.10}$$

substituting Eq. (3.5) into Eq. (3.10), and using some trigonometric identities, it is shown that

$$\Delta\varepsilon(t_r, \phi) = f(t_r)\sin(t_r + 2\phi) + g(t_r, \phi)x_0, \tag{3.11}$$

$$\text{where } f(t_r) = \frac{\sin\frac{t_r}{2}\Big(2\sin\frac{t_r}{2} - t_r\cos\frac{t_r}{2}\Big)}{t_r}, \tag{3.12}$$

$$\text{and } g(t_r, \phi) = \frac{2\sin\frac{t_r}{2}\sin(\frac{t_r}{2} + \phi)}{t_r}. \tag{3.13}$$

We first treat the case of the electron starting very close to the core, i.e. $x_0 = 0$. In that case Eq. (3.11) simplifies to

$$\Delta\varepsilon_0(t_r, \phi) = f(t_r)\sin(t_r + 2\phi). \tag{3.14}$$

To compute the maximum of this function, we first note that all the $\phi$ dependence is contained in the multiplicative sine term. Also, one may find a $\phi$ such that $\sin(t_r + 2\phi) = \pm 1$ for any $t_r$. Therefore, the absolute maximum of $\Delta\varepsilon_0$ occurs where $|f(t_r)|$ is at its absolute maximum for $t_r > 0$, and $\sin(t_r + 2\phi)$ is the sign of $f(t_r)$ at the extremum. Then we obtain the absolute extremum of $f(t_r)$ in Eq. (3.12) by setting $\partial_{t_r} f = 0$ and using trigonometric

double angle identities, yielding

$$2 - 2t_r \sin t_r + (t_r^2 - 2)\cos t_r = 0, \tag{3.15}$$

in agreement with the literature. This equation's first positive root, $t^*_{r,0} \approx 4.09$, is the absolute extremum of $f(t_r)$ for $t_r > 0$, and $f(t_r) > 0$. Thus, we obtain the exact relation between the return time and the initial phase $\phi_0^*$ maximizing $\Delta\varepsilon_0$,

$$\sin(t^*_{r,0} + 2\phi_0^*) = 1, \tag{3.16}$$
$$\text{or equivalently, } t^*_{r,0} + 2\phi_0^* = \frac{\pi}{2} + 2\pi n, \text{ for } n \geq 0.$$

For $n = 1$, this gives $\phi_0^* \approx 1.88$. Substituting $(t^*_{r,0}, \phi_0^*)$ into Eq. (3.14), we finally get the maximum change in energy $\Delta\varepsilon_0^* \approx 3.17U_p$, where $U_p = E_0^2/4\omega^2$, or simply $1/4$ in rescaled units, is the pondermotive energy.

Remarkably, we have found a very simple relation in Eq. (3.16) between the initial phase of the laser and the return time by maximizing the change in energy instead of the return energy itself. This relation is borne out by the numerical results for the local maxima of $\dot{x}(t_r, \phi)$ shown in Table 1 of Ref. [70], when taking care to subtract $\pi/2$ from each of the phases in that table to reconcile our choice of sine versus cosine for the laser field term in Hamiltonian (3.2). All odd multiples of $\pi/2$ appear in that table because local extrema are being considered, and $f(t_r) < 0$ for the minima, requiring $\sin(t_r + 2\phi) = -1$. Equation (3.16) follows naturally from maximizing $\Delta\varepsilon$, and in our view, $\Delta\varepsilon$ is the fundamental quantity to maximize because it is the energy gained by the electron from the laser field. Thus, we will only consider maximizing $\Delta\varepsilon$ for the remainder of this chapter.

Now we will consider the effect of allowing $x_0 \neq 0$ on the trajectories that maximize $\Delta\varepsilon$ in the SFA, because in the three-step model the electron's tunnel ionization implies its starting position is not exactly $x_0 = 0$. Though the consequences of $x_0 \neq 0$ are investigated in Ref. [70], these simulations include the Coulomb field. Therefore it is not clear whether

the observed effects are due to the inclusion of the Coulomb field or the relaxation of the $x_0 = 0$ condition, and we intend to clarify this. We have already shown that $\dot{x}(t = 0) = 0$ will persist when $x_0 \neq 0$, but to see the effect on the other quantities $\Delta\varepsilon$ in Eq. (3.11) must be maximized. If we restrict $x_0 \ll 1$, then we can treat the effect of $x_0 \neq 0$ on the maximization of $\Delta\varepsilon$ perturbatively. This is not an unreasonable restriction because $x_0$ just needs to be small compared to the quiver radius. For example, if one assumes that ionization occurs around 1 a.u., the laser intensity is $I = 6 \times 10^{13}\,\mathrm{W \cdot cm^{-2}}$, and the laser wavelength is $800$ nm, the corresponding value of $x_0$ in rescaled units is $x_0 \approx 0.08$. For the same frequency but an intensity of $I = 10^{16}\,\mathrm{W \cdot cm^{-2}}$, which is used for numerical simulations in this chapter, the corresponding value of $x_0$ in rescaled units is even smaller: $x_0 \approx 6 \times 10^{-3}$.

To do the calculation, we assume first order perturbation expansions of $t_r^*$ and $\phi^*$ in integral powers of $x_0$,

$$t_r^* = t_{r,0}^* + t_1 x_0 + \mathcal{O}(x_0^2), \tag{3.17}$$

$$\phi^* = \phi_0^* + \phi_1 x_0 + \mathcal{O}(x_0^2), \tag{3.18}$$

with the zeroth order terms taking their values from the $x_0 = 0$ case. We carry out the calculation to first order by computing $(t_1, \phi_1)$. Recalling Eqs. (3.13) and (3.14) and setting the partial derivatives of Eq. (3.11) with respect to $t_r$ and $\phi$ equal to $0$, we get

$$\partial_{t_r}(\Delta\varepsilon_0) + x_0\,\partial_{t_r} g = 0, \tag{3.19}$$

$$\partial_{\phi}(\Delta\varepsilon_0) + x_0\,\partial_{\phi} g = 0. \tag{3.20}$$

Now we substitute the perturbation expansions (3.17) and (3.18) into Eqs. (3.19) and (3.20) and discard terms of order $\mathcal{O}(x_0^2)$. By Taylor-expanding the derivatives of $\Delta\varepsilon_0$ to first order in $x_0$ and applying phase relation (3.16) to the $(t_{r,0}^*, \phi_0^*)$ terms, we get the system of linear

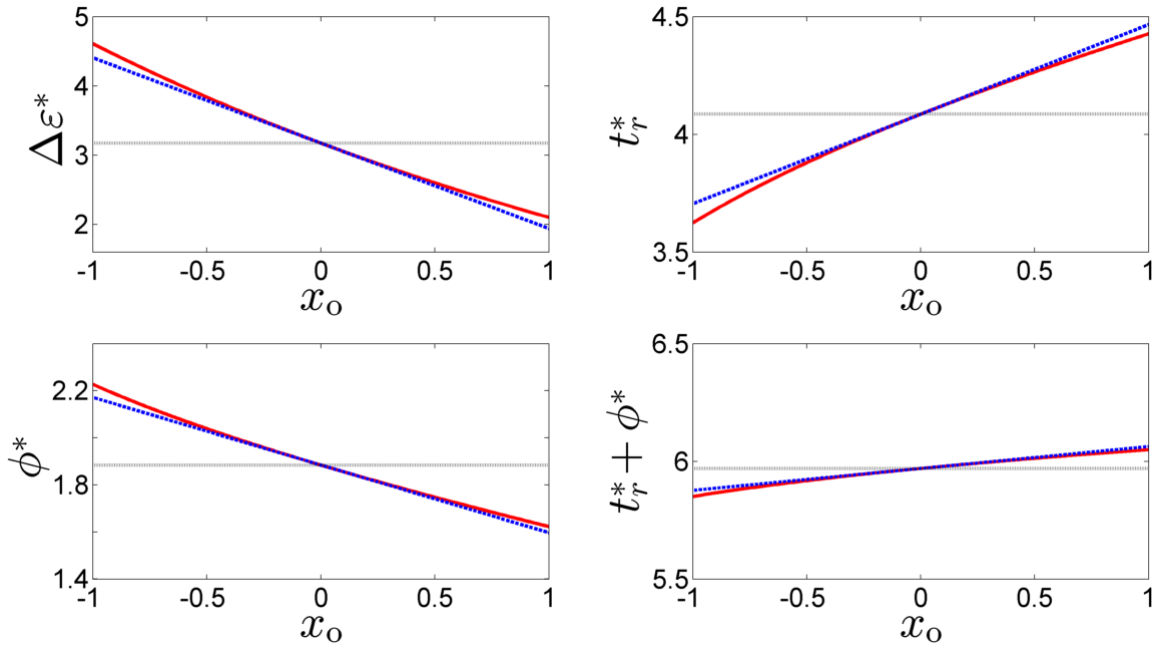


Figure 3.1: Dependence on $x_0$ of the maximum energy exchange $\Delta\varepsilon^*$ (upper left panel), return time $t_r^*$ (upper right panel), laser phase $\phi^*$ (lower left panel) and $t_r^* + \phi^*$ (lower right panel) from Hamiltonian (3.2). Solid red curves are the numerical values and the dashed blue lines are the first order approximations. Grey dotted lines are the values for $x_0 = 0$. $x_0$ is in units of $E_0/\omega^2$, $\Delta\varepsilon^*$ is in units of $U_p$, $t_r^*$ and $\phi^*$ are in radians.

equations

$$\begin{pmatrix} -\partial^2_{t_r t_r}(\Delta\varepsilon_0)\big|_0 & 2\Delta\varepsilon_0^* \\ 2\Delta\varepsilon_0^* & 4\Delta\varepsilon_0^* \end{pmatrix} \begin{pmatrix} t_1 \\ \phi_1 \end{pmatrix} = \begin{pmatrix} \partial_{t_r} g \\ \partial_\phi g \end{pmatrix}\Big|_0, \tag{3.21}$$

where "$|_0$" means to evaluate at the parameters from the $x_0 = 0$ case. Equation (3.21) yields $(t_1, \phi_1) \approx (0.38, -0.29)$.

The results of these approximations are compared against numerical maximization of Eq. (3.11) in Fig. 3.1. These approximations do work well for $|x_0| \ll 1$, and even appear to do a fair job closer to $|x_0| = 1$. Note that the shift of the final phase $t_r + \phi$ is slightly less pronounced than for $t_r$ and $\phi$, as its first order coefficient is small, $t_1 + \phi_1 = 0.09$, so that $t_r^* + \phi^*$ appears fairly constant.

We notice on the upper left panel of Fig. 3.1 that $\Delta\varepsilon^*$ significantly exceeds the well-known value of $3.17U_p$. This has already been noted in Ref. [70] [and is also easily seen from Eq. (3.10) using Eq. (3.9)]: The maximum is expected to be at $8U_p$ which occurs

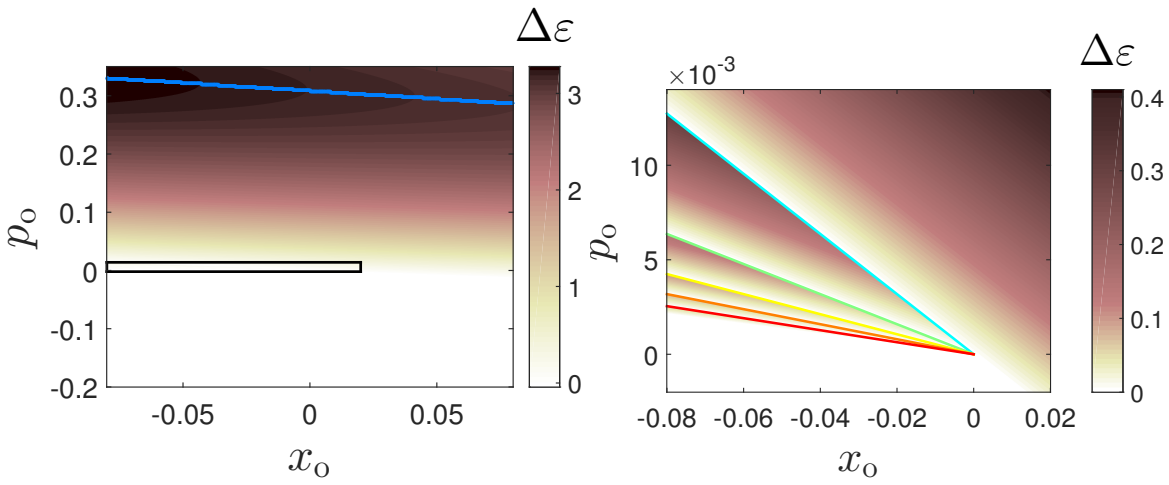


Figure 3.2: Energy exchange $\Delta\varepsilon$ at first recollision (after a six laser cycle integration) as a function of initial condition, $(x_0, p_0)$. The initial phase $\phi$ is fixed by Poincaré section condition (3.22). Darker points correspond to higher energy. Left panel: The initial conditions $(x_0, p_0)$ bringing the maximum energy $\Delta\varepsilon$ at first recollision for each $x_0$ are the blue curve. Right panel: Zoom of the black-framed region on the left. Solid colored lines separate regions of initial conditions that have their first recollision during different laser cycles, with the colors corresponding to Fig. 3.3. $x_0$ is in units of $E_0/\omega^2$, $p_0$ is in units of $E_0/\omega$, $\Delta\varepsilon$ is in units of $U_p$.

at $x_0 = \pi$ (e.g., with parameters $\phi = \pi$ and $t_r = 3\pi$ with $p_0 = 1$). However only the region close to the core is physically relevant since the electron is initially bound to the core. Therefore we do not expect significant variations of initial laser phase, ionization time and maximum return energy from the values obtained from $x_0 = 0$. In summary, the typical energy-maximizing recollision occurs within one laser cycle and brings an amount of energy close to $3U_p$. When the laser field is large, we expect a similar result by taking into account the Coulomb field, and this is what we are going to investigate in the next section.

When examining the effect of the Coulomb field on the energy-maximizing trajectories, we need to study the location of their initial conditions in phase space in detail. Before proceeding, it is enlightening to look at the phase space picture of energy-maximizing trajectories in the SFA. In order to locate these trajectories in phase space, we consider a Poincaré section of the trajectories. In the left panel of Fig. 3.2, we consider a grid of initial

conditions $(x_0, p_0)$ beginning on the Poincaré section

$$\dot{x} = 0 \text{ with } \ddot{x} < 0, \tag{3.22}$$

and integrated for six laser cycles, with $x_0 \in [-0.08, 0.08]$ and $p_0 \in [-0.2, 0.35]$ in rescaled units. We notice that the Poincaré section determines the initial phase such that $\cos\phi = -p_0$ and $\sin\phi > 0$. Since $\dot{x} = p_0 + \cos(t + \phi)$, the Poincaré section is a stroboscopic plot with period $2\pi$ in the SFA. The condition $\dot{x} = 0$ is a natural section because we have just shown that all of the trajectories maximizing $\Delta\varepsilon$ satisfy this condition in the SFA. For all trajectories beginning on this Poincaré section, the electron begins at rest and starts to move to the left. The reversal of the laser field causes the electron to reverse its direction and move to the right, towards the core again. It is then possible for a recollision to occur, and thus we define a "recollision" as crossing $x = 0$ moving to the right, i.e. with $\dot{x} > 0$.

In Fig. 3.2, we show the energy $\Delta\varepsilon$ brought back the electron on its first recollision as a function of its initial condition. When starting at the top of the left panel of Fig. 3.2 and moving down, we observe a continuous gradient of $\Delta\varepsilon$, until a series of discontinuous changes beginning at small $p_0 > 0$ and $x_0 < 0$. These discontinuities are seen clearly in the right panel of Fig. 3.2, which shows that the first discontinuous change in $\Delta\varepsilon$ is a sudden increase in energy, followed by another continuous decreasing gradient of $\Delta\varepsilon$. This behavior repeats over and over as $p_0$ gets closer and closer to $0$. It turns out that these sudden changes in energy as the initial conditions are varied correspond to changes to the laser cycle during which the electron has its first recollision. These trajectories are referred to as delayed recollisions in what follows, as opposed to immediate recollisions which occur during the first laser cycle. The delayed recollisions are analogous to the "higher-order returns" of Ref. [66].

In Fig. 3.3 we determine which laser cycle the first recollision will occur for a given initial condition analytically using Eq. (3.4) and the Poincaré section condition (3.22). The

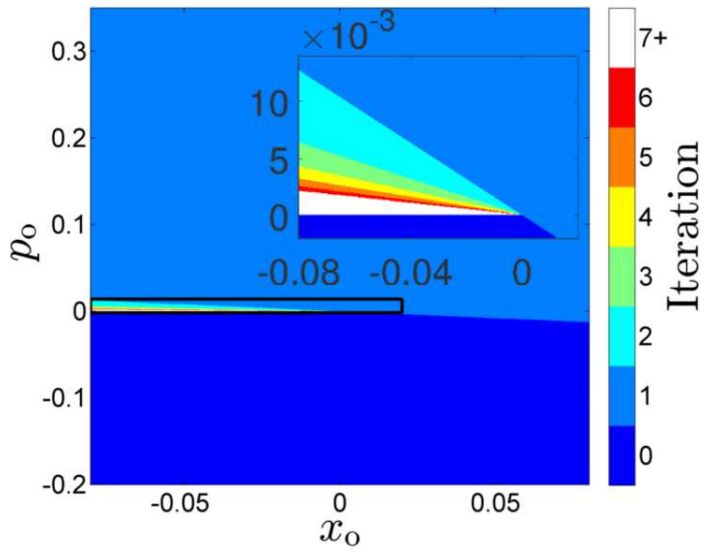


Figure 3.3: Number of iterations of Poincaré map $\mathcal{P}$ until the first recollision has occurred, as a function of initial conditions $(x_0, p_0)$, where $\phi$ is fixed by the Poincaré section condition (3.22). In the SFA, a single iteration of this map always corresponds exactly to the duration of one laser cycle. $x_0$ is in units of $E_0/\omega^2$, $p_0$ is in units of $E_0/\omega$.

general structure in Fig. 3.3 is that immediate recollisions in the "1" region are separated from the immediate ionizations in the "0" region by a small triangle in which the delayed recollisions live. A closer look at the delayed recollision triangle in the inset of Fig. 3.3 shows that the triangle is bounded below by the line $p_0 = 0$ and its rightmost point is $(x_0, p_0) = (0, 0)$. Furthermore, the triangle is clearly stratified, with each stratum corresponding to a delayed recollision with a particular delay. The strata are well ordered in phase space: as $p_0$ decreases, the delay time increases. These observations are explained by considering the mechanical scenario in this region: All trajectories starting on the section will first move to the left, and as is evident from Eq. (3.4), they will eventually come to rest (at approximately half of the laser cycle for small $p_0$), move to the right, and come to rest again, this time on the Poincaré section (with exactly one laser cycle elapsed). They will have a displacement from their initial position of $\Delta x = 2\pi p_0$. Therefore, trajectories beginning with $x_0 < 0$ and a small enough $p_0 > 0$ such that $x_0 + \Delta x < 0$ will not experience a recollision in the first laser cycle: they must wait for enough laser cycles $n$ such that the displacements accumulate and satisfy $x_0 + n\Delta x > 0$. The smaller the $p_0$, the

more laser cycles are needed for a recollision to occur, which explains the ordering of the strata. This argument also explains why there are no recollisions if $x_0 < 0$ and $p_0 < 0$, and none for $x_0 > 0$ and $p_0 < -x_0/2\pi$. The lines that form the boundaries between the delayed recollisions of differing delay times are plotted in the right panel of Fig. 3.2. We note that the boundaries occur precisely where the return energy has discontinuous jumps, as claimed earlier.

It should be noted that the highest energies associated with delayed recollisions are an order of magnitude smaller than the immediate recollisions, which is reflected in the change of color scale between the left and right panels of Fig. 3.2. Thus, when searching for energy-maximizing trajectories in the SFA, these kinds of trajectories appear irrelevant, not bringing enough energy to play a significant role in recollision-driven processes. However it should be emphasized that this is only on their *first* recollision. In the SFA, these trajectories with very small $p_0$ will have many recollisions, as is evident from Eq. (3.4). With $\dot{x} = p_0 + \cos(t + \phi)$, the return kinetic energy of the later recollisions can only get slightly higher than $2U_p$, still significantly below the usual prediction of $3.17U_p$. Moreover, the maximum return kinetic energy of any recollision (i.e. not necessarily the trajectory's *first* recollision) occurring after the first laser cycle for a trajectory initiated near $x = 0$ is bounded at approximately $2.4U_p$ [70]. This changes when we turn on the Coulomb field: even if the laser field is large, the Couloumb field allows delayed recollisions to bring back energy greater than $3.17U_p$ on their very first recollision. In addition, the trajectories experiencing delayed recollision are particularly interesting because they spend a longer time close to the core where they can exchange energy and experience the influence of the core potential.

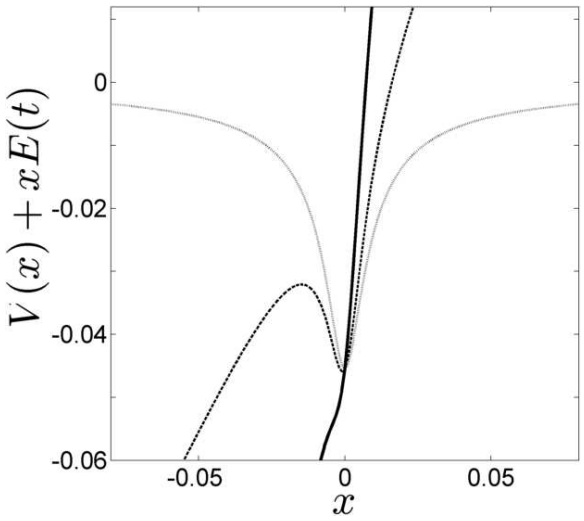


Figure 3.4: The potential of Hamiltonian (3.24) in the length gauge, i.e. $V(x) + xE(t)$, as a function of $x$. Grey dotted is with $E(t) = 0$, black dashed with $E(t) = 0.25\ E_0$ (the maximum field amplitude when $I = 6.3 \times 10^{14}\,\mathrm{W \cdot cm^{-2}}$), and solid black with $E(t) = E_0$. $x$ is in units $E_0/\omega^2$ and $V$ is in units of $U_p$.

## 3.3 Maximizing the return energy with the Coulomb field: Nonlinear dynamics of delayed recollisions

### 3.3.1 Delayed Recollisions

In Sec. 3.2, we have identified the effects of $x_0 \neq 0$ on the recollision mechanism in the strong field approximation. In particular we have assessed the effect of $x_0 \neq 0$ on the maximum $\Delta\varepsilon$ trajectories. We have shown that the energy-maximizing trajectories are the ones which recollide within one laser cycle. In this section, we turn on the Coulomb interaction and investigate how the strong field approximation picture for recollision trajectories is affected by this interaction. The Hamiltonian, in atomic units, now becomes

$$H(x,p,t) = \frac{1}{2}\Big(p + \frac{E_0}{\omega}\cos(\omega t + \phi)\Big)^2 - \frac{1}{\sqrt{x^2+1}}\,, \tag{3.23}$$

where we have used the infinite-mass approximation for the core and a soft-Coulomb potential with a softening parameter of 1 [84, 97]. The soft-Coulomb potential is sufficiently generic as to model any neutral single-active-electron atom or small molecule in a strong

laser field. The general phase space picture associated with Hamiltonian (3.23) is composed of two distinct regions [99]: the region near the core, referred to as the bounded region, where the Coulomb attraction dominates compared to the laser forcing, and the region sufficiently far from the core, referred to as the unbounded region, where the laser field dominates. For low enough laser intensities, the electron never escapes the bounded region. A common assumption in the unbounded region is to neglect the Coulomb interaction for sufficiently large intensity, which corresponds to the second step in the three-step model of recollisions. Here we investigate the validity of this assumption, using numerical solutions of the equations of motion arising from Hamiltonian (3.23). In order to focus on the effect of the Coulomb field in the unbounded region, we choose the parameters in such a way that the bounded region is completely suppressed. In particular, we use a laser intensity $I = 10^{16}\,\mathrm{W}\cdot\mathrm{cm}^{-2}$ and frequency $\omega = 0.057$ a.u. (corresponding to an $800$ nm wavelength). At this laser frequency, the bounded region only exists for intensities below $I = 4.9\times 10^{15}\,\mathrm{W}\cdot\mathrm{cm}^{-2}$. Thus, our choice of laser intensity is high enough that almost every initial condition will lead eventually to ionization, meaning there are almost no trajectories that remain indefinitely bounded to the core. In fact, this intensity is so high that there is not even a potential barrier when the laser field is at its maximum, as shown in Fig. 3.4, so classical ionization can account for all ionizations; it is not necessary to invoke a tunneling argument.

We rescale this Hamiltonian as in Sec. 3.2, yielding

$$\mathcal{H}(x,p,t) = \frac{1}{2}\Big(p+\cos(t+\phi)\Big)^2 - \frac{\epsilon}{\sqrt{x^2+a^2}}, \tag{3.24}$$

where $a = \omega^2/E_0 = 6.077\times 10^{-3}$ and $\epsilon = \omega^4/E_0^3 = 6.918\times 10^{-5}$. The parameter $\epsilon$ is the effective strength of the Coulomb potential in the presence of the laser field: as the intensity goes to infinity, $\epsilon$ goes to zero as does $\epsilon/a$ so the Coulomb potential becomes negligible. In this parameter regime it would appear that the Coulomb potential is ignorable

due to the small magnitude of the maximum Coulomb energy, $\epsilon/a \approx 0.046U_p$. However, the relative importance of terms in the Hamiltonian is not determined by the absolute values of the terms themselves but by the absolute values of the gradients of the terms, because it is the gradients that actually appear in the equations of motion. In this parameter regime, the Coulomb force, equal to $-\epsilon x/(x^2+a^2)^{3/2}$ has a maximum amplitude of $2\epsilon/(3a^2\sqrt{3}) \approx 0.7E_0$, which is comparable to the maximum electric force, and therefore cannot be neglected.

In the same way as we did in Sec. 3.2, we examine the trajectories that maximize the change in energy $\Delta\varepsilon$ between some starting position $x_0$ at $t = 0$ and the final position at the center of the core, $x = 0$, at the return time $t_r$. With the inclusion of the Coulomb field, the translational invariance of the SFA is broken, meaning the momentum $p$ is no longer conserved. Thus, this system is no longer integrable, so trajectories cannot be obtained analytically. Here we numerically integrate the equations of motion associated with Hamiltonian (3.24) in order to find the trajectories that maximize $\Delta\varepsilon$. We notice that the discrete symmetry (3.3) remains, meaning we may still confine our simulations to initial conditions with $\phi \in [0, \pi)$. Using an explicit second-order symplectic integrator [100], we again consider a large number of initial conditions (typically of the order of one thousand for each value of $x_0$) beginning on the Poincaré section (3.22), and look for the trajectories that yield the highest $\Delta\varepsilon$ at the first recollision. The range of initial conditions is the same as in the previous section, and with this choice of laser parameters the ranges of initial conditions in atomic units correspond to $x_0 = [-13, 13]$ and $p_0 = [-1.9, 3.3]$.

In the top left panel of Fig. 3.5, we show the energy $\Delta\varepsilon$ brought back by the electron on its first recollision as a function of its initial condition. Comparing this with Fig. 3.2, we can evaluate the effect of the Coulomb field on the recolliding trajectories. The shape of the curve of initial conditions leading to $\Delta\varepsilon$-maximizing immediate recollisions is deformed compared to the SFA, due to the presence of the Coulomb field. The actual energies of these recollisions as a function of $x_0$ are seen more clearly in Fig. 3.6. We see that the

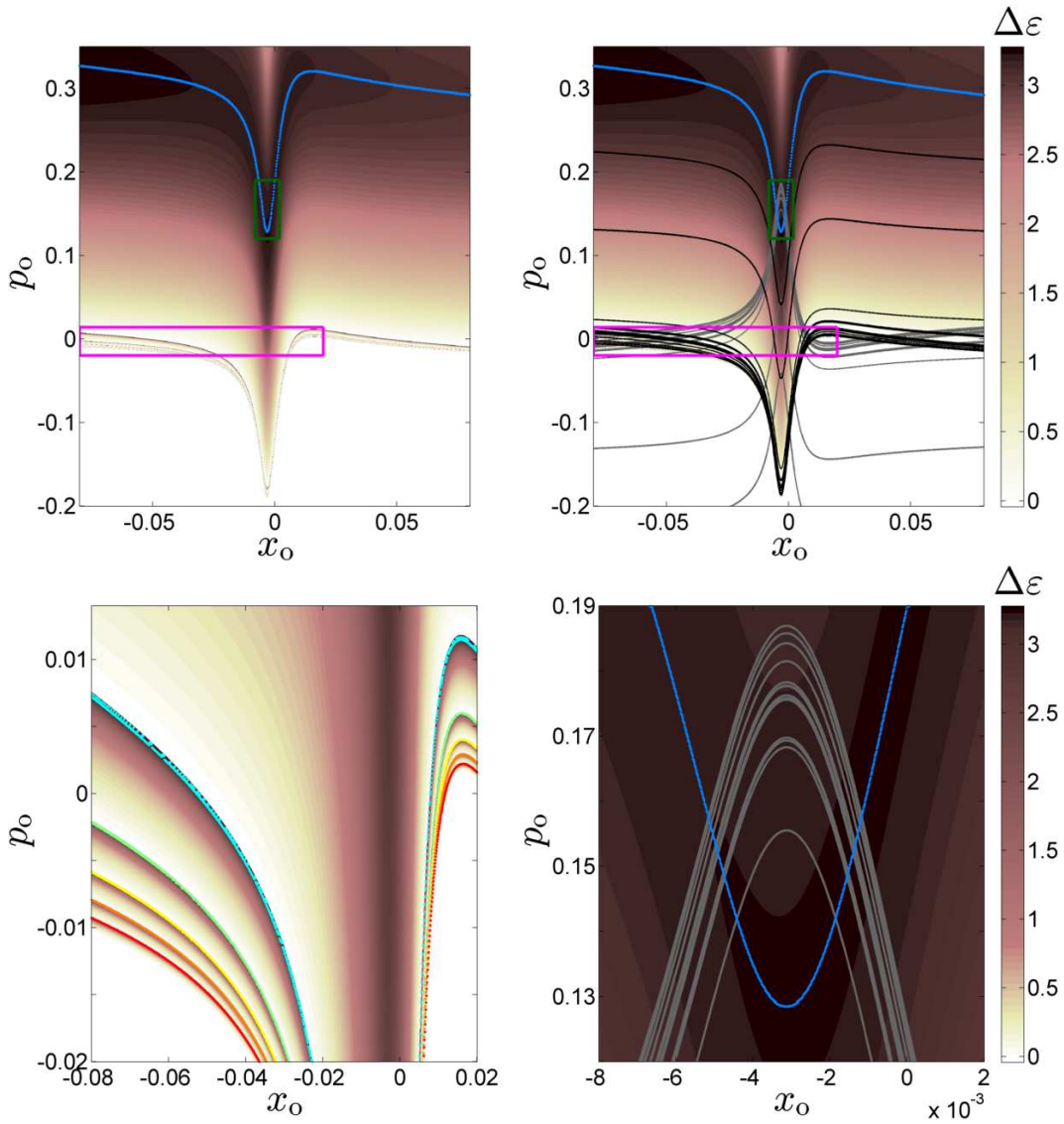


Figure 3.5: Energy exchange $\Delta\varepsilon$ at first recollision after a six laser cycle integration of Hamiltonian (3.24) with $a = 6.077 \times 10^{-3}$ and $\epsilon = 6.918 \times 10^{-5}$, as a function of initial conditions, $(x_0, p_0)$ with the initial phase $\phi$ is fixed by Poincaré section condition (3.22). Darker points correspond to higher energy. Top left panel: The initial conditions $(x_0, p_0)$ bringing the maximum energy $\Delta\varepsilon$ at first recollision in the first laser cycle for each $x_0$ are the blue curve. Top right panel: Same as top left, with the stable manifold $\mathcal{W}^s$ of $\mathcal{O}$ plotted in black and its unstable manifold $\mathcal{W}^u$ in grey. Bottom left panel: Zoom of the lower magenta framed region on top. Colored curves are the initial conditions $(x_0, p_0)$ bringing the maximum energy at first recollision for each $x_0$ and iteration of Poincaré map $\mathcal{P}$ during which the recollision happens. The colors correspond to Figs. 3.3 and 3.7. Bottom right panel: Zoom of green framed region above. $x_0$ is in units of $E_0/\omega^2$, $p_0$ is in units of $E_0/\omega$, $\Delta\varepsilon$ is in units of $U_p$.

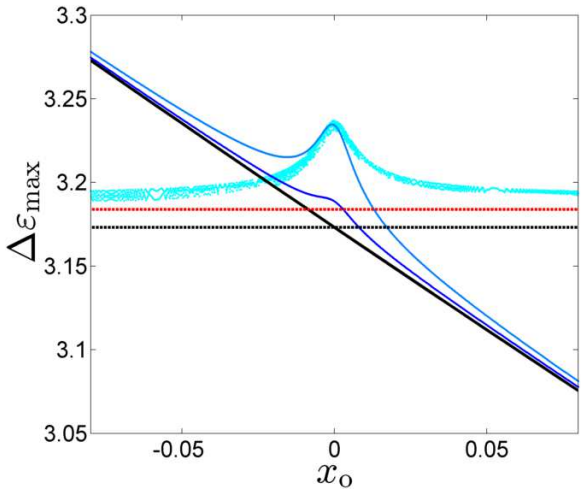


Figure 3.6: Maximum change in energy $\Delta\varepsilon$ as a function of $x_0$. Thick black line: SFA, immediate recollision. Light blue curve: Coulomb included, immediate recollision. Cyan points: Coulomb included, second cycle delayed recollision. Thin blue curve: Coulomb included, immediate recollision final energy, $\varepsilon(t_r)$. Dotted black line: 3.17 $U_p$. Red line: Estimate of delayed recollision energy "cutoff." $x_0$ is in units of $E_0/\omega^2$, $\varepsilon$ is in units of $U_p$.

immediate recollision curve is mostly close to the SFA curve, especially as $|x_0|$ increases. At such a high laser intensity, its deviations from the SFA curve are in large part due to the leading Coulomb correction to the final return energy $\varepsilon(t_r)$ [20], which is indeed even closer to the SFA curve. Therefore, we now see clearly the differing effects of varying $x_0$ versus turning on the Coulomb field on the return energy. If one considers the total energy at return (as opposed to the energy difference or only the return kinetic energy), then the effect of the Coulomb field on the value of the return energy compared with the SFA is small for this laser intensity. The major deviations from $3.17U_p$ come from varying $x_0$, and in the previous section we account for these effects using the SFA.

Now we re-examine the delayed recollisions with the Coulomb field included. The continuous gradient of $\Delta\varepsilon$ in the upper left panel of Fig. 3.5 near the maximum energy of immediate recollisions is again interrupted, at low values of $p_0$, by a series of jumps, seen more closely in the bottom left panel of Fig. 3.5. This is where the delayed recollisions originate, which can be confirmed by inspecting Fig. 3.7. Like Fig. 3.3, Fig. 3.7 shows the iteration of the Poincaré map during which each initial condition has its first recollision.

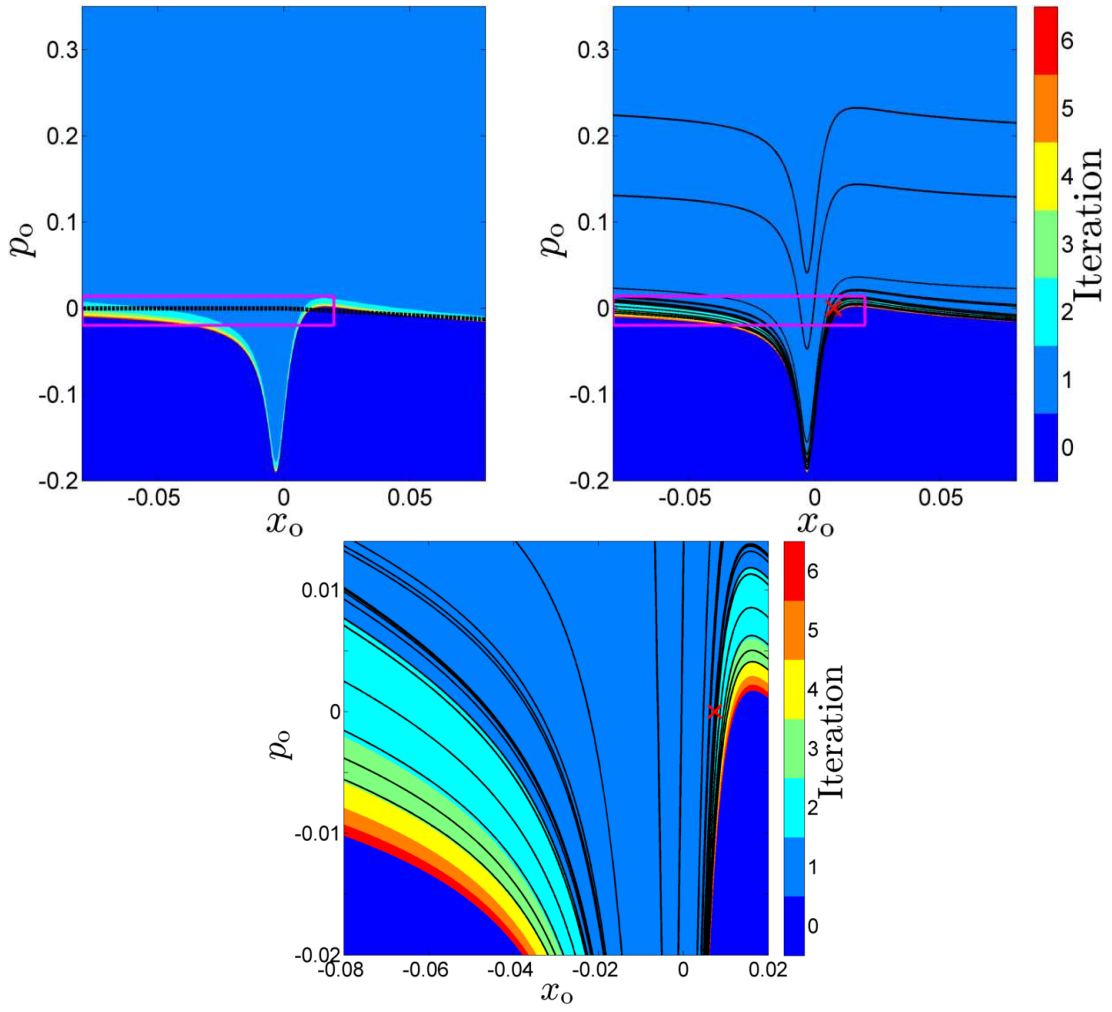


Figure 3.7: Number of iterations of Poincaré map $\mathcal{P}$ until the first recollision has occured after a six laser cycle integration, as a function of initial condition $(x_0, p_0)$. The initial phase $\phi$ is fixed by Poincaré section condition (3.22). Top left panel: The black dotted line separates immediately ionizing trajectories from recolliding trajectories in the SFA. Top right panel: Same as top left panel, with stable manifold $\mathcal{W}^s$ of $\mathcal{O}$ plotted in black. Location of $\mathcal{O}_-$ marked as the red cross. Bottom: Zoom of the magenta framed region above. $x_0$ is in units of $E_0/\omega^2$, $p_0$ is in units of $E_0/\omega$.

The Poincaré map is the discrete map $(x_{i+1}, p_{i+1}) = \mathcal{P}(x_i, p_i)$ that takes a point $(x_i, p_i)$ on the Poincaré section (3.22) to the next point $(x_{i+1}, p_{i+1})$ at which the trajectory started with $(x_i, p_i)$ pierces the surface of section. Thus, for the range of initial conditions we consider, the iteration of the map $\mathcal{P}$ during which an initial condition $(x_0, p_0)$ has its first recollision is the smallest $n$ such that $x_n > 0$. As we stated earlier, in the SFA the map $\mathcal{P}$ corresponds exactly to the duration of one laser cycle. With the Coulomb field included and a large laser intensity, this correspondence continues to hold only approximately. Still, for the remainder of the chapter, when we refer to a "cycle" during which a recollision occurs, we really mean the iteration $n$ of the Poincaré map $\mathcal{P}$. Comparing Fig. 3.7 and Fig. 3.3 makes the significant qualitative differences between the SFA and the full Hamiltonian (3.24) apparent. For example, the Coulomb focusing effect is clearly manifested by the greater area of phase space that leads to recollisions compared with the SFA picture. The curve that separates immediate ionizations from recolliding trajectories in Fig. 3.3 is plotted on the upper panel of Fig. 3.7. The reduced spread of the electronic wave packet can be inferred from the observation that a substantial area of the immediate ionizations in the SFA are converted into recolliding trajectories with the Coulomb field on, especially in the core region (small $x_0$). In particular, the delayed recollisions are enhanced by the Coulomb field. In the previous section we observe from Fig. 3.3 that the delayed recollision initial conditions lay between the immediate recollisions and immediate ionizations in the region of phase space with a small $p_0 > 0$ and $x_0 < 0$. With the Coulomb field on, we see in Fig. 3.7 that the delayed recollision boundary extends to $x_0 > 0$ and near $x_0 = 0$ it takes a significant dip in the direction $p_0 < 0$, so the presence of the Coulomb field enables more delayed recollisions.

In addition, the Coulomb field allows certain delayed recollisions to bring energy that slightly exceeds the well known $3.17U_p$ upon their very first recollision. This is shown in the lower left panel of Fig. 3.5, where although we have changed the distribution of colors on the color scale compared with the panel above it, the overall scale remains the same. It is

true that most of each recollision region of a particular delay contains trajectories that first recollide with a low amount of energy close to that brought by delayed recollisions in the SFA, $\lesssim 0.5U_p$. However, the energy at first recollision rapidly increases near the boundaries of the recollision regions of differing delays. The initial conditions bringing back the maximum energy for each $x_0$ and delay time are the colored curves. Actually these curves are made up of discrete points (one for each $x_0$ on our grid) that in most places are so close together that they appear to form a continuous curve. The energies of the second-cycle delayed recollisions as a function of $x_0$ are plotted in Fig. 3.6. We observe that for any $x_0$, there exists a second-cycle delayed recollision that brings back energy exceeding $3.17U_p$. Moreover, the amount of energy brought back by these delayed recollisions does not display the approximately linear dependence of $\Delta\varepsilon_{\text{max}}$ on $x_0$ characteristic of the immediate recollisions, but rather approaches a constant value for large $|x_0|$ and has a jump near $x = 0$. Surprisingly, the Coulomb well is all but invisible at maximum laser amplitude, yet its presence causes certain delayed recollisions to recollide with an energy above the usual SFA prediction on their very first recollision. Though we do not show the maximum energies brought by higher order delayed recollisions in Fig. 3.6, we argue in the next section that for every $x_0$ in the range we consider, there is a recollision of arbitrary delay that carries the same energy as we observe the maximum energy second-cycle recollisions carry [1]. Therefore, during every laser cycle there are energetic recollisions with energies close to $3.17U_p$, and this is due to the Coulomb field. We emphasize that the SFA misses this completely - as discussed in Section 3.2, the energetic immediate recollisions are ionized after one laser cycle, and only trajectories with sufficiently low drift momenta will continue to recollide with energies $\lesssim 2.4U_p$. In the next section, we explain the nonlinear dynamical origin of the delayed recollisions, and the origin of the cutoff in their energy exchange.

[1] We omitted the maximum energies of the higher order delayed recollisions because the shrinking size of the regions of phase space leading to recollisions with increasingly longer delays (see Fig. 3.7) makes it challenging to accurately compute the initial condition that recollides with the maximum energy for a particular delay.

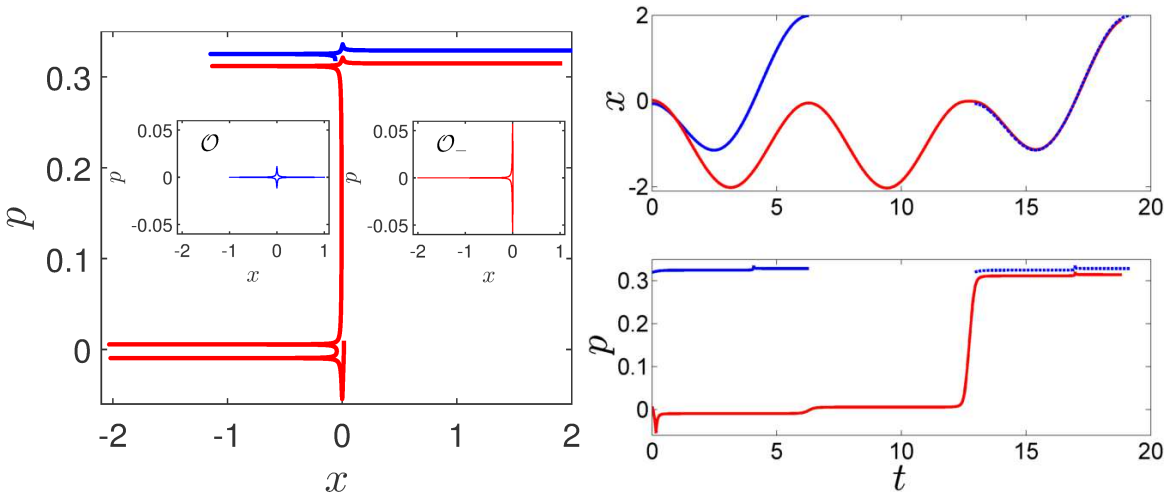


Figure 3.8: Left: Two typical $\Delta\varepsilon$-maximizing trajectories in $x$-$p$ phase space. An immediate recollision is in blue, and a third-cycle delayed recollision is in red. Left inset: Periodic orbit $\mathcal{O}$. Right inset: Periodic orbit $\mathcal{O}_-$. Right: $\Delta\varepsilon$-maximizing trajectories of the left figure plotted as $x$ vs. $t$, upper, and $p$ vs. $t$, lower. The immediate recollision is also shown as a dotted blue line, translated in time so its laser phase matches that of the delayed recollision. $x$ is in units of $E_0/\omega^2$, $p$ is in units of $E_0/\omega$, $t$ is in radians.

### 3.3.2 Building Blocks of Recollisions: Periodic Orbits and Their Invariant Manifolds

The qualitative character of both immediate and delayed recolliding trajectories can be understood by considering some periodic orbits of the system. The most relevant periodic orbits are $\mathcal{O}$ and $\mathcal{O}_-$, shown as the insets on the left plot of Fig. 3.8. The importance of $\mathcal{O}$ for recollisions was first described in Ref. [20], and in Ref. [101] it is shown that $\mathcal{O}_-$ [and $\mathcal{O}_+$, its symmetric copy via symmetry (3.3)] underlie ionization stabilization in ultra-intense laser fields. Due to our choice of Poincaré section and our interest in initial conditions beginning near the core, we need not consider $\mathcal{O}_+$ here. Each orbit has a period of exactly one laser cycle. For the parameters we have chosen, both $\mathcal{O}$ and $\mathcal{O}_-$ are hyperbolic, i.e. they are unstable. Thus, initial conditions in the vicinity of these orbits may take trajectories qualitatively similar to the orbits for some time, before eventually ionizing.

This is precisely what we observe when we examine both the immediate and delayed recollision trajectories in phase space and compare them with the periodic orbits. In the left panel of Fig. 3.8, we have plotted an energetic immediate recollision and an energetic

third-cycle delayed recollision. The immediate recollision resembles the motion of $\mathcal{O}$, as was noted in Ref.[20]. $\mathcal{O}$'s main characteristics are motion between $x \approx -E_0/\omega^2$ and $x \approx E_0/\omega^2$, with a small momentum kick due to the Coulomb field upon recollision. Correspondingly, the energetic immediate recollision also travels out to $x \approx -E_0/\omega^2$, before recolliding, receiving a small momentum kick, and ionizing forever. Delayed recollisions on the other hand spend some time following the orbit $\mathcal{O}_-$, before reaching the part of phase space where immediate recollisions live and the motion of $\mathcal{O}$ dominates. $\mathcal{O}_-$ is distinguished by its motion between $x \approx -2E_0/\omega^2$ and $x \approx 0$, with a comparatively large momentum kick at the core. Inspection of the third-cycle delayed recollision confirms that it has exactly this behavior for two laser cycles. After the end of the second laser cycle, the momentum kick received by the electron is so large that the trajectory is moved into the region of phase space from which the energetic immediate recollisions originate. Thus, delayed recollisions follow the motion of $\mathcal{O}_-$ for some number of laser cycles until they are converted into immediate recollisions. At this stage, their motion is the same as an immediate recollision. This can be observed from the right panels of Fig. 3.8, where we have plotted the energetic recollisions of the left panel as both $x$ vs. $t$ and $p$ vs. $t$, with the immediate recollision also translated forward in time so that its laser phase matches that of the delayed recollision. Clearly, these trajectories nearly overlap, illustrating that the delayed recollisions eventually become immediate recollisions.

The arrangement of the delayed recollision initial conditions in phase space and their transport to the realm of immediate recollisions is determined by the stable and unstable manifolds, respectively, of $\mathcal{O}$. The stable manifold $\mathcal{W}^s$ of a periodic orbit $\mathcal{O}$ is defined as the set of initial conditions that approach $\mathcal{O}$ as $t \to \infty$. Conversely, the unstable manifold $\mathcal{W}^u$ is the set of initial conditions that approach $\mathcal{O}$ as $t \to -\infty$, meaning those trajectories escape from the orbit moving forward in time. It was already shown in Ref. [20] that $\mathcal{O}$'s invariant manifolds regulate the recollision dynamics. There, the initial conditions leading to many recollisions were found to be concentrated near $\mathcal{W}^s$, and trajectories would follow

$\mathcal{W}^u$ on their way to ionization. It turns out that these manifolds also organize the delayed recollisions: delayed recollisions begin near $\mathcal{O}$'s stable manifold and then follow its unstable manifold to eventually recollide with the core. The former is seen in the right panel of Fig. 3.7, where we show $\mathcal{W}^s$ [2]. $\mathcal{W}^s$ is obtained from the numerically calculated $\mathcal{W}^u$ by the time-reversal symmetry $(x, p, \phi) \rightarrow (x, -p, \pi - \phi)$. We compute $\mathcal{W}^u$ using the algorithm of Ref. [102]. Briefly, (i) the initial part of the manifold is approximated by a very short curve on the Poincaré section near $\mathcal{O}$ and along its unstable direction; (ii) points along this curve are integrated to obtain the next section of the curve, with the points being selected adaptively in order to sufficiently resolve the new section; (iii) step (ii) is repeatedly iterated on the newest section of the manifold that has been calculated. Comparing the left and right upper panels of Fig. 3.7 shows that all the delayed recollisions come from a region of phase space in which the curves of the stable manifold are dense (compared with other regions of phase space). Looking at the delayed recollision region more closely in the lower panel of Fig. 3.7 shows that the stable manifold actually separates regions with differing recollision delay times. This is seen at the boundaries between immediate/second cycle recollisions, second/third cycle recollisions, and third/fourth cycle recollisions. We expect that if the manifold is computed for longer times then it would also be seen to separate the higher order recollisions. We note that there are parts of the manifold that are entirely contained in a region of a particular recollision delay time. While these parts of the manifold are not relevant for separating initial conditions with different delay times, we expect they separate trajectories with another type of qualitative difference; for example, they may separate regions of initial conditions that have differing total numbers of recollisions, as in Ref. [20]. Additionally, the delayed recollisions are indeed located near the orbit $\mathcal{O}_-$, as was suggested earlier by noting the similarities of the delayed recollision trajectories to the periodic orbit.

When the initial conditions leading to delayed recollision are integrated, they follow

[2] We have not marked the location of $\mathcal{O}$ on the figure because on this Poincaré section $\mathcal{O}$ is located at approximately $(x, p) = (E_0/\omega^2, 0)$, far from the core.

$\mathcal{W}^u$, the unstable manifold of $\mathcal{O}$, and this process underlies our observations regarding the maximum energy available to a delayed recollision and the particular dependence of the maximum energy on $x_0$. Consider an initial condition leading to an $n$-cycle delayed recollision. By definition, after one iteration of the Poincaré map, it must move into the region of phase space from which $(n-1)$-cycle recollisions originate, with $x < 0$. This will happen repeatedly until the iteration immediately prior to recollision, when the trajectory reaches the immediate recollision region of phase space. Additionally, the trajectories accomplish this motion by following $\mathcal{W}^u$. Therefore, the recollision energies accessible to delayed recollisions are the immediate recollision energies in the vicinity of the unstable manifold. These can be read off by looking at the upper right panel of Fig. 3.5. $\mathcal{W}^u$ enters the immediate recollision region above the region where $\mathcal{W}^s$ is dense and delayed recollisions proliferate. We observe that in this region $\mathcal{W}^u$ is thickest for smaller $p_0$, and in this region the recollision energies are low, $\sim 0.5U_p$. This explains why most of the delayed recollisions recollide with an energy $\lesssim 0.5U_p$, as we remarked earlier in reference to the lower left panel of Fig. 3.5. However, $\mathcal{W}^u$ does enter the region of high energy immediate recollisions, and in fact it is seen to intersect the curve of maximum $\Delta\varepsilon$ immediate recollisions in the lower right panel of Fig. 3.5. The delayed recollisions that end up in the region near this intersection are the delayed recollisions maximizing $\Delta\varepsilon$.

We look more carefully at the intersection of $\mathcal{W}^u$ with the curve of $\Delta\varepsilon$-maximizing immediate recollisions in Fig. 3.9. Here we have also plotted many second-cycle recollisions on their first return to the Poincaré section (3.22). Firstly, the points are seen clearly to lie very close to $\mathcal{W}^u$, confirming our earlier claim that the delayed recollisions follow $\mathcal{W}^u$. Next, we observe that there are always continuous gradients of $x_0$ perpendicular to the manifold, including in the region where the manifold intersects the curve of maximum energy immediate recollisions. This region is magnified in the inset of Fig. 3.9. This is exactly why for any $x_0$, it is possible to find a second-cycle delayed recollision with $\Delta\varepsilon$

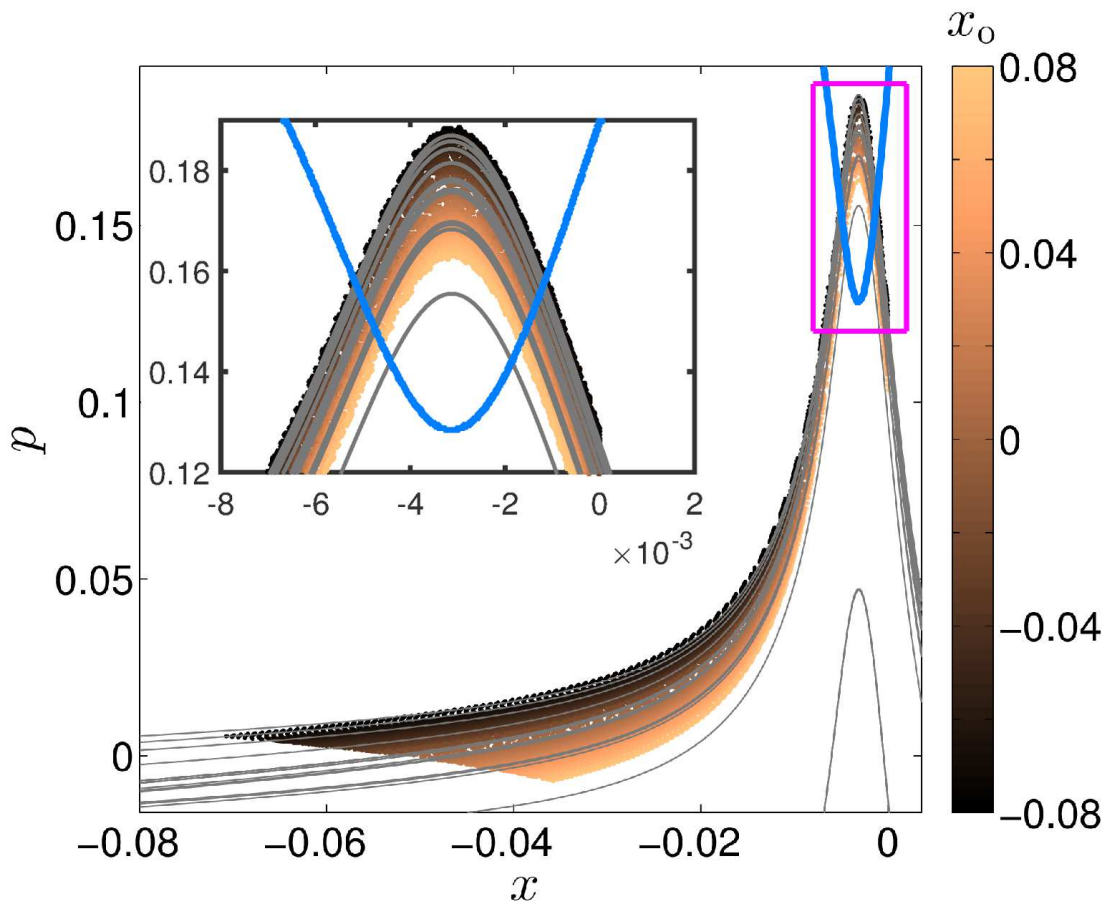


Figure 3.9: $\mathcal{P}(x_0, p_0)$ for the initial conditions $(x_0, p_0)$ in Fig.3.7 leading to a second-cycle delayed recollision. Color scale shows $x_0$. Light blue curve is the initial conditions leading to a maximum $\Delta\varepsilon$ immediate recollision. Thin grey curve is $\mathcal{W}^u$ of $\mathcal{O}$ . Inset: Zoom of the magenta-framed region. $x$ is in units of $E_0/\omega^2$, $p$ is in units of $E_0/\omega$.

exceeding $3.17U_p$. The energy of these delayed recollisions is

$$\Delta\varepsilon_{\text{max}} = \Delta\varepsilon_{\text{max,imm}}(x_p) + \Delta V(x_p, x_0), \tag{3.25}$$

where $\Delta\varepsilon_{\text{max,imm}}(x)$ is the maximum energy of an immediate recollision beginning at $x$, $x_p$ is the position of the delayed recollision's return to the Poincaré section on the cycle immediately prior to its recollision, and $\Delta V(x_p, x_0)$ is the change in energy between the delayed recollision at $t = 0$ and the time it returned to the Poincaré section prior to recollision. Because the section condition is zero velocity, there is no change in kinetic energy so $\Delta V$ is just the change in Coulomb potential energy. Therefore we can obtain an estimate of the minimal $\Delta\varepsilon_{\text{max}}$ for a delayed recollision by taking $\Delta V(x_p, x_0) = -\epsilon/a$ and $\Delta\varepsilon_{\text{max,imm}}$ to be the minimal maximum energy accessible to an immediate recollision in the vicinity of $\mathcal{W}^u$. This estimate is plotted for second-cycle delayed recollisions in Fig. 3.6, and does a good job of providing a "cutoff" for the minimal maximum energy second-cycle delayed recollision. The remaining shape of the maximum energies for the delayed recollisions resembles the Coulomb potential and is mostly due to $\Delta V(x_p, x_0)$. Intuitively, because $x_p$ takes a quite limited range of values, $\Delta\varepsilon_{\text{max,imm}}(x_p)$ is approximately constant and $\Delta V(x_p, x_0) \approx V(\tilde{x}_p) - V(x_0)$, where $\tilde{x}_p$ is some position where $\mathcal{W}^u$ intersects the maximum energy immediate recollision curve. This explains why the delayed recollision energy curve approximately takes the shape of minus the Coulomb potential.

In Fig. 3.9, $\mathcal{W}^u$ is seen to intersect the curve of $\Delta\varepsilon$-maximizing immediate recollisions in two places. In between the two intersections, $\mathcal{W}^u$ crosses into a region of lower energy recollisions, seen in the lower right panel of Fig. 3.5, and thus we should expect that there should actually be two energy maximizing delayed recollisions for each $x_0$. Indeed this is what we see, and this is the cause for the thickness of the set of points giving energy maximizing delayed recollisions in Fig. 3.6. This is seen even more clearly in Fig. 3.10, where we have magnified a region containing second-cycle delayed recollision initial conditions

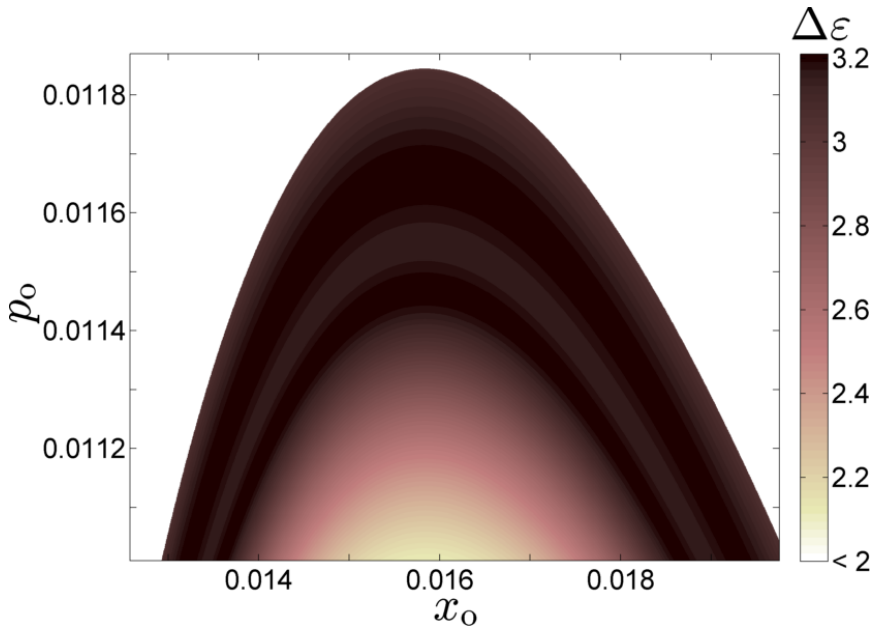


Figure 3.10: Energy exchange $\Delta\varepsilon$ at first recollision as a function of initial conditions $(x_0, p_0)$. A region of second-cycle delayed recollisions is highly magnified here, revealing two local maxima in $\Delta\varepsilon$. Second-cycle delayed recollision initial conditions are in the colored region, immediate recollisions in the white region. Darker colors correspond to higher recollision energies. $x_0$ is in units of $E_0/\omega^2$, $p_0$ is in units of $E_0/\omega$, $\Delta\varepsilon$ is in units of $U_p$.

and shown their energy exchange upon their first recollisions. We observe two ridges, corresponding to the predicted two maximum energy recollisions for each $x_0$.

It is also possible to find higher order delayed recollisions of an arbitrary delay that return with an energy at least at the delayed recollision cutoff. As we have argued, every laser cycle a delayed $n$-cycle recollision will move into the region of phase space from which the $n-1$-cycle recollisions originate, with $x < 0$. Therefore, eventually any $n$-cycle delayed recollision will end up in the second-cycle delayed recollision region of phase space with $x < 0$, i.e. two laser cycles before its recollision. But we have just shown that for any $x_0$, there are second cycle delayed recollisions that recollide with an energy above the delayed recollision cutoff. Thus, every laser cycle, there are delayed recollisions arriving that bring an energy near $3.17U_p$ to the core. Though the SFA does a reasonable job of providing the energy cutoff, these kinds of trajectories are absent in the SFA, and are a direct consequence of the ion's Coulomb field and the organization of the dynamics by the periodic orbits $\mathcal{O}$ and $\mathcal{O}_\pm$ and the invariant manifolds of $\mathcal{O}$.

### 3.4 Summary

In summary, we have shown that even in the high laser intensity regime where the strong field approximation is expected to hold, the Coulomb field significantly impacts the dynamics by inhibiting the spatial spread of the electronic wave packet and allowing delayed recollisions to bring high energy to the core region. We reported the effectiveness of Coulomb focusing in a one-dimensional model, which is usually attributed to higher dimensional models. We found that while the SFA gives adequate estimates of the maximum possible return energy in the strong field regime, it misses the behavior of the electron for times beyond the first laser cycle, when the Coulomb field causes trajectories to continue to recollide with energies near $3.17U_p$. We have unraveled the dynamical organization of these delayed recollisions by looking at specific periodic orbits and their invariant manifolds. The delayed recollision trajectories that we focused on are important not only because of

the high energy they may recollide with, but also because they spend potentially many laser cycles near the core. Thus, they have many opportunities to exchange energy with the ion and the electromagnetic field (due to the acceleration imparted on such electrons by the Coulomb force). We expect that the delayed recollisions are the mechanism underlying HHG and thus explain the observation of the appearance of the plateau and $\sim 3.17U_p$ high-harmonic cutoff only *after* the first laser cycle, as in Ref. [20].

# CHAPTER 4

# VARIATIONAL FORMULATION OF CLASSICAL AND QUANTUM MODELS FOR INTENSE LASER PULSE PROPAGATION

The self-consistent interaction between charged particles and electromagnetic fields is pervasive in physics. Some common examples include laser-plasma interactions [103], free electron lasers [104], and laboratory and astrophysical plasmas [21]. Attacking such problems theoretically or even numerically poses a formidable challenge due to the high dimensionality of these systems: The coupling of Maxwell's equations to the charged particle dynamics leads to an infinite-dimensional dynamical system on large spatial scales. Even if a complete representation of these dynamics were obtainable, it would contain far too much information to allow a clear explanation of the results. In fact, frequently the results may be explained in terms of simple physical mechanisms which are not substantially affected by the fine details contained in the complete description of the field-particle interaction. See, for example, the single-wave model for the free electron laser [87, 104] and the beam-plasma instability [105]. Therefore, we are constantly motivated to seek reduced descriptions which are both numerically tractable and simple enough to permit theoretical analysis of the results and novel experimental predictions.

A powerful and widely-used framework for the reduction of parent models of self-consistent field-particle interaction is the variational formulation [23]. It consists of casting the first-principles equations either as an action principle or a Hamiltonian system. For instance, an action principle for the Vlasov-Maxwell equations is given in Ref. [106] and the corresponding Hamiltonian structure is found in Refs. [107, 108]. Then, simplifying hypotheses for a given problem are incorporated directly into the variational formulation, whether by applying the hypotheses to the action, the Hamiltonian and Poisson bracket [87], or some combination of the two, as in gyrokinetic theory [86]. Employing a vari-

ational formulation poses several advantages over a reduction performed directly on the equations of motion. Consistently working in a variational formulation allows the reduced models to preserve conserved quantities possessed by the parent model, avoiding the introduction of unphysical dissipation to the system [23, 109]. Further, variational formulations can provide convenient frameworks for performing arbitrary coordinate transformations [85]. Lastly, they provide a foundation for the development of specialized numerical schemes which inherently respect the variational structure of the system [110–115] and thus may be suitable for long-time integration [116, 117].

In this chapter, we consider a variational formulation suitable for describing the propagation of intense, low-frequency laser pulses in gases. This is the setting for high-harmonic generation (HHG) [24, 44], terahertz (THz) generation [118, 119], and filamentation [120, 121], to name a few examples. The parent model which most accurately describes this system is the Maxwell-Schrödinger model [58], which describes the self-consistent interaction between the three-dimensional macroscopic electromagnetic fields and the microscopic wavefunctions describing the atomic or molecular response to the fields. A first-principles description of the atomic or molecular response is essential for accurately capturing the spatiotemporal evolution of the laser field over experimentally relevant propagation distances [122, 123], which can be hundreds to thousands of times the initial spatial extent of the pulse. In particular, a quantum or semi-classical description is required to obtain the high-harmonic part of the radiation spectrum with quantitative accuracy [83]. In Ch. 5, we show that a classical description of the atoms self-consistently coupled to the fields can successfully capture the low-frequency part of the spectrum during propagation, as compared with a reduced Maxwell-Schrödinger model. The classical description is also germane for THz generation, where the characteristics of the THz emission may be explained by studying electron trajectories [119].

Here, our objective is to use the variational formulations of both the quantum and classical parent models describing intense laser pulse propagation to derive the simplest reduced

models possible, whose behavior we investigate in detail in Ch. 5. We note that variational formulations of Maxwell-Schrödinger models have already been considered for the case of microscopic electromagnetic fields [96, 112, 124, 125], though they have not yet been considered for macroscopic fields to the best of our knowledge. Also, Hamiltonian formulations of reduced laser pulse propagation equations have been found *a posteriori*, i.e. after reduction from a parent model at the level of the equations of motion [126, 127].

This chapter is organized as follows. In Sec. 4.1, we state the parent models for the classical and quantum systems and the main assumptions that we will incorporate sequentially in order to build a hierarchy of reduced models. In Sec. 4.2, we provide the Lagrangian and Hamiltonian derivations of the model with classical dynamics for the particles. In Sec. 4.3, we provide the Lagrangian and Hamiltonian derivations of the model with quantum dynamics for the particles. In Sec. 4.4, we consider the spatial discretization of the fields in the Hamiltonian formulation, which is a precursor to obtaining variational integrators for the reduced-model equations. Finally, in Sec. 4.5, we summarize and make some concluding remarks. In App. B, we discuss the Lagrangian and Hamiltonian formulations of a more general classical model, from which the parent classical model of this chapter can be derived.

## 4.1 Parent model

Our parent model consists of a classical electromagnetic field interacting with a gas under some reasonable physical assumptions. For simplicity, we restrict ourselves to the case of single-species single-active-electron (SAE) atomic gases. The SAE approximation means that we assume the atom consists of a singly-charged ionic core and an electron. Further, we assume the ions are heavy enough that they may be considered static, at least on the short time scale of the laser pulse. We also assume the electron motion can be treated in the dipole approximation. This means the electrons are non-relativistic and move on spatial scales small compared to those of the spatial variations of the electromagnetic field,

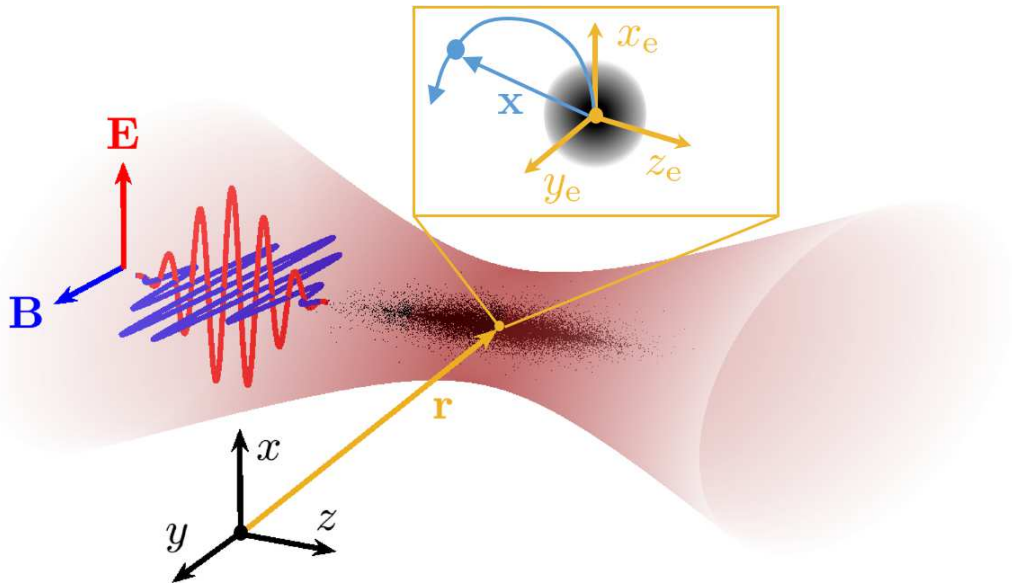


Figure 4.1: Schematic illustrating the typical geometry of an intense, linearly-polarized laser pulse propagating through an atomic gas. The incident pulse is on the left and it propagates in the positive $z$ direction. The intensity profile of the focused laser beam is shown in dark red. The gas atoms are the black dots distributed around the focus of the laser beam. $\mathbf{r}$ is the macroscopic coordinate, such that the laser electric field is $\mathbf{E}(\mathbf{r}, t)$ (in red), the magnetic field is $\mathbf{B}(\mathbf{r}, t)$ (in blue), and the gas density is $\rho(\mathbf{r})$. The inset shows that at each point $\mathbf{r}$, a microscopic coordinate $\mathbf{x}$ is attached, giving the position of the electron of an atom located at $\mathbf{r}$.

implying magnetic effects are neglected. Lastly, we assume a low-density gas such that collisions between electrons and neighboring atoms may be neglected, so each electron only interacts with its parent ion and the macroscopic electric field. A more basic model, where the dipole approximation is not made but the electrons are still non-relativistic, is the subject of App. B.

We define the dynamical variables and coordinate systems of our parent model, illustrated in Fig. 4.1, as follows. The dipole approximation leads naturally to a separation of length scales into a macroscopic scale and a microscopic scale. The coordinate of the macroscopic scale, $\mathbf{r} = (x, y, z)$, gives the position of an arbitrary point in the gas. Meanwhile, the coordinate of the microscopic scale, $\mathbf{x} = (x_e, y_e, z_e)$, gives the position of the electron relative to the ionic core of an atom. The dynamical variables for the electromagnetic field are $\mathbf{E}(\mathbf{r}, t)$ and $\mathbf{B}(\mathbf{r}, t)$. The atomic number density is $\rho(\mathbf{r})$, which is time-

independent due to the assumption of static ions. For the quantum model, the dynamical field variable for the particles is the electronic wavefunction $\psi(\mathbf{x}, t; \mathbf{r})$ of an atom located at $\mathbf{r}$. For the classical model, the dynamical field variable for the particles is $\mathbf{x}(\mathbf{r}, t; \mathbf{x}_0, \mathbf{v}_0)$, which gives the position $\mathbf{x}$ of the electron of an atom located at $\mathbf{r}$ at time $t$. The labels $\mathbf{x}_0$ and $\mathbf{v}_0$ define the initial position and velocity, respectively, i.e. $\mathbf{x}(\mathbf{r}, 0; \mathbf{x}_0, \mathbf{v}_0) = \mathbf{x}_0$ and $\dot{\mathbf{x}}(\mathbf{r}, 0; \mathbf{x}_0, \mathbf{v}_0) = \mathbf{v}_0$.

The equations of motion for the electromagnetic fields are Maxwell's equations, which read [58]

$$\dot{\mathbf{E}} = c^2 \nabla \times \mathbf{B} - 4\pi \dot{\mathbf{P}}, \tag{4.1a}$$

$$\dot{\mathbf{B}} = -\nabla \times \mathbf{E}, \tag{4.1b}$$

$$\nabla \cdot \mathbf{E} = -4\pi \nabla \cdot \mathbf{P}, \tag{4.1c}$$

$$\nabla \cdot \mathbf{B} = 0. \tag{4.1d}$$

Here, $\mathbf{P}$ is the macroscopic polarization which, in this case, can be expressed as

$$\mathbf{P}(\mathbf{r}, t) = -\rho(\mathbf{r}) \overline{\mathbf{x}}(\mathbf{r}, t), \tag{4.2}$$

where $\overline{\mathbf{x}}$ is the ensemble-averaged electron position of the atoms located near $\mathbf{r}$ at time $t$. That is, we average over the large number of atoms $\rho(\mathbf{r}) \mathrm{d}^3\mathbf{r}$ contained in a small volume $\mathrm{d}^3\mathbf{r}$ around $\mathbf{r}$ (see Fig. 4.1). In order to solve Eqs. (4.1), we must specify a microscopic model for the response of a single atom to the field, which allows one to determine $\overline{\mathbf{x}}$ from $\mathbf{E}$.

Typically, a quantum model is employed to obtain the single-atom response to the field,

as in the Maxwell-Schrödinger model [58]. The equations are

$$i\dot{\psi} = -\frac{1}{2}\nabla_{\mathbf{x}}^2\psi + \big[V(\mathbf{x}) + \mathbf{E}(\mathbf{r},t)\cdot\mathbf{x}\big]\psi, \tag{4.3a}$$

$$\overline{\mathbf{x}}(\mathbf{r},t) = \int \mathbf{x}\,|\psi(\mathbf{x},t;\mathbf{r})|^2\ \mathrm{d}^3\mathbf{x}. \tag{4.3b}$$

Here, Eq. (4.3a) is the Schrödinger equation for the wave function $\psi(\mathbf{x},t;\mathbf{r})$. The ion-electron interaction is described by an effective potential $V$, such as the soft-Coulomb potential $V(\mathbf{x}) = -(|\mathbf{x}|^2+1)^{-1/2}$ [84, 91, 97]. The use of the dipole approximation is evident from the fact that $\mathbf{E}$ depends on the macroscopic coordinate $\mathbf{r}$, but not on the microscopic coordinate $\mathbf{x}$. The latter is the sole degree of freedom of the electron, as illustrated in Fig. 4.1. Equation (4.3b) is the quantum expectation value of the observable $\mathbf{x}$, with the integration carried out over all $\mathbf{x}\in\mathbb{R}^3$. We assume that the ensemble of atoms located at $\mathbf{r}$ is initially in a pure state $\psi(\mathbf{x},0;\mathbf{r}) = \psi_0(\mathbf{x})$, i.e. each of the atoms is in the same initial state, so we do not need to consider a density matrix to describe the ensemble. Note that, in principle, $\psi_0$ could also depend on $\mathbf{r}$, but we choose to make it independent of $\mathbf{r}$ so that the initial state of the atoms is uniform. Thus, the expectation value $\overline{\mathbf{x}}$ in Eq. (4.3b) is indeed the ensemble-averaged electron position of the atoms at $\mathbf{r}$. Together, Eqs. (4.1)-(4.3) constitute the Maxwell-Schrödinger model, which we refer to here as the parent quantum model.

The quantum model is particularly effective in the context of HHG, where it accurately describes the evolution of the high harmonic radiation during propagation [58, 59]. However, the description of the electron dynamics in terms of a time-dependent wave function lacks the intuitive and very relevant dynamical picture provided by the underlying classical electron trajectories [2, 3, 20]. To address this issue, one option is to use purely classical models for the electron dynamics [48, 49, 83, 91, 128, 129], in which the Schrödinger equation is replaced with the corresponding classical equations of motion for $\mathbf{x}(\mathbf{r},t;\mathbf{x}_0,\mathbf{v}_0)$, and the quantum expectation value is replaced with a classical average over an ensemble of ini-

tial conditions. The ensemble of initial conditions is typically chosen to capture as much as possible the effects one would observe in a quantum description, such as wavepacket spreading. The corresponding equations are

$$\ddot{\mathbf{x}} = -\nabla_{\mathbf{x}} V(\mathbf{x}) - \mathbf{E}(\mathbf{r}, t), \tag{4.4a}$$

$$\overline{\mathbf{x}}(\mathbf{r}, t) = \int \mathbf{x}(\mathbf{r}, t; \mathbf{x}_0, \mathbf{v}_0) f_0(\mathbf{x}_0, \mathbf{v}_0) \mathrm{d}^3\mathbf{x}_0 \mathrm{d}^3\mathbf{v}_0. \tag{4.4b}$$

The dipole approximation is reflected in the same way in Eq. (4.4a) as in the quantum case. The integral in Eq. (4.4b) is carried out over all $(\mathbf{x}_0, \mathbf{v}_0) \in \mathbb{R}^3 \times \mathbb{R}^3$. Meanwhile, $f_0$ is the probability distribution function to find an electron with the given initial conditions. By averaging with respect to $f_0$ in Eq. (4.4b), we obtain the ensemble-averaged position of the electron relative to the ion $\overline{\mathbf{x}}$, which allows us to obtain the polarization using Eq. (4.2). As in the quantum case, we assume the initial state of the atoms $f_0$ is independent of $\mathbf{r}$. Together, Eqs. (4.1), (4.2), and (4.4) constitute the parent classical model. In App. B, we show how this classical parent model can be derived from one where the dipole approximation is not assumed, so that magnetic effects are fully included. There, we show that the source terms of Maxwell's equations in the more general model are the microscopic charge and current densities, as opposed to the macroscopic polarization and current.

For both parent models, it is not possible to solve the microscopic dynamics nor the macroscopic dynamics analytically. Hence, one must resort to numerical simulations. However, the computational cost of simulating the parent models is immense due to the multiscale nature of the problem. For instance, numerically solving the quantum model requires one to obtain the solution $\psi(\mathbf{x}, t; \mathbf{r})$ of Eq. (4.3a) at every time step for all $\mathbf{r}$ and $\mathbf{x}$ in the computational domain. In the present day, such a feat can only be accomplished using super-computers [58, 59]. Thus, reduced models with smaller computational requirements are highly desirable.

In the following sections, we will build a hierarchy of reduced models stemming from

Table 4.1: The various hypotheses underlying our reduced models. The left column contains hypotheses on the response of the particles to the field (HP), while the right column contains hypotheses on the fields themselves (HF).

| | |
|---|---|
| **HP 1** *SAE approximation* | **HF 1** *Electromagnetic fields solely depend on propagation coordinate $z$* |
| **HP 2** *static ions* | **HF 2** *$z$-component of the electric field is negligible* |
| **HP 3** *dipole approximation* | **HF 3** *linearly polarized fields* |
| **HP 4** *Particle fields solely depend on propagation coordinate $z$* | **HF 4** *backward-propagating waves are negligible* |
| **HP 5** *reduced electron phase space* | |

the two parent models by sequentially incorporating the hypotheses outlined in Table 4.1. The parent models already incorporate hypotheses HP 1-3. In this work, we choose to focus on the simplification of the field part of the equations, because any dimensional reduction on the macroscopic scale automatically results in fewer computationally-costly microscopic computations [130]. Furthermore, reductions on the particle dynamics tend to be less general and rely on specific hypotheses particular to certain sets of field parameters. Such reductions typically do not interfere with the structure of the self-consistent interaction between the field and the particles, so they may be built on top of the models we arrive at in this article. In fact, because we focus on reducing the electromagnetic fields, the models we obtain may be readily generalized to other types of gas species or condensed phase systems, simply by specifying the appropriate microscopic model for the reponse of the medium to the fields [130].

## 4.2 Classical reduced models

### 4.2.1 Lagrangian formulation

The classical model, Eqs. (4.1), (4.2), and (4.4), admits a Lagrangian formulation. First, we introduce the electromagnetic potentials, the scalar potential $\varphi(\mathbf{r}, t)$ and the vector potential $\mathbf{A}(\mathbf{r}, t)$, from which the electric and magnetic fields are obtained as

$$\mathbf{E} = -\nabla\varphi - \dot{\mathbf{A}}, \tag{4.5a}$$

$$\mathbf{B} = \nabla \times \mathbf{A}. \tag{4.5b}$$

Now, we define the action functional $\mathcal{A}[\mathbf{x}(\mathbf{r}, t; \mathbf{x}_0, \mathbf{v}_0), \varphi(\mathbf{r}, t), \mathbf{A}(\mathbf{r}, t)]$ as

$$\mathcal{A}[\mathbf{x}, \varphi, \mathbf{A}] = \int (\mathcal{L}_{\mathrm{P}} + \mathcal{L}_{\mathrm{EM}}) \mathrm{d}t, \tag{4.6a}$$

$$\mathcal{L}_{\mathrm{P}} = 4\pi \int \rho(\mathbf{r}) \left[ \frac{|\dot{\mathbf{x}}|^2}{2} - V(\mathbf{x}) + \mathbf{x} \cdot \nabla\varphi(\mathbf{r}, t) - \dot{\mathbf{x}} \cdot \mathbf{A}(\mathbf{r}, t) \right] \mathrm{d}\mu_0 \mathrm{d}^3\mathbf{r}, \tag{4.6b}$$

$$\mathcal{L}_{\mathrm{EM}} = \frac{1}{2} \int \left( |\nabla\varphi(\mathbf{r}) + \dot{\mathbf{A}}(\mathbf{r})|^2 - c^2 |\nabla \times \mathbf{A}(\mathbf{r})|^2 \right) \mathrm{d}^3\mathbf{r}, \tag{4.6c}$$

where we have introduced the notation $\mathrm{d}\mu_0 = f_0(\mathbf{x}_0, \mathbf{v}_0)\mathrm{d}^3\mathbf{x}_0\mathrm{d}^3\mathbf{v}_0$ and we recall $\rho(\mathbf{r})$ is the number density of the atomic gas. Hence, the Lagrangian is decomposed into a particle Lagrangian $\mathcal{L}_{\mathrm{P}}$ and an electromagnetic Lagrangian $\mathcal{L}_{\mathrm{EM}}$, in a manner similar to the Low Lagrangian for the Vlasov-Maxwell equations [106]. We have made the dependence of the electromagnetic potentials on $\mathbf{r}$ explicit here to make the distinction from a more fundamental model without the dipole approximation discussed in App. B; however, for the remainder of this section we will suppress the functional dependence of the potentials.

Imposing $\delta\mathcal{A} = 0$, i.e. $\mathcal{A}_{\mathbf{x}} = \mathcal{A}_{\varphi} = \mathcal{A}_{\mathbf{A}} = 0$, and applying Eqs. (4.5) yields the parent model equations (4.1) and (4.4). The subscript denotes the functional derivative, defined

for a functional $\mathcal{F}[f(\mathbf{z})]$ of a function $f$ on an $n$-dimensional domain by

$$\mathcal{F}[f(\mathrm{z})+\varepsilon\delta f(\mathrm{z})]-\mathcal{F}[f(\mathrm{z})]=\varepsilon\int\mathcal{F}_f\delta f\,\mathrm{d}^n\mathbf{z}+\mathcal{O}(\varepsilon^2).$$

The first of these equations yields Eq. (4.4a), when one requires that $\mathcal{A}_{\mathbf{x}}=0$ for an arbitrary $f_0$. The second yields

$$-(\nabla^2\varphi+\nabla\cdot\dot{\mathbf{A}})=4\pi\nabla\cdot\left(\rho\int\mathbf{x}\,\mathrm{d}\mu_0\right). \tag{4.7}$$

This is equivalent to Gauss' Law, Eq. (4.1c), upon applying Eqs. (4.5a), (4.4b), and (4.2). Similarly, the third yields

$$-(\nabla\dot{\varphi}+\ddot{\mathbf{A}})=c^2\nabla\times(\nabla\times\mathbf{A})+4\pi\rho\int\dot{\mathbf{x}}\,\mathrm{d}\mu_0,$$

which is equivalent to the Maxwell-Ampère equation (4.1a). Meanwhile, Eqs. (4.1b) and (4.1d) are automatically satisfied by virtue of Eqs. (4.5).

We remark that the existence of a variational priniciple is a fundamental property of the system. That is, it is not a consequence of choosing a particular set of dynamical variables, such as the electromagnetic potentials. For example, one may write an action principle using the electric and magnetic fields themselves as dynamical variables, instead of the potentials, but the formulation is more complicated as it requires constrained variations. Thus, we use the electromagnetic potentials for convenience.

Now, we begin making assumptions and approximations appropriate to typical experimental situations in order to obtain a hierarchy of reduced models. In experiments, the radiation is generated by the propagation of spatially localized laser pulses with a given polarization through the gas. The spatial localization comes from the focusing of the laser beam, which typically leads to a Gaussian intensity profile with cylindrical symmetry about the propagation axis (see Fig. 4.1). As such, the vacuum field intensity only depends

on the propagation coordinate $z$ and the distance from the propagation axis $|\mathbf{r}_\perp|$, where $\mathbf{r}_\perp = (x, y)$. The time-dependent electric field then consists of the product of a spatial envelope due to focusing, a temporal envelope due to finite pulse duration, and an oscillation at the carrier frequency of the laser $\omega_L$. Notably, the focusing leads to a $z$-dependent maximum amplitude of the field as well as a $z$-dependent carrier-envelope phase, known as the Gouy phase shift [131], even in vacuum. Focusing effects can be described efficiently within the paraxial approximation, which is valid for laser beams that are not too tightly focused. However, even within the paraxial approximation, the dimensionality of the electromagnetic fields is not substantially reduced. The fields still depend on two spatial coordinates, $r_\perp$ and $z$. Furthermore, even though it is true that the fields are dominated by the transverse components, i.e. the $\mathbf{r}_\perp$ direction, Gauss' Law requires that they have a longitudinal component as well [131]. Hence, the fields are still three-dimensional vectors in the case of arbitrary laser polarization, and still two-dimensional in the simpler (and very common) case of linear polarization. Lastly, the paraxial approximation inherently assumes backward-propagating waves are negligible [123], but this is not necessarily the case if the gas density is high enough [132].

*Plane-wave fields (HP 1-4, HF 1)*

Here, we make strong assumptions on the fields to bypass these difficulties. Namely, we assume that the fields' only spatial dependence is on $z$, invoking hypotheses HF 1 and HP 4 of Table 4.1. We take the fields to be plane waves of the form

$$\rho = \rho(z), \tag{4.8a}$$

$$\mathbf{x} = \mathbf{x}(z, t; \mathbf{x}_0, \mathbf{v}_0), \tag{4.8b}$$

$$\varphi = \varphi(z, t), \tag{4.8c}$$

$$\mathbf{A} = \mathbf{A}_\perp(z, t) = A_x(z, t)\hat{\mathbf{x}} + A_y(z, t)\hat{\mathbf{y}}. \tag{4.8d}$$

In writing the vector potential, we have employed the radiation gauge $\nabla \cdot \mathbf{A} = 0$ which, for $z$-dependent fields, becomes $\partial_z A_z = 0$. While this technically allows $A_z$ to be a function of time, we have chosen $A_z = 0$ to avoid the presence of a uniform time-dependent electric field. As is evident from Eq. (4.7), the main appeal of adopting the radiation gauge is that all the space charge effects, i.e. those due to a spatially nonuniform charge distribution, are encoded in $\varphi$.

Inserting Eqs. (4.8) into Eqs. (4.6), we obtain the Lagrangians of the reduced system as

$$\mathcal{L}_{\mathrm{P}} = 4\pi \int \rho \left[ \frac{|\dot{\mathbf{x}}|^2}{2} - V(\mathbf{x}) + z_{\mathrm{e}}\, \partial_z \varphi - \dot{\mathbf{x}}_\perp \cdot \mathbf{A}_\perp \right] \mathrm{d}\mu_0 \mathrm{d}z, \tag{4.9a}$$

$$\mathcal{L}_{\mathrm{EM}} = \frac{1}{2} \int \left[ (\partial_z \varphi)^2 + |\dot{\mathbf{A}}_\perp|^2 - c^2 |\partial_z \mathbf{A}_\perp|^2 \right] \mathrm{d}z. \tag{4.9b}$$

By taking variations with respect to the present variables, we obtain the equations of motion

$$\ddot{\mathbf{x}} = -\nabla_{\mathbf{x}} V(\mathbf{x}) + (\partial_z \varphi)\hat{\mathbf{z}} + \dot{\mathbf{A}}_\perp, \tag{4.10a}$$

$$\partial_z^2 \varphi = -4\pi \partial_z (\rho \overline{z}_{\mathrm{e}}), \tag{4.10b}$$

$$c^2 \partial_z^2 \mathbf{A}_\perp - \ddot{\mathbf{A}} = 4\pi \rho \dot{\bar{\mathbf{x}}}_\perp. \tag{4.10c}$$

Lagrangians (4.9) and the corresponding equations of motion constitute the first reduced model we have obtained, including assumptions HP 1-4 and HF 1 in Table 4.1. Together, they describe the self-consistent dynamics of arbitrarily polarized transverse electromagnetic plane waves and longitudinal space charge waves propagating through a classical atomic gas. Treating the fields as plane waves corresponds to assuming that the laser beam is loosely focused and the focusing can be neglected altogether. Admittedly, this hypothesis is rarely met in experiments, but it is the key to obtaining a substantial dimensional reduction from the parent model. Later, we shall show how one can reintroduce some of

the focusing effects externally.

*Transverse, linearly-polarized fields (HP 1-4 and HF 1-3)*

Next, we make an assumption which allows us to remove the scalar potential $\varphi$. Specifically, we assume that the $E_z$ is negligible (HF 2). Since $E_z = -\partial_z\varphi$, this is equivalent to assuming $\partial_z\varphi$ is negligible. This is easily justified for atoms, where the symmetry of the ionic potential $V$ and initially purely transverse electric field guarantee that $\overline{z}_\mathrm{e}(z,t) = 0$ for all $z$ and $t$. In turn, this makes $\partial_z\varphi(z,t) = 0$ by virtue of Eq. (4.10b). Thus, the presence of $\partial_z\varphi$ makes no difference for the atomic response to the fields. However, $\overline{z}_\mathrm{e}$ need not be zero for anisotropic media such as aligned molecules, where $V$ is asymmetric. In that case, it may still be reasonable to neglect $\partial_z\varphi$ because it may be very small. In particular, this hypothesis can always be met for a small enough density $\rho$, since under hypothesis HF 1, the only possible source for the longitudinal component of the electric field is the radiation of the particles.

Assuming $\partial_z\varphi$ is negligible, we drop the terms containing it from the Lagrangian. Since these are the only places where $\varphi$ appears, it is eliminated as a dynamical field by hypothesis HF 2. This leaves us with the Lagrangians

$$\mathcal{L}_\mathrm{P} = 4\pi \int \rho \left[ \frac{|\dot{\mathbf{x}}|^2}{2} - V(\mathbf{x}) - \dot{\mathbf{x}}_\perp \cdot \mathbf{A}_\perp \right] \mathrm{d}\mu_0 \mathrm{d}z, \tag{4.11a}$$

$$\mathcal{L}_\mathrm{EM} = \frac{1}{2} \int \left[ |\dot{\mathbf{A}}_\perp|^2 - c^2 |\partial_z \mathbf{A}_\perp|^2 \right] \mathrm{d}z. \tag{4.11b}$$

Above we have the next reduced model in the hierarchy, incorporating hypotheses HP 1-4 and HF 1-2 of Table 4.1. The equations of motion are Eqs. (4.10a) and (4.10c), with the $\partial_z\varphi$ term in Eq. (4.10a) omitted.

In what follows, we will restrict our attention to linearly-polarized waves for simplicity, though our subsequent reductions apply equally well in the case of arbitrary polarization.

We invoke assumption HF 3 and take $A_y = 0$. In this case, the equations of motion are

$$\ddot{\mathbf{x}} = -\nabla_{\mathbf{x}} V(\mathbf{x}) + \dot{A}\hat{\mathbf{x}}, \tag{4.12a}$$

$$c^2 \partial_z^2 A - \ddot{A} = 4\pi\rho\dot{\bar{x}}_{\mathrm{e}}, \tag{4.12b}$$

where we have omitted the $x$-subscript on $A$. Thus, in Eq. (4.12a) we have the equation of motion for an atomic electron driven by the electric field $E = -\dot{A}$ of the electromagnetic wave. Meanwhile, in Eq. (4.12b) we have a 1D wave equation for $A$, with the $x$-component of the current density of the atoms on the right-hand side as a source term.

*Moving frame*

Before proceeding to the next reduced model, we perform a change of coordinates into a moving frame which is better suited to the analysis of propagating laser pulses. Because the laser pulse moves at nearly the speed of light through the gas, it is convenient to change the coordinates of the fields to $\xi = z$ and $\tau = t - z/c$. This leads to an equivalent action $\widetilde{\mathcal{A}}[\widetilde{\mathbf{x}}(\xi,\tau), \widetilde{A}(\xi,\tau)] = \int (\widetilde{\mathcal{L}}_{\mathrm{P}} + \widetilde{\mathcal{L}}_{\mathrm{EM}}) \mathrm{d}\tau$, defined such that $\widetilde{\mathcal{A}}[\widetilde{\mathbf{x}}, \widetilde{A}] = \mathcal{A}[\mathbf{x}, A]$. In particular, the new arguments of $\widetilde{\mathcal{A}}$ are defined such that

$$\widetilde{\mathbf{x}}(\xi, \tau; \widetilde{\mathbf{x}}_0, \widetilde{\mathbf{v}}_0) = \mathbf{x}(\xi, \tau + \xi/c; \mathbf{x}_0, \mathbf{v}_0),$$
$$\widetilde{A}(\xi, \tau) = A(\xi, \tau + \xi/c).$$

Here, we have introduced the positions and velocities of the atomic electrons at $\tau = 0$, when the laser pulse arrives to their location $\xi$ along the propagation direction,

$$\widetilde{\mathbf{x}}_0 = \mathbf{x}(\xi, \xi/c; \mathbf{x}_0, \mathbf{v}_0),$$
$$\widetilde{\mathbf{v}}_0 = \dot{\mathbf{x}}(\xi, \xi/c; \mathbf{x}_0, \mathbf{v}_0),$$

which play the role of initial conditions in the moving frame. We also define the distribution of electron initial conditions when the pulse arrives as $\widetilde{f}_0(\widetilde{\mathbf{x}}_0, \widetilde{\mathbf{v}}_0) = f_0(\mathbf{x}_0, \mathbf{v}_0)$. Applying the chain rule, we obtain the new Lagrangians

$$\mathcal{L}_{\mathrm{P}} = 4\pi \int \rho \left[ \frac{|\partial_\tau \mathbf{x}|^2}{2} - V(\mathbf{x}) - \partial_\tau x_{\mathrm{e}} A \right] \mathrm{d}\mu_0 \mathrm{d}\xi, \tag{4.15a}$$

$$\mathcal{L}_{\mathrm{EM}} = \int \left[ c\partial_\tau A \, \partial_\xi A - \frac{c^2}{2} (\partial_\xi A)^2 \right] \mathrm{d}\xi, \tag{4.15b}$$

where we have omitted the tildes over the new Lagrangians and the new field variables. The equations of motion for $\mathbf{x}$ have the same form in the moving frame because the microscopic coordinates are unaffected by the moving-frame transformation. The equation for $A$ becomes

$$c^2 \partial_\xi^2 A - 2c\partial_\xi \partial_\tau A = 4\pi\rho \partial_\tau \overline{x}_{\mathrm{e}}. \tag{4.16}$$

We observe that, in these coordinates, the equation for $A$ has become first-order in time $\tau$, though it is still second-order in space $\xi$.

*Unidirectional approximation (HP 1-4 and HF 1-4)*

By making a certain hypothesis on the derivatives of $A$, we remove the second-order derivative and obtain the next reduced model in our hierarchy. Looking at Lagrangian (4.15b), we observe that if $|\partial_\xi A| \ll |\partial_\tau A|/c$, then we can neglect the $(\partial_\xi A)^2$ term. Making the order-of-magnitude estimate $\partial_\tau \sim \omega_L/2\pi$ and defining $L_\xi$ as the typical propagation distance over which the field shape changes substantially, this condition becomes equivalent to $\lambda_L \ll L_\xi$, where $\lambda_L = 2\pi c/\omega_L$ is the incident laser wavelength. In other words, if the field evolves over spatial scales which are large compared to the laser wavelength, then the

second term of Lagrangian (4.15b) is negligible. In this case, the Lagrangians become

$$\mathcal{L}_{\mathrm{P}} = 4\pi \int \rho \left[ \frac{|\partial_\tau \mathbf{x}|^2}{2} - V(\mathbf{x}) - \partial_\tau x_{\mathrm{e}} A \right] \mathrm{d}\mu_0 \mathrm{d}\xi, \tag{4.17a}$$

$$\mathcal{L}_{\mathrm{EM}} = c \int \partial_\tau A \, \partial_\xi A \mathrm{d}\xi, \tag{4.17b}$$

where the particle Lagrangian is unchanged. The equations of motion become

$$\partial_\tau^2 \mathbf{x} = -\nabla_{\mathbf{x}} V(\mathbf{x}) + \partial_\tau A \hat{\mathbf{x}}, \tag{4.18a}$$

$$-\partial_\xi \partial_\tau A = \frac{2\pi\rho}{c} \partial_\tau \overline{x}_{\mathrm{e}}. \tag{4.18b}$$

Now, the field evolution equation (4.18b) is only first order in $\xi$. While it is still technically a second order equation for $A$, this equation can be seen as a first order equation for the electric field in the moving frame $\mathcal{E} = -\partial_\tau A$. In fact, $\mathcal{E}$ is the only quantity that appears in the electron equations of motion (4.18a), so we obtain a well-posed set of equations for $\mathbf{x}$ and $\mathcal{E}$. The model given by Eqs. (4.17) and (4.18) incorporates assumptions HP 1-4 and HF 1-4 and describes the propagation of a solely forward-propagating electromagnetic wave through a classical atomic gas. In Sec. 4.2.2, we will show that the assumption $\lambda \ll L_\xi$ is equivalent to assuming that backward-propagating waves are negligible (HF 4), making this a unidirectional approximation [130].

*One-dimensional electron dynamics (HP 1-5 and HF 1-4)*

A model with a reduced electron phase space may be obtained trivially. For example, the final hypothesis HP 5 may be implemented by assuming $\mathbf{x} = x_{\mathrm{e}}(\xi, \tau)\hat{\mathbf{x}}$. Doing so only leads to a modification of the particle Lagrangian $\mathcal{L}_{\mathrm{P}}$. We make an additional step to highlight the Lagrangian formulation with the Hamiltonian formulation to come. Namely, we pass from a Lagrangian description of the particles (in the sense of a Lagrangian description of a fluid) of Eq. (4.12a) to an Eulerian description in terms of $f(x_{\mathrm{e}}, v_x, \tau, \xi)$ [23]. The function

$f$ is the phase space probability distribution to find an electron with position $x_\mathrm{e}$ relative to the ion and velocity $v_x$ at time $\tau$ and position $\xi$ along the gas propagation direction, and it is such that $f(x_\mathrm{e}, v_x, 0, \xi) = f_0(x_\mathrm{e}, v_x)$. Hence, the model equations are obtained:

$$\partial_\tau f = -v_x \partial_{x_\mathrm{e}} f + \left[\partial_{x_\mathrm{e}} V + \mathcal{E}(\xi, \tau)\right] \partial_{v_x} f, \tag{4.19a}$$

$$\partial_\xi \mathcal{E} = \frac{2\pi\rho}{c} \overline{v}_x(\xi, \tau). \tag{4.19b}$$

*Focusing effects*

Lastly, we consider the possibility of reintroducing some of the focusing effects which are manifestly absent from the 1D wave equation. As mentioned earlier, the on-axis electric field of the focused laser pulse has a $z$-dependent (equivalently, $\xi$-dependent) maximum amplitude and phase, even in the vacuum. For example, it may be of the form

$$\mathcal{E}_0(\xi, \tau) = a(\xi) g(\tau) \cos\left(\omega\tau + \phi(\xi)\right). \tag{4.20}$$

Here, $a$ is the $\xi$-dependent amplitude, $\phi$ is the $\xi$-dependent phase, and $g$ is the temporal envelope. Notably, this type of solution is precluded by the 1D model in vacuum [133], because in that case, Eq. (4.18b) gives $-\partial_\xi \partial_\tau A_0 = \partial_\xi \mathcal{E}_0 = 0$, where $A_0$ is the on-axis vector potential of the focused laser pulse in vacuum. Therefore, we are not able to incorporate phase and amplitude modulations due to the 3D focusing of the laser beam self-consistently. However, we can incorporate them in an external fashion.

The idea is to let $A$ represent only the radiation generated by the particles, while the incident laser pulse is treated as a given external field $A_0$. $A_0(\xi, \tau)$ (or $A_0(z, t)$ in the static frame) should be calculated by first solving Maxwell's equations in vacuum for a focused laser pulse, and then evaluating the resulting vector potential on-axis, i.e. at $\mathbf{r}_\perp = 0$. By following this procedure, one would obtain an on-axis electric field like Eq. (4.20) from the relation $\mathcal{E}_0 = -\partial_\tau A_0$. Because Maxwell's equations are linear, the total vector potential is

then given by $A_0 + A$. As such, the only necessary modification to the Lagrangian is to add an $A_0$ term to $\mathcal{L}_{\mathrm{P}}$ so that it reads

$$\mathcal{L}_{\mathrm{P}} = 4\pi \int \rho \left[ \frac{|\dot{\mathbf{x}}|^2}{2} - V(\mathbf{x}) - \dot{x}_e(A + A_0) \right] \mathrm{d}\mu_0 \mathrm{d}z.$$

Consequently, Eq. (4.12a) would be modified by the addition of $\dot{A}_0 \hat{\mathbf{x}}$ on the right-hand side, while Eq. (4.18b) would be unchanged. Additionally, one would need to subject $\dot{A}$ to an initial condition that reflects that the radiation produced by the particles is zero before they are reached by the incident laser pulse.

### 4.2.2 Hamiltonian formulation

The derivation of the sequence of reduced models may also be performed using a Hamiltonian formulation. While this approach is generally more involved, it possesses some advantages over the Lagrangian derivation. Namely, the Hamiltonian formulation directly yields the equations of motion of the system as a dynamical system, i.e. a coupled set of differential equations which are first order in the evolution parameter $t$. In contrast, the Lagrangian formulation may produce equations which are second order in $t$, and it may even produce equations with multiple evolution parameters. For example, all the equations of motion in Sec. 4.2.1 before Eq. (4.16) are second order in $t$. Meanwhile, in Eqs. (4.19), there are two evolution parameters: $\tau$ is the evolution parameter for Eq. (4.19a), while $\xi$ is the evolution parameter for Eq. (4.19b). The Hamiltonian formulation also provides a natural way of identifying conserved quantities of the reduced models, including Casimir invariants.

In the following, we will specify the Hamiltonian structure of the classical parent model [Eqs. (4.1) and (4.4)] and implement the hypotheses in Table 4.1 to obtain the sequence of reduced Hamiltonian models corresponding to those derived in the previous section. The model equations obtained from the Hamiltonian framework will thus be completely

equivalent to those obtained from the Lagrangian framework.

We use the electron probability distribution function $f(\mathbf{x}, \mathbf{p}, \mathbf{r})$ as the particle dynamical variable, where $\mathbf{p} = (p_x, p_y, p_z)$ is the canonical momentum of the electron. It is normalized such that $\int f(\mathbf{x}, \mathbf{p}, \mathbf{r}) \mathrm{d}\mu = 1$, where here $\mathrm{d}\mu = \mathrm{d}^3\mathbf{x}\mathrm{d}^3\mathbf{p}$. The field dynamical variables are $\mathbf{E}(\mathbf{r})$ and $\mathbf{A}(\mathbf{r})$. Observables are thus functionals $\mathcal{F} = \mathcal{F}[f(\mathbf{x}, \mathbf{p}, \mathbf{r}), \mathbf{E}(\mathbf{r}), \mathbf{A}(\mathbf{r})]$. We have omitted the implicit time-dependence of the field variables $f$, $\mathbf{E}$, and $\mathbf{A}$. In analogy with the Vlasov-Maxwell system [108], the parent model Hamiltonian and non-canonical Poisson bracket are

$$\mathcal{H}[f, \mathbf{E}, \mathbf{A}] = \mathcal{H}_{\mathrm{P}} + \mathcal{H}_{\mathrm{EM}}, \tag{4.21a}$$

$$\mathcal{H}_{\mathrm{P}}[f, \mathbf{A}] = \int \rho(\mathbf{r}) \, f(\mathbf{x}, \mathbf{p}, \mathbf{r}) \left[ \frac{1}{2} \left| \mathbf{p} + \mathbf{A}(\mathbf{r}) \right|^2 + V(\mathbf{x}) \right] \mathrm{d}\mu \mathrm{d}^3\mathbf{r}, \tag{4.21b}$$

$$\mathcal{H}_{\mathrm{EM}}[\mathbf{E}, \mathbf{A}] = \frac{1}{8\pi} \int \left( |\mathbf{E}(\mathbf{r})|^2 + c^2 |\nabla \times \mathbf{A}(\mathbf{r})|^2 \right) \mathrm{d}^3\mathbf{r}, \tag{4.21c}$$

$$\{\mathcal{F}, \mathcal{G}\} = \int \left\{ \rho^{-1} \int f \left[ \mathcal{F}_f, \mathcal{G}_f \right] \mathrm{d}\mu + 4\pi \left( \mathcal{F}_{\mathbf{E}} \cdot \mathcal{G}_{\mathbf{A}} - \mathcal{F}_{\mathbf{A}} \cdot \mathcal{G}_{\mathbf{E}} \right) \right\} \mathrm{d}^3\mathbf{r}. \tag{4.21d}$$

We have introduced the canonical Poisson bracket notation $[f, g] = \partial_{\mathbf{x}} f \cdot \partial_{\mathbf{p}} g - \partial_{\mathbf{p}} f \cdot \partial_{\mathbf{x}} g$. Like the Lagrangian, Hamiltonian (4.21a) is split into a particle Hamiltonian $\mathcal{H}_{\mathrm{P}}$ and an electromagnetic Hamiltonian $\mathcal{H}_{\mathrm{EM}}$, a splitting which will likewise carry over to each of the reduced models in the hierarchy. Physically, $\mathcal{H}_{\mathrm{P}}$ is the energy of the atomic electrons—kinetic plus potential—while $\mathcal{H}_{\mathrm{EM}}$ is the energy of the electromagnetic field. Again, we have explicitly specified the $\mathbf{r}$ dependence of the vector potential and electric field here to distinguish this Hamiltonian from the dipole-approximation-free case, though this will be omitted for the rest of this section.

The equations of motion for an observable are obtained using the observable evolution

law $\dot{\mathcal{F}} = \{\mathcal{F}, \mathcal{H}\}$. For the dynamical variables, they are as follows:

$$\dot{f} = -(\mathbf{p} + \mathbf{A}) \cdot \nabla_{\mathbf{x}} f + \nabla_{\mathbf{x}} V \cdot \partial_{\mathbf{p}} f, \tag{4.22a}$$

$$\dot{\mathbf{E}} = c^2 \nabla \times (\nabla \times \mathbf{A}) + 4\pi\rho(\overline{\mathbf{p}} + \mathbf{A}), \tag{4.22b}$$

$$\dot{\mathbf{A}} = -\mathbf{E}. \tag{4.22c}$$

In Eq. (4.22b), we have used the normalization of the distribution function and introduced the ensemble average $\overline{\mathbf{p}}(\mathbf{r}) = \int \mathbf{p} f(\mathbf{x}, \mathbf{p}, \mathbf{r}) \mathrm{d}\mu$. This system is completely equivalent to Eqs. (4.1) and (4.4). Here, $f$ provides an Eulerian description of the particles corresponding to the Lagrangian description used in Eqs. (4.4). The substitutions $\overline{\mathbf{v}} = \overline{\mathbf{p}} + \mathbf{A}$ and $\mathbf{B} = \nabla \times \mathbf{A}$ make the equivalence of Eq. (4.22b) and Eq. (4.1a) apparent, while taking the curl of Eq. (4.22c) makes the equivalence to (4.1b) apparent. As before, Eq. (4.1d) is guaranteed by the definition of $\mathbf{A}$.

To obtain Gauss' Law, Eq. (4.1c), one needs to consider the conserved quantities of this system. Because the parent model equations (4.22) have a Hamiltonian structure given by (4.21), conserved quantities may be found by searching for observables $\mathcal{F}$ which Poisson commute with the Hamiltonian, i.e. $\{\mathcal{F}, \mathcal{H}\} = 0$. Thus, $\mathcal{H}$, the total energy of the system, is conserved. Gauss' Law is found by realizing that $\mathcal{C}(\mathbf{r}') = \nabla \cdot [\mathbf{E}(\mathbf{r}') - 4\pi\rho\overline{\mathbf{x}}(\mathbf{r}')]$ is also a conserved quantity. Therefore, Eq. (4.1c) is satisfied for all times if it is satisfied initially. There is also a family of global Casimir invariants of Poisson bracket (4.21d). This family is of the form $\mathcal{R}[f] = \int R(f) \mathrm{d}\mu \mathrm{d}^3\mathbf{r}$ [134], for arbitrary scalar functions $R$, and it is associated with the relabeling symmetry [135].

*From canonical momentum to velocity*

As a first step in the derivation, we make the standard transformation from canonical momentum $\mathbf{p}$ to velocity $\mathbf{v} = (v_x, v_y, v_z)$, by introducing the change of coordinates on the

distribution function (see Ref. [108] for more details)

$$\widetilde{f}(\mathbf{x},\mathbf{v},\mathbf{r}) = f(\mathbf{x},\mathbf{v}-\mathbf{A}(\mathbf{r}),\mathbf{r}). \tag{4.23}$$

The new observables are defined in terms of the old observables as $\widetilde{\mathcal{F}}[\widetilde{f},\mathbf{E},\mathbf{A}] = \mathcal{F}[f,\mathbf{E},\mathbf{A}]$. By using the chain rule, we obtain relations between the functional derivatives of the old observables and those of the new observables. They are

$$\mathcal{F}_f = \widetilde{\mathcal{F}}_{\widetilde{f}}, \quad \mathcal{F}_{\mathbf{E}} = \widetilde{\mathcal{F}}_{\mathbf{E}}, \quad \mathcal{F}_{\mathbf{A}} = \widetilde{\mathcal{F}}_{\mathbf{A}} + \int \widetilde{f}\partial_{\mathbf{v}}\widetilde{\mathcal{F}}_{\widetilde{f}}\mathrm{d}\mu.$$

As for the partial derivatives $\partial_{\mathbf{x}}$ and $\partial_{\mathbf{p}}$ which arise in the canonical Poisson bracket $[\cdot,\cdot]$, they transform according to the chain rule as

$$\partial_{\mathbf{x}}\mathcal{F}_f = \partial_{\mathbf{x}}\widetilde{\mathcal{F}}_{\widetilde{f}}, \;\; \partial_{\mathbf{p}}\mathcal{F}_f = \partial_{\mathbf{v}}\widetilde{\mathcal{F}}_{\widetilde{f}}. \tag{4.24}$$

This leads to the particle Hamiltonian and bracket

$$\mathcal{H}_{\mathrm{P}}[f] = \int \rho\, f\left[\frac{|\mathbf{v}|^2}{2} + V(\mathbf{x})\right]\mathrm{d}\mu\mathrm{d}^3\mathbf{r}, \tag{4.25a}$$

$$\begin{aligned}\{\mathcal{F},\mathcal{G}\} = \int \Bigg\{ &\rho^{-1}\int f\left[\mathcal{F}_f,\mathcal{G}_f\right]\mathrm{d}\mu + 4\pi\left(\mathcal{F}_{\mathbf{E}}\cdot\mathcal{G}_{\mathbf{A}} - \mathcal{F}_{\mathbf{A}}\cdot\mathcal{G}_{\mathbf{E}}\right) \\ &+ 4\pi\int f\left(\mathcal{F}_{\mathbf{E}}\cdot\partial_{\mathbf{v}}\mathcal{G}_f - \partial_{\mathbf{v}}\mathcal{F}_f\cdot\mathcal{G}_{\mathbf{E}}\right)\mathrm{d}\mu\Bigg\}\mathrm{d}^3\mathbf{r},\end{aligned} \tag{4.25b}$$

where the tildes have been neglected for notational simplicity and the canonical bracket $[\cdot,\cdot]$ is taken with respect to $(\mathbf{x},\mathbf{v})$. Meanwhile, $\mathcal{H}_{\mathrm{EM}}$ remains as Eq. (4.21c). Note that, now, $\mathrm{d}\mu = \mathrm{d}^3\mathbf{x}\mathrm{d}^3\mathbf{v}$. We also note that for bracket (4.25b), the family of Casimirs $\mathcal{R}$ becomes slightly restricted to only allow scalar functions $R$ that satisfy $R(0) = 0$. This family of Casimirs persists in this form for all of the reduced models which follow. So far, no approximations have been made.

We observe that the only change going from bracket (4.21d) to (4.25b) is the addition

of the electric field-electron velocity coupling term. However, when performing the analog of the change of coordinates Eq. (4.23) for the Vlasov-Maxwell system, an additional term coupling the magnetic field to the electron velocity is generated due to the fact that $\mathbf{A}$ depends explicitly on $\mathbf{x}$ [108]. It is absent here because magnetic effects are neglected in the dipole approximation, i.e. in Eq. (4.23), $\mathbf{A}$ does not depend on $\mathbf{x}$. This is just as well, for in the Vlasov-Maxwell system, when one additionally changes variables from $\mathbf{A}$ to the magnetic field $\mathbf{B}$, this leads to a bracket which only satisfies the Jacobi identity under the condition $\nabla \cdot \mathbf{B} = 0$ [95]. On the other hand, the bracket of Eq. (4.25b) and its analog in the Vlasov-Maxwell case satisfy the Jacobi identity everywhere in phase space. While this obstruction to the Jacobi identity when the variable $\mathbf{B}$ is used can be removed using projectors [136], we would not need to resort to this here even if we switched from $\mathbf{A}$ to $\mathbf{B}$ as the dynamical variable, because that bracket would still satisfy the Jacobi identity. A proof of this fact is given in App. C, where the Jacobi identity for bracket (4.25b) is also proved as a by-product.

*Plane-wave fields (HP 1-4, HF 1)*

Next, we implement hypotheses HF 1 and HP 4, that is, we restrict the fields' macroscopic spatial dependence to be on $z$ only. We assume

$$\begin{aligned}
\rho &= \rho(z), \\
f &= f(\mathbf{x}, \mathbf{v}, z), \\
\mathbf{E} &= \mathbf{E}(z), \\
\mathbf{A} &= \mathbf{A}_\perp(z).
\end{aligned}$$

Here, we have also assumed that $A_z = 0$ merely for convenience, since it will no longer appear in the Hamiltonian due to HF 1. Thus, we may consider restricting our model to the subset of observables $\mathcal{F}[f, \mathbf{E}, \mathbf{A}_\perp]$ which do not depend on $A_z$. This subset of observables

forms a Poisson subalgebra of the algebra of observables under the bracket (4.25b). That is, for two observables $\mathcal{F}$ and $\mathcal{G}$ which do not depend on $A_z$, $\{\mathcal{F},\mathcal{G}\}$ is also an observable which does not depend on $A_z$. As such, we are able to restrict our analysis to this subalgebra, meaning we are free to neglect the functional derivatives with respect to $A_z$ in bracket (4.25b). The electromagnetic Hamiltonian and bracket become

$$\mathcal{H}_{\mathrm{EM}}[\mathbf{E},\mathbf{A}_\perp] = \frac{1}{8\pi}\int \left(|\mathbf{E}|^2 + c^2|\partial_z \mathbf{A}_\perp|^2\right)\mathrm{d}z, \tag{4.27a}$$

$$\begin{aligned}\{\mathcal{F},\mathcal{G}\} = \int \Bigg\{ &\rho^{-1}\int f\left[\mathcal{F}_f,\mathcal{G}_f\right]\mathrm{d}\mu + 4\pi\left(\mathcal{F}_{\mathbf{E}}\cdot\mathcal{G}_{\mathbf{A}_\perp} - \mathcal{F}_{\mathbf{A}_\perp}\cdot\mathcal{G}_{\mathbf{E}}\right)\\ &+ 4\pi\int f\left(\mathcal{F}_{\mathbf{E}}\cdot\partial_{\mathbf{v}}\mathcal{G}_f - \partial_{\mathbf{v}}\mathcal{F}_f\cdot\mathcal{G}_{\mathbf{E}}\right)\mathrm{d}\mu\Bigg\}\mathrm{d}z,\end{aligned} \tag{4.27b}$$

while the particle Hamiltonian is that of Eq. (4.25a) with $\mathrm{d}^3\mathbf{r}$ replaced with $\mathrm{d}z$. The equations of motion at this stage become

$$\dot{f} = -\mathbf{v}\cdot\nabla_{\mathbf{x}} f + \left(\nabla_{\mathbf{x}} V + \mathbf{E}\right)\cdot\partial_{\mathbf{v}} f, \tag{4.28a}$$

$$\dot{\mathbf{E}} = -c^2\partial_z^2\mathbf{A}_\perp + 4\pi\rho\overline{\mathbf{v}}, \tag{4.28b}$$

$$\dot{\mathbf{A}}_\perp = -\mathbf{E}_\perp, \tag{4.28c}$$

while the conserved quantity associated with $\mathcal{C}$ becomes $\mathcal{C}(z') = \partial_z[E_z(z') - 4\pi\rho\overline{z}_{\mathrm{e}}(z')]$. For this system, it turns out that $\mathcal{C}$ is conserved because its primitive, $\widetilde{\mathcal{C}}(z') = E_z(z') - 4\pi\rho\overline{z}_{\mathrm{e}}(z')$ is a Casimir invariant of bracket (4.27b). Thus, the longitudinal electric field is simply obtained from the longitudinal component of the microscopic dipole moment. An additional global pair of conserved quantities is created by HP 4 and HF 1, given by $\mathcal{Q}_\perp = \int(\mathbf{E}_\perp - 4\pi\rho\overline{\mathbf{x}}_\perp)\mathrm{d}z$.

*Transverse, linearly-polarized fields (HP 1-4 and HF 1-3)*

To implement HP 2, i.e. the assumption that $E_z$ is negligible, we drop the $E_z^2$ term from the Hamiltonian. Thus, $\mathcal{H}$ no longer depends on $E_z$, and we may consider restricting our

model to the subset of observables $\mathcal{F}[f, \mathbf{E}_\perp, \mathbf{A}_\perp]$ which do not depend on $E_z$. This subset of observables forms a Poisson subalgebra of the algebra of observables under bracket (4.27b). That is, for two observables $\mathcal{F}$ and $\mathcal{G}$ which do not depend on $E_z$, $\{\mathcal{F}, \mathcal{G}\}$ is also an observable which does not depend on $E_z$. As such, we are able to restrict our analysis to this subalgebra, meaning we are free to neglect the functional derivatives with respect to $E_z$ in bracket (4.27b). In effect, the new bracket is (4.27b) with $\mathbf{E}$ replaced by $\mathbf{E}_\perp$. Henceforth, we will also invoke hypothesis HF 3, so we shall drop the $E_y$ and $A_y$ terms from the Hamiltonian. They may also be removed from the bracket with a subalgebra argument. The electromagnetic Hamiltonian and bracket for the system under hypotheses HP 1-4 and HF 1-3 become

$$\mathcal{H}_{\mathrm{EM}}[E, A] = \frac{1}{8\pi} \int \left[E^2 + c^2(\partial_z A)^2\right] \mathrm{d}z, \tag{4.29a}$$

$$\begin{aligned}\{\mathcal{F}, \mathcal{G}\} = \int \Bigg\{ &\rho^{-1} \int f \left[\mathcal{F}_f, \mathcal{G}_f\right] \mathrm{d}\mu + 4\pi \left(\mathcal{F}_E \mathcal{G}_A - \mathcal{F}_A \mathcal{G}_E\right) \\ &+ 4\pi \int f \left(\mathcal{F}_E \partial_{v_x} \mathcal{G}_f - \partial_{v_x} \mathcal{F}_f \mathcal{G}_E\right) \mathrm{d}\mu \Bigg\} \mathrm{d}z,\end{aligned} \tag{4.29b}$$

where we have dropped the $x$ subscripts on the electromagnetic fields and $\mathcal{H}_{\mathrm{P}}$ remains unchanged. Now, the equations of motion are

$$\dot{f} = -\mathbf{v} \cdot \nabla_{\mathbf{x}} f + (\nabla_{\mathbf{x}} V + E\hat{\mathbf{x}}) \cdot \partial_{\mathbf{v}} f, \tag{4.30a}$$

$$\dot{E} = -c^2 \partial_z^2 A + 4\pi\rho\overline{v}_x, \tag{4.30b}$$

$$\dot{A} = -E. \tag{4.30c}$$

*Forward- and backward- propagating waves*

Before implementing hypothesis HF 4, we perform a reduction on the field variables which elucidates the natural separation of the electromagnetic field into a forward- and backward-

propagating wave. The reduction is given by

$$\alpha = \frac{1}{2}\left(E + c\partial_z A\right), \tag{4.31a}$$

$$\beta = \frac{1}{2}\left(E - c\partial_z A\right), \tag{4.31b}$$

where $\alpha$ is the forward-propagating wave and $\beta$ is the backward-propagating wave. The electric field is simply expressed in these reduced variables as $E = \alpha + \beta$. The functional derivatives appearing in bracket (4.29b) are obtained in terms of the new variables using the chain rule:

$$\mathcal{F}_E = \frac{1}{2}\left(\widetilde{\mathcal{F}}_\alpha + \widetilde{\mathcal{F}}_\beta\right),$$
$$\mathcal{F}_A = -\frac{c}{2}\left(\partial_z\widetilde{\mathcal{F}}_\alpha - \partial_z\widetilde{\mathcal{F}}_\beta\right).$$

The electromagnetic Hamiltonian and bracket become

$$\mathcal{H}_{\mathrm{EM}}[\alpha,\beta] = \frac{1}{4\pi}\int\left[\alpha^2 + \beta^2\right]\mathrm{d}z, \tag{4.33a}$$

$$\{\mathcal{F},\mathcal{G}\} = \int\Bigg\{\rho^{-1}\int f\left[\mathcal{F}_f,\mathcal{G}_f\right]\mathrm{d}\mu - 2\pi c\left(\mathcal{F}_\alpha\partial_z\mathcal{G}_\alpha - \mathcal{F}_\beta\partial_z\mathcal{G}_\beta\right)$$
$$+ 2\pi\int f\left(\mathcal{F}_\alpha\partial_{v_x}\mathcal{G}_f - \partial_{v_x}\mathcal{F}_f\mathcal{G}_\alpha + \mathcal{F}_\beta\partial_{v_x}\mathcal{G}_f - \partial_{v_x}\mathcal{F}_f\mathcal{G}_\beta\right)\mathrm{d}\mu\Bigg\}\mathrm{d}z, \tag{4.33b}$$

while $\mathcal{H}_{\mathrm{P}}$ is unaffected. In these coordinates, the equations of motion are

$$\dot{f} = -\mathbf{v}\cdot\nabla_{\mathbf{x}}f + \left[\nabla_{\mathbf{x}}V + (\alpha+\beta)\hat{\mathbf{x}}\right]\cdot\partial_{\mathbf{v}}f, \tag{4.34a}$$

$$\dot{\alpha} = -c\partial_z\alpha + 2\pi\rho\overline{v}_x, \tag{4.34b}$$

$$\dot{\beta} = c\partial_z\beta + 2\pi\rho\overline{v}_x. \tag{4.34c}$$

From these equations, it is clear that $\alpha$ is the forward-propagating part of the electromagnetic field and $\beta$ is the backward-propagating part. Indeed, in vacuum ($\rho = 0$), the solution

of Eq. (4.34b) would be $\alpha(z,t) = \alpha_0(z - ct)$, where $\alpha(z,0) = \alpha_0(z)$, and the solution of equation Eq. (4.34c) would be $\beta(z,t) = \beta_0(z + ct)$, where $\beta(z,0) = \beta_0(z)$.

Equations (4.31) do not constitute a change of variables because it is not possible to determine $A$ uniquely from $\alpha$ and $\beta$; it is only determined up to a constant. This constant has no physical significance because Hamiltonian (4.29a) only depends on $\partial_z A$. In fact, it is a manifestation of the gauge freedom inherent to the potential description of the magnetic field. Due to the reduction to $\alpha$ and $\beta$, which eliminates the remaining gauge freedom, two global Casimir invariants of bracket (4.33b) are created. They are related to $\mathcal{Q}_\perp$, a conserved quantity of the previous system, and are given by

$$\mathcal{Q}_\alpha = \int (\alpha - 2\pi\rho\overline{x}_\mathrm{e})\mathrm{d}z, \tag{4.35a}$$

$$\mathcal{Q}_\beta = \int (\beta - 2\pi\rho\overline{x}_\mathrm{e})\mathrm{d}z. \tag{4.35b}$$

By direct calculation, it is possible to verify that bracket (4.33b) satisfies the Jacobi identity, so it is a genuine Poisson bracket and this reduction has preserved the Hamiltonian structure of the previous model.

*Unidirectional approximation (HP 1-4 and HF 1-4)*

Having clearly separated the forward- and backward- propagating parts of the electromagnetic field, it becomes straightforward to make the unidirectional approximation and remove the backward-propagating part (HF 4). If $\beta$ is assumed to be small, then the $\beta^2$ term may be neglected from Hamiltonian (4.33a). Then, the Hamiltonian no longer depends on $\beta$, and it happens that observables $\mathcal{F}[f,\alpha]$ which do not depend on $\beta$ form a Poisson subalgebra under bracket (4.33b). This leaves the electromagnetic Hamiltonian and bracket for

the system incorporating hypotheses HP 1-4 and HF 1-4:

$$\mathcal{H}_{\mathrm{EM}}[\alpha] = \int \frac{\alpha^2}{4\pi} \mathrm{d}z, \tag{4.36a}$$

$$\{\mathcal{F}, \mathcal{G}\} = \int \Bigg\{ \rho^{-1} \int f \left[\mathcal{F}_f, \mathcal{G}_f\right] \mathrm{d}\mu - 2\pi c \mathcal{F}_\alpha \partial_z \mathcal{G}_\alpha + 2\pi \int f \left(\mathcal{F}_\alpha \partial_{v_x} \mathcal{G}_f - \partial_{v_x} \mathcal{F}_f \mathcal{G}_\alpha\right) \mathrm{d}\mu \Bigg\} \mathrm{d}z. \tag{4.36b}$$

The equations of motion are Eqs. (4.34a) and (4.34b), with $\beta = 0$.

Now, we are able to justify that neglecting backward-propagating waves is equivalent to assuming $\lambda \ll L_\xi$, which is used in Sec. 4.2.1 to implement HF 4. In the unidirectional approximation, the electric field becomes $E = \alpha$. Thus, Eq. (4.34b) is the evolution equation for the electric field of the laser. Comparing this equation to the corresponding one from the Lagrangian derivation, Eq. (4.18b), we find that they are completely equivalent. The equivalence may be seen either by moving Eq. (4.18b) back to the rest frame, or by moving Eq. (4.34b) to the moving frame [$\mathcal{E}(\xi, \tau) = \alpha(\xi, \tau + \xi/c)$] and recalling that $E = -\dot{A}$. Each of these equations is obtained under seemingly unrelated hypotheses: that $\beta$ is negligible for Eq. (4.34b), versus that $\lambda \ll L_\xi$ for Eq. (4.18b). Because the field evolution equations resulting from each hypothesis are equivalent, we conclude that the hypotheses are in fact equivalent. Therefore, the unidirectional approximation is the same as assuming the laser field evolves over large length scales compared to the incident laser wavelength.

*One-dimensional electron dynamics (HP 1-5 and HF 1-4)*

As in the Lagrangian case, a reduced electron phase space model (HP 5) is straightforward to implement. One simply considers a distribution function on a lower-dimensional phase space. For example, for one-dimensional electron motion, one assumes $f = f(x_\mathrm{e}, v_x, z)$, with the obvious modifications to Eqs. (4.36).

*Focusing effects*

For incorporating focusing effects, the procedure is also similar to the Lagrangian case. The dynamical field $\alpha$ is considered to be the radiation generated solely by the particles. Meanwhile, the incident laser radiation is taken to be a given external, time-dependent field $E_0(z,t)$. Then, one only needs to modify the particle Hamiltonian (4.25a) such that it reads

$$\mathcal{H}_{\mathrm{P}}[f,t] = \int \rho\, f \left[\frac{|\mathbf{v}|^2}{2} + V(\mathbf{x}) + x_{\mathrm{e}} E_0(z,t)\right] \mathrm{d}\mu \mathrm{d}z, \tag{4.37}$$

while $\mathcal{H}_{\mathrm{EM}}$ remains Eq. (4.36a) and the Poisson bracket remains Eq. (4.36b). Note that Hamiltonian (4.37) is time-dependent, so we must expand our set of observables to allow observables of the type $\mathcal{F}[f,\alpha,t]$. Further, we must redefine the evolution law as $\dot{\mathcal{F}} = \{\mathcal{F},\mathcal{H}\} + \partial_t \mathcal{F}$. Consequently, total Hamiltonian $\mathcal{H} = \mathcal{H}_{\mathrm{P}} + \mathcal{H}_{\mathrm{EM}}$ is no longer a conserved quantity. However, $\mathcal{Q}_\alpha$ remains a conserved quantity (because $\partial_t \mathcal{Q}_\alpha = 0$), and it may be restored to the status of Casimir invariant by autonomizing the system and extending the Poisson bracket appropriately. We remark that focusing effects may also be incorporated in this way to each of the previous reduced models in the hierarchy by adding the focusing field to the model's particle Hamiltonian (and using the corresponding bracket). Therefore, $\mathcal{Q}_\beta$ and $\widetilde{\mathcal{C}}(z')$ are also conserved in the presence of a time-dependent external field.

## 4.3 Quantum reduced models

Each of the reduced models derived in the previous section has a quantum analog. These models may be found by sequentially applying the assumptions of Table 4.1 to the parent quantum model, Eqs. (4.1) and (4.3), and this may be also accomplished using a variational formulation. Due to the similarity between the variational formulations of the classical and quantum models and our focus on reducing the degrees of freedom associated with the electromagnetic field, the derivation of the quantum models is nearly identical to that of the classical models. Hence, we give few details on the calculations and focus on the results.

### 4.3.1 Lagrangian formulation

The action for the parent quantum model is given by

$$\mathcal{A}[\psi(\mathbf{x},t;\mathbf{r}),\psi^*(\mathbf{x},t;\mathbf{r}),\varphi(\mathbf{r},t),\mathbf{A}(\mathbf{r},t)] = \int (\mathcal{L}_{\mathrm{P}} + \mathcal{L}_{\mathrm{EM}})\mathrm{d}t.$$

The electron displacement field $\mathbf{x}(\mathbf{r},t;\mathbf{x}_0,\mathbf{v}_0)$ is replaced by the wave function $\psi$ and its complex conjugate, $\psi^*$. Here, and in each of the models of the hierarchy, $\mathcal{L}_{\mathrm{EM}}$ will be the same as in the corresponding classical model. Meanwhile, for the parent quantum model, $\mathcal{L}_{\mathrm{P}}$ is given by

$$\mathcal{L}_{\mathrm{P}} = 4\pi \int \rho \left\{ i\psi^*\dot{\psi} - \psi^* \left[ -\frac{1}{2}\nabla_{\mathbf{x}}^2 + V(\mathbf{x}) - \mathbf{x}\cdot(\nabla\varphi + \dot{\mathbf{A}}) \right] \psi \right\} \mathrm{d}^3\mathbf{x}\mathrm{d}^3\mathbf{r}. \tag{4.38}$$

Recognizing the appearance of the Hamiltonian operator $\hat{H} = -\nabla_{\mathbf{x}}^2/2 + V(\mathbf{x}) + \mathbf{E}\cdot\mathbf{x}$ in Eq. (4.38), it is clear that $\mathcal{L}_{\mathrm{P}}$ has a phase-space Lagrangian form [125]. Imposing $\mathcal{A}_{\psi^*} = 0$ yields Schrödinger equation (4.3a) (with its complex conjugate for $\mathcal{A}_{\psi} = 0$), while setting the variations with respect to the potentials to zero yields

$$-(\nabla^2\varphi + \nabla\cdot\dot{\mathbf{A}}) = 4\pi\nabla\cdot\left(\rho\int \mathbf{x}\psi^*\psi\,\mathrm{d}^3\mathbf{x}\right), \tag{4.39a}$$

$$-(\nabla\dot{\varphi} + \ddot{\mathbf{A}}) = c^2\nabla\times(\nabla\times\mathbf{A}) + 4\pi\rho\,\partial_t\left(\int \mathbf{x}\psi^*\psi\,\mathrm{d}^3\mathbf{x}\right). \tag{4.39b}$$

The integrals on the right-hand sides of Eqs. (4.39) are clearly recognized as $\overline{\mathbf{x}}$, as defined in Eq. (4.3b). With this and the definition of the potentials in mind, we confirm the correspondence with Eqs. (4.1).

The first model in the hierarchy is obtained by applying hypotheses HP 4 and HF 1. These hypotheses are summed up by Eqs. (4.8), with Eq. (4.8b) replaced by

$$\psi = \psi(\mathbf{x},t;z).$$

The particle Lagrangian becomes

$$\mathcal{L}_{\mathrm{P}} = 4\pi \int \rho \left\{ i\psi^* \dot{\psi} - \psi^* \left[ -\frac{1}{2}\nabla_{\mathbf{x}}^2 + V(\mathbf{x}) - \mathbf{x} \cdot (\partial_z \varphi \hat{\mathbf{z}} + \dot{\mathbf{A}}_\perp) \right] \psi \right\} \mathrm{d}^3\mathbf{x}\mathrm{d}z,$$

and the Schrödinger equation becomes

$$i\dot{\psi} = -\frac{1}{2}\nabla_{\mathbf{x}}^2 \psi + \left[ V(\mathbf{x}) - \partial_z \varphi(z,t) z_{\mathrm{e}} - \dot{\mathbf{A}}_\perp(z,t) \cdot \mathbf{x}_\perp \right] \psi.$$

Meanwhile, the field equations remain Eqs. (4.10b) and (4.10c), with the ensemble averages of the electron positions computed using the corresponding quantum expectation values. In general, the field equations at each level of the hierarchy will be the same in the quantum case as in the classical case.

Next, we implement hypothesis HF 2. The particle Lagrangian is

$$\mathcal{L}_{\mathrm{P}} = 4\pi \int \rho \left\{ i\psi^* \dot{\psi} - \psi^* \left[ -\frac{1}{2}\nabla_{\mathbf{x}}^2 + V(\mathbf{x}) - \mathbf{x}_\perp \cdot \dot{\mathbf{A}}_\perp \right] \psi \right\} \mathrm{d}^3\mathbf{x}\mathrm{d}z.$$

When also making assumption HF 3 ($A_y = 0$), the Schrödinger equation becomes

$$i\dot{\psi} = -\frac{1}{2}\nabla_{\mathbf{x}}^2 \psi + \left[ V(\mathbf{x}) - \dot{A}(z,t) x_{\mathrm{e}} \right] \psi. \tag{4.40}$$

The corresponding field equation is Eq. (4.12b). Eqs. (4.40) and (4.12b) are equivalent to the model used in Ref. [137]. Now, we go into the moving frame $\xi = z, \tau = t - z/c$. The wave function in the moving frame $\widetilde{\psi}$ is defined

$$\widetilde{\psi}(\mathbf{x}, \tau; \xi) = \psi(\mathbf{x}, \tau + \xi/c; \xi).$$

As in the classical case, the functional form of $\mathcal{L}_{\mathrm{P}}$ is unchanged by this transformation. The moving-frame formulation of this model is employed in Ref. [132]. Finally, hypothesis HF 4 is implemented only on $\mathcal{L}_{\mathrm{EM}}$, just as in the classical model. The resulting model

corresponds to what is referred to as the reduced model of Ref. [132]. Adding on hypothesis HP 5 (taking $\psi = \psi(x_{\rm e}, \tau; \xi)$) leads to the particle Lagrangian

$$\mathcal{L}_{\rm P} = 4\pi \int \rho \left\{ i\psi^* \partial_\tau \psi - \psi^* \left[ -\frac{1}{2}\partial_{x_{\rm e}}^2 + V(x_{\rm e}) - x_{\rm e}\partial_\tau A \right] \psi \right\} {\rm d}x_{\rm e}{\rm d}\xi, \tag{4.41}$$

with the corresponding field Lagrangian (4.17b). This leads to the quantum model equations that we used in Ref. [91],

$$i\partial_\tau \psi = -\frac{1}{2}\partial_{x_{\rm e}}^2 \psi + \big[V(x_{\rm e}) + \mathcal{E}(\xi, \tau) x_{\rm e}\big]\psi, \tag{4.42a}$$

$$\partial_\xi \mathcal{E} = \frac{2\pi\rho}{c} \overline{v}_x(\xi, \tau), \tag{4.42b}$$

where we have again made the substitution $\mathcal{E} = -\partial_\tau A$. Also, in Eq. (4.42b), we have used Ehrenfest's theorem, $\overline{v}_x = -i \int \psi^* \partial_{x_{\rm e}} \psi \, {\rm d}x_{\rm e} = \partial_\tau \overline{x}_{\rm e}$. If desired, focusing effects may be added by adding the appropriate term to Eq. (4.41), similarly to the classical case.

### 4.3.2 Hamiltonian formulation

Now we provide the derivation of the quantum reduced model in the Hamiltonian formulation. In this case, observables are functionals

$$\mathcal{F} = \mathcal{F}[\psi(\mathbf{x}; \mathbf{r}), \psi^*(\mathbf{x}; \mathbf{r}), \mathbf{E}(\mathbf{r}), \mathbf{A}(\mathbf{r})],$$

where we omit the implicit time-dependence of the variables. The Hamiltonian and bracket of the quantum parent model are

$$\mathcal{H}[\psi, \psi^*, \mathbf{E}, \mathbf{A}] = \mathcal{H}_{\mathrm{P}} + \mathcal{H}_{\mathrm{EM}} \tag{4.43a}$$

$$\mathcal{H}_{\mathrm{P}}[\psi, \psi^*, \mathbf{A}] = \int \rho\psi^* \left[\frac{1}{2}\left(-i\nabla_{\mathbf{x}} + \mathbf{A}\right)^2 + V(\mathbf{x})\right] \psi \, \mathrm{d}^3\mathbf{x}\mathrm{d}^3\mathbf{r}, \tag{4.43b}$$

$$\{\mathcal{F}, \mathcal{G}\} = \int \left\{ -i\rho^{-1} \int \left(\mathcal{F}_\psi \mathcal{G}_{\psi^*} - \mathcal{F}_{\psi^*}\mathcal{G}_\psi\right) \mathrm{d}^3\mathbf{x} + 4\pi \left(\mathcal{F}_{\mathbf{E}} \cdot \mathcal{G}_{\mathbf{A}} - \mathcal{F}_{\mathbf{A}} \cdot \mathcal{G}_{\mathbf{E}}\right) \right\} \mathrm{d}^3\mathbf{r}. \tag{4.43c}$$

The full Hamiltonian $\mathcal{H}$ has the same splitting into particle and electromagnetic parts, with the electromagnetic part given by Eq. (4.21c), as in the classical case. In fact, at every level of the hierarchy, the electromagnetic Hamiltonian of the quantum model will by identical to that of the classical model. The particle Hamiltonian Eq. (4.43b) is recognized to be the expectation value of the Hamiltonian operator $\hat{H} = (-i\nabla_{\mathbf{x}} + \mathbf{A})^2/2 + V(\mathbf{x})$, integrated over the macroscopic gas. Thus, the physical meaning of $\mathcal{H}_{\mathrm{P}}$—the sum of the energies of all the atoms—is also the same in both the quantum and classical cases.

The equations of motion are obtained from $\dot{\mathcal{F}} = \{\mathcal{F}, \mathcal{H}\}$ which, for the wave function, gives

$$\dot{\psi} = -i\left[\frac{1}{2}(-i\nabla_{\mathbf{x}} + \mathbf{A})^2\psi + V(\mathbf{x})\psi\right], \tag{4.44}$$

while those of the fields are given by Eqs. (4.22b) and (4.22c), as in the classical case. Here, the ensemble-averaged canonical momentum is given by $\overline{\mathbf{p}} = -i\int \psi^* \nabla_{\mathbf{x}} \psi \mathrm{d}^3\mathbf{x}$. This system also possesses the same conserved quantity $\mathcal{C}(\mathbf{r}')$ as in the classical case, with the ensemble average $\overline{\mathbf{x}}$ computed in the appropriate way. In fact, each of the conserved quantities of the classical hierarchy of reduced models have an analog in the quantum hierarchy of reduced models. For instance, here also the quantum Hamiltonian Eq. (4.43a) is conserved. Additionally, instead of the Casimirs $\mathcal{R}$, the quantum system conserves the norms of the wave functions, $\mathcal{N}(\mathbf{r}') = \int \psi^*(\mathbf{x}; \mathbf{r}')\psi(\mathbf{x}; \mathbf{r}')\mathrm{d}^3\mathbf{x}$ (though they are not Casimirs of bracket (4.43c)).

Equation (4.44) is equivalent to Eq. (4.3a), which can be seen by making an appropriate unitary transformation on $\psi$. This transformation is referred to as going from the velocity gauge to the length gauge in the quantum description [96], and it is the analog of the change from canonical momentum to velocity in the classical derivation (Eq. (4.23)). The change of variables is given by

$$\widetilde{\psi} = \exp[i\mathbf{x}\cdot\mathbf{A}]\psi, \tag{4.45}$$

with the corresponding equation for $\psi^*$. Using the chain rule, the functional derivatives transform as

$$\mathcal{F}_{\psi} = \exp[i\mathbf{x}\cdot\mathbf{A}]\widetilde{F}_{\widetilde{\psi}}, \tag{4.46a}$$

$$\mathcal{F}_{\psi^*} = \exp[-i\mathbf{x}\cdot\mathbf{A}]\widetilde{F}_{\widetilde{\psi}^*}, \tag{4.46b}$$

$$\mathcal{F}_{\mathbf{A}} = i\mathbf{x}\widetilde{\psi}\widetilde{\mathcal{F}}_{\widetilde{\psi}} - i\mathbf{x}\widetilde{\psi}^*\mathcal{F}_{\widetilde{\psi}^*}, \tag{4.46c}$$

$$\mathcal{F}_{\mathbf{E}} = \widetilde{\mathcal{F}}_{\mathbf{E}}. \tag{4.46d}$$

Substituting Eqs. (4.45) and (4.46) into Hamiltonian (4.43b) and bracket (4.43c), respectively, yields

$$\mathcal{H}_{\mathrm{P}}[\psi,\psi^*] = \int \rho\psi^*\left[-\frac{1}{2}\nabla_{\mathbf{x}}^2 + V(\mathbf{x})\right]\psi\,\mathrm{d}^3\mathbf{x}\mathrm{d}^3\mathbf{r}, \tag{4.47a}$$

$$\begin{aligned}\{\mathcal{F},\mathcal{G}\} = \int\Bigg\{ &-i\rho^{-1}\int\left(\mathcal{F}_{\psi}\mathcal{G}_{\psi^*} - \mathcal{F}_{\psi^*}\mathcal{G}_{\psi}\right)\mathrm{d}^3\mathbf{x} + 4\pi\left(\mathcal{F}_{\mathbf{E}}\cdot\mathcal{G}_{\mathbf{A}} - \mathcal{F}_{\mathbf{A}}\cdot\mathcal{G}_{\mathbf{E}}\right)\\ &+ 4\pi i\int\left[\psi\left(\mathcal{F}_{\mathbf{E}}\mathcal{G}_{\psi} - \mathcal{F}_{\psi}\mathcal{G}_{\mathbf{E}}\right) - \psi^*\left(\mathcal{F}_{\mathbf{E}}\mathcal{G}_{\psi^*} - \mathcal{F}_{\psi^*}\mathcal{G}_{\mathbf{E}}\right)\right]\cdot\mathbf{x}\,\mathrm{d}^3\mathbf{x}\Bigg\}\mathrm{d}^3\mathbf{r},\end{aligned} \tag{4.47b}$$

where the tildes have been removed. Now, computing the equation of motion for $\psi$, one obtains Eq. (4.3a).

Deriving the hierarchy of quantum models is straightforward because, as mentioned previously, $\mathcal{H}_{\mathrm{EM}}$ is always the same as in the classical case. Furthermore, since only $\mathcal{H}_{\mathrm{EM}}$ and the Poisson bracket are modified in deriving the classical reduced models (see

Sec. 4.2.2), the only new information here is the relevant Poisson bracket for each quantum model. Meanwhile, $\mathcal{H}_{\mathrm{P}}$ is essentially always given by Eq. (4.47a). The first quantum model in the hierarchy, taking into account hypotheses HP 1-4 and HF 1, has the following Poisson bracket:

$$\{\mathcal{F},\mathcal{G}\} = \int \Big\{ -i\rho^{-1} \int \left(\mathcal{F}_{\psi}\mathcal{G}_{\psi^*} - \mathcal{F}_{\psi^*}\mathcal{G}_{\psi}\right) \mathrm{d}^3\mathbf{x} + 4\pi \left(\mathcal{F}_{\mathbf{E}} \cdot \mathcal{G}_{\mathbf{A}_\perp} - \mathcal{F}_{\mathbf{A}_\perp} \cdot \mathcal{G}_{\mathbf{E}}\right) \\ + 4\pi i \int \left[\psi \left(\mathcal{F}_{\mathbf{E}}\mathcal{G}_{\psi} - \mathcal{F}_{\psi}\mathcal{G}_{\mathbf{E}}\right) - \psi^* \left(\mathcal{F}_{\mathbf{E}}\mathcal{G}_{\psi^*} - \mathcal{F}_{\psi^*}\mathcal{G}_{\mathbf{E}}\right)\right] \cdot \mathbf{x}\, \mathrm{d}^3\mathbf{x} \Big\} \mathrm{d}z. \tag{4.48}$$

Like in the classical case, this bracket has $\widetilde{\mathcal{C}}$ as a Casimir invariant and $\mathcal{Q}_\perp$ as a conserved quantity. The corresponding Schrödinger equation is unchanged from the parent model, while the field equations are given by Eqs. (4.28b) and (4.28c). Note that, here, the definition of $\overline{\mathbf{v}}$ is the same as the definition of $\overline{\mathbf{p}}$ in the quantum case given previously. The second quantum model, incorporating also HF 2, has the same bracket with $\mathbf{E}$ replaced by $\mathbf{E}_\perp$.

Adding on HF 3, the bracket is simplified to

$$\{\mathcal{F},\mathcal{G}\} = \int \Big\{ -i\rho^{-1} \int \left(\mathcal{F}_{\psi}\mathcal{G}_{\psi^*} - \mathcal{F}_{\psi^*}\mathcal{G}_{\psi}\right) \mathrm{d}^3\mathbf{x} + 4\pi \left(\mathcal{F}_{E}\mathcal{G}_{A} - \mathcal{F}_{A}\mathcal{G}_{E}\right) \\ + 4\pi i \int \left[\psi \left(\mathcal{F}_{E}\mathcal{G}_{\psi} - \mathcal{F}_{\psi}\mathcal{G}_{E}\right) - \psi^* \left(\mathcal{F}_{E}\mathcal{G}_{\psi^*} - \mathcal{F}_{\psi^*}\mathcal{G}_{E}\right)\right] x_{\mathrm{e}}\, \mathrm{d}^3\mathbf{x} \Big\} \mathrm{d}z. \tag{4.49}$$

Performing reduction (4.31) on the field variables, the bracket becomes

$$\{\mathcal{F},\mathcal{G}\} = \int \Big\{ -i\rho^{-1} \int \left(\mathcal{F}_{\psi}\mathcal{G}_{\psi^*} - \mathcal{F}_{\psi^*}\mathcal{G}_{\psi}\right) \mathrm{d}^3\mathbf{x} - 2\pi c \left(\mathcal{F}_{\alpha}\partial_z\mathcal{G}_{\alpha} - \mathcal{F}_{\beta}\partial_z\mathcal{G}_{\beta}\right) \\ + 2\pi i \int [\psi \left(\mathcal{F}_{\alpha}\mathcal{G}_{\psi} - \mathcal{F}_{\psi}\mathcal{G}_{\alpha}\right) - \psi^* \left(\mathcal{F}_{\alpha}\mathcal{G}_{\psi^*} - \mathcal{F}_{\psi^*}\mathcal{G}_{\alpha}\right) \\ + \psi \left(\mathcal{F}_{\beta}\mathcal{G}_{\psi} - \mathcal{F}_{\psi}\mathcal{G}_{\beta}\right) - \psi^* \left(\mathcal{F}_{\beta}\mathcal{G}_{\psi^*} - \mathcal{F}_{\psi^*}\mathcal{G}_{\beta}\right)] x_{\mathrm{e}}\, \mathrm{d}^3\mathbf{x} \Big\} \mathrm{d}z. \tag{4.50}$$

Again, the Casimirs (4.35) are created by the reduction. As in the classical case, implementing HF 4 consists of removing the terms with functional derivatives with respect to $\beta$

from bracket (4.50). Finally, hypothesis HP 5 is implemented by taking $\psi = \psi(x_{\rm e}; z)$. For reference, the Hamiltonian and bracket of the model taking into account HP 1-5 and HF 1-4 are

$$\mathcal{H}_{\rm P}[\psi, \psi^*] = \int \rho\psi^* \left[-\frac{1}{2}\partial_{x_{\rm e}}^2 + V(x_{\rm e})\right] \psi \, {\rm d}x_{\rm e}{\rm d}z, \tag{4.51a}$$

$$\{\mathcal{F}, \mathcal{G}\} = \int \Big\{ - i\rho^{-1} \int \left(\mathcal{F}_\psi \mathcal{G}_{\psi^*} - \mathcal{F}_{\psi^*}\mathcal{G}_\psi\right) {\rm d}x_{\rm e} - 2\pi c \mathcal{F}_\alpha \partial_z \mathcal{G}_\alpha$$
$$+ 2\pi i \int \left[\psi \left(\mathcal{F}_\alpha \mathcal{G}_\psi - \mathcal{F}_\psi \mathcal{G}_\alpha\right) - \psi^* \left(\mathcal{F}_\alpha \mathcal{G}_{\psi^*} - \mathcal{F}_{\psi^*}\mathcal{G}_\alpha\right)\right] x_{\rm e} \, {\rm d}x_{\rm e} \Big\} {\rm d}z, \tag{4.51b}$$

with $\mathcal{H}_{\rm EM}$ given by Eq. (4.36a). The equations of motion stemming from this Hamiltonian system are equivalent to Eqs. (4.42). Focusing effects may be incorporated by adding $E_0(z,t)x_{\rm e}$ to the Hamiltonian operator in Eq. (4.51a).

## 4.4 Towards variational integrators for intense laser pulse propagation

In this section, we consider some elements of variational schemes for the numerical solution of the model equations derived in this chapter. We restrict our attention to the classical model with one-dimensional atoms and plane-wave fields. For the numerical integration of this model, the fields $f(x_{\rm e}, v_x, z)$, $\alpha(z)$ and $\beta(z)$ must be discretized in space. If we perform the spatial discretization at the level of the Hamiltonian and Poisson bracket, we obtain a finite system of Hamiltonian ODEs that inherits the variational structure of the parent model. From this point, one could then endeavor to construct a variational time-integrator specific to this system using a temporal discretization of the Hamiltonian and bracket, though we will not consider this here. We focus on the spatial discretization of the field-part of the equations, and refer to [110] for the spatial and phase-space discretization of the particle part of the equations.

### 4.4.1 Fourier basis for forward and backward propagating waves

Here, the objective is to discretize the field part of Eqs. (4.34). One possibility is to use a Fourier basis. We make a coordinate transformation from the radiated fields $(\alpha(z), \beta(z))$ to their Fourier modes $(\{\alpha_k\}, \{\beta_k\})$, defined as follows:

$$\alpha_k = \frac{1}{L}\int \alpha(z) \exp\left[-i\left(\frac{2\pi k}{L}\right) z\right] \mathrm{d}z \tag{4.52a}$$

$$\beta_k = \frac{1}{L}\int \beta(z) \exp\left[-i\left(\frac{2\pi k}{L}\right) z\right] \mathrm{d}z, \tag{4.52b}$$

where $L$ is the length of the domain we intend to simulate and $k$ takes integer values. The inverse Fourier transform gives the fields as sum of their Fourier components

$$\alpha(z) = \sum_{k=-\infty}^{\infty} \alpha_k \exp\left[i\left(\frac{2\pi k}{L}\right) z\right], \ \beta(z) = \sum_{k=-\infty}^{\infty} \beta_k \exp\left[i\left(\frac{2\pi k}{L}\right) z\right]. \tag{4.53}$$

Now, we must express Hamiltonian (4.33a) and bracket (4.33b) in terms of the new functionals $\widetilde{F}[f, \{\alpha_k\}, \{\beta_k\}] = F[f, \alpha, \beta]$. With the above relations and the definition of the functional derivative one can show that

$$F_\alpha = \frac{1}{L}\sum_{k=-\infty}^{\infty} \partial_{\alpha_k} \widetilde{F} \exp\left[-i\left(\frac{2\pi k}{L}\right) z\right], \tag{4.54}$$

and similarly for $F_\beta$. Substituting (4.54) into Eqs. (4.33) and using the orthogonality relation for Fourier modes,

$$\frac{1}{L}\int \exp\left[i\left(\frac{2\pi}{L}\right)(k+k')z\right] \mathrm{d}z = \delta_{k,-k'}, \tag{4.55}$$

we obtain

$$\mathcal{H}_{\mathrm{EM}}[\{\alpha_k\},\{\beta_k\}] = \frac{L}{4\pi}\sum_{k=-\infty}^{\infty}\left(\alpha_k\alpha_{-k}+\beta_k\beta_{-k}\right), \tag{4.56a}$$

$$\begin{aligned}\{\mathcal{F},\mathcal{G}\} = &\int \rho^{-1} f\left[\mathcal{F}_f,\mathcal{G}_f\right]\mathrm{d}\mu\mathrm{d}z - \frac{4\pi^2 ci}{L^2}\sum_{k=-\infty}^{\infty}\left[k\left(\partial_{\alpha_k}\mathcal{F}\partial_{\alpha_{-k}}\mathcal{G}-\partial_{\beta_k}\mathcal{F}\partial_{\beta_{-k}}\mathcal{G}\right)\right]\\ &+\frac{2\pi}{L}\sum_{k=-\infty}^{\infty}\int f\exp\left[-i\left(\frac{2\pi k}{L}\right)z\right]\Big(\partial_{\alpha_k}\mathcal{F}\partial_{v_x}\mathcal{G}_f-\partial_{v_x}\mathcal{F}_f\partial_{\alpha_k}\mathcal{G}\\ &+\partial_{\beta_k}\mathcal{F}\partial_{v_x}\mathcal{G}_f-\partial_{v_x}\mathcal{F}_f\partial_{\beta_k}\mathcal{G}\Big)\mathrm{d}\mu\mathrm{d}z.\end{aligned} \tag{4.56b}$$

In terms of these new coordinates, the Casimirs $\mathcal{Q}_\alpha$ and $\mathcal{Q}_\beta$ become

$$\mathcal{Q}_\alpha = L\alpha_0 - 2\pi\int\rho\overline{x}_{\mathrm{e}}\mathrm{d}z, \tag{4.57a}$$

$$\mathcal{Q}_\beta = L\beta_0 - 2\pi\int\rho\overline{x}_{\mathrm{e}}\mathrm{d}z. \tag{4.57b}$$

From here, obtaining a finite number of degrees-of-freedom for the wave variables is straightforward. One may simply select a maximum mode $k_{\max}$, and truncate all modes such that $|k| > k_{\max}$. The observables $\mathcal{F}[f,\{\alpha_k\}_{|k|\leq k_{\max}},\{\beta_k\}_{|k|\leq k_{\max}}]$ form a Poisson subalgebra of the observables $F[f,\{\alpha_k\},\{\beta_k\}]$. Therefore, as long as one truncates both Hamiltonian (4.56a) and the bracket (4.56b), the truncated system preserves the Hamiltonian structure.

### 4.4.2 Hamiltonian formulation for the moving-frame

Equations (4.56) are necessary to consider backward-propagating waves in the lab frame, but may be reduced even further for the study of unidirectional propagation in the moving frame. As we showed in Sec. 4.2.2, removing backward-propagating waves is as simple as removing the $\beta$ terms from the Hamiltonian and bracket, since the remaining variables form a Poisson subalgebra. However, an even greater simplification from a practical point of view is going into the moving frame. The resulting equations (4.19) require much less

computational effort to solve than Eqs. (4.34a) and (4.34b) in the lab frame because the former only require the solution of the Liouville equation at a single $\xi$ at a time, while the latter require it to be solved at every $z$ simultaneously for the entire simulation. While we provided a Lagrangian formulation for the moving-frame equations, it is not obvious how to obtain the Hamiltonian formulation. Namely, it is not clear how to translate the key step in the Lagrangian formulation—going from $A(z,t)$ to $\widetilde{A}(\xi,\tau)$—to the Hamiltonian formulation. Even by extending the phase space of the Hamiltonian system to include a time variable (and its canonically-conjugate, energy-like variable), making the transformation $\tau = t - z/c$ does not make sense, because $z$ is a label for the field variables, not a dynamical variable. Here, we illustrate another approach towards a Hamiltonian formulation of the moving-frame equations, although the end result is not exactly equivalent to Eqs. (4.19) and not as useful in practice.

Our starting point is the Fourier-decomposed electromagnetic Hamiltonian and bracket only considering the forward-propagating waves, for simplicity, with phase space extended to contain the variables $(\tau, h)$. $\tau$ is equivalent to the time variable and $h$ is the energy-like variable canonically conjugate to $\tau$. That is, we have

$$\mathcal{H}_{\mathrm{EM}}[\{\alpha_k\},\tau,h] = \frac{L}{4\pi}\sum_{k=-\infty}^{\infty}\alpha_k\alpha_{-k} + h, \tag{4.58a}$$

$$\{\mathcal{F},\mathcal{G}\} = \int \rho^{-1} f\left[\mathcal{F}_f,\mathcal{G}_f\right]\mathrm{d}\mu\mathrm{d}z - \frac{2\pi i}{L}\sum_{k=-\infty}^{\infty}\omega_k\partial_{\alpha_k}\mathcal{F}\partial_{\alpha_{-k}}\mathcal{G} + \partial_\tau\mathcal{F}\partial_h\mathcal{G} - \partial_h\mathcal{F}\partial_\tau\mathcal{G}$$
$$+\frac{2\pi}{L}\sum_{k=-\infty}^{\infty}\int f\exp\left[-\frac{i\omega_k z}{c}\right]\left(\partial_{\alpha_k}\mathcal{F}\partial_{v_x}\mathcal{G}_f - \partial_{v_x}\mathcal{F}_f\partial_{\alpha_k}\mathcal{G}\right)\mathrm{d}\mu\mathrm{d}z, \tag{4.58b}$$

where we have introduced the notation $\omega_k \equiv 2\pi ck/L$. Note that, because this Hamiltonian has no $\tau$ dependence, $h$ is a conserved quantity. First, it is useful to make a time-dependent coordinate transformation on the $\alpha_k$ variables which accounts for their trivial time dependence due to wave propagation. This will allow us to express the electric field as a function

of the variable $\zeta = z - ct$ as opposed to $z$. The transformation is specified by

$$\widetilde{\alpha}_k = \alpha_k e^{i\omega_k \tau} \quad \text{for } k \neq 0, \tag{4.59a}$$

$$\widetilde{h} = h + \frac{L}{4\pi} \sum_{k \neq 0} \alpha_k \alpha_{-k}, \tag{4.59b}$$

where we see $\widetilde{h}$ contains the energy of the forward propagating waves. This leads us to the following Hamiltonian

$$\mathcal{H}_{\mathrm{EM}}[\{\alpha_k\}, \tau, h] = \frac{L}{4\pi} \alpha_0^2 + h, \tag{4.60}$$

and bracket

$$\begin{aligned} \{\mathcal{F}, \mathcal{G}\} = &\int \rho^{-1} f \left[\mathcal{F}_f, \mathcal{G}_f\right] \mathrm{d}\mu \mathrm{d}z + \partial_\tau \mathcal{F} \partial_h \mathcal{G} - \partial_h \mathcal{F} \partial_\tau \mathcal{G} - \frac{2\pi i}{L} \sum_{k=-\infty}^{\infty} \omega_k \partial_{\alpha_k} \mathcal{F} \partial_{\alpha_{-k}} \mathcal{G} \\ &+ \frac{2\pi}{L} \sum_{k=-\infty}^{\infty} \int f \exp\left[-\frac{i\omega_k \zeta}{c}\right] \left(\partial_{\alpha_k} \mathcal{F} \partial_{v_x} \mathcal{G}_f - \partial_{v_x} \mathcal{F}_f \partial_{\alpha_k} \mathcal{G}\right) \mathrm{d}\mu \mathrm{d}z \\ &+ \int f \left(\partial_h \mathcal{F} \partial_{v_x} \mathcal{G}_f - \partial_{v_x} \mathcal{F}_f \partial_h \mathcal{G}\right) \left(\alpha_{\mathrm{mov}}(z, \tau) - \alpha_0\right) \mathrm{d}\mu \mathrm{d}z, \end{aligned} \tag{4.61}$$

where we have omitted the tildes. The bracket differs from bracket (4.58b) on the second line, where the electron location $z$ has been replaced by $\zeta \equiv z - c\tau$, and additionally contains the last line, where the field in the moving frame is

$$\alpha_{\mathrm{mov}}(z, \tau) = \sum_{k=-\infty}^{\infty} \alpha_k \exp\left[\frac{i\omega_k \zeta}{c}\right]. \tag{4.62}$$

Additionally, because in the previous system (Eqs. (4.58)) we had $h$ as a conserved quantity, transformations (4.59) imply that in this system, we have a conserved quantity $\mathcal{Q}_h$ given by

$$\mathcal{Q}_h = h - \frac{L}{4\pi} \sum_{k \neq 0} \alpha_k \alpha_{-k}. \tag{4.63}$$

This is readily verified by using Eqs. (4.60) and (4.61) and checking that $\{\mathcal{Q}, \mathcal{H}\} = 0$.

Indeed, this is just a restatement of the fact that $h$ is the energy of the forward propagating waves.

At present, the variables $\{\alpha_k\}$ describe the shape of the field on the domain of length $L$. In principle, $L$ is infinite: electromagnetic waves can propagate over unbounded domains. In practice, i.e. for numerical simulations, $L$ is finite and must be large enough to contain the entire gas. Still, we may only be interested in the field profile over an even smaller domain of length $L_0$, co-moving with the incident laser pulse. Thus, we introduce a new set of variables, $\{\widetilde{\alpha}_m\}$ for describing the shape of the fields on a domain of reduced finite length $L_0$. Henceforth, we will retain the tildes in order to refer to the Fourier modes on the reduced domain. Accordingly, the possible wave vectors for this domain size have the form $(2\pi/L_0)m$, for integer $m$. We establish the relationship between the tilde amplitudes and the old amplitudes by imposing

$$\alpha_{\mathrm{mov}}(z,\tau) = \sum_{k=-\infty}^{\infty} \alpha_k \exp\left[\frac{i\omega_k\zeta}{c}\right] = \Pi_{L_0}(\zeta) \sum_{m=-\infty}^{\infty} \widetilde{\alpha}_m \exp\left[\frac{i\omega_m\zeta}{c}\right] \tag{4.64}$$

$\Pi_{L_0}(\zeta)$ is the gate function, which we define using Heaviside step functions $\Theta(\zeta)$ as

$$\Pi_{L_0}(\zeta) = \Theta(\zeta + L_0) - \Theta(\zeta) = \begin{cases} 0 & \text{if } \zeta < -L_0 \\ 1 & \text{if } -L_0 < \zeta < 0 \\ 0 & \text{if } \zeta > 0 \end{cases} \tag{4.65}$$

In what follows, $j$ and $k$ will always refer to Fourier modes on the domain of length $L$, while $m$ and $n$ will be refer to Fourier modes on the domain of length $L_0$. Hence, when we write $\omega_m$, we mean $\omega_m \equiv 2\pi cm/L_0$.

We may obtain expressions of the new coordinates in terms of the old coordinates by carrying out integrations of both sides of Eq. (4.64) by $L_0^{-1}\int_{-L_0}^{0} \mathrm{d}\zeta \, \exp\left[-i\omega_n\zeta/c\right]$. By Fourier orthogonality, this isolates a single new variable on the right hand side corresponding to mode $n$, which yields an equation for each new variable in terms of the old variables.

These equations are

$$\widetilde{\alpha}_0 = \alpha_0 - \frac{ic}{L_0}\sum_{k\neq 0}\frac{1-\exp\left[-i\omega_k L_0/c\right]}{\omega_k}\alpha_k \text{ for } n=0, \text{ otherwise,} \tag{4.66a}$$

$$\widetilde{\alpha}_n = -\frac{ic}{L_0}\sum_{k\neq 0}\frac{1-\exp\left[-i\omega_k L_0/c\right]}{\omega_k-\omega_n}\alpha_k. \tag{4.66b}$$

Likewise, we may obtain expressions of the old coordinates in terms of the new coordinates by integrating both sides of Eq. (4.64) by $L^{-1}\int_{-L_0}^{L-L_0}\mathrm{d}\zeta\exp\left[-i\omega_j\zeta/c\right]$. The expressions are

$$\alpha_0 = \frac{L_0}{L}\widetilde{\alpha}_0 \text{ for } j=0, \text{ otherwise,} \tag{4.67a}$$

$$\alpha_j = \frac{ic(1-\exp[i\omega_j L_0/c])}{L}\sum_{m=-\infty}^{\infty}\frac{\widetilde{\alpha}_m}{\omega_j-\omega_m}. \tag{4.67b}$$

Note that we have taken $\zeta\in[-L_0, L-L_0]$ for the original domain.

We remark that, although we can write both sets of coordinates in terms of the other, this is not actually an invertible transformation. Obviously, we cannot describe a field of arbitrary shape on the domain of length $L$, such as the one on the left-hand side of Eq. (4.64), using only the variables $\{\widetilde{\alpha}_m\}$. Eq. (4.64) is like a projection of a vector in a vector space to a vector subspace. We project the electric field on the full domain of length $L$, described by the set of variables $\{\alpha_k\}$, to the part of the electric field on the subdomain of length $L_0$, described by another set of variables $\{\widetilde{\alpha}_m\}$. It just so happens that both of these sets are infinite, so the dimensional reduction is not apparent from counting the number of variables as it would be for a projection in the finite-dimensional case. However, the transformation to $\{\widetilde{\alpha}_m\}$ is indeed a dimensional reduction, and like a projection in the finite-dimensional case, this transformation is not invertible.

Now that we have the new variables expressed as functions of the old variables, we may begin compute the new Poisson bracket by computing the Poisson matrix between the new variables. Using Eqs. (4.66) and the relevant nonzero elements of the old Poisson matrix,

given by

$$\{\alpha_k, \alpha_j\} = \frac{2\pi i\omega_j}{L}\delta_{-k,j} \tag{4.68a}$$

$$\{\alpha_k, f\} = -\frac{2\pi}{L}\exp[-i\omega_k\zeta/c]\partial_{v_x} f \tag{4.68b}$$

we obtain

$$\{\widetilde{\alpha}_0, f\} = -\frac{2\pi\partial_{v_x} f}{L}\left(1 - \frac{ic}{L_0 L}\sum_{k\neq 0}\frac{(1-\exp\left[-i\omega_k L_0/c\right])}{\omega_k}\exp[-i\omega_k\zeta/c]\right) \tag{4.69a}$$

$$\{\widetilde{\alpha}_n, f\} = \frac{2\pi ic\partial_{v_x} f}{LL_0}\sum_{k\neq 0}\frac{(1-\exp\left[-i\omega_k L_0/c\right])}{\omega_k - \omega_n}\exp[-i\omega_k\zeta/c] \tag{4.69b}$$

$$\{\widetilde{\alpha}_0, \widetilde{\alpha}_n\} = -\frac{8\pi ic^2}{LL_0^2}\sum_{k\neq 0}\frac{\sin^2(\frac{\omega_k L_0}{2c})}{(\omega_k + \omega_n)} \tag{4.69c}$$

$$\{\widetilde{\alpha}_m, \widetilde{\alpha}_n\} = -\frac{8\pi ic^2}{LL_0^2}\sum_{k\neq 0}\frac{\omega_k\sin^2(\frac{\omega_k L_0}{2c})}{(\omega_k - \omega_m)(\omega_k + \omega_n)} \tag{4.69d}$$

First, we focus on Eqs. (4.69a) and (4.69b). These brackets may be identified with the Fourier representations of two particular functions of $\zeta$ on the domain $[-L_0, L - L_0]$. Specifically, one can show that

$$\Pi_{L_0}(\zeta) = \frac{1}{L}\left(L_0 - ic\sum_{k\neq 0}\frac{(1-\exp[-i\omega_k L_0/c])}{\omega_k}\exp[-i\omega_k\zeta/c]\right), \tag{4.70a}$$

$$\Pi_{L_0}(\zeta)\exp[-i\omega_m\zeta/c] = -\frac{ic}{L}\sum_{k\neq 0}\frac{(1-\exp[-i\omega_k L_0/c])}{\omega_k - \omega_m}\exp[-i\omega_k\zeta/c]. \tag{4.70b}$$

Substituting Eqs. (4.70) into brackets (4.69a) and (4.69b) brings them to the following transparent form:

$$\{\widetilde{\alpha}_0, f\} = -\frac{2\pi\partial_{v_x} f}{L_0}\Pi_{L_0}(\zeta), \tag{4.71a}$$

$$\{\widetilde{\alpha}_n, f\} = -\frac{2\pi\partial_{v_x} f}{L_0}\Pi_{L_0}(\zeta)\exp[-i\omega_n\zeta/c]. \tag{4.71b}$$

Meanwhile, the sums in Eqs. (4.69c) and (4.69d) may be evaluated analytically in the limit $L \to \infty$. Here we sketch the procedure to evaluate the sums, while additional details are in App. D. To proceed, we define $\Delta = L_0/L$. Taking Eq. (4.69d) as an example, we factor out $2\pi c/L_0$ from the $\omega$ variables and multiply by $\Delta/\Delta$, yielding

$$\{\widetilde{\alpha}_m, \widetilde{\alpha}_n\} = -\frac{4ic}{L_0^2} \sum_{k=-\infty}^{\infty} \frac{\Delta k \sin^2(\pi \Delta k)}{(\Delta k - m)(\Delta k + n)} \Delta \tag{4.72}$$

We are able to include $k = 0$ term in the sum above which is not present in Eq. (4.69d), because this term is simply zero. Evidently, the sum in Eq. (4.72) is the Riemann sum approximation of the integral of the expression in the summand. We are interested in the limit $L \to \infty$, which is equivalent to $\Delta \to 0$ and thus corresponds exactly to integral, that is,

$$\lim_{L\to\infty} \{\widetilde{\alpha}_m, \widetilde{\alpha}_n\} = -\frac{4ic}{L_0^2} \int_{-\infty}^{\infty} \frac{R \sin^2(\pi R)}{(R - m)(R + n)} \mathrm{d}R. \tag{4.73}$$

In App. D, we show that

$$\int_{-\infty}^{\infty} \frac{R \sin^2(\pi R)}{(R - m)(R + n)} \mathrm{d}R = -n\pi^2 \delta_{-m,n}. \tag{4.74}$$

Thus, substituting Eq. (4.74) into Eq. (4.73) and reverting back to the frequencies $\omega_m$ and $\omega_n$, we get

$$\lim_{L\to\infty} \{\widetilde{\alpha}_m, \widetilde{\alpha}_n\} = \frac{2\pi i \omega_n}{L_0} \delta_{-m,n}. \tag{4.75}$$

By following the procedure sketched here and in App. D, we can take the limit $L \to \infty$ for Eq. (4.69c) as well, yielding

$$\{\widetilde{\alpha}_0, \widetilde{\alpha}_n\} = 0. \tag{4.76}$$

For brackets (4.71a) and (4.71b), there is no change in the $L \to \infty$ limit. The last step to writing the full bracket in terms of the new variables is to rewrite the last line of bracket (4.61) in terms of the new variables. This is straightforward, because we already know

$\alpha_{\rm mov}(z,t)$ in terms of the new variables is given by the right-hand side of Eq. (4.64), by construction. On the other hand, $\alpha_0$ is given by Eq. (4.67a), and thus it vanishes in the limit $L \to \infty$. Therefore, the final bracket is given by

$$\begin{aligned}\{\mathcal{F},\mathcal{G}\} = &\int \rho^{-1} f\left[\mathcal{F}_f, \mathcal{G}_f\right] \mathrm{d}\mu \mathrm{d}z + \partial_\tau \mathcal{F} \partial_h \mathcal{G} - \partial_h \mathcal{F} \partial_\tau \mathcal{G} - \frac{2\pi i}{L_0} \sum_{m=-\infty}^{\infty} \omega_m \partial_{\widetilde{\alpha}_m} \mathcal{F} \partial_{\widetilde{\alpha}_{-m}} \mathcal{G} \\ &+ \frac{2\pi}{L_0} \sum_{m=-\infty}^{\infty} \int f \Pi_{L_0}(\zeta) \exp\left[-\frac{i\omega_m \zeta}{c}\right] \left(\partial_{\widetilde{\alpha}_m} \mathcal{F} \partial_{v_x} \mathcal{G}_f - \partial_{v_x} \mathcal{F}_f \partial_{\widetilde{\alpha}_m} \mathcal{G}\right) \mathrm{d}\mu \mathrm{d}z \\ &+ \int f \left(\partial_h \mathcal{F} \partial_{v_x} \mathcal{G}_f - \partial_{v_x} \mathcal{F}_f \partial_h \mathcal{G}\right) \Pi_{L_0}(\zeta) \sum_{m=\infty}^{\infty} \widetilde{\alpha}_m \exp[i\omega_m \zeta / c] \mathrm{d}\mu \mathrm{d}z. \end{aligned} \tag{4.77}$$

and the Hamiltonian is given by

$$\mathcal{H}_{\rm EM}[\{\widetilde{\alpha}_m\}, \tau, h] = h. \tag{4.78}$$

In this system, a conserved quantity is obtained from $\mathcal{Q}_h$ by substituting Eq. (4.67b) into Eq. (4.63), giving

$$\mathcal{Q}_h = h - \frac{1}{\pi L} \sum_{m,n=-\infty}^{\infty} \sum_{k \neq 0} \frac{\sin^2(\frac{\omega_k L_0}{2c})}{(\omega_k - \omega_m)(\omega_k + \omega_n)} \widetilde{\alpha}_m \widetilde{\alpha}_n. \tag{4.79}$$

By using the same strategy used to evaluate the $\{\widetilde{\alpha}_m, \widetilde{\alpha}_n\}$ brackets in the $L \to \infty$ limit, we can evaluate the above sum over $k$ as well. This gives

$$\mathcal{Q}_h = h - \frac{L_0}{4\pi} \sum_{m=-\infty}^{\infty} \widetilde{\alpha}_m \widetilde{\alpha}_{-m}. \tag{4.80}$$

Eq. (4.80) shows that $h$ is now equivalent to the energy of the part of the field in the moving window. One can confirm that with Hamiltonian (4.78) and bracket (4.77), $\{\mathcal{Q}_h, \mathcal{H}\} = 0$ indeed holds.

Lastly, we take the distribution function into the moving frame as well. Recall that the

particle Hamiltonian is

$$\mathcal{H}_{\mathrm{P}}[f] = \int \rho\, f \left[\frac{v_x^2}{2} + V(x_{\mathrm{e}})\right] \mathrm{d}\mu \mathrm{d}z. \tag{4.81}$$

We make the coordinate transformation

$$\widetilde{f}(x, v, \zeta) = f(x, v, z) = f(x, v, \zeta + c\tau). \tag{4.82}$$

With this change of variables, Hamiltonian (4.81) is essentially unchanged—one simply makes the substitutions $f \to \widetilde{f}$ and $\mathrm{d}z \to \mathrm{d}\zeta$. To obtain the bracket, we use the chain rule, which yields

$$\partial_\tau \mathcal{F} = \partial_\tau \widetilde{\mathcal{F}} + c \int \widetilde{\mathcal{F}}_{\widetilde{f}} \partial_\zeta \widetilde{f}, \mathrm{d}\mu \mathrm{d}\zeta. \tag{4.83}$$

Meanwhile, all the other terms in bracket (4.77) are unchanged. Thus, the new bracket is

$$\begin{aligned}
\{\mathcal{F}, \mathcal{G}\} = &\int \rho^{-1} f \left[\mathcal{F}_f, \mathcal{G}_f\right] \mathrm{d}\mu \mathrm{d}\zeta + \partial_\tau \mathcal{F} \partial_h \mathcal{G} - \partial_h \mathcal{F} \partial_\tau \mathcal{G} - \frac{2\pi i}{L_0} \sum_{m=-\infty}^{\infty} \omega_m \partial_{\widetilde{\alpha}_m} \mathcal{F} \partial_{\widetilde{\alpha}_{-m}} \mathcal{G} \\
&+ \frac{2\pi}{L_0} \sum_{m=-\infty}^{\infty} \int f \Pi_{L_0}(\zeta) \exp\left[-\frac{i\omega_m \zeta}{c}\right] \left(\partial_{\widetilde{\alpha}_m} \mathcal{F} \partial_{v_x} \mathcal{G}_f - \partial_{v_x} \mathcal{F}_f \partial_{\widetilde{\alpha}_m} \mathcal{G}\right) \mathrm{d}\mu \mathrm{d}\zeta \\
&+ \int f \left(\partial_h \mathcal{F} \partial_{v_x} \mathcal{G}_f - \partial_{v_x} \mathcal{F}_f \partial_h \mathcal{G}\right) \Pi_{L_0}(\zeta) \sum_{m=\infty}^{\infty} \widetilde{\alpha}_m \exp[i\omega_m \zeta / c] \mathrm{d}\mu \mathrm{d}\zeta \\
&+ c \int f \left(\partial_h \mathcal{F} \partial_\zeta \mathcal{G}_f - \partial_\zeta \mathcal{F}_f \partial_h \mathcal{G}\right) \mathrm{d}\mu \mathrm{d}\zeta.
\end{aligned} \tag{4.84}$$

where we have also performed an integration by parts on the last line.

*Equations of motion*

Now, we have obtained the Hamiltonian and bracket for the propagation of a compactly-supported laser pulse through a gas in the moving frame. Using Eqs. (4.81), (4.78), and

(4.84), the equations of motion are

$$\dot{f} = -v_x \partial_{x_e} f + \left( \partial_{x_e} V + \Pi_{L_0}(\zeta) \sum_{m=-\infty}^{\infty} \widetilde{\alpha}_m \exp[i\omega_m \zeta/c] \right) \partial_{v_x} f + c\partial_\zeta f, \tag{4.85a}$$

$$\dot{\widetilde{\alpha}}_m = \frac{2\pi}{L_0} \int v_x \rho f \Pi_{L_0}(\zeta) \exp[-i\omega_m \zeta/c] \mathrm{d}\mu \mathrm{d}\zeta, \tag{4.85b}$$

$$\dot{\tau} = 1, \tag{4.85c}$$

$$\dot{h} = \int v_x \rho f \Pi_{L_0}(\zeta) \sum_{m=-\infty}^{\infty} \widetilde{\alpha}_m \exp[i\omega_m \zeta/c] \, \mathrm{d}\mu \mathrm{d}\zeta. \tag{4.85d}$$

Equation (4.85a) is the Liouville equation, with an additional term (the last one) causing the advection of particles in the $-\zeta$ direction. This comes from our moving coordinate frame. What is notable about the reduction to the domain of length $L_0$ is that, due to the gate function in Eq. (4.85a), the particles only experience the field for the finite time $L_0/c$ during which they traverse $\zeta \in [-L_0, 0]$, the present location of the pulse. Likewise, it is only the particles in this region which contribute to the evolution of the field modes (Eq. (4.85b)) and exchange energy with the field (Eq. (4.85d)). Hence, Eqs. (4.85) are an improvement over Eqs. (4.34a) and (4.34b), because only the particles in the region of interest need to be accounted for at any given time, rather than those in the entire gas. However, they are still not as convenient as Eqs. (4.19) (see Sec. 5.3.3 for their discretization). In a nutshell, this is because the latter only require a representation of the particles at a single $z$ location at a time, whereas Eqs (4.85) require a representation of the particles over the entire spatial domain $\zeta \in [-L_0, 0]$ at each time. Therefore, the search for a variational integrator of these equations might best begin from the action principle with Lagrangians (4.17), which directly yields the more efficiently-solved Eqs. (4.19).

## 4.5 Summary

To summarize, we have presented derivations of a hierarchy of reduced classical and quantum models for the propagation of intense laser pulses in atomic gases. Along the way, we

derived the reduced quantum models used in Refs. [132, 137]. By consistently applying simplifying hypotheses within a variational formulation, whether Lagrangian or Hamiltonian, we have ensured that our reduced models preserve the mathematical structure of the parent models. Using the Hamiltonian formulation, we were able to easily identify conserved quantities of both the classical and quantum systems. In particular, the conserved quantities $\widetilde{\mathcal{C}}(z')$, $\mathcal{Q}_\alpha$, and $\mathcal{Q}_\beta$ are interesting because as Casimir invariants, they are conserved even in the presence of a time-dependent external field, unlike the Hamiltonian. Knowledge of these conservation laws can provide a useful benchmark for numerical codes for solving these model equations. While we focus on first-principles microscopic models of the atomic response in gases, we anticipate that our methodology can be extended to employ reduced models of the atomic response (e.g. in terms of a macroscopic polarization with an explicit nonlinear dependence on the electric field) which are commonly used in nonlinear optics [123, 130]. Further, variational formulations employing microscopic models of condensed phase systems should also be possible.

# CHAPTER 5
# ANALYSIS OF REDUCED MODELS FOR INTENSE LASER PULSE PROPAGATION

## 5.1 Introduction

The propagation of intense, low-frequency laser pulses through gases triggers a variety of highly nonlinear, nonperturbative phenomena, such as high-harmonic generation (HHG) [24, 44], terahertz (THz) generation [118, 119], and filamentation [120, 121]. These phenomena intrinsically tie together two disparate length scales: the microscopic scale, defined by the coupling of individual atoms (or molecules) to the electromagnetic field, and the macroscopic scale, defined by the coupling of the electromagnetic field to the mean polarization induced across the entire gas. Further, the self-consistent interaction between the gas particles and the field plays a paramount role in these processes. In the case of HHG and THz generation, the observed spectra depend sensitively on which frequencies are phase-matched over sufficiently long distances as the laser field is reshaped during propagation by the radiation emitted by ionizing atoms; see [40, 44, 45] for examples in HHG and [138–140] for examples in THz generation. Meanwhile, the interplay between the radiation of bounded electrons and that of the tunnel-ionized electrons during propagation is at the heart of filamentation [120]. Therefore, theoretical descriptions of these phenomena must bridge the gap between the microscopic electron dynamics and the macroscopic evolution of the laser field during propagation.

The most accurate description of this system is the Maxwell-Schrödinger model [58, 141]. This a first-principles model consisting of Maxwell's equations in three-dimensions for the macroscopic electromagnetic field, with source terms obtained from the microscopic electronic wave functions of the gas atoms. Due to the vast separation of scales, simula-

tions of this model under realistic conditions are only feasible using super-computers at present [58, 141]. Therefore, reduced models are required. The most popular consist of dimensionally-reduced unidirectional propagation equations for the electomagnetic field [130], which are typically coupled to models of tunneling ionization [42] and nonlinear polarization [123, 142] for the low-frequency part of the atomic response, and a semi-classical trajectory model for the high-frequency part [44, 55]. Besides missing intrinsically three-dimensional effects, the approximations on the atomic response in these models can miss important features of ionization and the generation of THz and low-order harmonic radiation [73, 143], which become particularly important when propagation effects are taken into account [65, 122].

As an intermediate alternative, dimensionally-reduced propagation models which retain a first-principles description of the atomic response may be employed. For example, reduced Maxwell-Schrödinger models have been derived, which retain a first-principles wave-function description of the atomic response and its coupling to the electromagnetic field [132, 137, 144]. Also, a reduced purely classical model has been considered, where the wave-function is modeled by a distribution of classical trajectories [48, 128] coupled to the field [90, 91]. This model combines a trajectory picture [2, 3], heavily relied upon in control applications [17, 119], with an accurate description of the low-frequency part of the spectrum that is in agreement with the corresponding quantum model [91]. The reduced dimensionality of these models manifestly precludes their use for studying three-dimensional effects, such as the spatial confinement a laser beam in a filament. At the same time, they are still versatile enough to provide a rigorous description of other ubiquitous propagation effects, such as ionization losses, dynamical blueshifting [43, 145], and high-pressure phase-matching [132], which are of vital importance in cutting-edge experiments [33, 40, 146].

In this chapter, we describe the behavior of some of the first-principles reduced models derived in Ch. 4. In Sec. 5.2, we specify the models we consider here and the protocol for

their numerical simulation, as well as the observables used for the analysis of the simulation results. In Sec. 5.3, we report the numerical methods used for the solution of the model equations. In Sec. 5.4, an analysis of the unidirectional pulse-propagation equation coupled to one-dimensional model atoms initiated in their ground states is presented, with an emphasis on the phenomena of ionization losses and dynamical blueshifting. In Sec. 5.5, we study the high-harmonic spectra obtained from this model. Lastly, in Sec. 5.6, we report on results of simulations of some of the higher-dimensional reduced models obtained in Ch. 4.

## 5.2 Framework for the simulations

### 5.2.1 Models

The reduced models we consider in this chapter describe the evolution of the electric field $\mathcal{E}(z,\tau)$ of a linearly-polarized (in the $x$ direction) laser pulse propagating in the $z$-direction. We will consider both one- and two-dimensional models for the motion of the atomic electrons, either moving only in the $x$ direction or moving in the $x$-$y$ plane, respectively. In principle, a two-dimensional model of the electron motion should be coupled to a two-dimensional laser field, i.e. with a $y$ component also. However, for the reduced models in which the $(x,y)$ dependence of the fields are neglected, an initially linearly-polarized laser pulse will remain linearly-polarized due to the symmetry $(y_\mathrm{e}, v_y) \to (-y_\mathrm{e}, -v_y)$ of the electron in the combined laser and Coulomb fields. Hence, we are able to ignore the $y$ component of the laser field.

*Unidirectional pulse with one-dimensional atoms*

The first model we shall consider is that of a solely-forward propagating laser pulse through a gas of one-dimensional model atoms. For the classical model, this was derived as Eq. (4.19), and for the quantum model, this was derived as Eq. (4.42). We employ a coordinate frame moving at the speed of light $c$ with the incident laser pulse, i.e. $\tau = t - z/c$. In both the

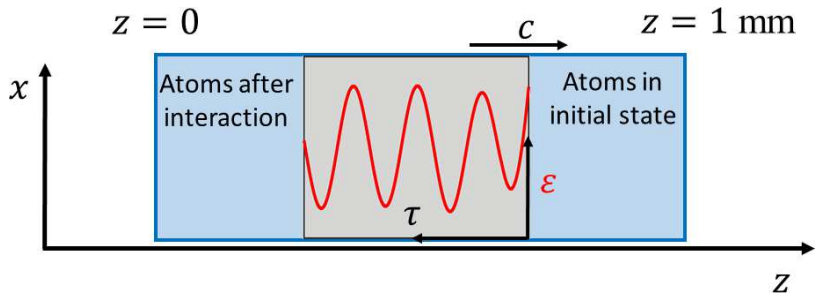


Figure 5.1: Schematic of the reduced model. The time-dependence of the laser electric field $\mathcal{E}(z,\tau)$ evolves as the pulse position advances in $z$ through the gas.

classical and quantum models, the evolution equation for the field is given by

$$\partial_z \mathcal{E} = \frac{2\pi\rho}{c}\overline{v}(z,\tau), \tag{5.1}$$

where $\rho$ is the number density of the gas, $\overline{v}$ is the mean dipole velocity of the atoms, and the $x$ subscript has been omitted. Unless stated otherwise, we assume that $\rho$ is constant, independent of $z$. In Eq. (5.1), the evolution parameter is $z$, and it may be solved as an initial-value problem with initial condition $\mathcal{E}(0,\tau) = \mathcal{E}_0(\tau)$. One simply needs to specify how to compute $\overline{v}$ at a given $z$ for the electric field at that position, $\mathcal{E}(z,\tau)$. Unless stated otherwise, we consider $\tau$ in the domain $\tau \in [0, \tau_f]$.

In the quantum model, the electron is described by the wave function $\psi(x,z,\tau)$, where we have omitted the "e" subscript on the electron position $x$. The Schrödinger equation governing the evolution of $\psi$ and mean dipole velocity are then given by

$$i\partial_\tau \psi = [-\frac{1}{2}\partial_x^2 + V(x) + \mathcal{E}(z,\tau)x]\psi, \tag{5.2a}$$

$$\overline{v}(z,\tau) = \overline{v}_0(z) - \int_0^\tau \left[\mathcal{E}(z,\tau') + \int \partial_x V |\psi(x,z,\tau')|^2 \mathrm{d}x\right] \mathrm{d}\tau', \tag{5.2b}$$

where $x$ is the electron position relative to the ion and $V$ is the electron-ion interaction potential, which we take to be the soft-Coulomb potential $V(x) = -(x^2+2)^{-1/2}$ [84, 97].

The initial dipole velocity $\overline{v}_0(z)$ is given by

$$\overline{v}_0(z) = -i \int \psi^*(x, 0; z) \partial_x \psi(x, z, 0) \mathrm{d}x.$$

We compute $\overline{v}$ in Eq. 5.2b by integrating the dipole acceleration in the given form instead of computing the dipole velocity directly (as in Eq. (5.2.1)) because it also accounts for the part of the wave function which has escaped beyond the finite-sized computational domain used to represent it. This part of the wave function, typically representing ionized electrons which never return to the core, still contributes to the dipole velocity through the oscillating motion of these electrons in the laser field. This contribution is accounted for by the first term of Eq. (5.2b), while the second term accounts for the part of the electron dipole velocity due to the Coulomb interaction for the part of the wave function that remains on the computational grid. On the other hand, in the classical model, the dipole velocity is computed by averaging over an ensemble of electron trajectories with a probability distribution on the phase space $f(x, v, z, \tau)$. The Liouville equation governing the evolution of $f$ and the mean dipole velocity are then given by

$$\partial_\tau f = -v \partial_x f + [\partial_x V + \mathcal{E}(z, \tau)] \partial_v f, \tag{5.3a}$$

$$\overline{v}(z, \tau) = \int v f(x, v, z, \tau) \mathrm{d}x \mathrm{d}v. \tag{5.3b}$$

Thus, to compute $\overline{v}$ at a given $z$ in the quantum model, Eq. (5.2a) must be integrated in time, from $\tau = 0$ to $\tau = \tau_f$, with the electric field $\mathcal{E}(z, \tau)$ at that $z$ and an initial condition $\psi(x, z, 0) = \psi_0(x, z)$. With the solution $\psi(x, z, \tau)$ in hand, $\overline{v}$ may be evaluated with Eq. (5.2b), and the field equation Eq. (5.1) may be advanced in $z$. In the classical model, on the other hand, $\overline{v}$ is obtained by integrating Eq. (5.2a) from $\tau = 0$ to $\tau = \tau_f$ with initial condition $f(x, v, z, \tau) = f_0(x, v, z)$ and applying Eq. (5.3b). Neither the Liouville equation nor the Schrödinger equation have analytical solutions in this case, so we integrate them numerically using the methods described in Sec. 5.3.

*Unidirectional pulse with two-dimensional atoms*

For the propagation of a unidirectional linearly-polarized pulse through a two-dimensional model atom, the propagation equation becomes

$$\partial_z \mathcal{E} = \frac{2\pi\rho}{c}\overline{v}_x(z,\tau), \tag{5.4}$$

where $\overline{v}_x$ is the $x$ component of the dipole velocity. Here, we only consider the quantum model, where now the electronic wave function is $\psi(x,y,z,\tau)$. Its equation of motion and the dipole velocity are given by

$$i\partial_\tau \psi = \left[-\frac{1}{2}(\partial_x^2+\partial_y^2) + V(x,y) + \mathcal{E}(z,\tau)x\right]\psi, \tag{5.5a}$$

$$\overline{v}_x(z,\tau) = \overline{v}_{x,0}(z) - \int_0^\tau \left[\mathcal{E}(z,\tau') + \int \partial_x V |\psi(x,y,z,\tau')|^2 \mathrm{d}x\mathrm{d}y\right]\mathrm{d}\tau', \tag{5.5b}$$

where now the potential is $V(x,y) = -(x^2+y^2+2)^{-1/2}$.

*Forward- and backward- propagating waves with one-dimensional atoms*

In deriving Eq. (5.1), one of the assumptions invoked in the reduction process is that backward-propagating waves are negligible. In Sec. 5.6, we provide evidence that this hypothesis is met by investigating the behavior of a model that does contain backward-propagating waves. Here, the total electric field becomes $E(z,t) = \alpha(z,t)+\beta(z,t)$, where $\alpha$ and $\beta$ are the forward- and backward- propagating waves, respectively, and we remain in the lab frame. The Hamiltonian formulation (4.33) provides the most convenient form of the field propagation equations,

$$\dot{\alpha} = -c\partial_z\alpha + 2\pi\rho\overline{v}, \tag{5.6a}$$

$$\dot{\beta} = c\partial_z\beta + 2\pi\rho\overline{v}. \tag{5.6b}$$

We have neglected the $x$ subscript for the dipole velocity because we shall only consider one-dimensional atoms here. Further, we shall use the classical model, for which the Liouville equation is

$$\dot{f} = -v\partial_x f + \left[\partial_x V + \alpha(z,t) + \beta(z,t)\right]\partial_v f. \tag{5.7}$$

### 5.2.2 Observables

We will assess the behavior of the models by looking at the electric field energy, electron energy, instantaneous carrier frequency, and high-harmonic spectrum throughout propagation. Because the field spectrum is typically dominated by a narrow range of frequencies around the laser fundamental $\omega_L$, even after propagation, the field energy and instantaneous carrier frequency mainly reflect this part of the spectrum. We define the time-averaged field energy density in the moving frame as

$$U_{\mathrm{EM}}(z) = \frac{1}{4\pi\tau_f}\int_0^{\tau_f} \mathcal{E}(z,\tau)^2 \mathrm{d}\tau. \tag{5.8}$$

In the lab frame, the conservation of energy allows one to relate the instantaneous field energy to the instantaneous electron energy. This is not possible in the moving frame, but nevertheless the change in $U_{\mathrm{EM}}(z)$ may be related to the change in particle energy using Eq. (5.1). In particular, multiplying both sides by $\mathcal{E}$ yields

$$\partial_z\left(\frac{\mathcal{E}^2}{4\pi}\right) = \frac{\rho}{c}\overline{v}(z,\tau)\mathcal{E}(z,\tau). \tag{5.9}$$

This equation provides a local energy conservation law in the moving frame, analogous to Poynting's theorem, stating that the change in the field energy density is equal and opposite to the power $-\rho\overline{v}\mathcal{E}$ supplied by the field to the electrons. Integrating Eq. (5.9) over $\tau$ yields

$$\partial_z U_{\mathrm{EM}} = \frac{\rho}{c\tau_f}\int_0^{\tau_f} \overline{v}(z,\tau)\mathcal{E}(z,\tau)\mathrm{d}\tau = -\frac{\rho}{c\tau_f}\Delta\overline{E}(z), \tag{5.10}$$

where $\Delta\overline{E}(z) \equiv \overline{E}(z,\tau_f) - \overline{E}(z,0)$ is the change in mean electron energy between times $\tau = 0$ and $\tau = \tau_f$ for the electrons located at $z$. For the quantum model, the mean electron energy $\overline{E}$ is defined as the expectation value of the electron Hamiltonian operator in the absence of the electric field,

$$\overline{E}(z,\tau) = \int \psi^*(x,\tau;z)\left[-\frac{1}{2}\partial_x^2 + V(x)\right]\psi(x,z,\tau)\mathrm{d}x. \tag{5.11}$$

Meanwhile, in the classical model it is defined as the ensemble-average of the corresponding classical electron energy $H_0(x,v) = \frac{v^2}{2} + V(x)$, i.e.

$$\overline{E}(z,\tau) = \int H_0(x,v) f(x,v,z,\tau)\mathrm{d}x\mathrm{d}v. \tag{5.12}$$

In practice, Eq. (5.11) may be inconvenient to implement, because part of the electronic wave function typically escapes outside of the finite computational domain on which $\psi$ is defined due to ionization. Thus, $\overline{E}(z,\tau_f)$ does not account for the energy of this part of the wave function and therefore underestimates the true electron energy. This effect can be mitigated by choosing large enough computational domains. On the other hand, this drawback is not present for the implementation of Eq. (5.12) because the numerical scheme we choose for solving the Liouville equation consists of integrating the electron trajectories, i.e. the characteristics of Eq. (5.3a) (see Sec. 5.3).

For computing the instantaneous carrier frequency, we use the Wigner-Ville transform [147] of the electric field

$$W(\tau,\omega;z) = \frac{1}{\pi}\int_{-\infty}^{\infty} \hat{\mathcal{E}}^*(z,\tau-\tau')\hat{\mathcal{E}}(z,\tau+\tau')e^{-2i\omega\tau'}\mathrm{d}\tau', \tag{5.13}$$

where the asterisk denotes the complex conjugate and $\hat{\mathcal{E}}(z,\tau)$ is the analytic representation of the field $\mathcal{E}(z,\tau)$. The analytic representation is, roughly speaking, the inverse Fourier

transform of the positive-frequency part of a function's Fourier transform, i.e.

$$\hat{\mathcal{E}}(z,\tau) = \frac{1}{\pi}\int_0^\infty \tilde{\mathcal{E}}(z,\omega)e^{i\omega\tau}\mathrm{d}\omega, \text{ where}$$
$$\tilde{\mathcal{E}}(z,\omega) = \int_{-\infty}^\infty \mathcal{E}_p(z,\tau)e^{-i\omega\tau}\mathrm{d}\tau.$$

Here, $\mathcal{E}_p$ refers to the field $\mathcal{E}$ after post-processing, which may be necessary to perform a meaningful Fourier analysis. For instance, post-processing may consist of windowing the field with the function $w(\tau)$, in which case $\mathcal{E}_p(z,\tau) = \mathcal{E}(z,\tau)w(\tau-\tau_c)$. We specify the post-processing applied for each example we consider.

The analytic representation, itself complex, is a useful representation of the real field because it satisfies $\mathcal{E}_p(z,\tau) = \mathrm{Re}[\hat{\mathcal{E}}(z,\tau)]$. Thus, it naturally decomposes the field into its amplitude, $|\hat{\mathcal{E}}(z,\tau)|$, and phase, $\arg[\hat{\mathcal{E}}(z,\tau)]$ [147]. The Wigner transform (which uses $\mathcal{E}$ instead of $\hat{\mathcal{E}}$ in Eq.(5.13)) has proven effective at analyzing frequency-related propagation effects [145, 148], and we have found that the Wigner-Ville transform is even better suited to this task, especially in the case where $\mathcal{E}$ contains multiple frequency components. At a given $z$, $W(\tau,\omega;z)$ provides information on the frequency content of $\mathcal{E}$ at time $\tau$. When $\mathcal{E}$ consists of multiple frequency components, $W(\tau,\omega;z)$ will typically contain several peaks for at a given $\tau$, one for each component. The instantaneous carrier frequency $\omega_c(z,\tau)$ is defined as the frequency such that $W(\tau,\omega_c;z)$ is the maximum for a finite interval of frequencies near $\omega_L$, the dominant frequency component of the field [148]. Further, we define the maximum instantaneous carrier frequency as $\omega_{\max}(z) = \max_\tau \omega_c(z,\tau)$.

We assess high harmonic generation using several methods. On the field side, we evaluate the field spectrum $|\tilde{\mathcal{E}}(z,\omega)|^2$ throughout propagation. Also, to understand the coherent buildup of radiation in a particular frequency band $[\omega_a,\omega_b]$, we track the evolution of the frequency-filtered analytic field [44], i.e.

$$\hat{\mathcal{E}}_{ab}(z,\tau) = \frac{1}{\pi}\int_{\omega_a}^{\omega_b} \tilde{\mathcal{E}}(z,\omega)e^{i\omega\tau}\mathrm{d}\omega. \tag{5.14}$$

On the particle side, we study the evolution of the spectrogram of the dipole acceleration $d_a(\tau) = -\overline{\partial_x V}(\tau)$ in the quantum model, which provides information on the time-frequency properties of the emission [56, 149]. These spectrograms may be related to the statistics of recollisions in the classical model [91]. We monitor recollisions by computing a quantity $R(\kappa, \tau; z)$ that we call the recollision flux. This quantity is a measure of the probability of a recollision with kinetic energy $\kappa$ occurring at time $\tau$ for the atoms at $z$, and is defined

$$R(\kappa, \tau; z) = \int f(x, v, z, \tau)\Theta(x_c - |x|)\Theta(\kappa_c - |v^2/2 - \kappa|)\,\mathrm{d}x\mathrm{d}v, \tag{5.15}$$

where $\Theta$ is the Heaviside step function. We take $x_c = 5$ a.u. and adjust $\kappa_c$ based on the kinetic energy scale of a given simulation. To gain deeper insight into the classical dynamics, we also visualize $f(x, v, z, \tau)$ itself and examine the electron trajectories which underlie it.

## 5.3 Numerical methods

### 5.3.1 Schrödinger equation

The TDSEs (5.2a) and (5.5a) were solved using a second-order operator splitting scheme [150]. Derivatives of the wave function with respect to the electron position (i.e. for the application of the momentum and kinetic energy operators) were performed in the Fourier domain. Absorbing boundary conditions were employed [151], consisting of sending the wave function smoothly to zero within $32$ a.u. of each domain boundary using a $\cos^{1/8}$ function. For the 1D case, the computational domain selected was $x \in [-1800, 1800]$ a.u., discretized with a spatial step size of $\Delta x = 5/16$ a.u. A fixed time-step of $\Delta\tau = 0.1$ a.u. was used. We verified that for this set of integration parameters, the high-harmonic spectrum of a single atom in an external, monochromatic field (the one used as the initial field in Sec. 5.5.1) was converged. That is, we compared the dipole velocity spectrum with

these parameters to a spectrum calculated with either (i) a larger domain, (ii) a smaller $\Delta x$, or (iii) a smaller $\Delta\tau$, and each of these was indistinguishable from the spectrum with the above set of parameters. For the 2D case, the computational domain selected was $(x, y) \in [-450, 450] \times [-300, 300]$ a.u., discretized with a spatial step size of $\Delta x = \Delta y = 7/16$ a.u. A fixed time-step of $\Delta\tau = 0.1$ a.u. was used. These parameters were determined to give an almost-converged spectrum for a single atom in an external field, but they were used nevertheless because a more accurate calculation would have taken too long.

### 5.3.2 Liouville equation (unidirectional pulse case)

To solve Liouville Eq. (5.3a), we employ the particle-in-cell (PIC) scheme described in [110]. In a nutshell, the distribution function $f(x, v, z, \tau)$ at a fixed $z$ is discretized at $\tau = 0$ on a uniform grid in phase space, and subsequently each grid point follows the characteristics, or particle trajectories, of Eq. (5.3a). More precisely, we represent $f$ by $N$ particles with trajectories $(x_j(z, \tau), v_j(z, \tau))$, such that

$$f(x, v, z, \tau) = \sum_{j=1}^{N} w_j \delta(x - x_j(z, \tau))\delta(v - v_j(z, \tau)). \tag{5.16}$$

The particle trajectories obey the equations of motion of a classical electron in the combined Coulomb and laser fields, i.e.

$$\partial_\tau x_j = v_j, \tag{5.17a}$$

$$\partial_\tau v_j = -\partial_x V(x_j) - \mathcal{E}(z, \tau). \tag{5.17b}$$

These may be derived from the single-particle time-dependent Hamiltonian

$$H(x, v, z, \tau) = \frac{v^2}{2} + V(x) + \mathcal{E}(z, \tau)x, \tag{5.18}$$

where $x$ and $v$ are canonically conjugate and $z$ acts as a label. Taking advantage of the fact that Hamiltonian (5.18) is separable into kinetic and potential energy terms, we compute the trajectories $(x_j(z,\tau), v_j(z,\tau))$ using a third-order explicit symplectic scheme [100]. We used a fixed time-step of $\Delta\tau = 0.1$ a.u., as in the quantum case. This value of $\tau$ allows a point-wise comparison of the electric fields computed in the classical and quantum models, and we verified that the single-atom dipole velocity spectrum for an external monochromatic field (again, the initial field of Sec. 5.5.1) with this $\Delta\tau$ is converged.

Because $\mathcal{E}(z,\tau)$ is computed numerically at every $z$ by solving Eq. (5.1), it is only known at discrete values of $\tau$. In other words, an explicit expression for $\mathcal{E}(z,\tau)$ that may be evaluated at any $\tau$ is unavailable. On the other hand, the scheme used for obtaining $(x_j(z,\tau), v_j(z,\tau))$ requires the evaluation of $\mathcal{E}(z,\tau)$ at times in between adjacent time steps. To compute these values, it is ideal to discretize $\mathcal{E}(z,\tau)$ with the same time steps as those used in the trajectory calculation, with spacing $\Delta\tau$. Then, intermediate values are obtained by quadratic interpolation of $\mathcal{E}(z,\tau)$ using the values of $\mathcal{E}(z,\tau)$ at the nearest available time steps. That is, when advancing the trajectories from $\tau_m$ to $\tau_m + \Delta\tau$, the requisite intermediate-time values of $\mathcal{E}$ are obtained by quadratic interpolation of $\mathcal{E}(z,\tau_m - \Delta\tau)$, $\mathcal{E}(z,\tau_m)$, and $\mathcal{E}(z,\tau_m+\Delta\tau)$. Quadratic interpolation provides the intermediate values of $\mathcal{E}$ to second-order accuracy in $\Delta\tau$, which is sufficiently accurate to retain the third-order accuracy of the time integration scheme.

In Eq. (5.16), trajectory $j$'s contribution to $f$ is weighted by $w_j$, which is determined by the trajectory's initial condition $(x_j(z,0), v_j(z,0))$ and the initial distribution function $f_0(x,v)$. $N$ of these initial conditions are selected from a uniform, equally-spaced grid of points on the $(x,v)$ phase space. The boundaries of this grid are selected such that $f_0$ is sufficiently large (i.e. non-negligble) for points within the boundaries, and the initial conditions $(x_j(z,0), v_j(z,0))$ kept are those within the boundaries of the grid and with $f_0(x_j(z,0), v_j(z,0)) > 0$. Hence, $N$ depends on how many points are contained in the area of the grid where $f_0(x,v) > 0$. In practice, we estimate the necessary resolution of

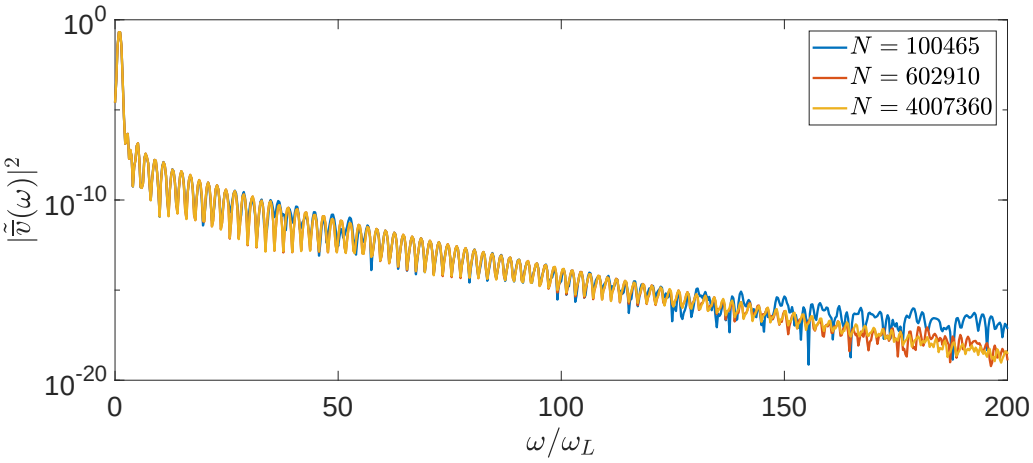


Figure 5.2: Convergence of the classical dipole velocity spectrum with increasing $N$. A $\sin^4$ window was applied to $\overline{v}(\tau)$ prior to the calculation of the power spectrum. Each curve corresponds to a different value of $N$ used in the discretization Eq. 5.16 of the distribution function.

our grid such that the number of grid cells in the nonzero-$f_0$ area is approximately equal to a target number of trajectories $N_{\text{goal}}$. We typically choose a nice, round number for $N_{\text{goal}}$, and this yields an actual number $N$ of trajectories which is close to $N_{\text{goal}}$. For example, the values of $N$ reported in the legend of Fig. 5.2 correspond to $N_{\text{goal}} = 10^5$, $N_{\text{goal}} = 6 \times 10^5$, and $N_{\text{goal}} = 4 \times 10^6$, respectively. Finally, the weights are given by $w_j = f_0(x_j(z,0), v_j(z,0))/\mathcal{N}$, where $\mathcal{N} = \sum_j f_0(x_j(z,0), v_j(z,0))$ is a normalization constant. Selecting the initial conditions on a uniform grid, rather than performing a Monte-Carlo simulation, leads the spectrum of the dipole velocity $\overline{v}(z,\tau)$ to converge more quickly with increasing $N$ [129].

The choice of $N$ determines how many harmonics are accurately resolved by the classical calculation. In Fig. 5.2, we show classical dipole velocity spectra obtained from the solution of Eq. (5.3a) with different values of $N$. The calculation was performed with the initial electric field $\mathcal{E}_0(\tau)$ and the electron initial conditions $f_0(x,v)$ of the scattering experiment (see Sec. 5.5.1). Increasing $N$ is equivalent to increasing the fineness of the grid from which the particle initial conditions are sampled from, because we make the boundaries of the grid independent of $N$. Naturally, this should improve the representation of

the distribution function. As a consequence, we see in Fig. 5.2 that more and more harmonics are converged as $N$ increases. Comparing the spectrum for $N = 100465$ to the one with $N = 602910$, we see that they are in agreement up until about $25\omega_L$, after which there are some deviations from $25$–$60\omega_L$ and significant deviations for $\omega > 120\omega_L$. This indicates that the spectrum with $N = 100465$ is converged up until about $25\omega_L$. Similarly, the $N = 602910$ spectrum is seen to be converged up to about $135\omega_L$ by comparison with the $N = 4007360$ spectrum. Evidently, a very large number of particles is required to accurately calculate the high harmonics in the classical model, which however are of very low intensity. Unless stated otherwise, the calculations presented in this chapter employ $N_{\text{goal}} = 10^5$, which for the scattering-propagation experiment would correspond to $N = 100465$.

### 5.3.3 Unidirectional pulse equation

The numerical methods of the previous sections are used to evaluate $\overline{v}$, which is the source term of the unidirectional pulse-propagation equation (5.1) in the moving frame. Hence, given $\mathcal{E}(z,\tau)$, we can calculate $\overline{v}(z,\tau)$ and advance the electric field in space by $\Delta z$ to obtain $\mathcal{E}(z+\Delta z,\tau)$. To do this, we discretize $\mathcal{E}(z,\tau)$ by Fourier transform, i.e.

$$\tilde{\mathcal{E}}_k(z) = \frac{1}{\tau_f}\int_0^{\tau_f} \mathcal{E}(z,\tau)\exp\left[-i\left(\frac{2\pi k}{\tau_f}\right)\tau\right]\mathrm{d}\tau. \tag{5.19}$$

for integer values of $k$. We take $|k| \leq k_{\max}$, where $k_{\max}$ depends on the number of time steps $n = \lfloor \tau_f/\Delta\tau \rfloor$ used in the time-discretization of Eqs. (5.2a) or (5.3a). It is given by

$$k_{\max} = \begin{cases} n/2 & \text{for } n \text{ even,} \\ (n-1)/2 & \text{for } n \text{ odd.} \end{cases} \tag{5.20}$$

Applying the Fourier transform to both sides of (5.1), we obtain

$$\partial_z \tilde{\mathcal{E}}_k = \frac{2\pi\rho}{c}\tilde{\overline{v}}_k(z) \tag{5.21}$$

for each $k$. Hence, we have converted the PDE (5.1) into a finite set of coupled ODEs (5.21). We solve this system of ODEs using the two-step implicit Adams-Moulton method in Predict-Evaluate-Correct-Evaluate (PECE) mode [152], which is of third-order accuracy in the spatial step $\Delta z$. Justification for the use of this method is provided in the next subsection. In order to evaluate $\overline{v}(z,\tau)$, one needs the electric field at the discrete time positions $\tau_m = m\Delta\tau$, which is obtained directly from the discrete inverse-Fourier transform of $\tilde{\mathcal{E}}_k(z)$.

As an aside, we remark that it is important to use local interpolation, such as the quadratic interpolation described in Sec. 5.3.2, to obtain the values of $\mathcal{E}(z,\tau)$ in between time steps, rather than evaluating the discrete inverse-Fourier transform at intermediate times. That is, one may construct an approximation to $\mathcal{E}(z,\tau)$ from the finite set Fourier components of $\mathcal{E}$, as

$$\mathcal{E}(z,\tau) \approx \sum_{|k|\leq k_{\max}} \tilde{\mathcal{E}}_k(z)\exp\left[i\left(\frac{2\pi k}{\tau_f}\right)\tau\right]. \tag{5.22}$$

In principle, one could then use this approximation to obtain $\mathcal{E}(z,\tau)$ at arbitrary times, including the intermediate times required for the integration of Eq. (5.3a). However, in general, $\mathcal{E}(z,\tau)$ is not periodic on its domain $\tau \in [0,\tau_f]$, and as a result, Eq. (5.22) exhibits Gibbs oscillations. This leads to incorrect approximations of $\mathcal{E}(z,\tau)$ at values in between the time steps, especially near $\tau = 0$ and $\tau = \tau_f$. This issue may be successfully avoided by using local interpolation of the field.

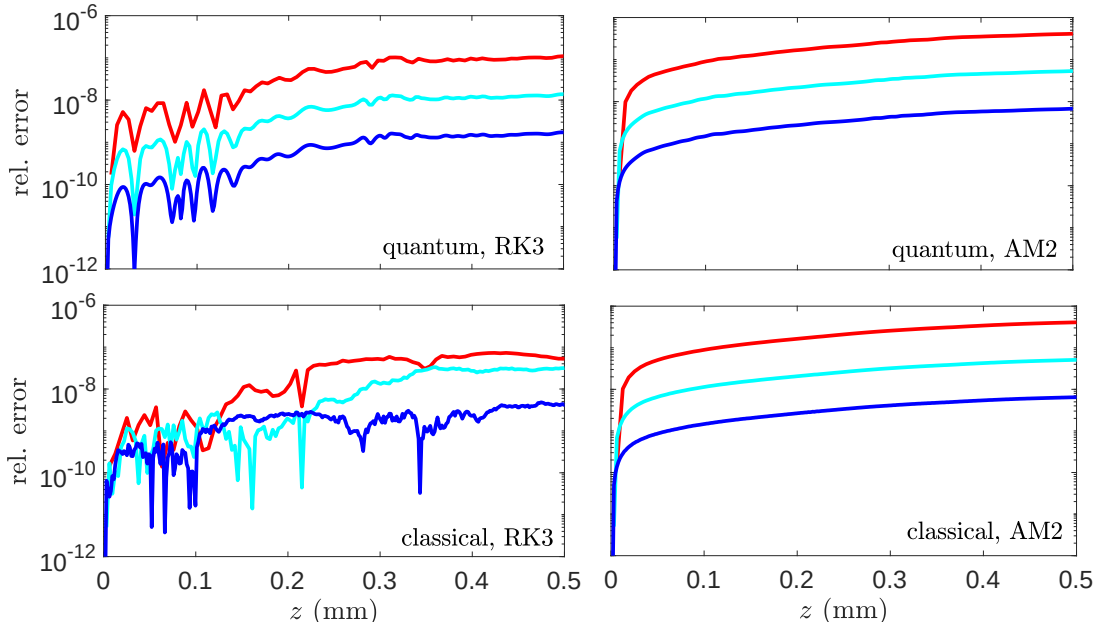


Figure 5.3: Comparison of the relative energy error for the propagation simulations with a third-order Runge-Kutta scheme (RK3) and the two-step Adams-Moulton scheme (AM2). The scattering-propagation experiment setup was used for the field and particle initial conditions. Each curve was computed with a different $\Delta z$. Red curves: $\Delta z = (21/4)\lambda_L = 6.33$ $\mu$m. Cyan curves: $\Delta z = (21/8)\lambda_L = 3.16$ $\mu$m. Blue curves: $\Delta z = (21/16)\lambda_L = 1.58$ $\mu$m. For the classical calculation, $N \approx 6 \times 10^5$ particles were used for the solution of the Liouville equation.

*Verification*

Here, we present evidence for the accuracy of our numerical computations. In the moving frame, there are no conserved quantities, but we can build one using Eq. (5.10). We augment our system of equations (5.21) for the field modes with an equation for a variable $h(z)$ representing the mean field energy density, satisfying

$$\partial_z h = \frac{\rho}{c\tau_f} \int_0^{\tau_f} \overline{v}(z,\tau)\mathcal{E}(z,\tau)\mathrm{d}\tau. \tag{5.23}$$

Hence, $h(z) - U_{\mathrm{EM}}(z)$ should be conserved during propagation, where $U_{\mathrm{EM}}(z)$ is computed using Eq. (5.8). Specifically, the integrand of Eq. (5.8) is discretized at times $\tau_m = m\Delta\tau$, with the values of the field $\mathcal{E}(z,\tau_m)$ obtained by discrete inverse-Fourier transform of the modes $\{\tilde{\mathcal{E}}_k\}$, and it is summed using the trapezoidal rule. The right-hand side of (5.23) is computed similarly. We take $h(0) = U_{\mathrm{EM}}(0)$ and monitor the accuracy of our simulations through the error $|h(z) - U_{\mathrm{EM}}(z)|/h(0)$.

The error for the quantum and classical models is plotted in Fig. 5.3 for simulations in the scattering-propagation experiment setup (see Sec. 5.5.1) for different values of $\Delta z$. The values of $\Delta z$ are reported in the caption of Fig. 5.3, where $\lambda_L = 2\pi c/\omega_L$ is the wavelength of the incident field. We also compare the behavior of a third-order Runge-Kutta method (RK3) [152] with the two-step Adams-Moulton method (AM2) employed throughout this chapter. We use the RK3 method here because it is of the same order as the AM2 method. These plots show that $h(z) - U_{\mathrm{EM}}(z)$ is a good indicator for the numerical accuracy of our computations, in the sense that the error in the conservation of this quantity has the expected scaling with $(\Delta z)^3$: when $\Delta z$ is divided by $2$, the error goes down by a factor of $8$. This scaling is observed in all cases, except the classical RK3 case. In general, the behavior of the energy error for the AM2 method–a gradual growth at a constant rate–is more typical than the behavior of the error for the RK3 method, which exhibits some erratic oscillations. The cause of this behavior for the RK3 method is unclear, and may be

a sign of stiffness of the model equations. Also, while both methods have a comparable error for each $\Delta z$, the AM2 method only requires two evaluations of $\overline{v}(z,\tau)$ for each space step (in PECE mode), compared to three for the RK3 method. Because evaluating $\overline{v}(z,\tau)$ is the computationally-expensive step of solving the model equations, this is a significant advantage of AM2. For these reasons, we selected the AM2 method for the integration of the model equations.

Next, we check the convergence of our calculations for the spectrum of $\mathcal{E}$ after propagation to a given $z$. Figure 5.4 shows the spectra of $\mathcal{E}(z,\tau)$ at $z = 0.5$ mm in the quantum and classical models, with each of the $\Delta z$ of Fig. 5.3 used for propagation. In both calculations, we see that the spectra are in good agreement for each $\Delta z$, indicating that this range of $\Delta z$ is small enough to obtain converged results. Furthermore, we see in both cases that the spectra are indistinguishable up to a particular high frequency, after which the differences between the spectra with different $\Delta z$ are visible. For the quantum case, this frequency is $\omega \approx 170\omega_L$, near the high harmonic cutoff, where the spectrum with $\Delta z = (21/4)\lambda_L$ (red curve) is seen to depart from the spectra computed with smaller $\Delta z$ (cyan and blue curves). The calculations with $\Delta z = (21/8)\lambda_L$ and $\Delta z = (21/16)\lambda_L$ are indistinguishable from each other, indicating that the quantum calculation has converged with $\Delta z = (21/8)\lambda_L$. Meanwhile for the classical case, $\omega \approx 80\omega_L$ is the frequency where the $\Delta z = (21/4)\lambda_L$ spectrum begins to depart from the other two spectra. Further, the $\Delta z = (21/8)\lambda_L$ spectrum is only in excellent agreement with the $\Delta z = (21/16)\lambda_L$ spectrum up until $\omega \approx 100\omega_L$, after which some small deviations are visible. Thus, the classical calculation is not completely converged with respect to $\Delta z$ for these frequencies. Note that here, $N \approx 6 \times 10^5$ particles were used in the classical calculation, indicating that the Liouville equation is converged up to $\omega \approx 135\omega_L$, as shown in Fig. 5.2. Thus, while we cannot draw any conclusions about frequencies greater than $135\omega_L$, we can say that the frequencies from 100–$135\omega_L$ experience propagation dynamics on scales smaller than than those resolved by $\Delta z = (21/8)\lambda_L$. Nevertheless, the behavior of these high, very low-intensity

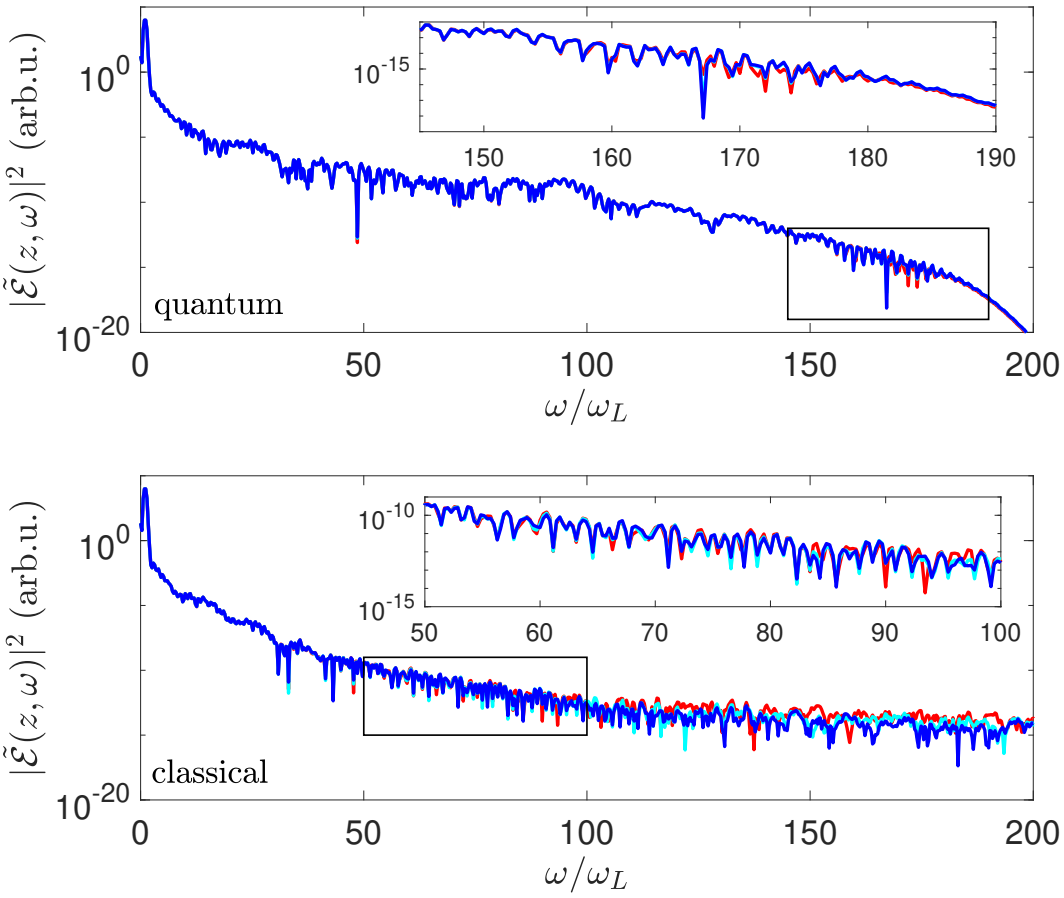


Figure 5.4: Comparison of the electric field spectra after propagation to $z = 0.5$ mm (using the two-step Adams-Moulton method). The scattering-propagation experiment setup was used for the field and particle initial conditions. A $\sin^4$ window was applied to $\mathcal{E}(z,\tau)$ prior to computation of the spectrum. The insets show magnifications of the rectangles, where the discrepancies between calculations with different $\Delta z$ begin to be observable. Red curves: $\Delta z = (21/4)\lambda_L = 6.33$ $\mu$m. Cyan curves: $\Delta z = (21/8)\lambda_L = 3.16$ $\mu$m. Blue curves: $\Delta z = (21/16)\lambda_L = 1.58$ $\mu$m. For the classical calculation, $N \approx 6 \times 10^5$ particles were used for the solution of the Liouville equation.

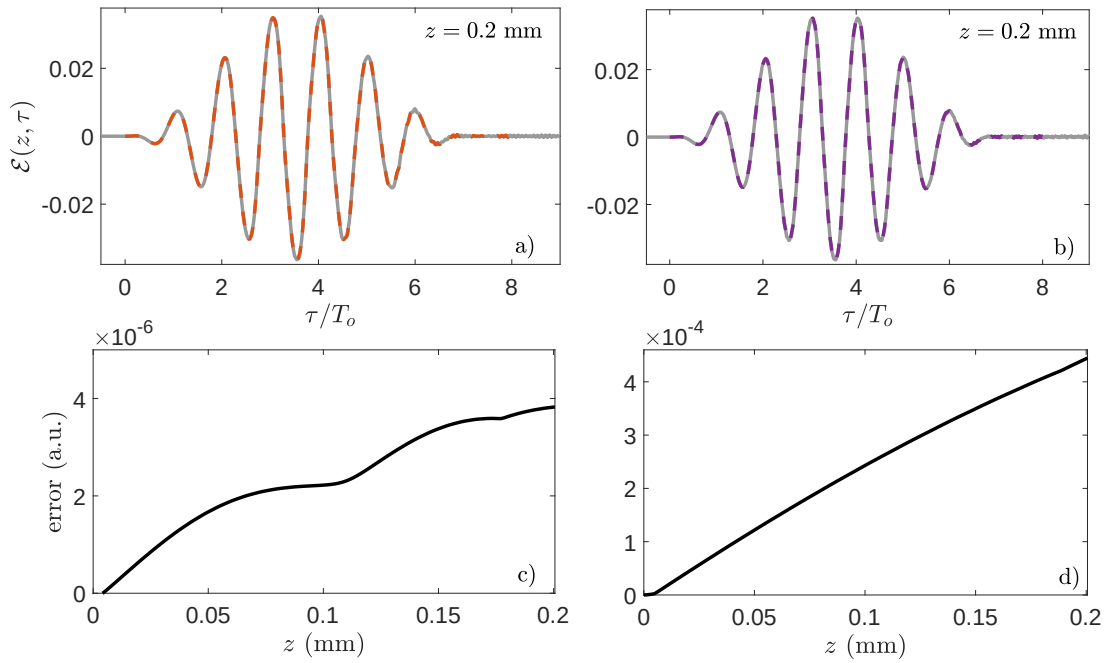


Figure 5.5: Effect of the time domain size on unidirectional pulse propagation with ground-state atoms. The upper panels show the electric field $\mathcal{E}(z,\tau)$ at $z = 0.2$ mm computed for for two different time domains. The grey curves are for the domain $\tau \in [-0.5T_o, 9T_o]$, and the dashed colored curves are the domain $\tau \in [0, 8T_o]$. The lower panels show the error (see text) between the fields in the two calculations as a function of $z$. a),c) Quantum model. b),d) Classical model.

harmonics does not seem to influence the lower frequency components of the field, because the latter are the same for each $\Delta z$. Therefore, we trust the results of the simulations for the lower, more intense harmonics in both the quantum and classical cases, even if we have not fully converged the highest harmonics. As we shall see in the following sections, it is the highest-intensity parts of the spectrum which are determinant for the electron dynamics.

We consider the effect of changing the time domain size for simulations in which a pulse propagates through atoms initiated in the ground state. If $\tau = 0$ is the time at which the incident pulse starts, meaning $\mathcal{E}(z,\tau) = 0$ for all $\tau < 0$, then extending the time domain over which the simulation takes places to values of $\tau < 0$ should not influence the results. For times $\tau$ that the field is zero, so too should be the dipole velocity $\overline{v}(z,\tau)$, so that $\partial_z \mathcal{E} = 0$. Also, if the atoms are in a stationary state before the onset of the laser pulse, then

we should have $\partial_\tau \psi = -iE\psi$ and $\partial_\tau f = 0$ in the quantum and classical cases, respectively, where $E$ is the energy of the quantum state. Thus, in theory, integrating the electron fields for times $\tau < 0$ should not influence their subsequent evolution. On the other hand, for a given final time $\tau_f$, changing the domain size to include times $\tau > \tau_f$ should not change the results for $\tau \leq \tau_f$. This is because, for an arbitrary time $\tau'$, $\overline{v}(z, \tau')$ depends on $\mathcal{E}(z, \tau)$ for all $\tau < \tau'$, but no $\tau \geq \tau'$.

Figure 5.5 shows the degree to which our numerical schemes respect these properties of the equations by comparing two different domain sizes: $\tau \in [-0.5T_o, 9T_o]$ on the one hand and $\tau \in [0, 8T_o]$ on the other. Here, $\rho = 2 \times 10^{19}$ cm$^{-3}$, $\Delta z = 1.6$ $\mu$m, and the initial conditions for the field and particles are those of Fig. 5.13. Figures 5.5a and 5.5b show that, overall, the fields from the two calculations are in agreement after propagation to $z = 0.2$ mm, for the times during which the domains overlap. Additionally, the field computed on the longer domain has remained zero for $\tau < 0$ throughout propagation. We define the error as $\max_\tau |\mathcal{E}_{\text{long}}(z, \tau) - \mathcal{E}_{\text{short}}(z, \tau)|$, where "long" and "short" refer to the fields calculated with the longer and shorter domains, respectively, and the maximum is taken over the time domain at which the two calculations overlap. This error is plotted in Figs. 5.5c and 5.5d. Note that we have subtracted off the error at $z = 0$, which is nonzero because the time steps in the two calculations were not exactly aligned. By the end of the simulations, the quantum model error relative to the peak amplitude of the incident field $E_0 = 0.0377$ a.u. is about $10^{-4}$, while for the classical model the relative error is about $10^{-2}$. In both cases, the errors are likely due to the deviations of numerical representations of the electron initial conditions $\psi_0(x)$ and $f_0(x, v)$ from true stationary states. This leads to differing electron fields at $\tau = 0$ in the long and short domain calculations. These errors may be reduced by reducing the time step $\Delta\tau$, and by reducing the spatial step $\Delta x$ in the quantum calculation or increasing the number of particles $N$ in the classical calculation.

### 5.3.4 Forward- and backward-propagating wave case

When we take backward propagating waves into account, we must solve Eqs. (5.6) coupled to Eq. (5.7), in the case of the classical model. Because we are in the lab frame, the scheme for solving these equations looks different than when we are in the moving frame. In that case, time and space integration are separated, i.e. we integrate the Liouville equation at a given $z$ over a length of time so that we may advance the fields to the next point in space. On the other hand, in the lab frame, we only perform time integration, i.e. the Liouville equation and the field equations are simultaneously advanced in time, and we need to account for the entire length of the $z$-domain at every time step. We will adopt the spatial discretization $z_m = m\Delta z$, with $m \in [-n_z + 1, n_z - 1]$ an integer. Hence, the total length of our domain is $L = (2n_z - 1)\Delta z$, discretized using $2n_z - 1$ points. Our reduction of the coupled system Eqs. (5.6) and (5.7) to a finite set of ODEs is described in the next two sections.

*Liouville equation*

For the discretization of the Liouville equation, we use a scheme similar to that described in Sec. 5.3.2. We will take the gas density as 0 for $z < 0$, and a constant $\rho$ for $z \geq 0$. Thus, we only need to consider the distribution function for $z \geq 0$. We generalize the PIC discretization used for $f$ in the unidirectional case, i.e. Eq. (5.16), by summing $n_z$ copies of the distribution function in that equation multiplied by a Dirac delta function at each $z_m$. Precisely, we take

$$f(x, v, z, t) = \Delta z \sum_{m=0}^{n_z-1} \sum_{j=1}^{N_p} w_j \delta(x - x_{jm}(t))\delta(v - v_{jm}(t))\delta(z - z_m). \tag{5.24}$$

At each $z_m \geq 0$, we have $N_p$ particles with trajectories $(x_{jm}(t), v_{jm}(t))$. For each $m$, we use the same set of $N_p$ initial conditions $(x_{jm}(0), v_{jm}(0))$ and weights $w_j$, which are selected

using the same scheme as in the unidirectional case. The particle trajectories satisfy

$$\dot{x}_{jm} = v_{jm}, \tag{5.25a}$$

$$\dot{v}_{jm} = -\partial_x V(x_{jm}) - \alpha(z_m) - \beta(z_m). \tag{5.25b}$$

*Field equations*

For the discretization of Eqs. (5.6), we use the Fourier transform, similarly to the moving frame. In this case, the discretization can be performed at the level of the Hamiltonian and Poisson bracket, as shown in Eqs. (4.56). Briefly, the dynamical variables for each field become the spatial Fourier modes $\{\alpha_k\}$ and $\{\beta_k\}$. We truncate the infinite set of Fourier modes such that we keep all modes with $k \leq |k_{\max}|$. Similarly to the moving-frame case, we determine $k_{\max}$ from our discretization of the $z$-axis. Because the $z$-axis is discretized using $2n_z - 1$ points, we have $k_{\max} = n_z$. The field equations of motion are then obtained from Hamiltonian (4.56a) and bracket (4.56b). They are

$$\dot{\alpha}_k = -i\omega_k \alpha_k + 2\pi \jmath_k, \tag{5.26a}$$

$$\dot{\beta}_k = i\omega_k \beta_k + 2\pi \jmath_k, \tag{5.26b}$$

where $\omega_k = 2\pi ck/L$ and $\jmath(z,t) = \rho(z)\overline{v}(z,t)$ is the current density, with spatial Fourier modes

$$\jmath_k(t) = \frac{1}{L}\int v\rho(z) f(x,v,z,t) \exp\left[-i\left(\frac{2\pi k}{L}\right) z\right] \mathrm{d}\mu \mathrm{d}z.$$

The values of the fields $\alpha(z_m)$ and $\beta(z_m)$ required for the particle equations (5.25) are obtained by the discrete inverse-Fourier transform of $\{\alpha_k\}$ and $\{\beta_k\}$, similarly to the moving-frame case.

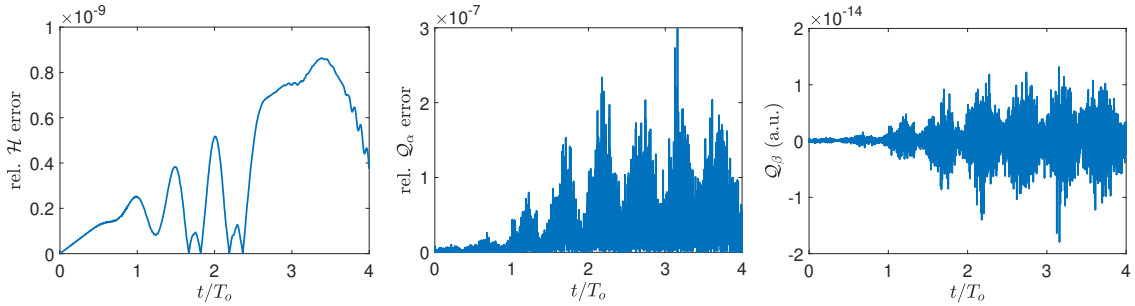


Figure 5.6: The time-dependence of the error in conserved quantities of the classical model with forward- and backward-propagation waves in the lab frame. Left panel: Relative error of the energy $\mathcal{H}(t)$. Middle panel: Relative error of the Casimir invariant $\mathcal{Q}_\alpha(t)$. Right panel: the Casimir invariant $\mathcal{Q}_\beta(t)$, for which $\mathcal{Q}_\beta(0) = 0$.

*Verification*

Equations (5.25) and (5.26) constitute a finite set of ODEs, which we integrate using the standard fourth-order Runge-Kutta method. We select $\Delta t = 0.1$ a.u., $\Delta z = c\Delta t$, and $N_p = 5048$, for a total of $n_z N_p = 25371248$ particles. We consider initial conditions in which $\beta(z, t = 0) = 0$, so that the initial field is solely forward propagating, and we take the initial field $\alpha(z, t = 0)$ such that the front of the pulse is at $z = 0$, but is zero for all $z \geq 0$. Under these conditions, this system can only be integrated until time $t = L/2c$, when the reflected waves, i.e. the backward-propagating waves generated at $z = 0$, first reach the left boundary of the computational domain. This is because our use of Fourier modes for the representation of the fields implies periodic boundary conditions. Thus, for times $t \geq L/2c$, the reflected waves would reappear at the right boundary and begin propagating through the gas, which is obviously unphysical.

Furthermore, these equations have inherited the Hamiltonian structure of Eqs. (5.7) and (5.6). The Hamiltonian structure of the field part of equations is contained in Eqs. (4.56). The Hamiltonian structure of the full system, in particular Eqs. (5.25), may be obtained from a discretization of Hamiltonian (4.56a) and bracket (4.56b) using Eq. (5.24) [110]. Thus, this system inherits the conserved quantities of the continuous system (4.56), namely the energy $\mathcal{H}$ [for the field part of the energy see Eq. (4.56a)] and the two Casimir invariants

$\mathcal{Q}_\alpha$ and $\mathcal{Q}_\beta$ [see Eqs. (4.57)]. The particle part of these quantities is obtained by substituting Eq. (5.24) into Eq. (4.25a). In Fig. (5.6), we show the error in the conservation of these quantities as a function of time for a simulation with the initial conditions described in Sec. 5.6.2. The relative error in the conservation of $\mathcal{H}$ is less than $10^{-9}$, while for $\mathcal{Q}_\alpha$ it is less than $3 \times 10^{-7}$. $\mathcal{Q}_\beta$, which is initially zero, remains less than $2 \times 10^{-14}$ a.u. throughout the simulation. These behaviors provide evidence of a proper numerical implementation of the model equations. However, we remark that the particle number of $N_p = 5048$ at each $z_m$ is not high enough to provide converged results for the radiated fields. Given that the total number of particles is $n_z N_p$, there is a limit to how much larger we can take $N_p$ while still maintaining reasonable computation times (and memory requirements). With this set of parameters, the calculation leading to Fig. 5.6 takes $9.44$ hours, running on a desktop computer with the evaluation of the right-hand side of the particle equations of motion (5.25) parallelized across $8$ cores with OpenMP. See Fig. 5.30 and the accompanying discussion for the manifestations of the lack of convergence of the simulations.

## 5.4 Unidirectional propagation through a gas of one-dimensional ground-state atoms

Here, we analyze the behavior of the reduced models for the propagation of a laser pulse through a gas of ground-state atoms. The initial conditions are plotted in Fig. 5.7. We take an incident laser pulse given by

$$\mathcal{E}_0(\tau) = \begin{cases} E_0 \sin^2(\frac{\pi\tau}{T_m}) \cos(\omega_L \tau) & \text{for } \ 0 < \tau < T_m, \\ 0 & \text{for } T_m < \tau < \tau_f, \end{cases}$$

where $E_0$ is the maximum field amplitude, $\omega_L$ is the laser frequency, and $T_m$ is the duration of the laser pulse. Here, we choose $\omega_L = 0.0378$ a.u., $T_m = 7T_o$, and $\tau_f = 8T_o$, where $T_o = 2\pi/\omega_L$ is one optical cycle. These values correspond to a laser wavelength $\lambda_L = 1.2$ $\mu$m, and a FWHM pulse duration of $T_m/2 = 14$ fs. Throughout this chapter,

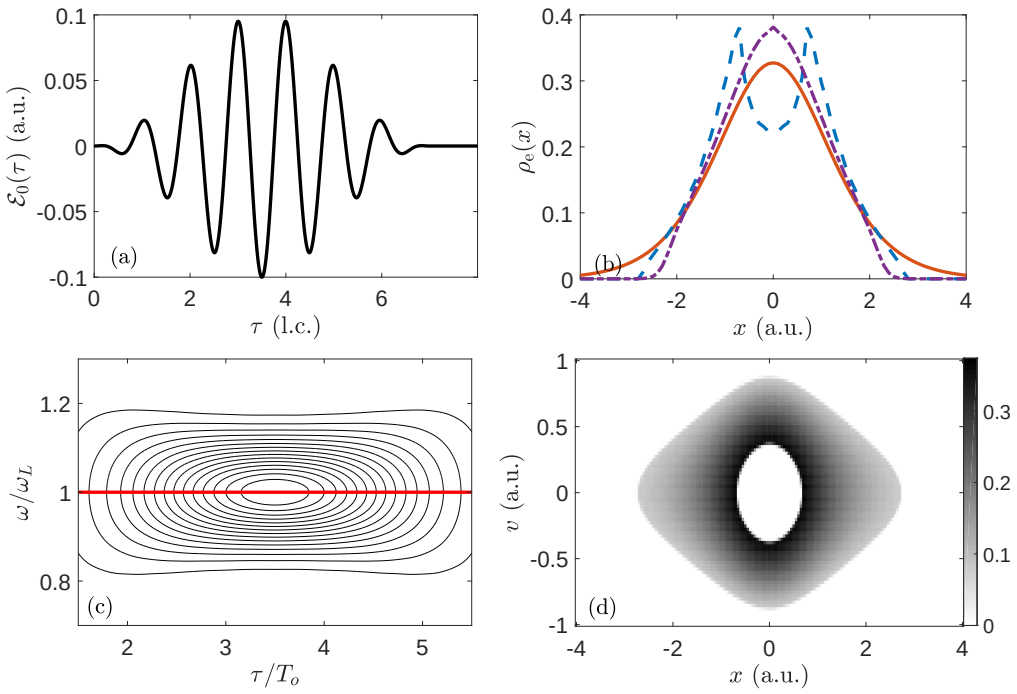


Figure 5.7: Initial conditions of the ground-state simulation. (a) Initial electric field $\mathcal{E}_0(\tau)$, with a peak intensity $I = 3.5 \times 10^{14}$ W $\cdot$ cm$^{-2}$. (b) Initial microscopic electron density $\rho_e(x)$. For the quantum model, $\rho_e(x) = |\psi_0(x)|^2$ is the orange solid curve, and for the classical model, $\rho_e(x) = \int f_0(x,v)\mathrm{d}v$. The blue dashed curve is the classical model with initial energy distribution $g_1$, while the classical model with $g_\sigma$ is the purple dash-dotted curve. (c) Contour plot of the Wigner transform $W(\tau,\omega)$ of the initial electric field. The red curve indicates the instantaneous carrier frequency $\omega_c(\tau)$. (d) Initial electron phase space distribution $f_0(x,v)$ for the classical model with $g_1$, with the probability density indicated by the linear color scale.

we employ this $\omega_L$ unless stated otherwise. We will consider positions of the laser pulse between $z = 0$ and $z = 1$ mm, where the gas is assumed to have a constant density $\rho$. Everywhere else is assumed to be vacuum, as illustrated in Fig. 5.1, and the field does not evolve in those regions.

For the quantum model, the initial state of the electron is taken as the ground state of Eq. (5.2a) in the absence of the electric field, with energy $I_p = -0.5$ a.u. [153],

$$\psi_0(x) = N_\psi(1 + \sqrt{x^2 + 2}) \exp\left[-\sqrt{x^2 + 2}\right],$$

where $N_\psi$ is a normalization constant. Note that we take $\psi_0$ to be independent of $z$, because the initial state of the atoms is assumed to be uniform.

For the classical model, a variety of options have been considered for designing a suitable initial phase space distribution $f_0(x, v)$ corresponding to the quantum ground state, given that it is not possible to obtain one in a strictly self-contained manner. If one is concerned with maximizing the quantitative agreement between the classical and quantum models, then the main difficulty is getting the classical model to exhibit a similar intensity-dependent ionization probability as the quantum model. In this respect, the most naïve option for the classical ground state—a microcanonical ensemble at the quantum ground-state energy $E = I_p$—does not perform well for the one-dimensional (1D) SAE model, in part because the onset of ionization occurs too suddenly [128, 154]. As an alternative, one can take a distribution of initial energies, $E \in [E_{\min}, E_{\max}]$ with a probability density $g(E)$, leading to a distribution function of the form

$$f_0(x, v) = \int_{E_{\min}}^{E_{\max}} g(E) N_E \delta(E - H_0(x, v)) \mathrm{d}E. \tag{5.27}$$

Meanwhile, $N_E$ is a normalization constant such that

$$N_E \int \delta(E - H_0(x, v)) \mathrm{d}x \mathrm{d}v = 1.$$

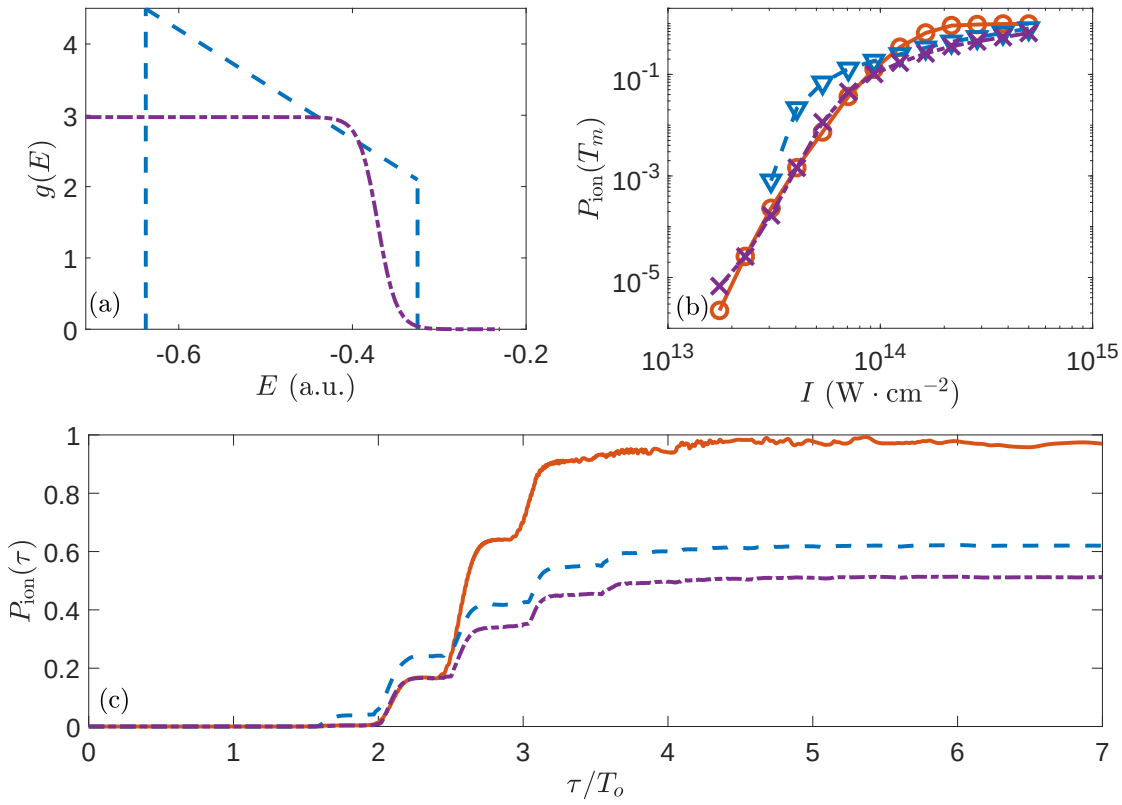


Figure 5.8: Classical energy distributions and ionization probability. (a) Distribution of initial energies $g(E)$ for the classical model. The distribution $g_1$, similar to that of Ref. [128], is the blue dashed curve, while the optimized sigmoid distribution $g_\sigma$ is the purple dash-dotted curve (see text). (b) Probability of ionization at the end of the laser pulse $P_{\rm ion}(T_m)$ as a function of the peak intensity $I$ of the incident pulse. The orange circles are the quantum calculation, the blue triangles are the classical calculation with $g_1$, and the purple crosses are the classical calculation with $g_\sigma$. (c) Time-dependent ionization probability for an incident pulse with peak intensity $I = 3.5 \times 10^{14}$ W · cm$^{-2}$. The solid orange curve is the quantum calculation.

Note that, because $f_0$ can be written as a function of $H_0$, which is conserved along a trajectory in the absence of the electric field, it is a stationary state of the field-free Liouville equation (5.3a).

In the first example, we shall take the energy range $E_{\rm min,1} = -0.638$, $E_{\rm max,1} = -0.325$, and the energy distribution $g_1(E) = a_0 + a_1 E$, with $a_1 = -7.656$ and $a_0$ chosen such that $g_1(E)$ is normalized to one. We choose this distribution because it is very close to the phase space distribution employed in Ref. [128], where it was shown to have reasonable agreement with the quantum model for the intensity-dependent ionization probability. It

also satisfies $\overline{E} = \int E g_1(E) \mathrm{d}E \approx I_p$, meaning the mean energy of the classical ensemble is equal to that of the quantum ground state. The energy distribution is plotted in Fig. 5.8a, in blue, and the corresponding phase space distribution is plotted in Fig. 5.7d. We define the time-dependent ionization probability $P_{\mathrm{ion}}(\tau)$ as the probability of finding the electron with $|x| > 10$ a.u. at time $\tau$ [44]. Then, the probability of the electron being ionized at the end of the pulse is $P_{\mathrm{ion}}(T_m)$. In Fig. 5.8b, we compare the variation of this quantity as a function of the peak-intensity $I$ of the incident laser pulse for the quantum model (orange circles) and the classical model with initial energy distribution $g_1$ (blue triangles). Evidently, for this laser frequency and pulse duration, there is much room for improvement in terms of the agreement between intensity-dependent ionization probabilities. This is seen across the range of intensities: at the lowest intensities, the classical model has no ionization; at intermediate intensities, it overestimates the ionization probability; at high intensity, it underestimates the ionization probability. We will see that it is possible to improve the agreement between the quantum and classical calculations by using another $g(E)$ for the classical model, for which the ionization probabilities are the purple crosses plotted in Fig. 5.8b.

### 5.4.1 High ionization fraction regime

Given these initial conditions, we simulate the propagation of the pulse from $z = 0$ to $z = 1$ mm for a gas with density $\rho = 5 \times 10^{17}$ cm$^{-3}$ using the quantum model and the classical model with initial energy distribution $g_1$. First, we will consider the high-ionization fraction regime. We choose the peak intensity of the incident pulse as $I = 3.5 \times 10^{14}$ W $\cdot$ cm$^{-2}$, corresponding to $E_0 = 0.1$ a.u. This gives an initial ionization probability, i.e. at $z = 0$, of $P_{\mathrm{ion}}(T_m) \sim 1$ for the quantum model and $P_{\mathrm{ion}}(T_m) \sim 0.6$ for the classical model, as shown in Fig. 5.8c. For the field integration, we select the spatial step $\Delta z = (21/8)\lambda_L = 3.16$ $\mu$m. We verified that with this spatial step size, the spectrum of the electric field after propagation was converged in both the quantum and classical

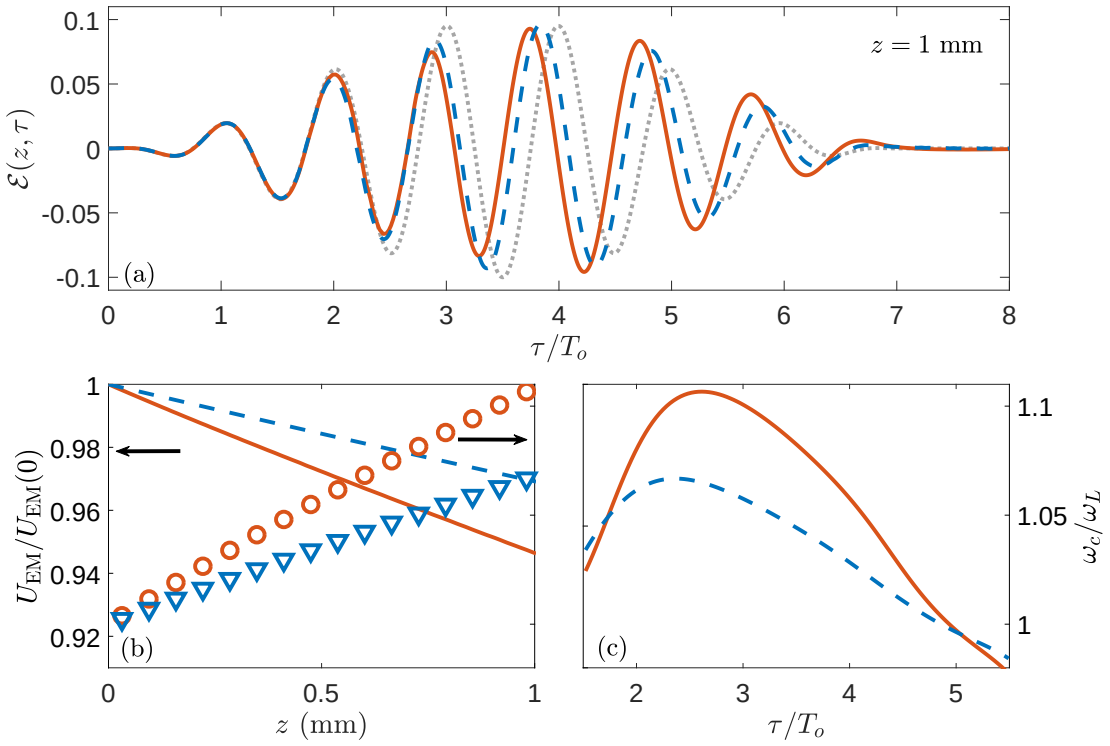


Figure 5.9: Results of pulse propagation through $1$ mm of ground-state atoms with density $\rho = 5 \times 10^{17}$ cm$^{-3}$, and peak incident pulse intensity $I = 3.5 \times 10^{14}$ W $\cdot$ cm$^{-2}$. The solid orange curves and circles correspond to the quantum model, while the blue dashed curves and triangles correspond to the classical model with $g_1$ as the initial energy distribution. (a) Time-dependent electric field $\mathcal{E}(z,\tau)$ at $z = 1$ mm. The dotted gray curve is the initial field $\mathcal{E}_0(\tau)$. (b) Normalized pulse energy density $U_{\rm EM}$ (curves, left axis) and maximum instantaneous carrier frequency $\omega_{\rm max}$ (markers, right axis) as a function of $z$. The scale of the right axis is the same as in (c). (c) Time-dependent carrier frequency $\omega_c(z,\tau)$ at $z = 1$ mm.

calculations. That is, reducing the spatial step size did not lead to significant changes to the spectrum, even the very low-intensity high-harmonic part.

In Fig. 5.9, we compare the electric fields $\mathcal{E}(z,\tau)$ at $z = 1$ mm computed from each model. We see the dominant propagation effects are captured by both models. Namely, we observe a variation in the field amplitudes compared to their initial values and a time-dependent blueshift [43, 133] in Fig. 5.9a. The field amplitudes are generally reduced during the laser cycles 2-4, when most of the ionization takes place (see Fig. 5.8c). Meanwhile, they are increased in the later cycles, when the high density of oscillating free electrons can provide energy to the field, as dicated by Eq. (5.9). Overall, we see that the field energy density $U_{\mathrm{EM}}$ decreases during propagation, as shown in Fig. 5.9b, due to the fact that ionized electrons have experienced a net increase in energy, in accordance with Eq. (5.10). The time-dependent blueshift is evidenced by the time-varying advance of the electric field wave crests with respect to $\mathcal{E}_0(\tau)$. The degree of the blueshift is well captured by the instantaneous carrier frequency $\omega_c(\tau, z)$, plotted in Fig. 5.9c, and its maximum in time $\omega_{\max}(z)$, also plotted in Fig. 5.9b.

While the classical and quantum calculations for these low-frequency observables are qualitatively similar, the quantitative agreement can be improved. Because these observables are driven by ionization and the interaction of ionized electrons with the field, the disagreement is likely due to the disagreement of intensity-dependent ionization probability between the classical and quantum models. We have explored mitigating this issue by searching for alternative initial energy distributions $g(E)$ for the classical model that lead to intensity-dependent ionization probabilities that are closer to the quantum calculation. Before presenting results on examples of such distributions, we present results of propagation simulations in the low ionization fraction regime for the quantum model and classical model with $g_1$. These simulations reveal another significant drawback of $g_1$ and suggest some guidelines for the shape of alternative distributions that will allow a good agreement between the quantum and classical propagation calculations over a range of incident peak

pulse intensities.

### 5.4.2 Low ionization fraction regime

Next, we simulate the propagation of a lower intensity laser pulse, with $I = 5 \times 10^{13}$ W $\cdot$ cm$^{-2}$, through $1$ mm of a gas with density $\rho = 2 \times 10^{19}$ cm$^{-3}$. This is the low ionization fraction regime, with the quantum model giving $P_{\text{ion}}(T_m) \sim 5 \times 10^{-3}$ and the classical model giving $P_{\text{ion}}(T_m) \sim 0.05$ for the incident pulse, as shown in Fig. 5.8b. We have increased the density compared to the previous simulation so that the maximum free-electron density, i.e. the density of ionized electrons, is comparable to the high ionization fraction case. For the field integration, we select the spatial step $\Delta z = 1.3\lambda_L = 1.57$ $\mu$m.

The results of the simulation are summarized in Fig. 5.10. Because of the much higher density of neutral atoms, the group velocity of the pulse is now noticeably less than $c$, which causes the pulse to drift to the right in the moving frame, as shown in Fig. 5.10a. Up until $z = 0.2$ mm, this effect is captured equally well by the quantum and classical calculations for $\tau/T_o < 3$, and the agreement between the fields for larger $\tau$ is fair. The classical field has a noticeable blueshift for larger $\tau$ and a much more substantial energy loss (Fig. 5.10b), both of which are signatures of the higher ionization fraction in the classical model.

However, for larger $z$, the classical calculation significantly departs from the quantum calculation. One symptom of the problem can be seen in Fig. 5.10b, where $U_{\text{EM}}(z)$ actually starts increasing at a certain propagation distance. By energy conservation, i.e. Eq. (5.10), this implies the mean electron energy must experience a net decrease. We can see the precursors to this behavior in Fig. 5.10d and Fig. 5.11a. In Fig. 5.10d, we have plotted the distribution of energies $E_f$ at the end of the pulse, computed from the distribution function $f(x, v, z, \tau_f)$ at $z = 0.2$ mm, shown in Fig. 5.11a. We see that states with energies lower than $E_{\text{min},1}$ become populated by the end of the pulse—these are the states inside the red ring in Fig. 5.11a. While this does not happen for the atoms at $z = 0$, such behavior manifests itself in the course of the pulse propagation. Further, the electron energy loss

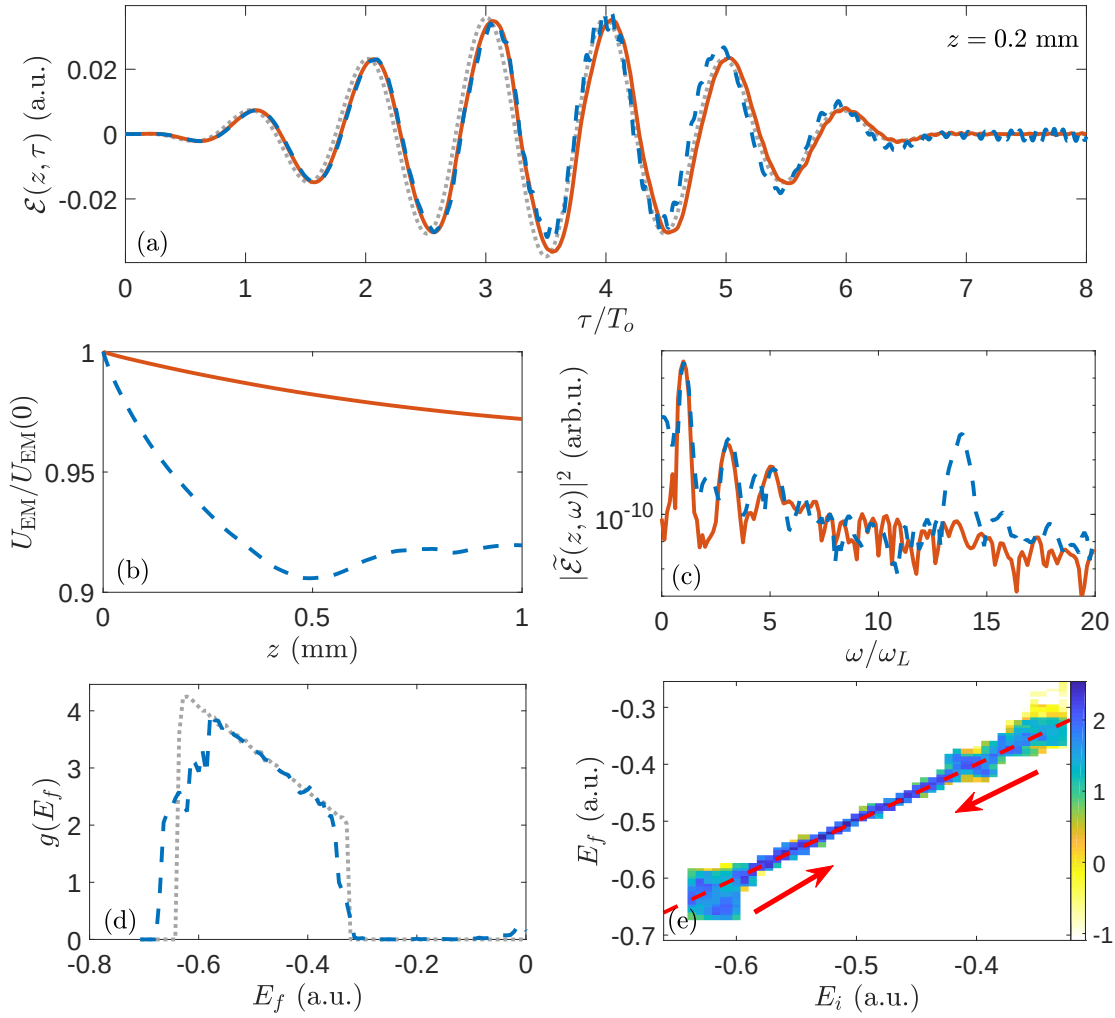


Figure 5.10: Results of pulse propagation through 1 mm of ground-state atoms with density $\rho = 2\times10^{19}$ cm$^{-3}$, with a peak incident pulse intensity of $I = 5\times10^{13}$ W$\cdot$cm$^{-2}$. The solid orange curves correspond to the quantum model, while the dashed blue curves correspond to the classical model with $g_1$ as the initial energy distribution. (a) Time-dependent electric field $\mathcal{E}(z,\tau)$ at $z = 0.2$ mm. The gray dotted curve is the initial field $\mathcal{E}_0(\tau)$. (b) Normalized time-averaged pulse energy density $U_{\rm EM}$ as a function of $z$. (c) Spectrum of the electric field $|\widetilde{\mathcal{E}}(z,\omega)|^2$ at $z = 0.2$ mm. A $\sin^2$ window was applied prior to computation of the spectrum. (d) Distribution of energies $g(E)$ at $\tau = \tau_f$ and $z = 0.2$ mm for the classical model. The gray dotted curve is the initial energy distribution $g_1(E)$. (e) Probability density for transitioning from a state with initial energy $E_i$ to a state with final energy (at $\tau = \tau_f$) $E_f$ for the classical model at $z = 0.2$ mm. The density is indicated by a logarithmic color scale. The red dashed line is $E_f = E_i$.

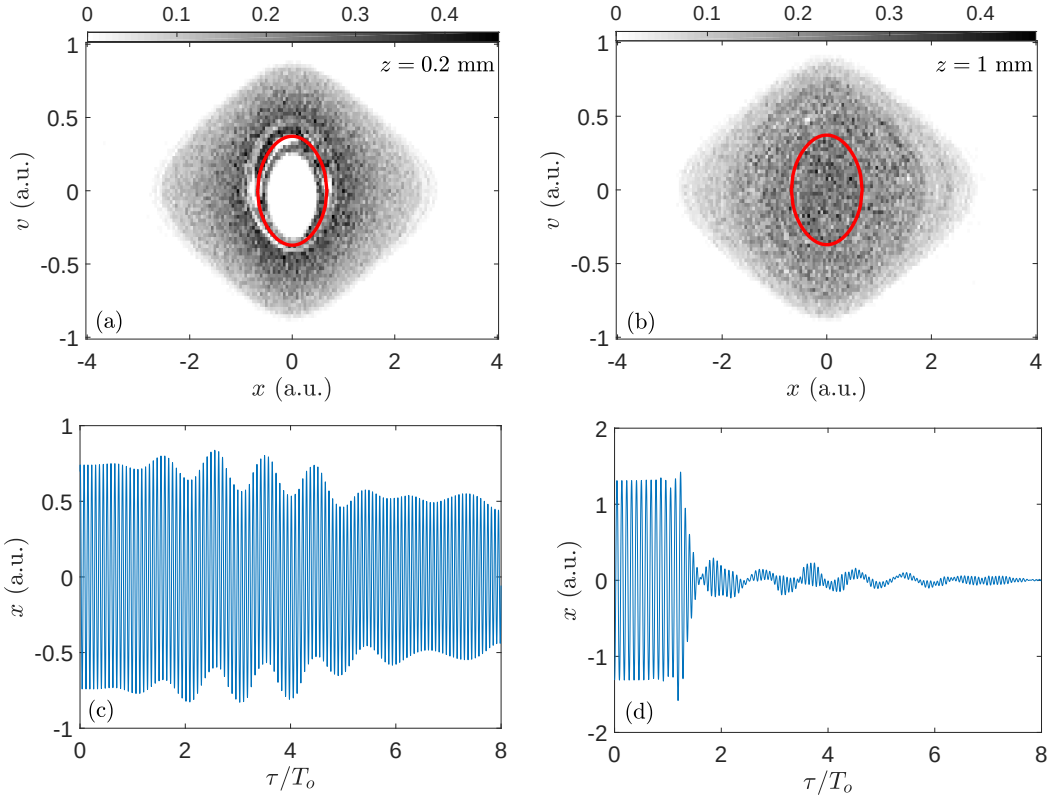


Figure 5.11: Electron energy loss in the classical model at $z = 0.2$ mm (a),(c) and $z = 1$ mm (b),(d). (a),(b) Electron distribution function at the end of the laser pulse $f(x, v, z, \tau_f)$. The red curve indicates the initial minimum energy $H_0(x, v) = E_{\text{min},1}$. (c),(d) Electron trajectory $x(\tau)$ which ends with the smallest energy $E$.

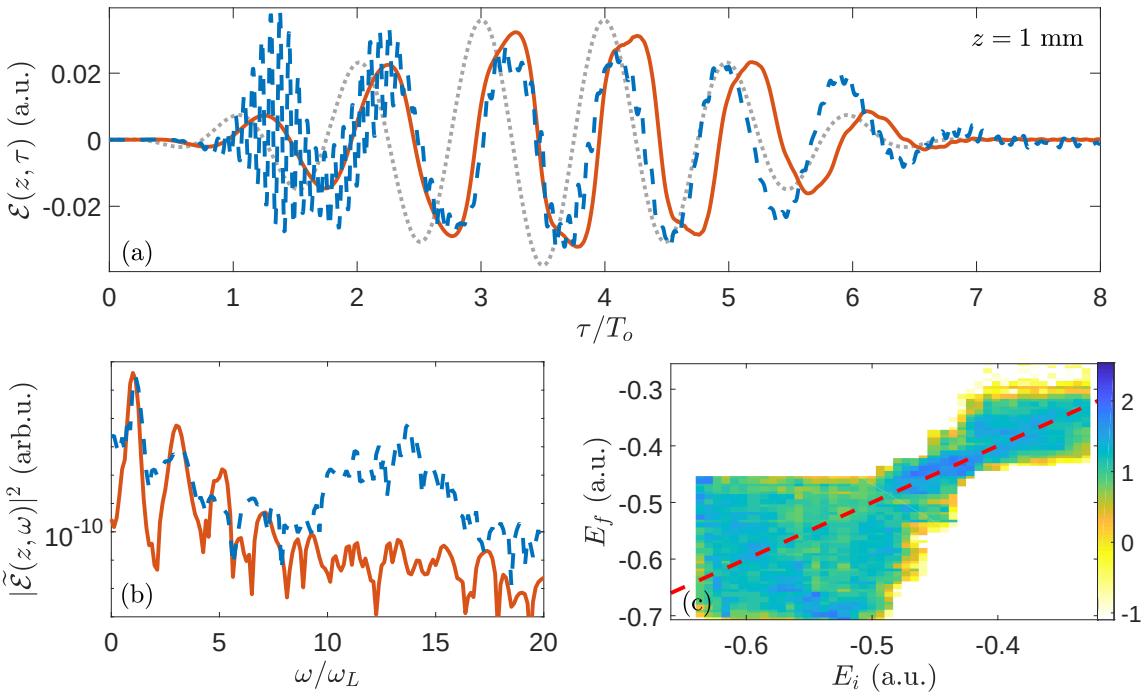


Figure 5.12: Same calculation as Fig. 5.10, with the results shown at $z = 1$ mm. (a) Time-dependent electric field $\mathcal{E}(z,\tau)$. The gray dotted curve is the initial field $\mathcal{E}_0(\tau)$. (b) Power spectrum of the filtered electric field $|\widetilde{\mathcal{E}}(z,\omega)|^2$. (c) Probability density for transitioning from a state with initial energy $E_i$ to a state with final energy (at $\tau = \tau_f$) $E_f$ for the classical model. The density is indicated by a logarithmic color scale. The red dashed line is $E_f = E_i$.

becomes more severe as $z$ increases, as seen in $f(x,v,z,\tau_f)$ at $z = 1$ mm in Fig. 5.11b. Eventually, the energy lost by these electrons outweighs the energy gained by the ionized electrons, leading to the increase in field energy seen in Fig. 5.10b at $z \sim 0.5$ mm. In the quantum model, this cannot possibly happen when all the electrons are initialized in the lowest possible energy state, i.e. the ground state. There, the pulse is always losing energy throughout propagation because the gas is always strictly gaining energy by excitation and ionization of the atoms. Hence, a net energy increase at any point throughout the pulse propagation is an unphysical effect that we would like to avoid when using the classical model for a gas of ground-state atoms.

### 5.4.3 Improving the classical model

Looking more closely at the mechanism for this anomalous behavior provides some intuition on what refinements may remedy the classical model. In Fig. 5.10e and 5.12c, we have plotted the joint probability density of $E_f$ and $E_i$, the initial energy at $\tau = 0$, for atoms at $z = 0.2$ mm and $z = 1$ mm, respectively. Here, we see that the electrons most likely to lose energy—which are represented by the part of the density below the line $E_f = E_i$—are those with energies near the two possible extremes, $E_{\mathrm{min},1}$ and $E_{\mathrm{max},1}$. In between these extremes, the energies of the electrons remain more or less at their initial values, a signature of bounded electron motion [154] on invariant tori [99, 155]. As propagation proceeds, we have observed that energy loss becomes more and more probable, with the range of energies at which this happens gradually creeping inward from both extremes, as indicated by the arrows. This is indeed evident from the joint distribution of $E_f$ and $E_i$ at $z = 1$ mm, plotted in Fig. 5.12c.

At the same time, we observe a resonant-like growth of the electric field modes with frequencies near $\omega \sim 14\omega_L$, visible in the spectrum of the field $|\widetilde{\mathcal{E}}(z,\omega)|^2$ at $z = 0.2$ mm in Fig. 5.10c and $z = 1$ mm in Fig. 5.12b. The classical spectrum displays a broad peak at these modes, whose intensity grows rapidly in $z$ and leads to a highly distorted electric field for $z > 0.2$ mm. For example, the field at $z = 1$ mm is plotted in Fig. 5.12a. This field bears only a faint resemblance to that of the quantum calculation, which does not exhibit this behavior at $z = 0.2$ mm, as shown in Fig. 5.10c, nor for larger values of $z$, in particular for $z = 1$ mm, as shown in Fig. 5.12b. In response to an incident quasi-monochromatic field, the classical model is known to exhibit radiation at frequencies near that of the field-free bounded electron motion [49, 156]. The frequency of the field-free orbits $\omega_a(E)$ can be approximated by expanding the exact expression for the frequency for small $E - E^*$ [155], where $E^* = -1/\sqrt{2}$ is the energy of the equilibrium at $x = 0$ and the lower bound on the electron energy in the classical model. In this case, the expansion to leading order is

$$\omega_a(E) \approx 2^{-3/4} - \frac{9}{2^{13/4}}(E - E^*). \tag{5.28}$$

Using Eq. (5.28), we obtain $\omega_a(E_{\min,1}) \approx 14\omega_L$, in striking agreement with the location of the broad peak in Fig. 5.10c. It is plausible that radiation at this particular frequency stands out compared to radiation at lower frequencies coming from electrons with a larger $E_i$, because $g_1(E)$ is effectively peaked at $E_{\min,1}$.

Thus, it is likely that the radiation generated at these frequencies builds up in the early part of the gas (for small $z$), until it is strong enough to interact resonantly with the electrons naturally oscillating at those same frequencies in the later parts of the gas. This probably triggers the electron energy loss observed at increasing $z$, beginning with the electrons with energies $E_i \sim E_{\min,1}$, while continuing to feed the growth of radiation at frequencies near $14\omega_L$. Evidence of this is shown in Figs. 5.11c and 5.11d, where we have plotted the trajectories $x(\tau)$ of the electron with the smallest energy at $\tau_f$, at $z = 0.2$ mm and $z = 1$ mm, respectively. At $z = 0.2$ mm, the electron experiences a gradual energy loss, inferred from the gradually decreasing amplitude of the oscillations. Eventually this becomes a sudden drop in energy, as seen for the electron trajectory at $z = 1$ mm right before $\tau/T_o = 2$, which one might expect for an electron driven by a resonant, out-of-phase forcing.

Given these observations, we propose to improve the classical model by judiciously selecting another initial energy distribution $g(E)$ to mitigate the pitfalls of $g_1$. On the one hand, we want a distribution that improves the agreement between the classical and quantum intensity-dependent ionization probabilities $P_{\text{ion}}(T_m)$. This ensures the classical model can mimic the quantum model with respect to the blueshift, ionization losses, and subluminal group velocity of the pulse. On the other, we want a distribution which is not sharply peaked at an energy greater than $E^*$. Avoiding this may prevent the amplification of the radiation of bounded electrons that subsequently also appears to trigger their energy loss.

We have found that the sigmoid distribution works well for low to intermediate ionization fractions, while mitigating the bound-electron resonance. The distribution is given by

$$g_\sigma(E) = \frac{N_\sigma}{1 + \exp\left[k(E - E_m)\right]}, \tag{5.29}$$

defined on the energy range $[E^*, E_{\max,\sigma}]$, with $N_\sigma$ a normalization constant. We choose $E_{\max,\sigma} = -0.23$ a.u. The free parameters $k$ and $E_m$ were optimized to maximize the agreement between the classical and quantum predictions for $P_{\text{ion}}(T_m)$ for the values of intensity plotted in Fig. 5.8, yielding $k = 93.22$ a.u. and $E_m = -0.3709$ a.u. In Fig. 5.8b, we see that the ionization probabilities of $g_\sigma$ agree very well with the quantum ones for ionization fractions below about $0.1$, in stark contrast to those of $g_1$. For higher ionization fractions, the performance of $g_\sigma$ is similar to $g_1$, with the ionization probabilities actually being slightly lower in this range, as shown in Fig. 5.8c for a pulse with $I = 3.5 \times 10^{14}$ $\mathrm{W \cdot cm^{-2}}$. However, even in Fig. 5.8c, we see that the improved performance of $g_\sigma$ for low-intensity pulses has translated into a better performance compared to $g_1$ for the time-dependent ionization probability $P_{\text{ion}}(\tau)$ during the low-intensity part of the pulse, i.e. for $\tau/T_o < 3$.

Using $g_\sigma$ as the initial energy distribution for the classical model, we are now able to successfully propagate the laser pulse to $z = 1$ mm in the low-ionization fraction regime, without the pulse energy ever increasing or a resonance at a bound-electron frequency developing. We show the results of the calculation under the same conditions as Fig. 5.10 in Figs. 5.13 and 5.14. The quantum and classical calculations agree well for the time-dependent electric field (Fig. 5.13a), as well as the ionization losses and instantaneous frequency (Figs. 5.13b and 5.13c, respectively). At the same time, we no longer see a significant probability of energy loss among the low-energy bounded trajectories at any point during the propagation. This can be seen by comparing Fig. 5.14 with Fig. 5.10e and Fig. 5.12c. We thus confirm that our strategy of matching ionization probabilities and appropriately shaping the classical initial energy distribution succeeds in improving the

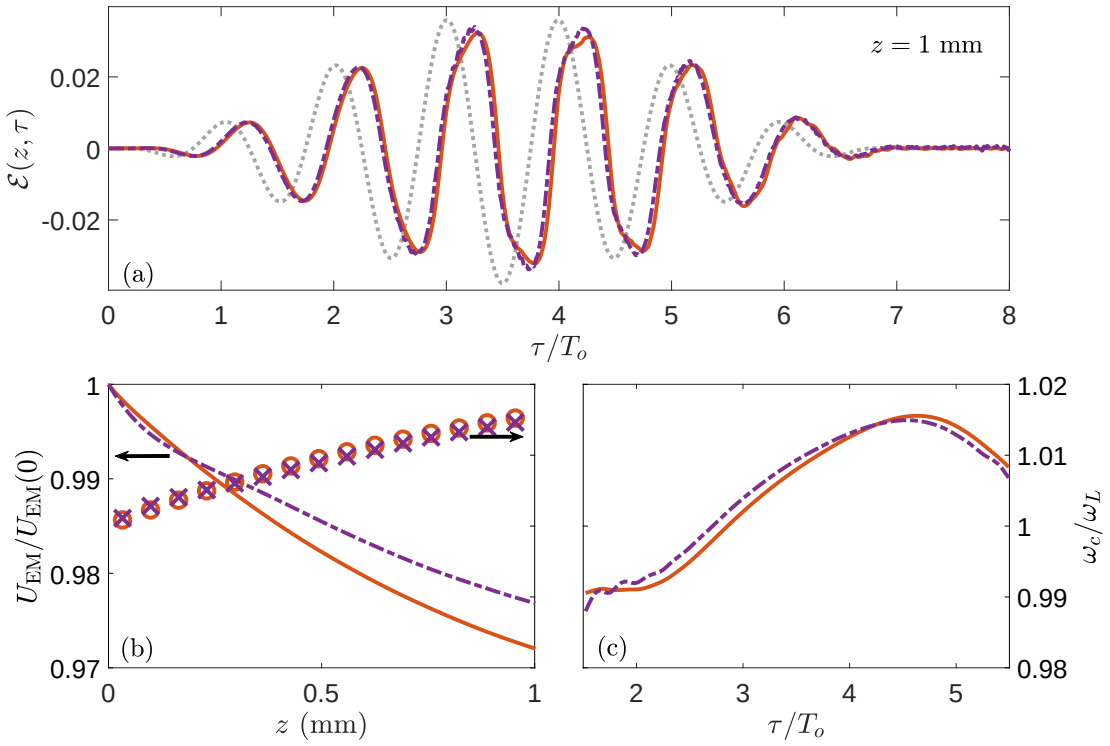


Figure 5.13: Results of pulse propagation through $1$ mm of ground-state atoms with density $\rho = 2 \times 10^{19}$ cm$^{-3}$, and peak incident pulse intensity $I = 5 \times 10^{13}$ W $\cdot$ cm$^{-2}$. The solid orange curves and circles correspond to the quantum model, while the dash-dotted purple curves and crosses correspond to the classical model with $g_\sigma$ as the initial energy distribution. (a) Time-dependent electric field $\mathcal{E}(z,\tau)$ at $z = 1$ mm. The gray dotted curve is the initial field $\mathcal{E}_0(\tau)$. (b) Normalized pulse energy $U_{\rm EM}$ (curves, left axis) and maximum instantaneous carrier frequency $\omega_{\rm max}$ (markers, right axis) as a function of $z$. The scale of the right axis is the same as in (c). (c) Time-dependent carrier frequency $\omega_c(z,\tau)$ at $z = 1$ mm.

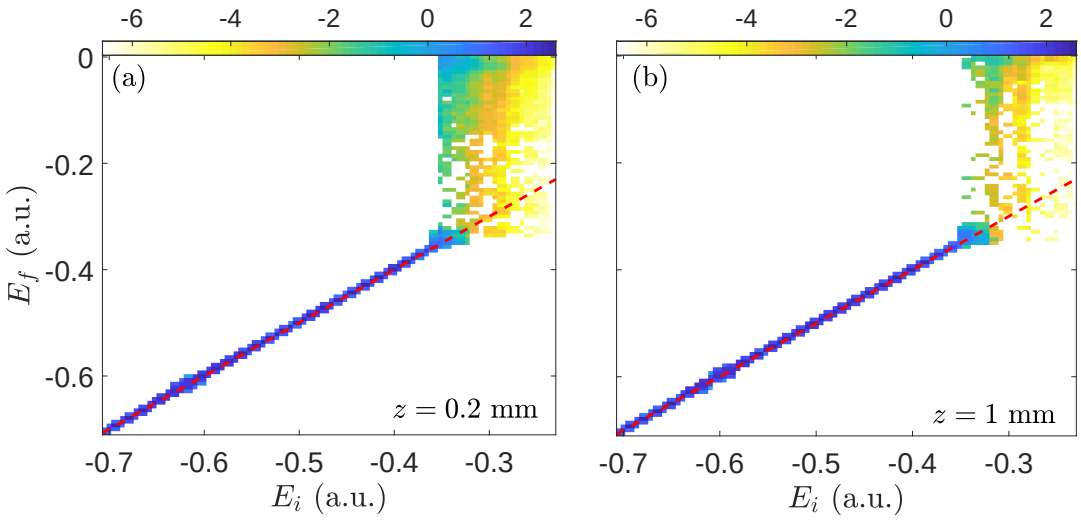


Figure 5.14: Final versus initial energy distributions for the classical model using $g_\sigma$ as the initial energy distribution, at $z = 0.2$ mm (a) and $z = 1$ mm (b). The pulse propagation parameters are the same as for Fig. 5.13. The dashed red line indicates $E_f = E_i$.

agreement between the classical and quantum propagation calculations.

We continue to observe this agreement in the intermediate ionization fraction regime, as show in Fig. 5.15. Here, we have propagated a pulse with initial peak intensity $I = 9 \times 10^{13}$ W $\cdot$ cm$^{-2}$ through 1 mm of a gas with density $\rho = 10^{18}$ cm$^{-3}$. For the field propagation, we selected $\Delta z = 2\lambda_L = 2.4$ $\mu$m. The density has been reduced by a factor of 20 compared to the previous simulation because the initial ionization fraction $P_{\text{ion}}(T_m) \sim 0.1$ is approximately 20 times higher than at $I = 5 \times 10^{13}$ W $\cdot$ cm$^{-2}$. In this regime, we observe that both calculations show that the laser field is not substantially reshaped during propagation, despite a maximum free electron density of about $10^{17}$ cm$^{-3}$. This is due to a balance between the neutral atom dispersion and free electron dispersion. These conditions are favorable for the phase-matching of high harmonic radiation [45], and thus we will use both models to investigate the coherent buildup of this radiation in the next section.

*Refined classical model in the high ionization fraction regime*

In Fig. 5.16, we show the results of a propagation calculation in the high ionization fraction regime, with $g_\sigma$ as the initial energy distribution of the classical model. The conditions are

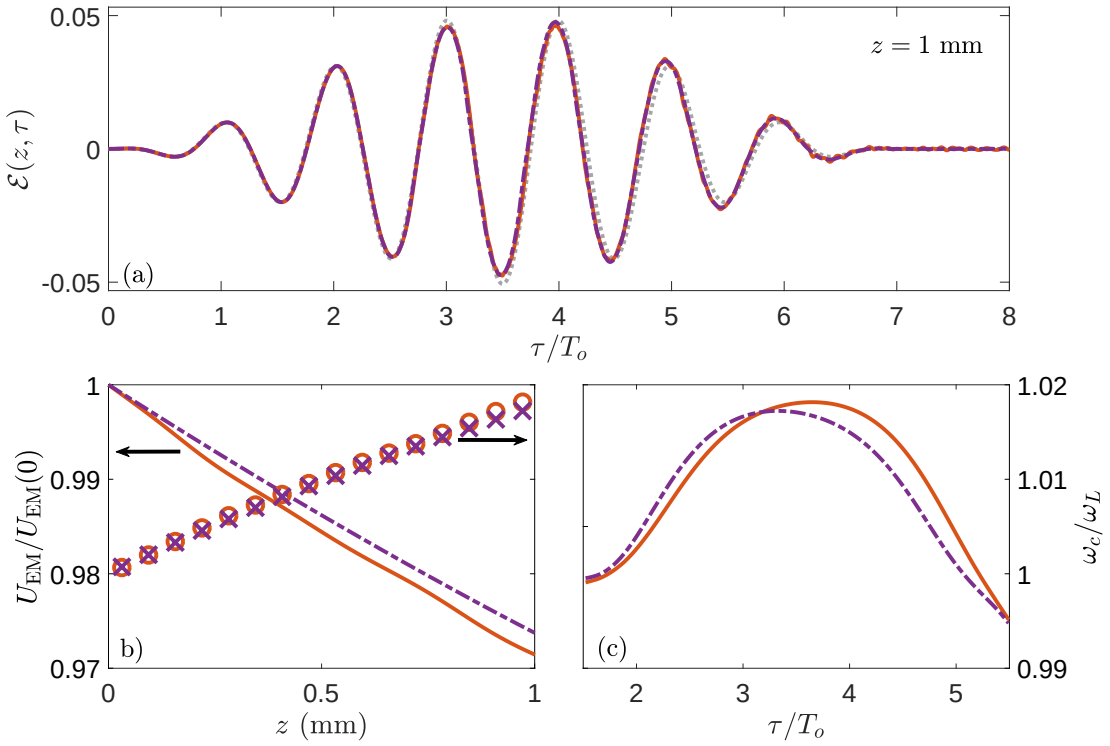


Figure 5.15: Results of pulse propagation through $1$ mm of ground-state atoms with density $\rho = 10^{18}$ cm$^{-3}$, and peak incident pulse intensity $I = 9 \times 10^{13}$ W$\cdot$cm$^{-2}$. The solid orange curves and circles correspond to the quantum model, while the dashed-dotted purple curves and crosses correspond to the classical model with $g_\sigma$ as the initial energy distribution. (a) Time-dependent electric field $\mathcal{E}(z,\tau)$ at $z = 1$ mm. The gray dotted curve is the initial field $\mathcal{E}_0(\tau)$. (b) Normalized pulse energy $U_{\rm EM}$ (curves, left axis) and maximum instantaneous carrier frequency $\omega_{\rm max}$ (markers, right axis) as a function of $z$. The scale of the right axis is the same as in (c). (c) Time-dependent carrier frequency $\omega_c(z,\tau)$ at $z = 1$ mm.

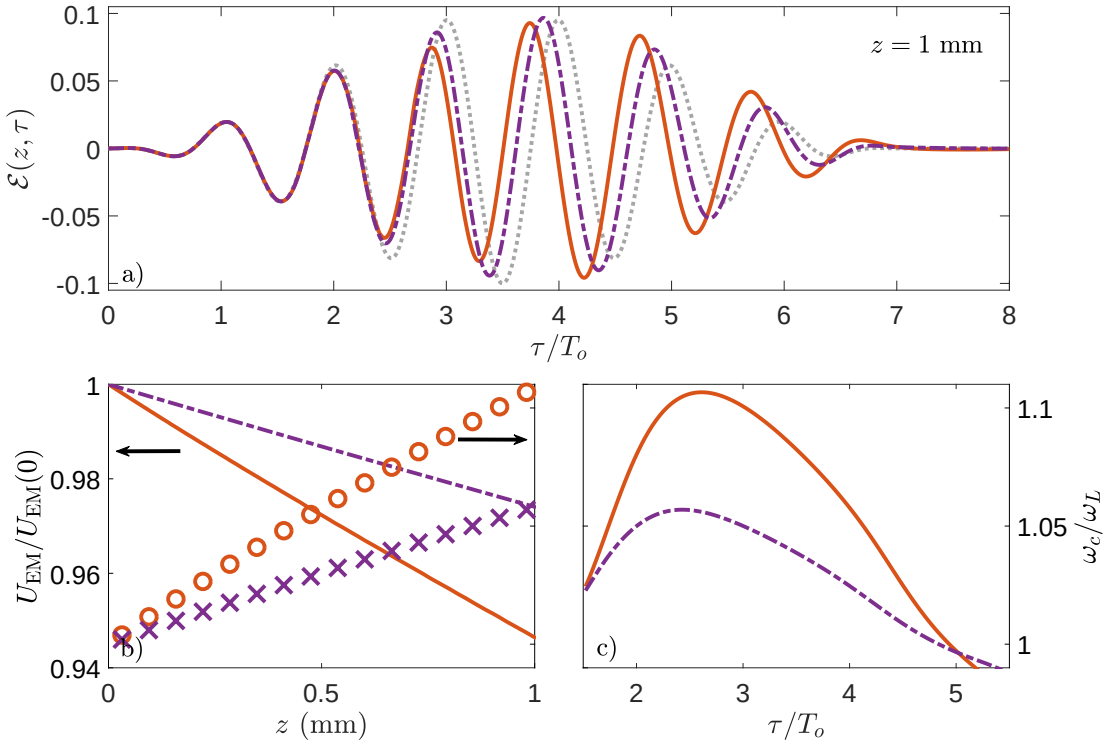


Figure 5.16: Results of pulse propagation through $1$ mm of ground-state atoms with density $\rho = 5 \times 10^{17}$ cm$^{-3}$, and peak incident pulse intensity $I = 3.5 \times 10^{14}$ W $\cdot$ cm$^{-2}$. The solid orange curves and circles correspond to the quantum model, while the dash-dotted purple curves and crosses correspond to the classical model with $g_\sigma$ as the initial energy distribution. (a) Time-dependent electric field $\mathcal{E}(z,\tau)$ at $z = 1$ mm. The gray dotted curve is the initial field $\mathcal{E}_0(\tau)$. (b) Normalized pulse energy $U_{\rm EM}$ (curves, left axis) and maximum instantaneous carrier frequency $\omega_{\rm max}$ (markers, right axis) as a function of $z$. The scale of the right axis is the same as in (c). (c) Time-dependent carrier frequency $\omega_c(z,\tau)$ at $z = 1$ mm.

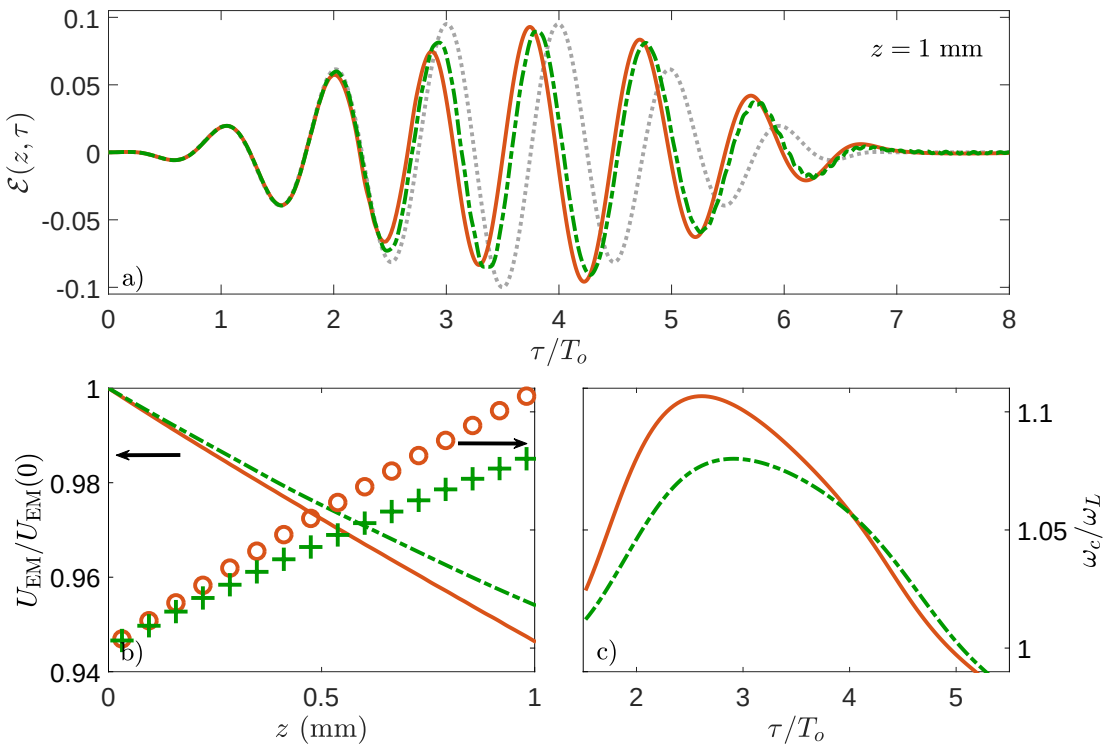


Figure 5.17: Results of pulse propagation through $1$ mm of ground-state atoms with density $\rho = 5 \times 10^{17}\text{cm}^{-3}$, this time using $g_2$ as the initial energy distribution of the classical model (green dash-dotted curves and crosses). The results of the quantum calculation from Fig. 5.9 are plotted again here for comparison. (a) Time-dependent electric field $\mathcal{E}(z,\tau)$ at $z = 1$ mm. The gray dotted curve is the initial field $\mathcal{E}_0(\tau)$. (b) Normalized time-averaged pulse energy density $U_{\rm EM}$ (curves, left axis) and maximum instantaneous carrier frequency $\omega_{\rm max}$ (markers, right axis) as a function of $z$. The scale of the right axis is the same as in (c). (c) Time-dependent carrier frequency $\omega_c(z,\tau)$ at $z = 1$ mm.

the same as those for Fig. 5.9. We see that generally, the classical model with $g_\sigma$ does not significantly outperform that with $g_1$. However, we found an alternative initial condition distribution, $g_2$, that gives better agreement with the quantum calculation than $g_1$ in the high ionization fraction regime.

After experimenting with some different functional forms for $g_2$, we found that the following form would allow us to significantly improve classical intensity-dependent ion-

ization probability:

$$g_2(E) = N_2(E - E_m)^4, \tag{5.30a}$$

$$N_2 = 5\left[(E_{\max,2} - E_m)^5 - (E_{\min,2} - E_m)^5\right]^{-1}, \tag{5.30b}$$

where $N_2$ ensures $g_2$ is normalized, and $E_m$ is a parameter. To optimize the parameters of $g_2$, we used the following procedure. We fixed $E_{\max,2} = -0.27$ a.u., and allowed $E_{\min,2}$ and $E_m$ to be free parameters. Then, we defined a cost function that penalizes discrepancies between the quantum and classical intensity-dependent ionization probabilities $P_{\text{ion}}(T_m)$ at the particular values of intensity plotted in the middle panel Fig. 5.7. Lastly, we optimized the free parameters of $g_2$ to minimize the cost function, under the constraint that $\overline{E} = I_p$. This resulted in $E_{\min,2} = -0.5481$ a.u. and $E_m = -0.2593$ a.u..

The results of the classical model propagation with $g_2$ with the quantum model are shown in Fig. 5.17. For each observable plotted in Fig. 5.17, the classical calculation with $g_2$ gets closer to the quantum calculation than the classical calculation with $g_1$. In particular, the time-dependent blueshift (right axis of middle panels and right panels of Figs. 5.9 and 5.17) of the quantum model is better reproduced by the classical model with $g_2$. However, when doing a propagation calculation with $g_2$ in the low-ionization fraction regime, we observed the same bound-electron resonance behavior that we saw for $g_1$.

For short pulses, a high ionization fraction is typically attained in the barrier-suppression regime, where the potential barrier in the combined Coulomb and maximum laser fields is depressed below the quantum ground-state energy [24]. At intensities above the barrier-suppression intensity $I_{\text{BS}}$, ionization takes place by over-the-barrier ionization, rather than tunneling or multiphoton ionization. For this system with $I_p = -0.5$ a.u., we have $I_{\text{BS}} = 1.4 \times 10^{14}$ W $\cdot$ cm$^{-2}$, and it turns out this is approximately where the intensity-dependent ionization probabilities of the classical model with $g_\sigma$ depart from those of the quantum model (Fig. 5.8b). Even though over-the-barrier ionization is essentially classical, our

model is not effective in this regime because of the apparent drawback of having an energy distribution which is peaked at an energy greater than $E^*$. In order to avoid the bound-electron resonant interaction that plagues the classical model at low intensities, we chose a distribution of energies that significantly populates classical states with energies $E < I_p$, as seen in Fig. 5.8a. The lower the energy of the state, the higher peak intensity required to ionize it [154]. Thus, many of these states remain bounded even for $I > I_{\mathrm{BS}}$, while in the quantum case the atom becomes fully ionized. Consequently, when tuning the classical model to accurately capture propagation effects, there is a trade-off between accuracy in the low-to-intermediate ionization fraction regime and accuracy in the high ionization fraction regime.

## 5.5 Dynamics of the high harmonic spectrum for unidirectional pulses with one-dimensional atoms

The discrepancy between the quantum and classical ionization probabilities that remains after optimization of the classical model is part of what hampers the agreement between the classical and quantum calculations for the low frequency components of the field, especially near $\omega_L$. This can make it challenging to use the classical model to explain properties of the quantum high harmonic spectrum after propagation directly. Because the electric fields driving the atoms at each $z$ are slightly different in the two calculations, the electron dynamics in the two calculations will also be slightly different. However, the ionization step can be artificially removed by performing a numerical experiment in which the electrons are initialized in a scattering state, the so-called scattering experiment [20, 83, 157]. We show that in this case, the quantum and classical propagation calculations are nearly indistinguishable for the dominant frequency component of the field. Hence, it is possible to directly apply the classical model to uncover the mechanisms of high harmonic radiation phenomena present in the quantum model.

In this section, we begin by close examination of this scenario, hereafter referred to as

the scattering-propagation experiment. We perform a phase space analysis of the classical model that explains the extension of the high harmonic cutoff past the $3.17U_p + |I_p|$ cutoff law observed in the quantum calculation. Then, we perform similar phase space analyses of the classical model calculations of pulse propagation through a gas of ground-state atoms. Our goal is to show that, even in the ground-state case, the classical model provides insight into the buildup of the quantum harmonic spectrum, including the mechanisms of low-order harmonic generation and the phase-matching of higher-order harmonics.

### 5.5.1 The scattering-propagation experiment

*Initial conditions*

We again consider the propagation of the laser electric field from $z = 0$ to $z = 1$ mm, through a gas of density $\rho = 5 \times 10^{17}$ cm$^{-3}$. Because we are not concerned with the gradual ionization of the atom here, we are not obliged to use a realistic pulse shape for the initial electric field. Thus, we initialize the field as a simple monochromatic wave, $\mathcal{E}_0(\tau) = E_0 \cos(\omega_L \tau)$, and we reduce the final time to $\tau_f = 3.5T_o$. We take the same field parameters as in the high-ionization fraction regime, i.e. $E_0 = 0.1$ a.u. for an intensity of $I = 3.5 \times 10^{14}$ W$\cdot$cm$^{-2}$, and for the field propagation, we use $\Delta z = (21/8)\lambda_L = 3.16$ $\mu$m. The electron is initialized as a Gaussian wave packet at rest, centered at the quiver radius $E_0/\omega_L^2$, as in Refs. [20, 83, 157]. Thus, for the quantum case, the initial wave function is

$$\psi_0(x) = \left(\frac{\pi}{\gamma^2}\right)^{-1/4} \exp\left[-\frac{\gamma^2}{2}\left(x - \frac{E_0}{\omega_L^2}\right)^2\right],$$

where the parameter controlling the wave packet width is chosen as $\gamma = 0.2236$ a.u. [83]. Meanwhile, in the classical case, the corresponding initial distribution function is also a Gaussian wave packet, with identical position and velocity spreads to the quantum wave packet, i.e.

$$f_0(x, v) = \frac{1}{\pi} \exp\left[-\gamma^2\left(x - \frac{E_0}{\omega_L^2}\right)^2 - \frac{v^2}{\gamma^2}\right]$$

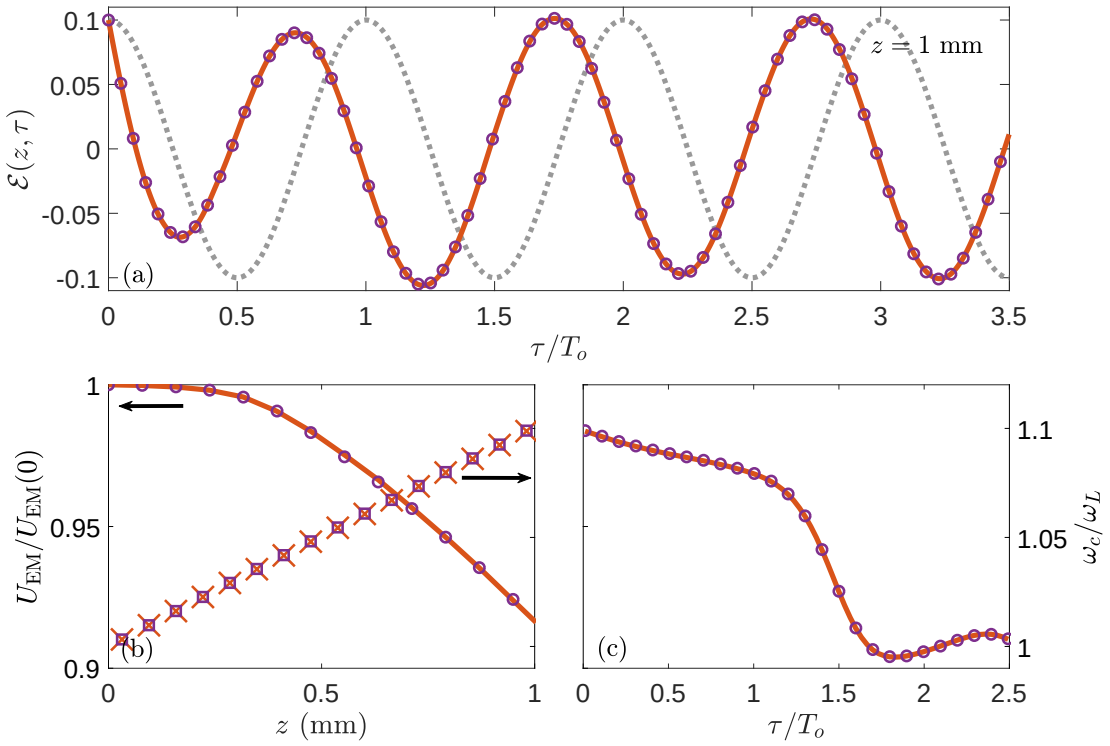


Figure 5.18: Results of pulse propagation through $1$ mm of a gas of atoms prepared in a scattering state (see text) with density $\rho = 5 \times 10^{17}$ cm$^{-3}$, and peak incident pulse intensity $I = 3.5 \times 10^{14}$ W $\cdot$ cm$^{-2}$. The solid orange curves and crosses correspond to the quantum model, while the purple circles and squares correspond to the classical model. (a) Time-dependent electric field $\mathcal{E}(z,\tau)$ at $z = 1$ mm. The dotted curve is the initial field $\mathcal{E}_0(\tau)$. (b) Normalized pulse energy $U_{\rm EM}$ (curve and circles, left axis) and maximum instantaneous carrier frequency $\omega_{\rm max}$ (crosses and squares, right axis) as a function of $z$. The scale of the right axis is the same as in (c). (c) Time-dependent carrier frequency $\omega_c(z,\tau)$ at $z = 1$ mm.

Unlike in the ground-state case, we have not performed any adjustments to the classical distribution to optimize the agreement between the quantum and classical propagation calculations. As we shall see, excellent agreement may already be obtained with this distribution. For the classical calculations, the number of particles chosen is $N = 4007360$.

*Evolution of the dominant component of the field*

Figure 5.18 shows the results of the pulse propagation calculations for the total field, energy loss, and blueshift. For the calculations of $\omega_c(z,\tau)$, the post-processed field $\mathcal{E}_p$ was defined on the interval $\tau \in [-3T_o, 3.5T_o]$, with a $z$-independent, smoothly ramped-up oscillation for $\tau < 0$, followed by $\mathcal{E}(z,\tau)$ multiplied by a window which sends the field smoothly to zero over the last computed laser cycle. Precisely, $\mathcal{E}_p$ is given by

$$\mathcal{E}_p(z,\tau) = \begin{cases} E_0 \cos^2\left(\frac{\pi\tau}{6T_o}\right)\cos(\omega\tau) & \text{for } -3T_o \leq \tau < 0, \\ \mathcal{E}(z,\tau) & \text{for } 0 \leq \tau < 2.5T_o, \\ \mathcal{E}(z,\tau)\cos^2\left(\frac{\pi(\tau-2.5T_o)}{2T_o}\right) & \text{for } 2.5T_o \leq \tau \leq 3.5T_o. \end{cases} \tag{5.31}$$

This post-processing prescription allowed the computation of a clean Wigner-Ville transform that leads to an instantaneous carrier frequency which clearly captures the blueshift concentrated between $0 < \tau < T_o$, as seen by looking at Figs. 5.18a and 5.18c. We observe that in the scattering-propagation experiment, the classical and quantum calculations are in excellent agreement for the observables reflecting the dominant frequency component of the field, even better than in the ground-state case (Figs. 5.13, 5.15, and 5.16). This corroborates our assertion that the main source of the discrepancy the classical and quantum ground-state calculations is the description of ionization. Indeed, by beginning in a fully ionized state instead of the ground state, we observe a massive improvement in the agreement between the two calculations for an incident pulse with the same peak laser intensity.

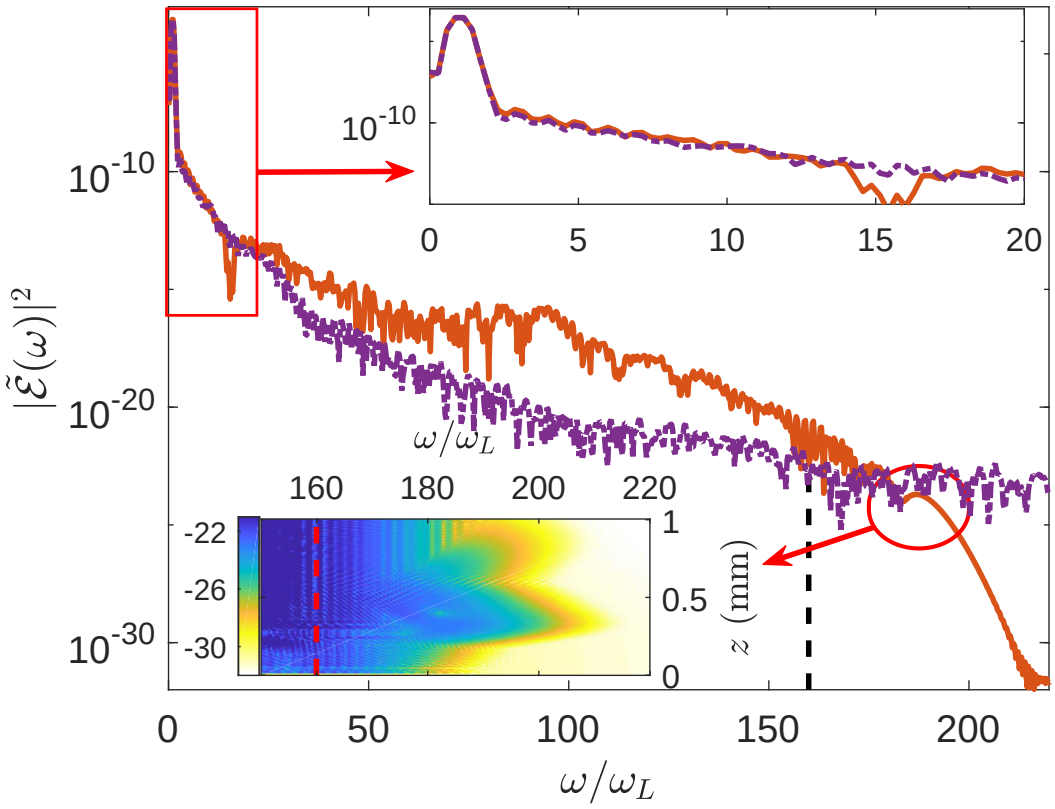


Figure 5.19: High harmonic spectra for the scattering-propagation experiment at $z = 0.37$ mm. The quantum model is the solid orange curve, and the classical model is the dash-dotted purple curve. The dashed lines indicate $3.17U_p + |I_p|$. Upper inset: a magnification of the spectrum of the low-order harmonics. Lower inset: Spectrum of the harmonics in the cutoff region for the quantum model as a function of $z$. The harmonic intensities are indicated by the logarithmic color scale.

*Evolution of the high harmonic spectrum*

Figure 5.19 shows the power spectra of the electric fields of the classical and quantum models at $z = 0.37$ mm. For these spectra, the post-processing consisted of applying a $\sin^4$ window to the calculated electric fields. The classical and quantum spectra agree well for the low-order harmonics, as shown in the upper inset of Fig. 5.19. However, a high-harmonic plateau and cutoff are only observed in the quantum model, as observed in single-atom calculations [83]. This confirms the fundamental role played by quantum interference effects for high-harmonic emission, even when propagation effects are taken

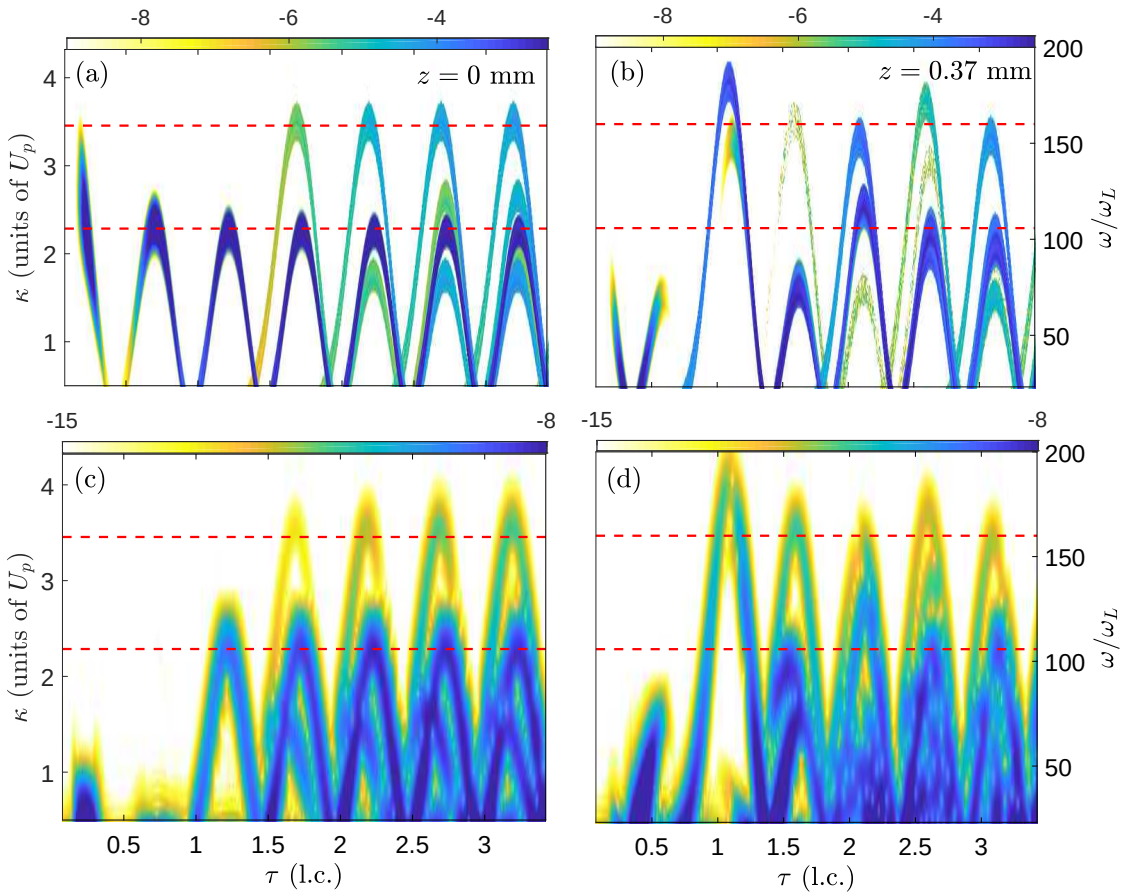


Figure 5.20: Electron dynamics at $z = 0$ (a),(c) and $z = 0.37$ mm (b),(d) for the scattering-propagation experiment. (a),(b) Recollision flux $R(\kappa, \tau; z)$ from the classical model. (c),(d) Spectrogram of the dipole acceleration $d_a(\tau)$ from the quantum model. The spectrograms were computed using a $\cos^4$ window of duration $0.15T_o$. The dotted lines indiciate $2U_p + |I_p|$ and $3.17U_p + |I_p|$. The left axes, indicating the recollision kinetic energy $\kappa$, are related to the right axes, indicating the radiated frequency $\omega$, by $\kappa = \omega$.

into account. In the quantum spectrum, we see that the cutoff is extended well past the usual $3.17U_p + |I_p|$ cutoff law, which is valid for SAE atoms in monochromatic fields. The lower inset of Fig. 5.19 shows the evolution of the cutoff region throughout propagation. While $3.17U_p + |I_p| = 160\omega_L$ is a reasonable approximation of the cutoff for small $z$, the cutoff increases significantly during propagation, reaching about $180\omega_L$ before receding again. To understand this anomalous cutoff extension driven by the pulse propagation, we examine the electron dynamics.

The correspondence between recollisions and radiation is clearly seen when comparing

the recollision flux of the classical model with the spectrogram of the dipole acceleration from the quantum model. High-harmonic emission occurs when multiple electron energy states are simultaneously occupied near the core, leading to interference in the quantum model at frequencies equal to the difference in energy between all possible pairs of states [56, 158]. Traditionally, one conceives of high harmonic radiation as occurring from the interference between a recolliding electron with kinetic energy $\kappa$ and the ground state of total energy $I_p$ [3, 55], which, estimating the potential energy of the recolliding electron as $I_p$, leads to radiation at the frequency $\omega = (\kappa + I_p) - I_p = \kappa$. One may also obtain high harmonic emission from the interference of recollisions of two different energies, $\kappa_1$ and $\kappa_2$, at a frequency $\omega = |\kappa_1 - \kappa_2|$ [158].

In Fig. 5.20, we observe both kinds of emission. First, we focus on Figs. 5.20a and 5.20c at $z = 0$, where the classical and quantum atoms are driven by an identical electric field, $\mathcal{E}_0(\tau)$. For $\tau < T_o$, even though there are recollisions, as seen in Fig. 5.20a, they are peaked around a single energy at each time, while the ground state is initially completely empty in the scattering experiment setup. Thus, no high harmonic emission is observed in the quantum model, (Fig. 5.20c). Beginning at $\tau \gtrsim T_o$, part of the electron wave packet becomes trapped near the core [83], leading to the population of the ground state [159]. Subsequently, high-harmonic emission from the interference of recolliding electrons with the trapped electrons is evident from the direct correspondence between the spectrogram of Fig. 5.20c and the recollision flux of Fig. 5.20a, particularly for the families of recollisions with a maximum kinetic energy near $2U_p + |I_p|$ and those with a maximum kinetic energy near $3.17U_p + |I_p|$. This second family of recollisions does not emerge until $\tau \gtrsim 1.5T_o$, and once it does, we also observe high-harmonic emission arising from the interference between these two families of recollisions. These are the dark blue stripes of radiation with a frequency decreasing in time from about $75\omega_L$ to $25\omega_L$ that appear every half laser cycle for $\tau > 1.5T_o$.

By $z = 0.37$ mm, the electric fields in the quantum and classical models are now

different, as they have been driven by different dipole velocities in Eq. (5.1). Nevertheless, the dominant component of the fields agree so closely throughout propagation, as shown in Fig. 5.18, that we continue to observe a close correspondence between the quantum and classical electron dynamics. This is reflected by the comparisons of the classical recollision flux and the quantum dipole acceleration spectrogram at $z = 0.37$ mm in Figs. 5.20b and 5.20d. In particular, we still observe high-harmonic emission in the quantum case with a timing and frequency matching the timing and energy of the classical recollisions. We also observe radiation from the interference between different families of recollisions, which is most clearly seen at $\tau \approx 1.5T_o$. Comparing the electron dynamics at $z = 0.37$ mm and $z = 0$, we notice two striking changes. The first is that, at $z = 0.37$ mm, recollision-driven radiation is observed for $\tau < T_o$, whereas it was not at $z = 0$. This implies that electron trapping near the core occurs earlier in the laser pulse as propagation proceeds. The second is that, at $z = 0.37$ mm around $\tau = T_o$, we observe recollisions and their corresponding radiation at energies that significantly exceed the usual $3.17U_p + |I_p|$ harmonic cutoff, whereas this does not occur at $z = 0$. These recollisions drive the extension of the high-harmonic cutoff that we observed in the electric field spectrum of the quantum calculation, as seen in Fig. 5.19. By studying the electron dynamics in phase space using the classical model, we can identify the mechanism of the cutoff extension.

In Fig. 5.21, we show snapshots of the classical electron distribution function $f(x, v, z, \tau)$ at particular times $\tau$ and propagation positions $z$. With the initial conditions we have chosen, the electron wave packet always begins at rest far on the right side of the core, and the field is positive and at a maximum. Therefore, the electron is always initially driven to the left, towards the core. At $z = 0$, the electron wave packet is predominantly on the left of the ion by time $\tau_m$ when the laser field has reversed direction once and is again at an extremum. When the field subsequently goes to zero at time $\tau_0$, the wave packet has almost completely vacated the core region. However, as propagation proceeds, the blueshift causes the laser field to reverse direction earlier in the pulse, and this causes the center of the wave packet

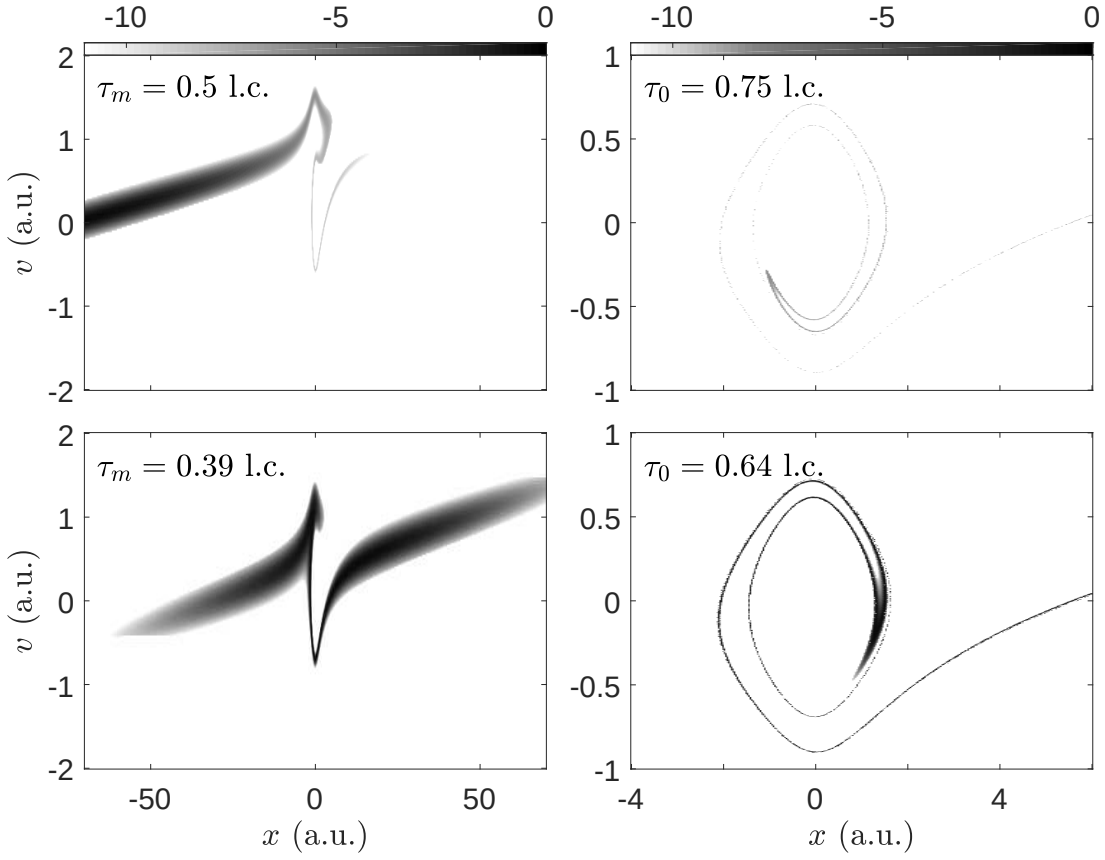


Figure 5.21: Snapshots of the distribution function $f(x, v, z, \tau)$ in a logarithmic scale. Left panels: $f(x, v, z, \tau_m)$, where $\tau_m > 0$ is the first field intensity maximum after the start of the pulse. Right panels: $f(x, v, z, \tau_0)$, where $\tau_0 > \tau_m$ is the first zero of the field following $\tau_m$. The upper panels are at $z = 0$, while the lower panels are at $z = 0.37$ mm.

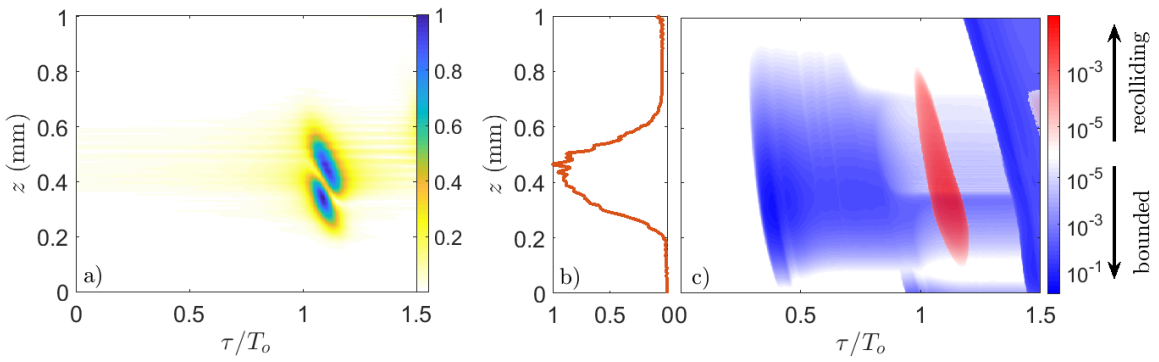


Figure 5.22: Evolution of the anomalously high-harmonic radiation. (a) Normalized spatiotemporal amplitude profile $|\hat{\mathcal{E}}_{ab}(z,\tau)|$ of the radiation in the $\omega > 175\omega_L$ frequency band, computed from the electric field of the quantum model. (b) Normalized yield of radiation with $\omega > 175\omega_L$, computed from the electric field of the quantum model. (c) Population of bound states $P_b$ and population of recolliding states $P_r$ with energies $\kappa > 3.78U_p$ as a function of $z$ and $\tau$, calculated from the classical model. The population of bound states is indicated by the logarithmic blue color scale, and the population of recolliding states is indicated by the logarithmic red color scale.

at time $\tau_m$ to be displaced to the right. By $z = 0.37$ mm, the wave packet is thus nearly centered over the ion, with the electron velocities distributed about zero. When part of the wave packet arrives to the core with a low kinetic energy like this, it has a high probability of becoming trapped there [159], and indeed a trapped part of the wave packet is clearly observed in the subsequent snapshot of the distribution function at $\tau_0$ (lower right panel of Fig. 5.21). An example of such an electron trajectory is shown in Fig. 5.22b. This confirms that a bound state is created earlier in the pulse after propagation through part of the gas. Furthermore, this explains the emergence of recollision-driven high-harmonic radiation for $\tau < 1$ l.c. at longer propagation distances, despite this radiation being absent in this time interval at $z = 0$.

Besides enabling the recollision-driven radiation for $\tau < T_o$, these trapped states are also important for the emergence of the anomalously high-frequency radiation. In Fig. 5.22c, we show calculations of the bound state populations $P_b(z,\tau)$ and the anomalously high energy recollisions $P_r(z,\tau)$ from the classical model. We estimate the bound-state population from the recollision flux by integrating $R(\kappa,\tau,z)$ over low kinetic energies, while we ob-

tain the probability of anomalously high recollision by integrating the same over the highest kinetic energies. Specifically, we define $P_b$ and $P_r$ as

$$P_b(z,\tau) = \int_0^{\kappa_b} R(\kappa,\tau,z)\mathrm{d}\kappa \;\text{ for } \kappa_b = 0.11U_p$$
$$P_r(z,\tau) = \int_{\kappa_r}^{\infty} R(\kappa,\tau,z)\mathrm{d}\kappa \;\text{ for } \kappa_r = 3.78U_p.$$

This choice of $\kappa_b$ ensures that the instantaneous energy of the counted electrons is negative, while this choice of $\kappa_r$ corresponds to radiation at $\omega_r = 175\omega_L$. Here, it is clear that the propagation induces the population of bound electron states earlier in the pulse. Indeed, for $z = 0$, these states are not occupied until $\tau \approx T_o$, while by $z = 0.1$ mm, they become occupied by $\tau = 0.5T_o$. Likewise, it is evident that the high-energy recollisions emerge only around $z = 0.2$ mm.

Figure 5.22b shows the yield of the harmonics greater than $\omega_r$ from the quantum calculation, i.e. the integral of the power spectrum $\int_{\omega_r}^{\infty} |\tilde{\mathcal{E}}(z,\omega)|^2\mathrm{d}\omega$. We see that these modes are either amplified or absorbed for $0.2 \text{ mm} < z < 0.7$ mm; at other positions, they are comparatively quiescent. This range corresponds exactly to the range of $z$ in which we observe an overlap in the bound state population and the recolliding population. Indeed, it is only when both of these states are occupied that interference between them can occur in the quantum model, leading to the emission (or absorbtion) of these modes of the field. Furthermore, we show the time-profile of these modes as a function of $z$ in Fig. 5.22a, by plotting the amplitude of the analytic representation $|\hat{\mathcal{E}}_{ab}(z,\tau)|$ computed for the modes $\omega > \omega_r$. We see that these high-harmonics are generated at the same times $\tau$ as the recollisions. However, they have a nontrivial spatiotemporal evolution, indicating rapidly evolving phase-matching conditions.

By looking at the electron trajectories, we can determine the mechanism of the increase of the recollision energy beyond the usual $3.17U_p + |I_p|$ cutoff. We have focused on the trajectories belonging to the first family of recollisions containing the anomalously high-

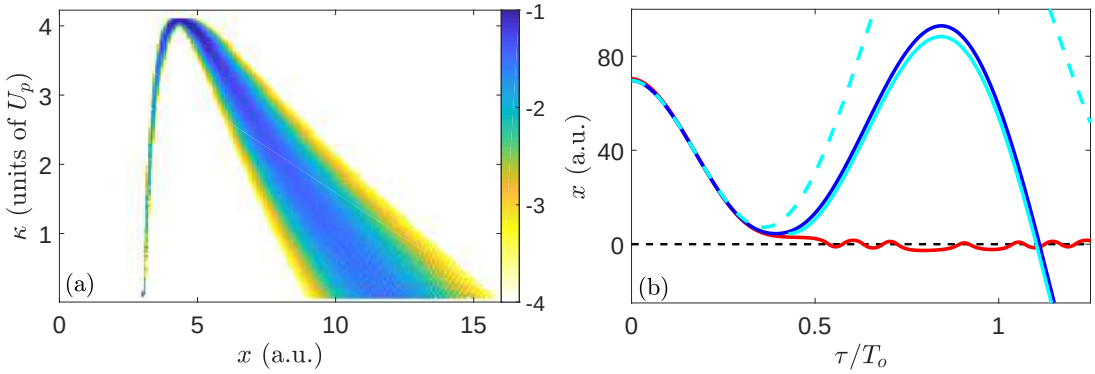


Figure 5.23: Trajectory analysis of $4U_p$ recollisions at $z = 0.37$ mm, using the classical model. (a) Joint probability distribution of $(x, \kappa)$ on a logarithmic scale, for electrons which come to rest at $x$ near the first extremum of the laser field, i.e. near times $\tau = \tau_m$, and then recollide with kinetic energy $\kappa$. (b) A typical trajectory from the classical model with $\kappa > 4U_p$ (blue line), a typical trapped trajectory (red line), the SFA trajectory with the same initial conditions as the $4U_p$ trajectory (dashed cyan line), and the SFA trajectory initiated at a time $\tau_0$ near time $\tau = \tau_m$ with the maximum recollision kinetic energy (solid cyan).

energy recollisions, with $\kappa > \kappa_r$ exceeding $4U_p$, at $z = 0.37$ mm. We have observed that most of these electrons come to rest at some position $x > 0$ near to the core, before achieving their first recollision. In Fig. 5.23a, we have plotted the joint probability distribution of $x$ and $\kappa$, the kinetic energy of each electron's subsequent recollision. We see that the electron's $x$ is highly correlated with its $\kappa$, and in particular the highest energy recollisions come to rest at about $x = 4.5$ a.u., very close to the core. A typical example of such a trajectory, with $\kappa > 4U_p$, is plotted in Fig. 5.23b. Because these trajectories approach the core with low kinetic energy, they very nearly become trapped there. This is evidenced by the initial similarity of this recolliding trajectory to the typical trapped trajectory plotted in Fig. 5.23b. Since these anomalously high energy recollisions come so close to the core that they barely escape trapping, one may expect the Coulomb field to play a central role in the increase in energy of these trajectories.

We assess the role of the Coulomb field through two calculations based on the strong-field approximation (SFA), one in which the Coulomb field is neglected entirely [3], and one in which it is treated a perturbation [20]. In the first calculation, we compute the

trajectory of the electron with the same initial conditions $(x_0, v_0)$ as the $4U_p$ trajectory plotted in Fig. 5.23, but neglecting the Coulomb field. Hence, $x_{\rm SFA}(\tau) = x_0 + v_0\tau - \int_0^\tau \int_0^{\tau'} \mathcal{E}(z,\tau'')\mathrm{d}\tau''\mathrm{d}\tau'$, where $z = 0.37$ mm, and this trajectory is plotted in Fig. 5.23. We see that $x_{\rm SFA}$ agrees well with the true trajectory until about $\tau = \tau_m = 0.39T_o$, the extremum of the electric field, at which point the close encounter with the core takes place. In the second calculation, we fix $x_0 = 4.5$ a.u. and $v_0 = 0$, and find the initial time $\tau_0$ near $\tau_m$ such that the subsequent recollision kinetic energy of the SFA trajectory with these initial conditions, $\kappa_{\rm SFA}$, is at a maximum. This results in $\kappa_{\rm SFA} = 3.69U_p$, and the corresponding trajectory is also plotted in Fig. 5.23. It is seen to be quite close to the true high-energy recolliding trajectory. Furthermore, the effect of the Coulomb field on the return kinetic energy may be included perturbatively [20]. This yields a maximum return kinetic energy of simply $\kappa_{\rm SFA} - V(0) = 4.1U_p$. This value of the maximum kinetic energy is in excellent agreement with the maximum energy recollision we observed for this $z$ (see Figs. 5.20b and 5.20d).

Therefore, while the Coulomb field has a decisive effect on the electron dynamics, it is not responsible for the increase in the high-harmonic cutoff energy *per se*. The maximum cutoff energy can be calculated using a Coulomb-perturbed SFA with $\mathcal{E}(z,\tau)$, the propagated electric field. Because the Coulomb perturbation is always present and independent of the field, the increase in energy must be solely due to the change of shape of the field. In other words, the SFA cutoff for an initially monochromatic field of $\kappa_{\rm SFA} = 3.17U_p$ becomes $\kappa_{\rm SFA} = 3.69U_p$ after propagation to $z = 0.37$ mm due to the accumulated radiation at other frequencies, and this causes the increase in the cutoff energy. Nevertheless, the Coulomb interaction near $\tau_m$, though brief, is critical for making these higher-energy recollisions accessible to the electrons. Indeed, the only way that the trajectory shown in Fig. 5.23 can bring back $4U_p$ to the core is by becoming momentarily trapped there; the SFA trajectory with the same initial condition, also shown in Fig. 5.23, does not come back to the core at all. This recalls the mechanism by which delayed recollisions acquire recollision energies

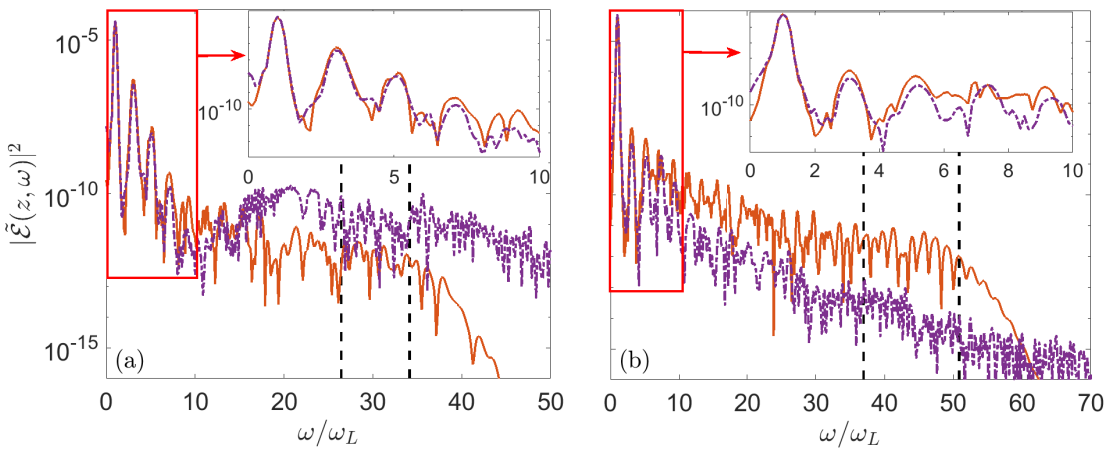


Figure 5.24: High harmonic spectra of the quantum and classical models at $z = 1$ mm in (a) the low-ionization fraction regime and (b) the intermediate-ionization fraction regime. The gas densities are chosen to give a similar peak free-electron density in each case. A $\sin^2$ window was applied to the fields prior to computation of the spectra. (a) Incident pulse peak intensity $I = 5 \times 10^{13}$ W $\cdot$ cm$^{-2}$, gas density $\rho = 2 \times 10^{19}$ cm$^{-3}$. (b) Incident pulse peak intensity $I = 9 \times 10^{13}$ W $\cdot$ cm$^{-2}$, gas density $\rho = 10^{18}$ cm$^{-3}$. The vertical axes are directly comparable.

near the high-harmonic cutoff in the high-intensity regime, as explored in Ch. 3.

### 5.5.2 Harmonic generation from ground-state atoms

Now, we return to the more realistic case of pulse propagation through ground-state atoms, focusing on the low- and intermediate-ionization fraction regimes. We will illustrate the extent to which it is possible to unravel the buildup of the quantum spectrum through phase-space analysis of the classical model.

*Low-order harmonic generation*

Figure 5.24 shows the spectra of the field $|\tilde{\mathcal{E}}(z,\omega)|^2$ at $z = 1$ mm for the quantum model and the classical model with the $g_\sigma$ distribution, henceforth referred to simply as the classical model. Similarly to the scattering-propagation experiment (Fig. 5.19), we see a good agreement for the low frequencies, and no agreement for the high frequencies. We can attribute the discrepancy in the structure of the high-harmonic spectrum to quantum in-

terference effects, as before. However, the agreement for the low-order harmonics in this case is actually quite remarkable, because here, most of the electrons are bound instead of ionized. To probe the extent of this agreement deeper, we study the spatiotemporal evolution of the harmonic radiation between $2\omega_L$ and $8\omega_L$, as shown in Fig. 5.25. In the low ionization fraction regime, the classical and quantum models agree for the amplitude of the radiation in this frequency band in both $z$ and $\tau$, as seen by comparing Fig. 5.25a to Fig. 5.25c, particularly for $\tau < 6T_o$. They also match in phase, as seen in the filtered time-dependent field at $z = 1$ mm in Fig. 5.25. This suggests that the generation mechanism for these low-order harmonics is the same in both cases. In the intermediate ionization fraction regime, the spatiotemporal evolution of the filtered field's amplitude and phase is close in the classical and quantum cases for $\tau < 3T_o$, but for larger $\tau$ there are significant discrepancies. This indicates that another mechanism of low-order harmonic generation takes over in the quantum case in this regime.

Because the prominent low-order harmonics of Fig. 5.24 are absent in the scattering spectrum in Fig. 5.19, we can conclude that these harmonics are due to the presence of bound electrons. Aside from interfering with the recolliding electrons, the large population of bound states contributes to harmonic radiation in two ways: through the nonlinear response of bound electrons to the field [48, 49, 129, 160, 161], and through the tunneling current. The radiation from the latter contribution is also known as Brunel radiation [50, 162]. Both of these mechanisms of bound state radiation dominate the response of the atoms at the fundamental frequency and the low harmonic orders, i.e. those magnified in the insets of Fig. 5.24. Because we tuned the classical model to match the ionization probabilities of the quantum model, we should expect the Brunel contribution of both models to be similar. On the other hand, if it turns out that the classical and quantum models also agree for the nonlinear response of bound electrons, this is an added bonus. The advantage of the classical model compared to the quantum model is that by looking in phase space, we can distinguish the contributions of bound electrons from ionizing electrons. This allows

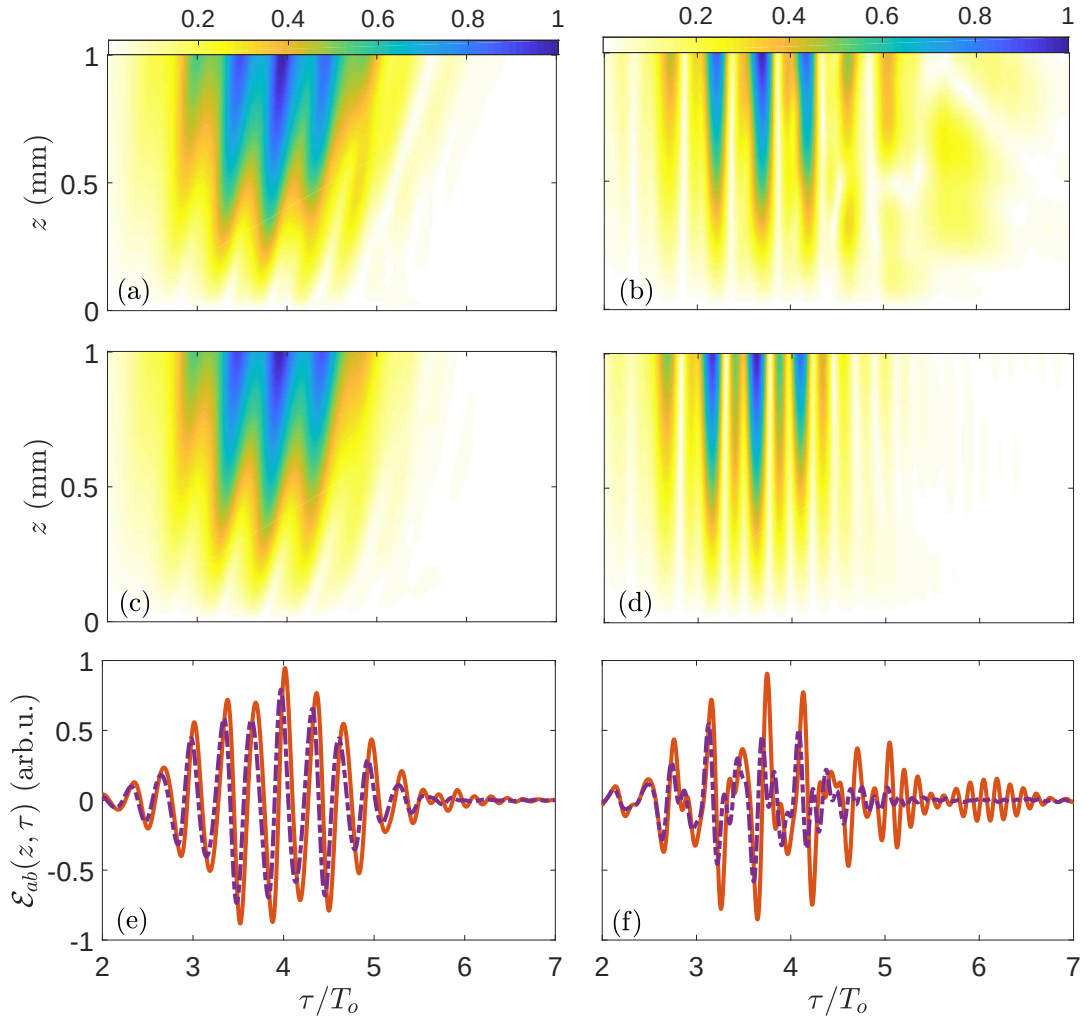


Figure 5.25: Spatiotemporal evolution of low-order harmonics in the low-ionization fraction case (a),(c),(e) and the intermediate ionization-fraction case (b),(d),(f). Frequencies in the range $[2\omega_L, 8\omega_L]$ were considered in the calculation of the filtered analytic field $\hat{\mathcal{E}}_{ab}(z,\tau)$, where the post-processing consisted of multiplying $\mathcal{E}$ by a $\sin^2$ window. (a),(b) Harmonic amplitude $|\hat{\mathcal{E}}_{ab}(z,\tau)|$ from the quantum model. (c),(d) Harmonic amplitude $|\hat{\mathcal{E}}_{ab}(z,\tau)|$ from the classical model. (e),(f) Time-dependent harmonic field $\mathrm{Re}[\hat{\mathcal{E}}_{ab}(z,\tau)]$ at $z = 1$ mm. In both sets of panels, the fields are normalized by the maximum harmonic amplitude obtained in the quantum model.

us to confirm that in fact, the classical model does capture the bound electron radiation.

As suggested by Fig. 5.14, the electrons in the classical model follow very different kinds of trajectories depending on their initial energy $E_i$. Bound electron trajectories are certain to end in a state with energy $E_f$ very close to $E_i$. In Fig. 5.14, there is clearly a critical energy which separates trajectories that are certain to remain bound from those which have a significant probability of ionizing, i.e. ultimately ending with an energy $E_f > 0$. Note that, in Fig. 5.14, we only represent $E_f < 0$, but the region of $E_i$ where we observe a wide-ranging distribution of $E_f$ far from $E_i$ actually coincides with the one from which ionization takes place. We obtained this critical energy $E_c(z)$ as a function of the propagation distance from our propagation simulations. Subsequently, we split the distribution function into two parts: the part consisting electrons with $E_i < E_c$ and the part consisting of electrons with $E_i \geq E_c$. By averaging over the latter distribution, we obtained the classical tunneling current $\overline{v}_t(z, \tau)$, which is the mean dipole velocity of the electrons likely to ionize, emulating quantum tunneling. Averaging over the former distribution gives the classical bound current $\overline{v}_b(z, \tau)$. Because the total distribution function is the sum of these two distribution functions, the total classical current (or mean dipole velocity) is $\overline{v} = \overline{v}_b + \overline{v}_t$.

Figure 5.26 compares the spectra of the tunneling current and the total current for $z = 0$ and $z = 0.5$ mm in both the low- and intermediate-ionization regimes. In the low-ionization fraction regime, where the initial ionization probability is about $5 \times 10^{-3}$, the tunneling current makes a small contribution to the first and third harmonics at $z = 0$, as show in Fig. 5.26a, and by $z = 0.5$ mm, its contribution to the fifth harmonic becomes relatively small as well, as shown in Fig. 5.26c. Therefore, most of the low-order harmonic signal throughout propagation in the low-ionization fraction regime is due to the bound-electron radiation, as opposed to Brunel radiation. The good agreement between the classical and quantum ionization probabilities implies that the classical tunneling current is in agreement with the tunneling current, and correspondingly the bound currents are in agreement as well. Thus, we conclude that in the low-ionization fraction regime, the pri-

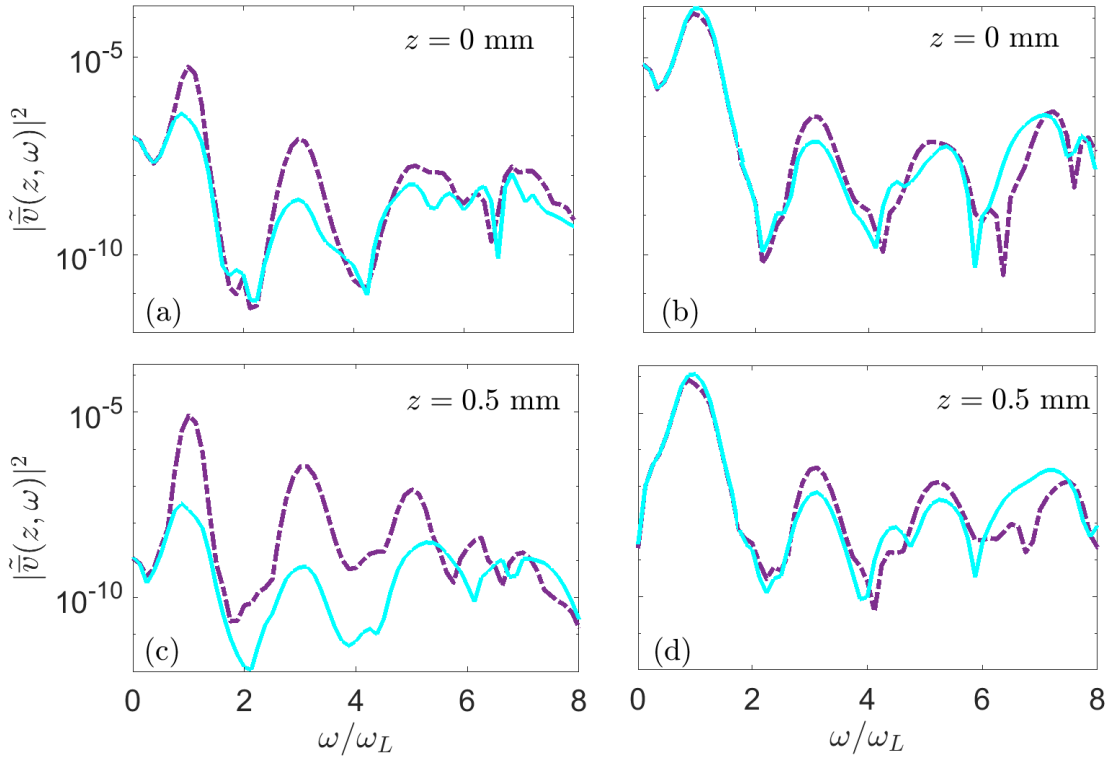


Figure 5.26: Evolution of the classical tunneling current spectrum in the low-ionization fraction case (a),(c) and the intermediate-ionization fraction case (b),(d). The dash-dotted purple curves are the full dipole velocity spectrum $|\tilde{\bar{v}}(z,\omega)|$ from the classical model, while the solid cyan curves are the spectrum of the classical tunneling current $|\tilde{\bar{v}}_t(z,\omega)|$. A $\sin^2$ window was applied to the velocities for the computation of the spectrum.

mary mechanism of low-order harmonic generation, at least up to the fifth harmonic, is the bound-electron nonlinearity. Furthermore, the classical model and quantum model are in agreement for the generation and propagation of these harmonics, as shown in Fig. 5.25.

For the intermediate-ionization regime, on the other hand, Figs. 5.26b and 5.26d indicate that the tunneling current is comparable to the total current. Indeed, it seems to dominate the total current at frequencies near $\omega_L$, and for the other harmonics the two currents are comparable, indicating the bound radiation and Brunel radiation are also comparable. However, in this regime the agreement between the classical and quantum low-order harmonics for $\tau < 3T_o$ (Fig. 5.25b, 5.25d, and 5.25f) gives way to gradually worse agreement for larger $\tau$. The agreement for smaller $\tau$, when the probability of ionization is still relatively small, suggests that the radiation due to the bound electron motion in the classical and quantum models are still in agreement, as in the low-ionization fraction regime. At the same time, we also expect the tunneling current and thus the Brunel radiation to be in agreement. Hence, the discrepancy must be due to quantum interference effects, which at these low-harmonic orders may come from low-energy recollisions [73] and electron trapping in excited states [163].

*High-order harmonic generation*

Now we consider the buildup of high-harmonic radiation during the laser pulse propagation through ground-state atoms. In Fig. 5.27a-b, we have plotted the amplitude of the field $\mathcal{E}$ in the quantum model for frequencies $\omega > 2U_p + |I_p|$ in the $(z, \tau)$ plane, for the low - and intermediate-ionization fraction regimes, respectively. Note that $U_p$ is larger in the intermediate-ionization fraction regime, because of the higher initial peak intensity of the pulse. We observe very different behavior in the two cases. In the low-ionization fraction regime, the maximum amplitude of the high-harmonic radiation oscillates considerably during propagation, a phenomenon known as Maker fringes [38, 164], limiting the coherent buildup of the high harmonics. On the other hand, in the intermediate-ionization fraction

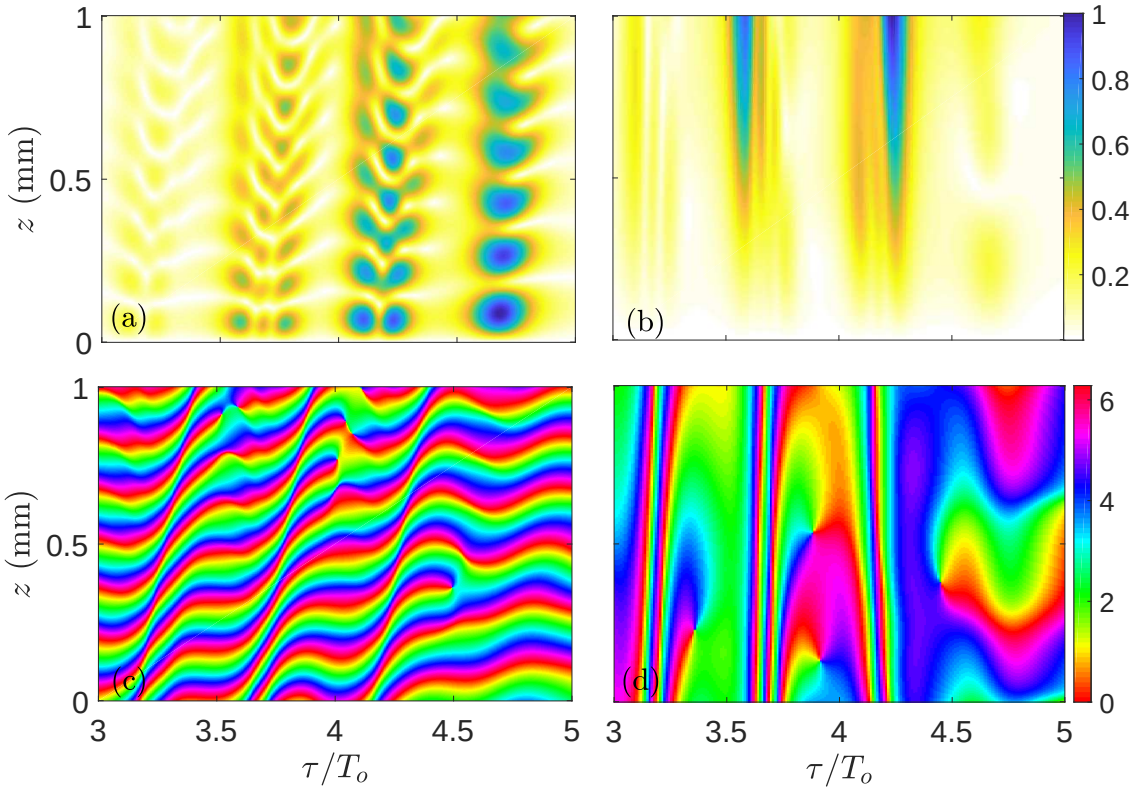


Figure 5.27: Spatiotemporal buildup of high-harmonic radiation in the quantum model in the low-ionization fraction case (a),(c) and the intermediate-ionization fraction case (b),(d). Frequencies in the range $[2U_p + I_p, \infty)$ were considered in the calculation of the filtered analytic field $\hat{\mathcal{E}}_{ab}(z,\tau)$ and the filtered analytic dipole velocity $\hat{\overline{v}}_{ab}(z,\tau)$, where the post-processing consisted of multiplication by a $\sin^2$ window. (a),(b) Amplitude of the high-harmonic part of the field, normalized to the maximum amplitude recorded in each simulation. (c),(d) Phase $\phi_{ab} \mod 2\pi$ of the high-harmonic emission, in radians, computed from the phase of $\hat{\overline{v}}_{ab}(z,\tau)$.

regime, we observe two bursts of radiation, around $\tau = 3.6T_o$ and $\tau = 4.2T_o$, which build up continuously throughout propagation. The improved coherent buildup in this regime compared to the low-ionization fraction regime is also reflected by the higher intensity high-harmonic spectrum at $z = 1$ mm in Fig. 5.24b compared to Fig. 5.24a.

This behavior indicates differing phase-matching conditions in each regime, and this can be revealed by computing the phase of the high-harmonic emission. The source of the radiation is the dipole velocity of the atoms $\overline{v}$. In order for the radiation to build up coherently over a given propagation distance, the phase of the radiation contained in $\overline{v}$ must not vary much over that distance. We compute the phase by first computing the analytic dipole velocity $\hat{\overline{v}}_{ab}(z,\tau)$ in the frequency range of interest, applying Eq. (5.14) to $\overline{v}$. Now, the phase of the complex $\hat{\overline{v}}_{ab}$ will tell us the phase of the emitted radiation. The phase will have a natural evolution at the carrier frequency of the signal in this frequency range, so we must subtract this off to observe variations in the phase about this reference phase. We define the reference phase as

$$\phi_{\mathrm{ref}}(\tau) = \arg[\hat{\overline{v}}_{ab}(0,0)] + \left(\frac{1}{\tau_f}\int_0^{\tau_f} \frac{d}{d\tau'}\arg[\hat{\overline{v}}_{ab}(0,\tau')]\mathrm{d}\tau'\right)\tau.$$

Hence, we define the phase of the high-harmonic emission as

$$\phi_{ab}(z,\tau) = \arg[\hat{\overline{v}}_{ab}(z,\tau)] - \phi_{\mathrm{ref}}(\tau).$$

We have plotted $\phi_{ab}(z,\tau)$ for the frequency range $\omega > 2U_p + |I_p|$ in Figs. 5.27c-d. In the low-ionization fraction regime, we see that the phase of emission varies significantly throughout propagation, possibly at a constant rate which depends on $\tau$. This behavior is consistent with the oscillations in the amplitude of the radiated field at these frequencies observed in Fig. 5.27a: a rotating phase during propagation would imply that the high-harmonic modes alternate growing and receding as the radiation at a particular $z$ alternates from in-phase to out-of-phase with the incoming radiation. On the other hand, in

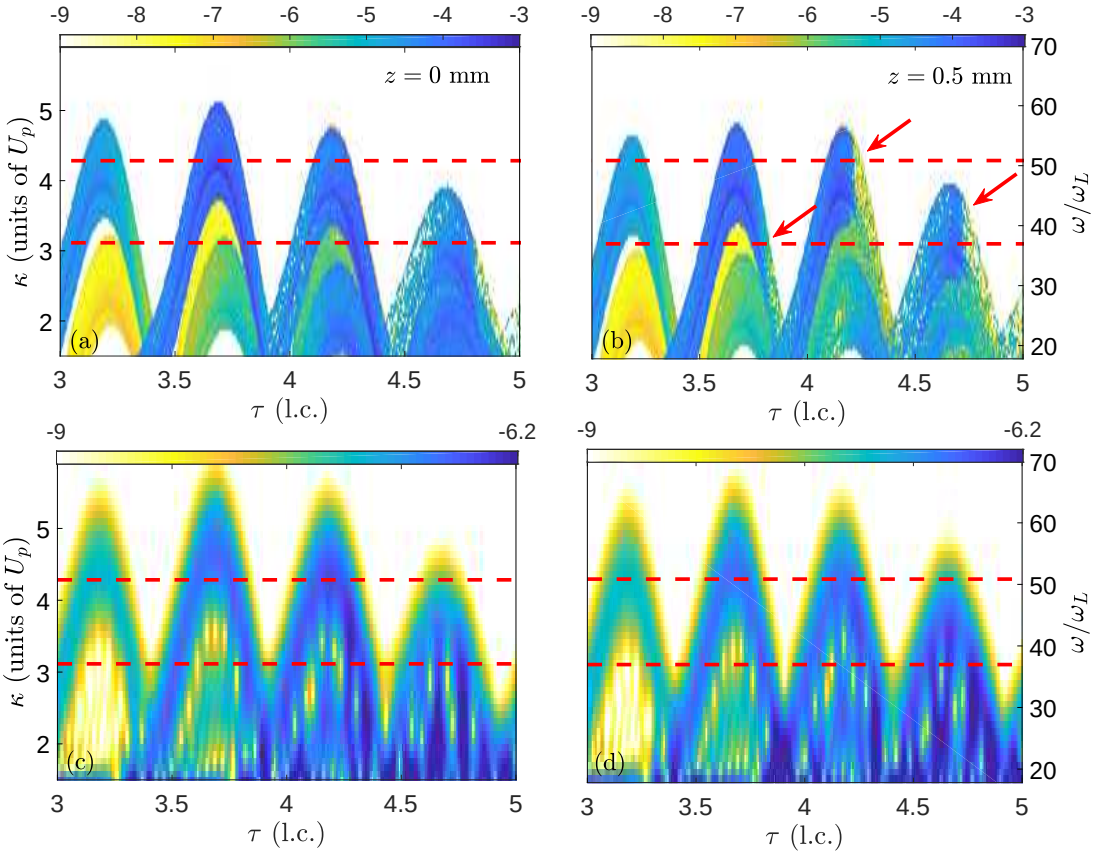


Figure 5.28: Electron dynamics at $z = 0$ (a),(c) and $z = 0.5$ mm (b),(d) during laser-pulse propagation through a ground-state gas in the intermediate-ionization fraction regime. (a),(b) Recollision flux $R(\kappa, \tau; z)$ from the classical model. (c),(d) Spectrogram of the dipole acceleration $d_a(\tau)$ from the quantum model. The spectrograms were computed using a $\cos^4$ window of duration $0.15T_o$. The dotted lines indiciate $2U_p + |I_p|$ and $3.17U_p + |I_p|$. The left axes, indicating the recollision kinetic energy $\kappa$, are related to the right axes, indicating the radiated frequency $\omega$, by $\kappa = \omega$.

the intermediate-ionization fraction regime, for certain fixed $\tau$, we see bands of phase of which are almost constant in $z$. The places where this occurs are consistent with the values of $\tau$ for which the bursts of high-harmonic radiation are seen to build up.

Can we explain the phase properties of the high-harmonic emission using the classical model? It is not immediately obvious how to do so. In Fig. 5.28, we compare the recollision flux from the classical model to the spectrogram of high-harmonic emission from the quantum model in the intermediate-ionization regime. As in the scattering-propagation experiment, we see a strong correspondence between the classical and quantum calculations,

even after propagation to $z = 0.5$ mm. Comparing Figs. 5.28c and 5.28d, we see that between $z = 0$ and $z = 0.5$ mm, the intensity of emission at given times and frequencies has not changed significantly. On the other hand, Fig. 5.27d shows that at certain times, the phase of the emission has changed significantly. Is there anything in the classical recollision flux plots which might provide an explanation for this behavior? One thing we have observed in these plots is the following. We look at each branch of recollisions containing the maximum-energy recollision for a given time-interval, i.e. the dark blue branches in Fig. 5.28a. As propagation proceeds, we observe the part of these branches colored blue (indicated the most probably trajectories) moves along these branches to the left, as indicated by the arrows in Fig. 5.28b. The branches remain, but where they were once blue, they are now either green or yellow, indicating a much lower probability. It is possible that the different colors of the branches represent different families of trajectories, but a more detailed trajectory analysis would be necessary to confirm this. Also, it appears that the coherent buildup seen in Fig. 5.27b occurs preferentially at the times $\tau$ where the recollision branches in Fig. 5.28 remain blue the longest. More work needs to be done to clarify this, in particular the relationship with the classical trajectories.

## 5.6 Higher-dimensional models

In this section, we report the results of simulations of models of higher dimensions than the unidirectional pulse propagating through a gas of one-dimensional atoms. Up until now, the analysis has focused on this case in part because its low dimension makes it fastest to simulate and easiest to analyze. However, it also seems to be the minimal description necessary to capture the HHG-related phenomena occurring in the parameter ranges of interest. The simulations presented here are intended to provide some evidence that this is indeed the case, i.e. that our results and conclusions are valid even when the dimension of the model is increased in certain ways.

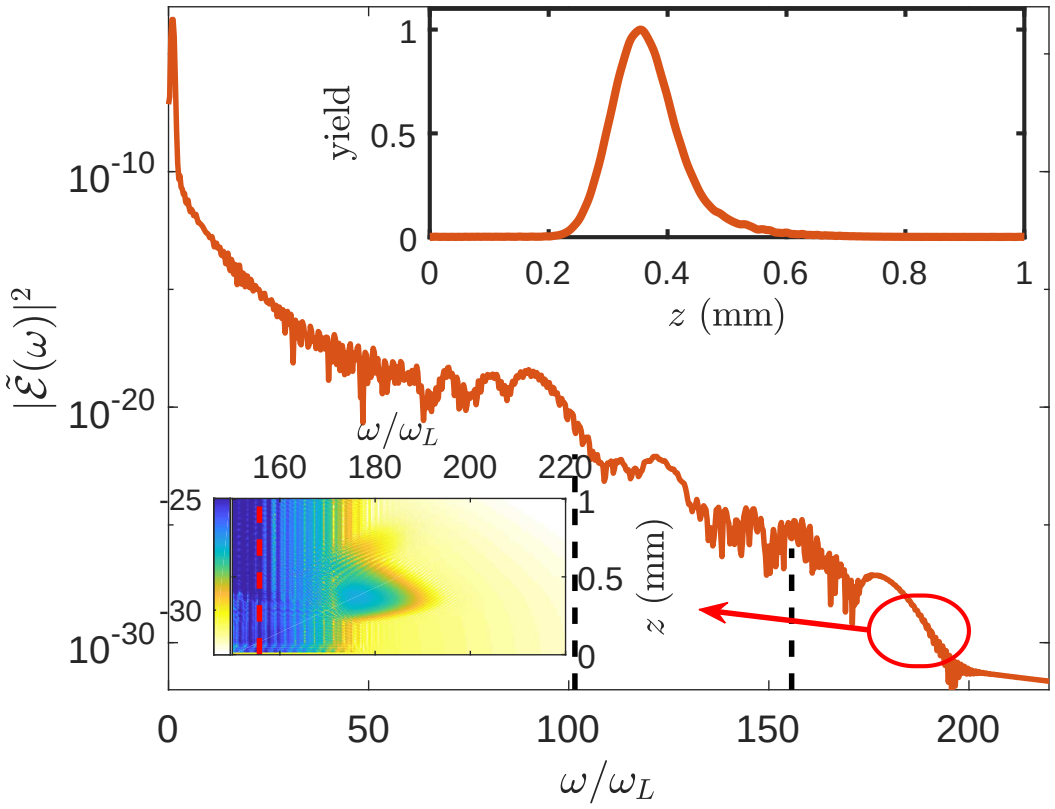


Figure 5.29: High harmonic spectrum for the scattering-propagation experiment for the quantum model with 2D atoms at $z = 0.37$ mm. The dashed lines indicate $2U_p + |I_p|$ $3.17U_p + |I_p|$. For the 2D quantum atom, we estimate $I_p \lesssim -0.339$ a.u. using the variational principle with a Gaussian trial wave function for the ground state. Upper inset: Normalized integrated yield of harmonics with $\omega > 175\omega_L$ as a function of $z$. Lower inset: Spectrum of the harmonics in the cutoff region as a function of $z$. The harmonic intensities are indicated by the logarithmic color scale.

### 5.6.1 Scattering-propagation experiment with two-dimensional quantum atoms

Figure 5.29 shows the result of a simulation of unidirectional pulse propagation through 2D quantum atoms, i.e. Eqs. (5.4) and (5.5), in the scattering-propagation setup. The initial conditions are the same as in Sec. 5.5.1, except with an initial condition for the 2D wave function of

$$\psi_0(x,y) = \left(\frac{\pi}{\gamma^2}\right)^{-1/2} \exp\left\{-\frac{\gamma^2}{2}\left[\left(x - \frac{E_0}{\omega_L^2}\right)^2 + y^2\right]\right\}.$$

The shape of the spectrum is qualitatively similar to the 1D case, seen in Fig. 5.19. This is true throughout propagation, in particular for the cutoff region of the spectrum, evidenced by the similarity between the lower insets of Figs. 5.19 and 5.29. The buildup and absorption of the anomalous high harmonics is also similar, seen when comparing the upper inset of Fig. 5.29 and Fig. 5.22b. The similarity between the 1D and 2D results suggest that the mechanism of the cutoff extension, namely the emergence of recollisions with higher maximum kinetic energies, is robust with respect to the dimension of the atomic model. This provides additional evidence that the 1D atomic models with a 1D field are sufficient to understand the mechanisms of HHG in linearly-polarized fields.

### 5.6.2 Forward- and backward-propagating waves with one-dimensional classical atoms

Here, we investigate the strength of the backward-propagating waves compared to the forward-propagating waves in the classical model with 1D atoms. We solve Eqs. (5.6) coupled to Eq. (5.7). Because these equations require a numerical representation of the particles at every $z$ simultaneously, a simulation for realistic gas lengths (on the order of millimeters) is prohibitively computationally expensive. Hence, we performed a much smaller-scale simulation of the pulse entering the gas from vacuum. The initial conditions of the fields $\alpha(z, t = 0) = \alpha_0(z)$ and $\beta(z, t = 0) = \beta_0(z)$ are taken as

$$\alpha_0(z) = \begin{cases} E_0 \cos\left(\frac{\omega_L z}{c}\right) \sin^2\left(\frac{2\pi(z-L/2)}{L}\right) & \text{for } -\frac{L}{2} \leq z < 0, \\ 0 & \text{for } 0 \leq z < \frac{L}{2}, \end{cases} \tag{5.32a}$$

$$\beta_0(z) = 0, \tag{5.32b}$$

where $E_0 = 0.0377$ a.u., $\omega_L = 0.05$ a.u., and $L = 8cT_o$. These parameters correspond to a peak incident pulse intensity of $I = 5 \times 10^{13}$ W$\cdot$cm$^{-2}$, a wavelength $\lambda_L = 0.9$ $\mu$m, and an incident FWHM pulse duration of $6$ fs, and a domain length of $L = 7$ $\mu$m. They are meant to be similar to the parameters of the low ionization fraction regime (Sec. 5.4.2), though a

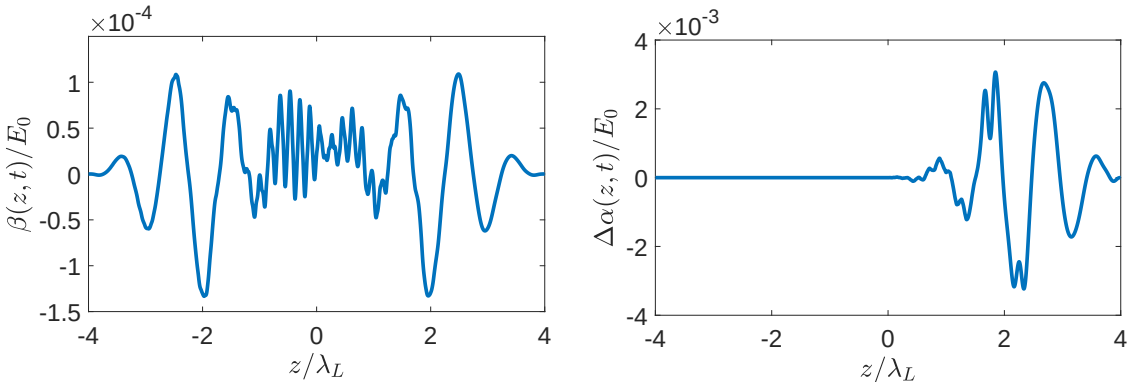


Figure 5.30: Forward and backward propagating waves at $t = 4T_o$. Left panel: backward propagating wave $\beta(z,t)$. Right panel: The part of the forward propagating wave due to radiation, i.e. $\Delta\alpha(z,t) = \alpha(z,t) - \alpha_0(z - ct)$.

smaller wavelength and pulse duration are chosen here to reduce the computational time. The gas density $\rho(z)$ is taken as

$$\rho(z) = \begin{cases} 0 & \text{for } -\frac{L}{2} \le z < 0, \\ 2 \times 10^{19}\ \text{cm}^{-3} & \text{for } 0 \le z < \frac{L}{2}. \end{cases}$$

With the above density and the field initial conditions (5.32), $t = 0$ corresponds to the time the front of the pulse first enters the gas. The initial electron distribution function $f(x, v, z, t = 0) = f_0(x, v)$ is given by Eq. (5.27) with $g_\sigma$ as the initial energy distribution.

Figure 5.30 shows the results of the simulation at $t = 4T_o$. We see that at at this point, the backward propagating wave reaches the left boundary of the domain (left panel Fig. 5.30) while the forward propagating wave reaches the right boundary. We have observed that the high-frequency oscillations around $z = 0$ seen in the left panel of Fig. 5.30 are at least in part caused by our relatively coarse discretization of the distribution function: when we increase $N_p$, the amplitude of these oscillations decreases. However, the maximum amplitude of the radiated fields seems close to converged. For a fair comparison of the typical amplitudes of the forward-propagating versus backward-propagating radiation, we have plotted only the forward-propagating radiation due to the particles $\Delta\alpha(z,t) =$

$\alpha(z,t) - \alpha_0(z - ct)$ in the right panel of Fig. 5.30. Because the propagation distance is so short, neither of the fields' amplitudes is comparable to $E_0$: the larger of the two, $\Delta\alpha(z,t)$ has a maximum amplitude of about $3 \times 10^{-3} E_0$. However, the maximum amplitude of $\beta(z,t)$ is about 23 times smaller than that. Because it is so small, it is unlikely that it has a significant influence on the electron dynamics. Thus, this provides some justification for neglecting backward propagating waves from the reduced models.

# CHAPTER 6
# CONCLUSION

The difficulty in painting a complete theoretical picture of high harmonic generation lies in the multiscale, nonperturbative nature of the process. On the single-atom level, ionization depends nonlinearly on the strength of the incident laser field, and the subsequent electron dynamics is chaotic. This underlying complexity is reflected on the macroscopic scale by the nontrivial spatiotemporal reshaping of the laser field during propagation. This reshaping impacts the recolliding trajectories further along the gas, with the coherent buildup of high harmonic radiation hinging on the continued in-phase emission from these trajectories all along the gas. In this thesis, we have examined these processes implicated in HHG on both microscopic and macroscopic scales using classical mechanics. We have focused on first-principles reduced models, which fully retain the nonlinear Coulomb interaction on the microscopic scale and the self-consistent field interaction on the macroscopic scale at the expense of describing the system's behavior in three-dimensional space. Their reduced dimension makes the models tractable to theoretical analysis and numerical simulation. Furthermore, we have exploited the phase space perspective provided by the classical model to identify the mechanisms behind recollisions, coherent harmonic radiation, and laser pulse reshaping observed in both classical and quantum calculations.

## 6.1 Summary

In Ch. 3, we undertook an analysis of recollision dynamics in very strong, external laser fields, when one would expect the strong-field approximation to be valid. We found instead that the Coulomb field plays an indispensable role, enhancing delayed recollisions and promoting them to energies as high as the high-harmonic cutoff. Besides the physical effect of recalling electrons, the Coulomb interaction introduces nonlinearity into the laser-atom

system, which leads to the creation of unstable periodic orbits. The invariant manifolds of one of these orbits was demonstrated to organize the delayed recollisions in phase space: the stable manifold separates trajectories with different delays and the unstable manifold regulates the recollision energy of each trajectory. Our results underscore the importance of fully accounting for Coulomb effects when one studies recollision-driven harmonic generation, even in the over-the-barrier ionization regime where complete single ionization is assured [158].

In Ch. 4, we derived tractable reduced models for intense laser pulse propagation from first principles using the variational formulation. The Maxwell-Schrödinger equations in the dipole approximation were cast as a classical field theory, with both an action principle and a Hamiltonian formulation. A variant of the Vlasov-Maxwell equations was proposed as the classical model corresponding to the Maxwell-Schrödinger equations, and its variational structure was shown to have similarities to that of the Vlasov-Mawell equations and the Maxwell-Schrödinger equations. This similarity facilitated parallel derivations of a hierarchy of classical and quantum reduced models for the self-consistent interaction between atomic electrons and electromagnetic waves. Because we consistently worked in the variational formulation, our reduced models preserve the variational structure of the parent models and contain no unphysical dissipation. The quantum model we derived agrees with previously obtained reduced models [132, 137]. Moreover, the Hamiltonian formulation of the reduced models allowed us to identify conservation laws for the classical and quantum models, which for the quantum models had not yet been deduced.

In Ch. 5, we investigated the implementation of the classical model for intense laser pulse propagation and used it to identify the mechanisms behind the coherent buildup of high-harmonic radiation in phase space. Through comparisons with quantum simulations, we showed how to build a classical analog of the electron's ground-state wave function that leads to quantitative agreement between quantum and classical propagation simulations. These simulations can agree stunningly well for the dominant frequency components of

the field near the incident laser frequency $\omega_L$, where ionization losses and the blueshift of the driving laser are encoded. On the other hand, for high frequencies, we found that quantum interference effects play an essential role in shaping the high-harmonic plateau and cutoff. Nevertheless, we found that the classical model accurately predicted the timing and frequency of HHG throughout propagation through its faithful portrayal of the recolliding trajectories. Thus, we were able to explain the unexpected extension of the high-harmonic cutoff seen in the quantum scattering-propagation calculation in terms of an increase of the maximum possible recollision energy seen in the classical calculation. Furthermore, when considering harmonic generation from ground-state atoms, we showed that the classical and quantum models can exhibit quantitative agreement for low-order harmonic generation, and in this case the classical model conclusively shows this radiation comes from the nonlinear response of bounded electrons.

## 6.2 Perspectives

We believe the reduced classical model for laser pulse propagation that we built in this thesis opens up several potential avenues of further investigation. For HHG, the connection between the phase properties of the high-harmonic emission observed in the quantum calculation and the corresponding recolliding trajectories of the classical calculation needs to be explored further. Semiclassical calculations show that the classical action accumulated along a trajectory and parameters such as the time between ionization and recollision largely determine the phase of radiation from that trajectory [55, 64]. These quantities can be directly extracted from our classical model, so perhaps combining a study of the evolution of these quantities throughout propagation with semiclassical arguments can form a more complete picture of high-harmonic buildup based on the classical model. There are opportunities to advance the model itself as well. One obvious route is to extend the model to allow for higher-dimensional electromagnetic fields. This is crucial not only for modeling HHG in elliptically- and circularly-polarized fields, but also for accounting for

three-dimensional effects, in particular plasma defocusing [40, 43].

Besides HHG, our model may also be relevant for understanding THz generation and filamentation. For the latter, the classical model may address the increasing need for first-principles models of the microscopic laser-atom interaction [121, 160]. An extension of the model into three dimensions would be a prerequisite for filamentation. For THz generation, our present reduced model may already prove useful. A significant source of on-axis THz emission is the spatially asymmetric distribution of ionized electrons with respect to the $x$-direction [143, 165]. Furthermore, control of the THz generation process has been demonstrated by modifying the electron trajectories after ionization using multicolor fields [119, 140]. With the successes of the classical model in reproducing quantum ionization rates and accurately describing electron trajectories during pulse propagation, it is likely that all the necessary elements are in place for a study of THz generation based on the classical model. A particularly intriguing possibility is connecting the conserved quantities, $\mathcal{Q}_\alpha$ and $\mathcal{Q}_\beta$, Eqs. (4.35), to THz emission. These quantities contain a term proportional to $\int \rho \overline{x}_\mathrm{e} \mathrm{d}z$, which is the average $x$-component of the electron's position along the propagation direction. This term should serve as a measure of the asymmetry of the ionized-electrons, thus providing a potential link to THz emission.

A last possibility concerns using Hamiltonian control theory to optimize properties of HHG emission, e.g. optimizing phase-matching to increase the range of coherent harmonic buildup. Knowledge of a Hamiltonian system's invariant solutions allows the application of Hamiltonian control theory to steer a system's behavior towards desired outcomes [166]. In the context of the free electron laser, which is also driven by the self-consistent interaction of electrons and the electromagnetic field, Hamiltonian control has been successful in stabilizing the intensity fluctuations of the radiated light [167, 168]. Hence, it natural wonder if, using Hamiltonian control of the classical model, one can stabilize the intensity fluctuations of the high-harmonic light that occur during propagation, also known as Maker fringes [38, 164].

# Appendices

# APPENDIX A
# PROOF OF MORRISON'S LEMMA

In our discussion of the Jacobi identity for finite-dimensional Hamiltonian systems in Ch. 2, we use a result sometimes referred to as Morrison's lemma [95], which we prove here. The lemma states that, for arbitrary observables $F(\mathbf{z})$, $G(\mathbf{z})$ and $H(\mathbf{z})$ and an antisymmetric Poisson matrix $\mathbf{\Pi}(\mathbf{z})$, we have

$$\Pi_{in}\Pi_{jk}\partial_i F\left(\partial^2_{nj}G\partial_k H+\partial_j G\partial^2_{nk}H\right)+\Pi_{in}\Pi_{jk}\partial_i G\left(\partial^2_{nj}H\partial_k F+\partial_j H\partial^2_{nk}F\right)$$
$$+\Pi_{in}\Pi_{jk}\partial_i H\left(\partial^2_{nj}F\partial_k G+\partial_j F\partial^2_{nk}G\right)=0,$$

where summation over each index is implied. To demonstrate this, we group together all the terms containing the same orders of differentiation for each of $F$, $G$, and $H$ on the left-hand side of the above equation and rearrange, yielding

$$\begin{aligned}&\Pi_{in}\Pi_{jk}\partial_i F\partial_k H\partial^2_{nj}G+\Pi_{in}\Pi_{jk}\partial_j F\partial_i H\partial^2_{nk}G\\+&\Pi_{in}\Pi_{jk}\partial_i G\partial_k F\partial^2_{nj}H+\Pi_{in}\Pi_{jk}\partial_j G\partial_i F\partial^2_{nk}H\\+&\Pi_{in}\Pi_{jk}\partial_i H\partial_k G\partial^2_{nj}F+\Pi_{in}\Pi_{jk}\partial_j H\partial_i G\partial^2_{nk}F\end{aligned}$$

We have arranged the terms above such that the sequence of indices appearing across each line are the same, with only the order of $F$, $G$, and $H$ changing from line to line. Because the indices in each term are just dummy indices that are summed over, they may be renamed however we like. By renaming the indices $k \leftrightarrow j$ followed by $n \leftrightarrow k$ for the first term of each line, and $i \leftrightarrow j$ for the second term of each line, and using the commutativity of derivatives, the $FGH$ terms may be factored out of each line. This gives a common factor

of a Poisson matrix term on each line, such that the final expression may be factored to give

$$\left(\Pi_{ik}\Pi_{nj} + \Pi_{ik}\Pi_{jn}\right)\left(\partial_i F \partial_j H \partial^2_{nk} G + \partial_i G \partial_j F \partial^2_{nk} H + \partial_i H \partial_j G \partial^2_{nk} F\right).$$

By the antisymmetry of $\mathbf{\Pi}$, the Poisson matrix term is zero, proving the lemma.

This lemma is extremely useful, because it simplifies calculations for verifying the Jacobi identity for Poisson brackets. Indeed, as long as the Poisson matrix is antisymmetric (which is a prerequisite), this lemma means one only needs to check whether Eq. (2.15) is satisfied in order to verify the Jacobi identity. In fact, in Ref. [95], this lemma is proved for the infinite-dimensional case. Specifically, it is shown that terms involving second-order functional derivatives which arise from the calculation of the Jacobi identity will automatically cancel out by virtue of the antisymmetry of the Poisson operator $\hat{\mathbf{\Pi}}$.

# APPENDIX B

# DERIVING THE DIPOLE APPROXIMATION WITHIN THE VARIATIONAL FORMULATION

In Ch. 4, our parent models in both the classical and quantum cases assume the dipole approximation from the outset. Here, we show a higher-level parent model, only requiring hypotheses HP 1-2. The electrons are still assumed to be nonrelativistic, but because we do not make the dipole approximation, magnetic effects are included. We only show the classical version here. We find it most natural to write down the action (or Hamiltonian) first, and subsequently deduce the model equations. The action is

$$\mathcal{A}[\mathbf{x}, \varphi, \mathbf{A}] = \int (\mathcal{L}_{\mathrm{P}} + \mathcal{L}_{\mathrm{EM}}) \mathrm{d}t, \tag{B.1a}$$

$$\mathcal{L}_{\mathrm{P}} = 4\pi \int \rho(\mathbf{r}) \left[ \frac{|\dot{\mathbf{x}}|^2}{2} - V(\mathbf{x}) - \varphi(\mathbf{r}, t) + \varphi(\mathbf{r} + \mathbf{x}, t) - \dot{\mathbf{x}} \cdot \mathbf{A}(\mathbf{r} + \mathbf{x}, t) \right] \mathrm{d}\mu_0 \mathrm{d}^3\mathbf{r}, \tag{B.1b}$$

$$\mathcal{L}_{\mathrm{EM}} = \frac{1}{2} \int \left( |\nabla \varphi(\mathbf{r}) + \dot{\mathbf{A}}(\mathbf{r})|^2 - c^2 |\nabla \times \mathbf{A}(\mathbf{r})|^2 \right) \mathrm{d}^3\mathbf{r}, \tag{B.1c}$$

Here, we have suppressed the functional dependence of the electron displacement field $\mathbf{x}$, though it is the same as before, namely $\mathbf{x} = \mathbf{x}(\mathbf{r}, t, \mathbf{x}_0, \mathbf{v}_0)$. Compared to the action Eq. (4.6) in the dipole approximation, the only change is to the particle Lagrangian $\mathcal{L}_{\mathrm{P}}$. The electrostatic potential $\varphi$ now appears in two terms, with the first representing the electrostatic energy of the ions, and the second the electrostatic energy of the electrons (which is why their sign differs). Also, $\varphi$ and $\mathbf{A}$ are now evaluated at $\mathbf{r} + \mathbf{x}$, the position of the electron in the lab frame, as opposed to $\mathbf{r}$, as was the case in Eq. (4.6b). This choice for the Lagrangian is natural: the electromagnetic potential part of $\mathcal{L}_{\mathrm{P}}$ is essentially the Low Lagrangian [106], with a term added to account for the electrostatic potential of the ions.

We confirm that this Lagrangian properly captures the physics by computing the Euler-Lagrange equations. These are

$$\ddot{\mathbf{x}} = -\nabla_{\mathbf{x}} V(\mathbf{x}) + \nabla\varphi(\mathbf{r}+\mathbf{x},t) + \dot{\mathbf{A}}(\mathbf{r}+\mathbf{x},t) - \dot{\mathbf{x}} \times \left[\nabla \times \mathbf{A}(\mathbf{r}+\mathbf{x},t)\right], \tag{B.2a}$$

$$-\left[\nabla^2\varphi(\mathbf{r},t) + \nabla\cdot\dot{\mathbf{A}}(\mathbf{r},t)\right] = 4\pi\left[\rho(\mathbf{r}) - \int \rho(\mathbf{r}')\delta^3\left(\mathbf{r}-\mathbf{r}'-\mathbf{x}(\mathbf{r}',t,\mathbf{x}_0,\mathbf{v}_0)\right)\mathrm{d}\mu_0\mathrm{d}^3\mathbf{r}'\right], \tag{B.2b}$$

$$-\left[\nabla\dot{\varphi}(\mathbf{r},t) + \ddot{\mathbf{A}}(\mathbf{r},t)\right] = c^2\nabla\times(\nabla\times\mathbf{A}(\mathbf{r},t)) + 4\pi\int \rho(\mathbf{r}')\dot{\mathbf{x}}(\mathbf{r}',t,\mathbf{x}_0,\mathbf{v}_0)\delta^3\left(\mathbf{r}-\mathbf{r}'-\mathbf{x}(\mathbf{r}',t,\mathbf{x}_0,\mathbf{v}_0)\right)\,\mathrm{d}\mu_0\mathrm{d}^3\mathbf{r}'. \tag{B.2c}$$

The first equation is the Lorentz-force law for the electrons, which now includes the magnetic force and also evaluates the fields at $\mathbf{r}+\mathbf{x}$, instead of $\mathbf{r}$. The second equation is Gauss' Law, with the source being the total microscopic charge density. This is the sum of the ion charge density and the electron charge density, which is an integral over the electrons whose present position in the lab frame is $\mathbf{r} = \mathbf{r}' + \mathbf{x}(\mathbf{r}',t,\mathbf{x}_0,\mathbf{v}_0)$. The last equation is the Maxwell-Ampère Law, where again the microscopic current density is computed by integrating over the electrons presently located at $\mathbf{r}$. Hence, the physical content of these equations is reasonable and contains the elements we expected. To implement the dipole approximation and derive the classical parent model of Ch. 4, one simply Taylor expands the electromagnetic potential parts of Eq. (B.1b) about $\mathbf{x}=0$ to first order in $\mathbf{x}$ (and $\dot{\mathbf{x}}$) and truncates higher-order terms. Hence, the particle Lagrangian in the dipole approximation Eq. (4.6b) is obtained. Using a similar approach, analogous results should be obtainable for the quantum model.

As for the Hamiltonian formulation of the classical model without the dipole approximation, only a simple change to Hamiltonian structure given by Eqs. (4.21) is required.

Here, the Hamiltonian and bracket are

$$\mathcal{H}[f, \mathbf{E}, \mathbf{A}] = \mathcal{H}_{\mathrm{P}} + \mathcal{H}_{\mathrm{EM}}, \tag{B.3a}$$

$$\mathcal{H}_{\mathrm{P}}[f, \mathbf{A}] = \int \rho(\mathbf{r})\, f(\mathbf{x}, \mathbf{p}, \mathbf{r}) \left[\frac{1}{2} \left|\mathbf{p} + \mathbf{A}(\mathbf{r} + \mathbf{x})\right|^2 + V(\mathbf{x})\right] \mathrm{d}\mu \mathrm{d}^3\mathbf{r}, \tag{B.3b}$$

$$\mathcal{H}_{\mathrm{EM}}[\mathbf{E}, \mathbf{A}] = \frac{1}{8\pi} \int \left(|\mathbf{E}(\mathbf{r})|^2 + c^2 |\nabla \times \mathbf{A}(\mathbf{r})|^2\right) \mathrm{d}^3\mathbf{r}, \tag{B.3c}$$

$$\{\mathcal{F}, \mathcal{G}\} = \int \left\{\rho^{-1} \int f \left[\mathcal{F}_f, \mathcal{G}_f\right] \mathrm{d}\mu + 4\pi \left(\mathcal{F}_{\mathbf{E}} \cdot \mathcal{G}_{\mathbf{A}} - \mathcal{F}_{\mathbf{A}} \cdot \mathcal{G}_{\mathbf{E}}\right)\right\} \mathrm{d}^3\mathbf{r}. \tag{B.3d}$$

The only change compared to Eqs. (4.21) is that in $\mathcal{H}_{\mathrm{P}}$, the vector potential is evaluated at $\mathbf{r} + \mathbf{x}$ instead of $\mathbf{r}$, just like in the Lagrangian. The equations of motion for this case are

$$\dot{f} = -\left[\mathbf{p} + \mathbf{A}(\mathbf{r} + \mathbf{x})\right] \cdot \nabla_{\mathbf{x}} f + \left\{\nabla V(\mathbf{x}) + \left[\mathbf{p} + \mathbf{A}(\mathbf{r} + \mathbf{x})\right] \cdot \nabla \mathbf{A}(\mathbf{r} + \mathbf{x})\right\} \cdot \partial_{\mathbf{p}} f,$$

$$\dot{\mathbf{E}}(\mathbf{r}) = c^2 \nabla \times (\nabla \times \mathbf{A}(\mathbf{r})) + 4\pi \int \rho(\mathbf{r} - \mathbf{x}) f(\mathbf{x}, \mathbf{p}, \mathbf{r} - \mathbf{x}) \left[\mathbf{p} + \mathbf{A}(\mathbf{r})\right] \mathrm{d}^3\mathbf{x} \mathrm{d}^3\mathbf{p},$$

$$\dot{\mathbf{A}} = -\mathbf{E}.$$

The first equation is very similar to the Vlasov equation, though it contains an additional label $\mathbf{r}$ for the parent ion position and an explicit interaction between the electron and its parent ion. By standard manipulations, this equation can be shown to be equivalent to Eq. (B.2a). The second equation is the Maxwell-Ampère Law, equivalent to Eq. (B.2c), with the current density again evaluated for the electrons with the present position $\mathbf{r}$. The last equation relates the electric field to the vector potential. To obtain Gauss' Law, one is again obliged to search for the corresponding conserved quantity of this Hamiltonian system. Here, it turns out to be

$$\mathcal{C}(\mathbf{r}) = \nabla \cdot \mathbf{E}(\mathbf{r}) + 4\pi \int \rho(\mathbf{r} - \mathbf{x}) f(\mathbf{x}, \mathbf{p}, \mathbf{r} - \mathbf{x}) \mathrm{d}^3\mathbf{x} \mathrm{d}^3\mathbf{p},$$

as can be verified by showing that $\{\mathcal{C}(\mathbf{r}), \mathcal{H}\} = 0$. Choosing $\mathcal{C}(\mathbf{r}) = 4\pi\rho(\mathbf{r})$ at $t = 0$ ensures that Gauss' Law, i.e. Eq. (B.2b), is satisfied at all times. Finally, the classical parent

Hamiltonian model of Ch. 4 is obtained by expanding the vector potential in Eq. (B.3b) to zeroth-order about $\mathbf{x} = 0$ and truncating higher-order terms. Put simply, one assumes that $\mathbf{A}(\mathbf{r} + \mathbf{x}) \approx \mathbf{A}(\mathbf{r})$.

## APPENDIX C

## PROOF OF THE JACOBI IDENTITY IN THE DIPOLE APPROXIMATION

In this appendix, we prove the Jacobi identity for the Poisson bracket of the parent classical model of Ch. 4, i.e. Eq. (4.25b), when the bracket is expressed in terms of the physical variables, $f(\mathbf{x}, \mathbf{v}, \mathbf{r})$, $\mathbf{E}(\mathbf{r})$, and $\mathbf{B}(\mathbf{r})$. We also show that this proves the Jacobi identity for the original bracket, which is expressed below as

$$\{\mathcal{F}, \mathcal{G}\} = \{\mathcal{F}, \mathcal{G}\}^{\mathrm{P}} + \{\mathcal{F}, \mathcal{G}\}^{\mathrm{EM}}, \text{ where} \tag{C.1a}$$

$$\{\mathcal{F}, \mathcal{G}\}^{\mathrm{P}} = \int f \left\{ \rho^{-1} \left[ \mathcal{F}_f, \mathcal{G}_f \right] + 4\pi \left( \mathcal{F}_{\mathbf{E}} \cdot \partial_{\mathbf{v}} \mathcal{G}_f - \partial_{\mathbf{v}} \mathcal{F}_f \cdot \mathcal{G}_{\mathbf{E}} \right) \right\} \mathrm{d}\mu \mathrm{d}^3\mathbf{r}, \tag{C.1b}$$

$$\{\mathcal{F}, \mathcal{G}\}^{\mathrm{EM}} = 4\pi \int \left( \mathcal{F}_{\mathbf{E}} \cdot \mathcal{G}_{\mathbf{A}} - \mathcal{F}_{\mathbf{A}} \cdot \mathcal{G}_{\mathbf{E}} \right) \mathrm{d}^3\mathbf{r}. \tag{C.1c}$$

Here, we have introduced the particle bracket $\{\cdot, \cdot\}^{\mathrm{P}}$, which is the part containing $f$, and the purely electromagnetic bracket $\{\cdot, \cdot\}^{\mathrm{EM}}$. To proceed, we replace $\mathbf{A}$ as a dynamical variable by the magnetic field $\mathbf{B} = \nabla \times \mathbf{A}$, as is done in the Hamiltonian formulation of the Vlasov-Maxwell equations. The functional derivatives transform as

$$\mathcal{F}_f = \widetilde{\mathcal{F}}_f, \;\; \mathcal{F}_{\mathbf{E}} = \widetilde{\mathcal{F}}_{\mathbf{E}}, \;\; \mathcal{F}_{\mathbf{A}} = \nabla \times \widetilde{\mathcal{F}}_{\mathbf{B}},$$

so that the particle bracket is unchanged and the electromagnetic bracket becomes

$$\{\mathcal{F}, \mathcal{G}\}^{\mathrm{EM}} = 4\pi \int \left\{ \mathcal{F}_{\mathbf{E}} \cdot \left( \nabla \times \mathcal{G}_{\mathbf{B}} \right) - \left( \nabla \times \mathcal{F}_{\mathbf{B}} \right) \cdot \mathcal{G}_{\mathbf{E}} \right\} \mathrm{d}^3\mathbf{r}. \tag{C.2}$$

In order to check the Jacobi identity for the full bracket expressed in these variables, we need to calculate the functional derivatives of the bracket with respect to each variable.

We obtain the following:

$$\{\mathcal{F},\mathcal{G}\}_f \approx \{\mathcal{F},\mathcal{G}\}_f^{\mathrm{P}} \approx \rho^{-1}\left[\mathcal{F}_f,\mathcal{G}_f\right] + 4\pi\left(\mathcal{F}_{\mathbf{E}}\cdot\partial_{\mathbf{v}}\mathcal{G}_f - \partial_{\mathbf{v}}\mathcal{F}_f\cdot\mathcal{G}_{\mathbf{E}}\right), \tag{C.3a}$$

$$\{\mathcal{F},\mathcal{G}\}_{\mathbf{E}} \approx 0, \tag{C.3b}$$

$$\{\mathcal{F},\mathcal{G}\}_{\mathbf{B}} \approx 0. \tag{C.3c}$$

Here, we have used the notation "$\approx$" to mean that we have only written the terms of the functional derivatives of the bracket that contain first-order functional derivatives, while neglecting to write any of the second-order derivative terms. Thanks to Morrison's lemma (see §A), we have no need to keep track of these terms, since the antisymmetry of bracket (C.1a) guarantees that they will vanish under cyclic-permutation-summation. Using Eqs. (C.3), we can calculate one of the terms of the Jacobi identity, $\{\mathcal{H},\{\mathcal{F},\mathcal{G}\}\}$, giving

$$\begin{aligned}\{\mathcal{H},\{\mathcal{F},\mathcal{G}\}\} &\approx \{\mathcal{H},\{\mathcal{F},\mathcal{G}\}\}^{\mathrm{P}} \approx \int \rho^{-2} f\Big[\mathcal{H}_f,[\mathcal{F}_f,\mathcal{G}_f]\Big]\mathrm{d}\mu\mathrm{d}^3\mathbf{r}\\ &+ 4\pi\int f\Big\{\rho^{-1}[\mathcal{H}_f,\mathcal{F}_{\mathbf{E}}\cdot\partial_{\mathbf{v}}\mathcal{G}_f - \partial_{\mathbf{v}}\mathcal{F}_f\cdot\mathcal{G}_{\mathbf{E}}] + \mathcal{H}_{\mathbf{E}}\cdot\partial_{\mathbf{v}}\Big(\rho^{-1}[\mathcal{F}_f,\mathcal{G}_f]\\ &+ 4\pi(\mathcal{F}_{\mathbf{E}}\cdot\partial_{\mathbf{v}}\mathcal{G}_f - \partial_{\mathbf{v}}\mathcal{F}_f\cdot\mathcal{G}_{\mathbf{E}})\Big)\Big\}\mathrm{d}\mu\mathrm{d}^3\mathbf{r}.\end{aligned} \tag{C.4}$$

The fact that $\{\mathcal{H},\{\mathcal{F},\mathcal{G}\}\} \approx \{\mathcal{H},\{\mathcal{F},\mathcal{G}\}\}^{\mathrm{P}}$ follows from Eqs. (C.3b)-(C.3c).

Now, summing the above equation over the cyclic permutations of $\mathcal{FGH}$ will yield the Jacobi identity. Doing so for just the first line of Eq. (C.4) yields a term proportional to $[\mathcal{H}_f,[\mathcal{F}_f,\mathcal{G}_f]] + [\mathcal{F}_f,[\mathcal{G}_f,\mathcal{H}_f]] + [\mathcal{G}_f,[\mathcal{H}_f,\mathcal{F}_f]] = 0$, by virtue of the Jacobi identity for the

canonical bracket $[\cdot,\cdot]$. Hence, we obtain

$$
\begin{aligned}
&\{\mathcal{H},\{\mathcal{F},\mathcal{G}\}\}+\{\mathcal{F},\{\mathcal{G},\mathcal{H}\}\}+\{\mathcal{G},\{\mathcal{H},\mathcal{F}\}\}\\
=&4\pi\int f\Big\{\rho^{-1}\Big(\mathcal{F}_{\mathbf{E}}\cdot[\mathcal{H}_f,\partial_{\mathbf{v}}\mathcal{G}_f]-\mathcal{G}_{\mathbf{E}}\cdot[\mathcal{H}_f,\partial_{\mathbf{v}}\mathcal{F}_f]+\mathcal{H}_{\mathbf{E}}\cdot[\partial_{\mathbf{v}}\mathcal{F}_f,\mathcal{G}_f]+\mathcal{H}_{\mathbf{E}}\cdot[\mathcal{F}_f,\partial_{\mathbf{v}}\mathcal{G}_f]\Big)\\
&+4\pi\Big((\mathcal{H}_{\mathbf{E}}\cdot\partial_{\mathbf{v}})(\mathcal{F}_{\mathbf{E}}\cdot\partial_{\mathbf{v}})\mathcal{G}_f-(\mathcal{H}_{\mathbf{E}}\cdot\partial_{\mathbf{v}})(\mathcal{G}_{\mathbf{E}}\cdot\partial_{\mathbf{v}})\mathcal{F}_f\Big)\\
&+\rho^{-1}\Big(\mathcal{G}_{\mathbf{E}}\cdot[\mathcal{F}_f,\partial_{\mathbf{v}}\mathcal{H}_f]-\mathcal{H}_{\mathbf{E}}\cdot[\mathcal{F}_f,\partial_{\mathbf{v}}\mathcal{G}_f]+\mathcal{F}_{\mathbf{E}}\cdot[\partial_{\mathbf{v}}\mathcal{G}_f,\mathcal{H}_f]+\mathcal{F}_{\mathbf{E}}\cdot[\mathcal{G}_f,\partial_{\mathbf{v}}\mathcal{H}_f]\Big)\\
&+4\pi\Big((\mathcal{F}_{\mathbf{E}}\cdot\partial_{\mathbf{v}})(\mathcal{G}_{\mathbf{E}}\cdot\partial_{\mathbf{v}})\mathcal{H}_f-(\mathcal{F}_{\mathbf{E}}\cdot\partial_{\mathbf{v}})(\mathcal{H}_{\mathbf{E}}\cdot\partial_{\mathbf{v}})\mathcal{G}_f\Big)\\
&+\rho^{-1}\Big(\mathcal{H}_{\mathbf{E}}\cdot[\mathcal{G}_f,\partial_{\mathbf{v}}\mathcal{F}_f]-\mathcal{F}_{\mathbf{E}}\cdot[\mathcal{G}_f,\partial_{\mathbf{v}}\mathcal{H}_f]+\mathcal{G}_{\mathbf{E}}\cdot[\partial_{\mathbf{v}}\mathcal{H}_f,\mathcal{F}_f]+\mathcal{G}_{\mathbf{E}}\cdot[\mathcal{H}_f,\partial_{\mathbf{v}}\mathcal{F}_f]\Big)\\
&+4\pi\Big((\mathcal{G}_{\mathbf{E}}\cdot\partial_{\mathbf{v}})(\mathcal{H}_{\mathbf{E}}\cdot\partial_{\mathbf{v}})\mathcal{F}_f-(\mathcal{G}_{\mathbf{E}}\cdot\partial_{\mathbf{v}})(\mathcal{F}_{\mathbf{E}}\cdot\partial_{\mathbf{v}})\mathcal{H}_f\Big)\Big\}\mathrm{d}^3\mu\mathrm{d}^3\mathbf{r}\\
=&0.
\end{aligned}
$$

Thus, we have proved the Jacobi identity for bracket (C.1a) with the electromagnetic bracket given by Eq. (C.2). In fact, we have also proved it when the electromagnetic bracket is instead given by Eq. (C.1c), because the property that this proof relies on—namely, $\{\mathcal{H},\{\mathcal{F},\mathcal{G}\}\}\approx\{\mathcal{H},\{\mathcal{F},\mathcal{G}\}\}^{\mathrm{P}}$—is also satisfied by bracket (C.1).

## APPENDIX D

## COMPUTATION OF THE INTEGRALS APPEARING IN THE POISSON MATRIX

Here we show how to arrive at Eq. (4.74) and indicate the way to obtain the $L \to \infty$ limits of Eqs. (4.69c)–(4.69d) and expressions like that in general. When $-m \neq n$, the integral in Eq. (4.74) is zero. This can be seen by splitting the integral into two parts using a partial fraction expansion:

$$\int_{-\infty}^{\infty} \frac{R \sin^2(\pi R)}{(R-m)(R+n)} \mathrm{d}R = A \int_{-\infty}^{\infty} \frac{R \sin^2(\pi R)}{R-m} \mathrm{d}R + B \int_{-\infty}^{\infty} \frac{R \sin^2(\pi R)}{R+n} \mathrm{d}R \quad \text{(D.1)}$$

$A$ and $B$ are the coefficients of the partial fraction expansion, and they satisfy $A + B = 0$ and $An - Bm = 1$. These improper integrals should be interpreted as

$$\lim_{R_{\max} \to \infty} \int_{-R_{\max}}^{R_{\max}} \mathrm{d}R. \quad \text{(D.2)}$$

This interpretation originates from considering a finite-dimensional version of the model described by Eqs.(4.60)–(4.62) by truncating the infinite set of harmonic modes with $|k| > k_{\max}$, and then letting $k_{\max} \to \infty$.

We shift $R$ by $-m$ and $n$ in the left and right integrals of Eq. (D.1), respectively, yielding

$$\begin{aligned} &A \left( \int_{-\infty}^{\infty} \sin^2(\pi R)\, \mathrm{d}R + m \int_{-\infty}^{\infty} \frac{\sin^2(\pi R)}{R} \mathrm{d}R \right) \\ &+B \left( \int_{-\infty}^{\infty} \sin^2(\pi R)\, \mathrm{d}R - n \int_{-\infty}^{\infty} \frac{\sin^2(\pi R)}{R} \mathrm{d}R \right) \end{aligned} \quad \text{(D.3)}$$

Thanks to interpretation (D.2) and the fact that $A + B = 0$, the first and third terms of

expression (D.3) cancel each other out. Meanwhile, since both limits of the integrals go to infinity simultaneously, we can safely say that the integral of any odd function is zero. Thus, the second and fourth terms of expression (D.3) go to zero independently.

When $-m = n$, the value of the integral is $-n\pi^2$. To find this, start from the left-hand side of Eq. (D.1) and immediately shift $R$ by $n$, yielding

$$\int_{-\infty}^{\infty} \frac{R\sin^2(\pi R)}{(R+n)^2}\mathrm{d}R = \int_{-\infty}^{\infty} \frac{\sin^2(\pi R)}{R}\mathrm{d}R - n\int_{-\infty}^{\infty} \frac{\sin^2(\pi R)}{R^2}\mathrm{d}R \tag{D.4}$$

Once again, the first integral vanishes. This leaves the second term, which is a standard integral that evaluates to $\pi^2$.

Thus, we have shown that, for integer $m$ and $n$,

$$\int_{-\infty}^{\infty} \frac{R\sin^2(\pi R)}{(R-m)(R+n)}\mathrm{d}R = -n\pi^2\delta_{-m,n}. \tag{D.5}$$

All of the sums (or integrals in the $L \to \infty$ limit) appearing in Eqs. (4.69c), (4.69d), and (4.79) may be evaluated using similar manipulations. In fact, based on the above sequence of calculations one can identify by inspection which integrals will be zero and which will not. The integrals that contain a $k^2$ or a $(k-m)^2$ term in the denominator will always survive because after splitting the integrand using a partial fraction decomposition, these terms will always integrate to a multiple of $\pi^2$. All the other terms in the decomposition will have only a term like $k$ or $k-m$ in the denominator, which leads to the integration of an odd function over a symmetric domain and equals zero. If the denominator does not contain any $k^2$ or a $(k-m)^2$ term [nor a $(k-m)(k+n)$ term which becomes $(k-m)^2$ when $n = -m$], then that integral has to be zero.

## REFERENCES


[1] M. Y. Kuchiev, "Atomic antenna," *JETP Lett.*, vol. 45, p. 404, 1987.

[2] K. Kulander, K. Schafer, and J. Krause, "Dynamics of short-pulse excitation, ionization and harmonic conversion," in *Super-intense laser-atom physics*, Springer, 1993, p. 95.

[3] P. B. Corkum, "Plasma perspective on strong field multiphoton ionization," *Phys. Rev. Lett.*, vol. 71, p. 1994, 1993.

[4] M. Lein, "Molecular imaging using recolliding electrons," *J. Phys. B*, vol. 40, R135, 2007.

[5] A. Ferré, A. E. Boguslavskiy, M. Dagan, V. Blanchet, B. D. Bruner, F. Burgy, A. Camper, D. Descamps, B. Fabre, N. Fedorov, *et al.*, "Multi-channel electronic and vibrational dynamics in polyatomic resonant high-order harmonic generation," *Nat. Commun.*, vol. 6, p. 5952, 2015.

[6] J. P. Marangos, "Development of high harmonic generation spectroscopy of organic molecules and biomolecules," *J. Phys. B*, vol. 49, p. 132 001, 2016.

[7] Y. Pertot, C. Schmidt, M. Matthews, A. Chauvet, M. Huppert, V. Svoboda, A. von Conta, A. Tehlar, D. Baykusheva, J.-P. Wolf, *et al.*, "Time-resolved x-ray absorption spectroscopy with a water window high-harmonic source," *Science*, vol. 355, p. 264, 2017.

[8] D. Popmintchev, B. R. Galloway, M.-C. Chen, F. Dollar, C. A. Mancuso, A. Hankla, L. Miaja-Avila, G. O′03, J. M. Shaw, G. Fan, *et al.*, "Near-and extended-edge x-ray-absorption fine-structure spectroscopy using ultrafast coherent high-order harmonic supercontinua," *Phys. Rev. Lett.*, vol. 120, p. 093 002, 2018.

[9] Y. Mairesse, A. De Bohan, L. J. Frasinski, H. Merdji, L. C. Dinu, P. Monchicourt, P. Breger, M. Kovačev, R. Taïeb, B. Carré, *et al.*, "Attosecond synchronization of high-harmonic soft x-rays," *Science*, vol. 302, p. 1540, 2003.

[10] N. Dudovich, O. Smirnova, J. Levesque, Y. Mairesse, M. Y. Ivanov, D. M. Villeneuve, and P. B. Corkum, "Measuring and controlling the birth of attosecond xuv pulses," *Nat. Phys.*, vol. 2, p. 781, 2006.

[11] M.-C. Chen, C. Mancuso, C. Hernández-García, F. Dollar, B. Galloway, D. Popmintchev, P. C. Huang, B. Walker, L. Plaja, A. A. Jaroń-Becker, *et al.*, "Generation

of bright isolated attosecond soft x-ray pulses driven by multicycle midinfrared lasers," *Proc. Natl. Acad. Sci. U. S. A.*, p. 201 407 421, 2014.

[12] X. Wang and J. H. Eberly, "Elliptical polarization and probability of double ionization," *Phys. Rev. Lett.*, vol. 105, p. 083 001, 2010.

[13] F. Mauger, C. Chandre, and T. Uzer, "Recollisions and correlated double ionization with circularly polarized light," *Phys. Rev. Lett.*, vol. 105, p. 083 002, 2010.

[14] A. Kamor, F. Mauger, C. Chandre, and T. Uzer, "How key periodic orbits drive recollisions in a circularly polarized laser field," *Phys. Rev. Lett.*, vol. 110, p. 253 002, 2013.

[15] M. Li, M.-M. Liu, J.-W. Geng, M. Han, X. Sun, Y. Shao, Y. Deng, C. Wu, L.-Y. Peng, Q. Gong, *et al.*, "Experimental verification of the nonadiabatic effect in strong-field ionization with elliptical polarization," *Phys. Rev. A*, vol. 95, p. 053 425, 2017.

[16] J. Dubois, S. A. Berman, C. Chandre, and T. Uzer, "Capturing photoelectron motion with guiding centers," *Phys. Rev. Lett.*, vol. 121, p. 113 202, 2018.

[17] L. E. Chipperfield, J. S Robinson, J. G. Tisch, and J. P. Marangos, "Ideal waveform to generate the maximum possible electron recollision energy for any given oscillation period," *Phys. Rev. Lett.*, vol. 102, p. 063 003, 2009.

[18] R. V. Jensen, S. M. Susskind, and M. M. Sanders, "Chaotic ionization of highly excited hydrogen atoms: Comparison of classical and quantum theory with experiment," *Phys. Rep.*, vol. 201, p. 1, 1991.

[19] L. Jie, C. Shi-Gang, and B. Hu, "Chaotic behavior of a one-dimensional model atom in an intense field," *Acta Phys. Sin. (Overseas Ed.)*, vol. 7, p. 89, 1998.

[20] A. Kamor, C. Chandre, T. Uzer, and F. Mauger, "Recollision scenario without tunneling: Role of the ionic core potential," *Phys. Rev. Lett.*, vol. 112, p. 133 003, 13 2014.

[21] T. J. M. Boyd and J. J. Sanderson, *The Physics of Plasmas*. Cambridge University Press, 2003.

[22] A. H. Boozer, "Physics of magnetically confined plasmas," *Rev. Mod. Phys.*, vol. 76, p. 1071, 2005.

[23] P. J. Morrison, "Hamiltonian and action principle formulations of plasma physics," *Phys. Plasmas*, vol. 12, p. 058 102, 2005.

[24] T. Brabec and F. Krausz, "Intense few-cycle laser fields: Frontiers of nonlinear optics," *Rev. Mod. Phys.*, vol. 72, p. 545, 2000.

[25] J. Wildenauer, "Generation of the ninth, eleventh, and fifteenth harmonics of iodine laser radiation," *J. Appl. Phys.*, vol. 62, p. 41, 1987.

[26] M. Ferray, A. L'Huillier, X. F. Li, L. A. Lompre, G. Mainfray, and C. Manus, "Multiple-harmonic conversion of 1064 nm radiation in rare gases," *J. Phys. B*, vol. 21, p. L31, 1988.

[27] A. L'Huillier, K. J. Schafer, and K. C. Kulander, "Theoretical aspects of intense field harmonic generation," *J. Phys. B*, vol. 24, p. 3315, 1991.

[28] P. Salieres, T. Ditmire, K. S. Budil, M. D. Perry, and A. L'Huillier, "Spatial profiles of high-order harmonics generated by a femtosecond cr:lisaf laser," *J. Phys. B*, vol. 27, p. L217, 1994.

[29] K. Miyazaki and H. Takada, "High-order harmonic generation in the tunneling regime," *Phys. Rev. A*, vol. 52, p. 3007, 1995.

[30] J. Zhou, J. Peatross, M. M. Murnane, H. C. Kapteyn, and I. P. Christov, "Enhanced high-harmonic generation using 25 fs laser pulses," *Phys. Rev. Lett.*, vol. 76, p. 752, 1996.

[31] M. Schnürer, C. Spielmann, P. Wobrauschek, C. Streli, N. H. Burnett, C. Kan, K. Ferencz, R. Koppitsch, Z. Cheng, T. Brabec, and F. Krausz, "Coherent 0.5-kev x-ray emission from helium driven by a sub-10-fs laser," *Phys. Rev. Lett.*, vol. 80, p. 3236, 1998.

[32] P. Colosimo, G. Doumy, C. I. Blaga, J. Wheeler, C. Hauri, F. Catoire, J. Tate, R. Chirla, A. M. March, G. G. Paulus, H. G. Muller, P. Agostini, and L. F. DiMauro, "Scaling strong-field interactions towards the classical limit," *Nat. Phys.*, vol. 4, p. 386, 2008.

[33] T. Popmintchev, M.-C. Chen, D. Popmintchev, P. Arpin, S. Brown, S. Ališauskas, G. Andriukaitis, T. Balčiunas, O. D. Mücke, A. Pugzlys, A. Baltuška, B. Shim, S. E. Schrauth, A. Gaeta, C. Hernández-García, L. Plaja, A. Becker, A. Jaron-Becker, M. M. Murnane, and H. C. Kapteyn, "Bright coherent ultrahigh harmonics in the kev x-ray regime from mid-infrared femtosecond lasers," *Science*, vol. 336, p. 1287, 2012.

[34] G. Li, J. Yao, H. Zhang, C. Jing, B. Zeng, W. Chu, J. Ni, H. Xie, X. Liu, J. Chen, Y. Cheng, and Z. Xu, "Influence of ionization suppression on high-harmonic generation in molecules: Dependence of cutoff energy on driver wavelength," *Phys. Rev. A*, vol. 88, p. 043 401, 2013.

[35] E. Constant, D. Garzella, P. Breger, E. Mével, C. Dorrer, C. Le Blanc, F. Salin, and P. Agostini, "Optimizing high harmonic generation in absorbing gases: Model and experiment," *Phys. Rev. Lett.*, vol. 82, p. 1668, 1999.

[36] E. A. Gibson, A. Paul, N. Wagner, R. Tobey, S. Backus, I. P. Christov, M. M. Murnane, and H. C. Kapteyn, "High-order harmonic generation up to 250 ev from highly ionized argon," *Phys. Rev. Lett.*, vol. 92, p. 033 001, 2004.

[37] S. Haessler, T. Balčiunas, G. Fan, G. Andriukaitis, A. Pugžlys, A. Baltuška, T. Witting, R. Squibb, A. Zaïr, J. W. G. Tisch, *et al.*, "Optimization of quantum trajectories driven by strong-field waveforms," *Phys. Rev. X*, vol. 4, p. 021 028, 2014.

[38] S. Kazamias, D. Douillet, F. Weihe, C. Valentin, A. Rousse, S. Sebban, G. Grillon, F. Augé, D. Hulin, and P. Balcou, "Global optimization of high harmonic generation," *Phys. Rev. Lett.*, vol. 90, p. 193 901, 2003.

[39] D. Popmintchev, C. Hernández-García, F. Dollar, C. Mancuso, J. A. Pérez-Hernández, M.-C. Chen, A. Hankla, X. Gao, B. Shim, A. L. Gaeta, *et al.*, "Ultraviolet surprise: Efficient soft x-ray high-harmonic generation in multiply ionized plasmas," *Science*, vol. 350, p. 1225, 2015.

[40] A. S. Johnson, D. R. Austin, D. A. Wood, C. Brahms, A. Gregory, K. B. Holzner, S. Jarosch, E. W. Larsen, S. Parker, C. S. Strüber, *et al.*, "High-flux soft x-ray harmonic generation from ionization-shaped few-cycle laser pulses," *Sci. Adv.*, vol. 4, eaar3761, 2018.

[41] S. C. Rae, K Burnett, and J Cooper, "Generation and propagation of high-order harmonics in a rapidly ionizing medium," *Phys. Rev. A*, vol. 50, p. 3438, 1994.

[42] M. Geissler, G. Tempea, A. Scrinzi, M. Schnürer, F. Krausz, and T. Brabec, "Light propagation in field-ionizing media: Extreme nonlinear optics," *Phys. Rev. Lett.*, vol. 83, p. 2930, 1999.

[43] M. B. Gaarde, M. Murakami, and R. Kienberger, "Spatial separation of large dynamical blueshift and harmonic generation," *Phys. Rev. A*, vol. 74, p. 053 401, 2006.

[44] M. B. Gaarde, J. L. Tate, and K. J. Schafer, "Macroscopic aspects of attosecond pulse generation," *J. Phys. B*, vol. 41, p. 132 001, 2008.

[45] T. Popmintchev, M.-C. Chen, P. Arpin, M. M. Murnane, and H. C. Kapteyn, "The attosecond nonlinear optics of bright coherent x-ray generation," *Nat. Photonics*, vol. 4, p. 822, 2010.

[46] K. C. Kulander and B. W. Shore, "Calculations of multiple-harmonic conversion of 1064-nm radiation in xe," *Phys. Rev. Lett.*, vol. 62, p. 524, 1989.

[47] J. L. Krause, K. J. Schafer, and K. C. Kulander, "High-order harmonic generation from atoms and ions in the high intensity regime," *Phys. Rev. Lett.*, vol. 68, p. 3535, 1992.

[48] G. Bandarage, A. Maquet, and J. Cooper, "Harmonic generation by a classical hydrogen atom in the presence of an intense radiation field," *Phys. Rev. A*, vol. 41, p. 1744, 1990.

[49] G. Bandarage, A. Maquet, T. Ménis, R. Taïeb, V. Véniard, and J. Cooper, "Harmonic generation by laser-driven classical hydrogen atoms," *Phys. Rev. A*, vol. 46, p. 380, 1992.

[50] F. Brunel, "Harmonic generation due to plasma effects in a gas undergoing multiphoton ionization in the high-intensity limit," *J. Opt. Soc. Am. B*, vol. 7, p. 521, 1990.

[51] F. Giammanco, "Collective effects in intense laser fields," *Phys. Rev. A*, vol. 43, p. 6939, 1991.

[52] M. F. Kling and M. J. Vrakking, "Attosecond electron dynamics," *Ann. Rev. Phys. Chem.*, vol. 59, p. 463, 2008.

[53] F. Krausz and M. Ivanov, "Attosecond physics," *Rev. Mod. Phys.*, vol. 81, p. 163, 2009.

[54] A. de Bohan, B. Piraux, L. Ponce, R. Taïeb, V. Véniard, and A. Maquet, "Direct and indirect pathways in strong field atomic ionization dynamics," *Phys. Rev. Lett.*, vol. 89, p. 113 002, 2002.

[55] M. Lewenstein, P. Balcou, M. Y. Ivanov, A. L'Huillier, and P. B. Corkum, "Theory of high-harmonic generation by low-frequency laser fields," *Phys. Rev. A*, vol. 49, p. 2117, 1994.

[56] A. Pukhov, S. Gordienko, and T. Baeva, "Temporal structure of attosecond pulses from intense laser-atom interactions," *Phys. Rev. Lett.*, vol. 91, p. 173 002, 2003.

[57] A. L'Huillier, M. Lewenstein, P. Salieres, P. Balcou, M. Y. Ivanov, J. Larsson, and C.-G. Wahlström, "High-order harmonic-generation cutoff," *Phys. Rev. A*, vol. 48, R3433, 1993.

[58] E. Lorin, S. Chelkowski, and A. Bandrauk, "A numerical maxwell–schrödinger model for intense laser–matter interaction and propagation," *Comput. Phys. Commun.*, vol. 177, p. 908, 2007.

[59] E. Lorin and A. D. Bandrauk, "Efficient and accurate numerical modeling of a micro–macro nonlinear optics model for intense and short laser pulses," *J. Comput. Sci.*, vol. 3, p. 159, 2012.

[60] M. B. Gaarde, C. Buth, J. L. Tate, and K. J. Schafer, "Transient absorption and reshaping of ultrafast xuv light by laser-dressed helium," *Phys. Rev. A*, vol. 83, p. 013 419, 2011.

[61] N. Milosevic, A. Scrinzi, and T. Brabec, "Numerical characterization of high harmonic attosecond pulses," *Phys. Rev. Lett.*, vol. 88, p. 093 905, 2002.

[62] M. V. Ammosov, N. B. Delone, and V. P. Krainov, "Tunnel ionization of complex atoms and atomic ions in a varying electromagnetic-field," *Sov. Phys. JETP*, vol. 91, 1986.

[63] M. Y. Ivanov, M. Spanner, and O. Smirnova, "Anatomy of strong field ionizaztion," *J. Mod. Opt.*, vol. 52, p. 165, 2005.

[64] P. Salières, B. Carré, L. Le Déroff, F. Grasbon, G. G. Paulus, H. Walther, R. Kopold, W. Becker, D. B. Milošević, A. Sanpera, *et al.*, "Feynman's path-integral approach for intense-laser-atom interactions," *Science*, vol. 292, p. 902, 2001.

[65] F. Brizuela, C. M. Heyl, P. Rudawski, D. Kroon, L. Rading, J. M. Dahlström, J. Mauritsson, P. Johnsson, C. L. Arnold, and A. L'Huillier, "Efficient high-order harmonic generation boosted by below-threshold harmonics," *Sci. Rep.*, vol. 3, p. 1410, 2013.

[66] T. Brabec, M. Y. Ivanov, and P. B. Corkum, "Coulomb focusing in intense field atomic processes," *Phys. Rev. A*, vol. 54, R2551, 1996.

[67] D. Shafir, B. Fabre, J. Higuet, H. Soifer, M. Dagan, D. Descamps, E. Mével, S. Petit, H. J. Wörner, B. Pons, N. Dudovich, and Y. Mairesse, "Role of the ionic potential in high harmonic generation," *Phys. Rev. Lett.*, vol. 108, p. 203 001, 2012.

[68] D. Shafir, H. Soifer, C. Vozzi, A. S. Johnson, A. Hartung, Z. Dube, D. M. Villeneuve, P. B. Corkum, N. Dudovich, and A. Staudte, "Trajectory-resolved coulomb focusing in tunnel ionization of atoms with intense, elliptically polarized laser pulses," *Phys. Rev. Lett.*, vol. 111, p. 023 005, 2013.

[69] D. Comtois, D. Zeidler, H. Pépin, J. C. Kieffer, D. M. Villeneuve, and P. B. Corkum, "Observation of coulomb focusing in tunnelling ionization of noble gases," *J. Phys. B*, vol. 38, p. 1923, 2005.

[70] A. D. Bandrauk, S. Chelkowski, and S. Goudreau, "Control of harmonic generation using two-colour femtosecond-attosecond laser fields: Quantum and classical perspectives," *J. Mod. Opt.*, vol. 52, p. 411, 2005.

[71] M. B. Gaarde and K. J. Schafer, "Quantum path distributions for high-order harmonics in rare gas atoms," *Phys. Rev. A*, vol. 65, p. 031 406, 2002.

[72] D. C. Yost, T. R. Schibli, J. Ye, J. L. Tate, J. Hostetter, M. B. Gaarde, and K. J. Schafer, "Vacuum-ultraviolet frequency combs from below-threshold harmonics," *Nat. Phys.*, vol. 5, p. 815, 2009.

[73] W.-H. Xiong, J.-W. Geng, J.-Y. Tang, L.-Y. Peng, and Q. Gong, "Mechanisms of below-threshold harmonic generation in atoms," *Phys. Rev. Lett.*, vol. 112, p. 233 001, 2014.

[74] W.-H. Xiong, L.-Y. Peng, and Q. Gong, "Recent progress of below-threshold harmonic generation," *J. Phys. B*, vol. 50, p. 032 001, 2017.

[75] M. B. Gaarde, K. J. Schafer, A. Heinrich, J. Biegert, and U. Keller, "Large enhancement of macroscopic yield in attosecond pulse train–assisted harmonic generation," *Phys. Rev. A*, vol. 72, p. 013 411, 2005.

[76] M. L. Pons and L. Plaja, "Coupling effects in the propagation of harmonics," *J. Mod. Opt.*, vol. 43, p. 1939, 1996.

[77] P. M. Abanador, F. Mauger, K. Lopata, M. B. Gaarde, and K. J. Schafer, "Semiclassical modeling of high-order harmonic generation driven by an elliptically polarized laser field: The role of recolliding periodic orbits," *J. Phys. B*, vol. 50, p. 035 601, 2017.

[78] T. Pfeifer, L. Gallmann, M. J. Abel, P. M. Nagel, D. M. Neumark, and S. R. Leone, "Heterodyne mixing of laser fields for temporal gating of high-order harmonic generation," *Phys. Rev. Lett.*, vol. 97, p. 163 901, 2006.

[79] C. Jin, G. Wang, H. Wei, A.-T. Le, and C. D. Lin, "Waveforms for optimal sub-kev high-order harmonics with synthesized two-or three-colour laser fields," *Nat. Commun.*, vol. 5, p. 4003, 2014.

[80] F. Calegari, M. Lucchini, K. S. Kim, F. Ferrari, C. Vozzi, S. Stagira, G. Sansone, and M. Nisoli, "Quantum path control in harmonic generation by temporal shaping of few-optical-cycle pulses in ionizing media," *Phys. Rev. A*, vol. 84, p. 041 802, 2011.

[81] K. Kovacs and V. Toşa, "Quantum trajectories of electrons in arbitrary laser fields," *J. Mod. Opt.*, vol. 57, p. 977, 2010.

[82] P. Cvitanović, R. Artuso, R. Mainieri, G. Tanner, and G. Vattay, *Chaos: Classical and Quantum*. Copenhagen: Niels Bohr Institute, 2008, `http://ChaosBook.org`.

[83] G. van de Sand and J. M. Rost, "Irregular orbits generate higher harmonics," *Phys. Rev. Lett.*, vol. 83, p. 524, 1999.

[84] W. Becker, X. Liu, P. J. Ho, and J. H. Eberly, "Theories of photoelectron correlation in laser-driven multiple atomic ionization," *Rev. Mod. Phys.*, vol. 84, p. 1011, 2012.

[85] R. G. Littlejohn, "A guiding center hamiltonian: A new approach," *J. Math. Phys.*, vol. 20, p. 2445, 1979.

[86] A. J. Brizard and T. S. Hahm, "Foundations of nonlinear gyrokinetic theory," *Rev. Mod. Phys.*, vol. 79, p. 421, 2007.

[87] R. Bachelard, C. Chandre, and M. Vittot, "Hamiltonian description of a self-consistent interaction between charged particles and electromagnetic waves," *Phys. Rev. E*, vol. 78, p. 036 407, 2008.

[88] M. Perin, "Hamiltonian fluid reductions of kinetic equations in plasma physics," PhD thesis, Aix-Marseille Université, 2016.

[89] S. A. Berman, C. Chandre, and T. Uzer, "Persistence of coulomb focusing during ionization in the strong-field regime," *Phys. Rev. A*, vol. 92, p. 023 422, 2015.

[90] S. A. Berman, C. Chandre, J. Dubois, F. Mauger, M. Perin, and T. Uzer, "Variational formulation of classical and quantum models for intense laser pulse propagation," *Ann. Phys.*, vol. 399, p. 66, 2018.

[91] S. A. Berman, J. Dubois, C. Chandre, M. Perin, and T. Uzer, "Coherent buildup of high-order harmonic radiation: The classical perspective," *Phys. Rev. A*, vol. 97, 061402(R), 2018.

[92] V. I. Arnold, *Mathematical Methods of Classical Mechanics*. Springer-Verlag New York, 1989.

[93] W. Thirring, *A course in mathematical physics 1 and 2: Classical dynamical systems and classical field theory*. Springer Science & Business Media, 2012.

[94] J. R. Cary and R. G. Littlejohn, "Noncanonical hamiltonian mechanics and its application to magnetic field line flow," *Ann. Phys.*, vol. 151, p. 1, 1983.

[95] P. J. Morrison, "Poisson brackets for fluids and plasmas," in *Mathematical Methods in Hydrodynamics and Integrability in Dynamical Systems*, M. Tabor and Y. M. Treve, Eds., vol. 88, American Institute of Physics, 1982, p. 13.

[96] A. D. Bandrauk, F. Fillion-Gourdeau, and E. Lorin, "Atoms and molecules in intense laser fields: Gauge invariance of theory and models," *J. Phys. B*, vol. 46, p. 153 001, 2013.

[97] J. Javanainen, J. H. Eberly, and Q. Su, "Numerical simulations of multiphoton ionization and above-threshold electron spectra," *Phys. Rev. A*, vol. 38, p. 3430, 1988.

[98] K. J. Schafer, B. Yang, L. F. DiMauro, and K. C. Kulander, "Above threshold ionization beyond the high harmonic cutoff," *Phys. Rev. Lett.*, vol. 70, p. 1599, 1993.

[99] F. Mauger, C. Chandre, and T. Uzer, "Strong field double ionization: The phase space perspective," *Phys. Rev. Lett.*, vol. 102, p. 173 002, 2009.

[100] R. Ruth, "A canonical integration technique," *IEEE Trans. Nucl. Sci.*, vol. 30, p. 2669, 1983.

[101] M. J. Norman, C. Chandre, T. Uzer, and P. Wang, "Nonlinear dynamics of ionization stabilization of atoms in intense laser fields," *Phys. Rev. A*, vol. 91, p. 023 406, 2015.

[102] D. Hobson, "An efficient method for computing invariant manifolds of planar maps," *J. Comput. Phys.*, vol. 104, p. 14, 1993.

[103] E. Esarey, C. B. Schroeder, and W. P. Leemans, "Physics of laser-driven plasma-based electron accelerators," *Rev. Mod. Phys.*, vol. 81, p. 1229, 2009.

[104] R. Bonifacio, F. Casagrande, and C. Pellegrini, "Hamiltonian model of a free electron laser," *Opt. Commun.*, vol. 61, p. 55, 1987.

[105] J. L. Tennyson, J. D. Meiss, and P. J. Morrison, "Self-consistent chaos in the beam-plasma instability," *Physica D*, vol. 71, p. 1, 1994.

[106] F. E. Low, "A lagrangian formulation of the boltzmann-vlasov equation for plasmas," in *Proc. R. Soc. Lond. A*, The Royal Society, vol. 248, 1958, p. 282.

[107] P. J. Morrison, "The maxwell-vlasov equations as a continuous hamiltonian system," *Phys. Lett. A*, vol. 80, p. 383, 1980.

[108] J. E. Marsden and A. Weinstein, "The hamiltonian structure of the maxwell-vlasov equations," *Physica D*, vol. 4, p. 394, 1982.

[109] C. E. Caligan and C. Chandre, "Conservative dissipation: How important is the jacobi identity in the dynamics?" *Chaos*, vol. 26, p. 053 101, 2016.

[110] E. G. Evstatiev and B. A. Shadwick, "Variational formulation of particle algorithms for kinetic plasma simulations," *J. Comput. Phys.*, vol. 245, p. 376, 2013.

[111] A. B. Stamm, B. A. Shadwick, and E. G. Evstatiev, "Variational formulation of macroparticle models for electromagnetic plasma simulations," *IEEE Trans. Plasma Sci.*, vol. 42, p. 1747, 2014.

[112] Q. Chen, H. Qin, J. Liu, J. Xiao, R. Zhang, Y. He, and Y. Wang, "Canonical symplectic structure and structure-preserving geometric algorithms for schrödinger–maxwell systems," *J. Comput. Phys.*, vol. 349, p. 441, 2017.

[113] M. Kraus, "Variational integrators in plasma physics," PhD thesis, Max-Planck-Institut für Plasmaphysik, 2013.

[114] M. Kraus, K. Kormann, P. J. Morrison, and E. Sonnendrücker, "Gempic: Geometric electromagnetic particle-in-cell methods," *J. Plasma Phys.*, vol. 83, 2017.

[115] P. J. Morrison, "Structure and structure-preserving algorithms for plasma physics," *Phys. Plasmas*, vol. 24, p. 055 502, 2017.

[116] R. I. McLachlan and P. Atela, "The accuracy of symplectic integrators," *Nonlinearity*, vol. 5, p. 541, 1992.

[117] M. Tao, "Explicit symplectic approximation of nonseparable hamiltonians: Algorithm and long time performance," *Phys. Rev. E*, vol. 94, p. 043 303, 2016.

[118] C. D. Amico, A. Houard, S. Akturk, Y. Liu, J. Le Bloas, M. Franco, B. Prade, A. Couairon, V. T. Tikhonchuk, and A. Mysyrowicz, "Forward thz radiation emission by femtosecond filamentation in gases: Theory and experiment," *New J. Phys.*, vol. 10, p. 013 015, 2008.

[119] P. G. de Alaiza Martínez, I. Babushkin, L. Bergé, S. Skupin, E. Cabrera-Granado, C. Köhler, U. Morgner, A. Husakou, and J. Herrmann, "Boosting terahertz generation in laser-field ionized gases using a sawtooth wave shape," *Phys. Rev. Lett.*, vol. 114, p. 183 901, 2015.

[120] L. Bergé, S. Skupin, R. Nuter, J. Kasparian, and J.-P. Wolf, "Ultrashort filaments of light in weakly ionized, optically transparent media," *Rep. Prog. Phys.*, vol. 70, p. 1633, 2007.

[121] K. Schuh, M. Kolesik, E. M. Wright, J. V. Moloney, and S. W. Koch, "Self-channeling of high-power long-wave infrared pulses in atomic gases," *Phys. Rev. Lett.*, vol. 118, p. 063 901, 2017.

[122] I. P. Christov, "Propagation of ultrashort pulses in gaseous medium: Breakdown of the quasistatic approximation," *Opt. Express*, vol. 6, p. 34, 2000.

[123] M. Kolesik and J. V. Moloney, "Modeling and simulation techniques in extreme nonlinear optics of gaseous and condensed media," *Rep. Prog. Phys.*, vol. 77, p. 016 401, 2013.

[124] Y. P. Chen, W. E. I. Sha, L. Jiang, M. Meng, Y. M. Wu, and W. C. Chew, "A unified hamiltonian solution to maxwell–schrödinger equations for modeling electromagnetic field–particle interaction," *Comput. Phys. Commun.*, vol. 215, p. 63, 2017.

[125] D. Masiello, E. Deumens, and Y. Öhrn, "Dynamics of an atomic electron and its electromagnetic field in a cavity," *Phys. Rev. A*, vol. 71, p. 032 108, 2005.

[126] S. Amiranashvili and A. Demircan, "Hamiltonian structure of propagation equations for ultrashort optical pulses," *Phys. Rev. A*, vol. 82, p. 013 812, 2010.

[127] S. Amiranashvili, "Hamiltonian framework for short optical pulses," in *New Approaches to Nonlinear Waves*, E. Tobisch, Ed. Cham: Springer International Publishing, 2016, pp. 153–196, ISBN: 978-3-319-20690-5.

[128] P. Botheron and B. Pons, "One-electron atom in a strong and short laser pulse: Comparison of classical and quantum descriptions," *Phys. Rev. A*, vol. 80, p. 023 402, 2009.

[129] R. Uzdin and N. Moiseyev, "Classical harmonic generation in rare gases," *Phys. Rev. A*, vol. 81, p. 063 405, 2010.

[130] M. Kolesik and J. V. Moloney, "Nonlinear optical pulse propagation simulation: From maxwell's to unidirectional equations," *Phys. Rev. E*, vol. 70, p. 036 604, 2004.

[131] A. Zangwill, *Modern Electrodynamics*. Cambridge University Press, 2013.

[132] N. H. Shon, A. Suda, and K. Midorikawa, "Generation and propagation of high-order harmonics in high-pressure gases," *Phys. Rev. A*, vol. 62, p. 023 801, 2000.

[133] J.-H. Kim and C. H. Nam, "Plasma-induced frequency chirp of intense femtosecond lasers and its role in shaping high-order harmonic spectral lines," *Phys. Rev. A*, vol. 65, p. 033 801, 2002.

[134] H. Ye and P. J. Morrison, "Action principles for the vlasov equation," *Phys. Fluids B*, vol. 4, p. 771, 1992.

[135] N. Padhye and P. J. Morrison, "Fluid element relabeling symmetry," *Phys. Lett. A*, vol. 219, p. 287, 1996.

[136] C. Chandre, L. de Guillebon, A. Back, E. Tassi, and P. J. Morrison, "On the use of projectors for hamiltonian systems and their relationship with dirac brackets," *J. Phys. A*, vol. 46, p. 125 203, 2013.

[137] I. P. Christov, M. M. Murnane, and H. C. Kapteyn, "Generation and propagation of attosecond x-ray pulses in gaseous media," *Phys. Rev. A*, vol. 57, R2285, 1998.

[138] G. Rodriguez and G. L. Dakovski, "Scaling behavior of ultrafast two-color terahertz generation in plasma gas targets: Energy and pressure dependence," *Optics express*, vol. 18, p. 15 130, 2010.

[139] N. Karpowicz and X.-C. Zhang, "Coherent terahertz echo of tunnel ionization in gases," *Phys. Rev. Lett.*, vol. 102, p. 093 001, 2009.

[140] I. Babushkin, W. Kuehn, C. Köhler, S. Skupin, L. Bergé, K. Reimann, M. Woerner, J. Herrmann, and T. Elsaesser, "Ultrafast spatiotemporal dynamics of terahertz generation by ionizing two-color femtosecond pulses in gases," *Phys. Rev. Lett.*, vol. 105, p. 053 903, 2010.

[141] E. Lorin, S. Chelkowski, and A. D. Bandrauk, "The wasp model: A micro-macro system of wave-schrödinger-plasma equations for filamentation.," *Commun. Comput. Phys.*, vol. 9, p. 406, 2011.

[142] T. Brabec and F. Krausz, "Nonlinear optical pulse propagation in the single-cycle regime," *Phys. Rev. Lett.*, vol. 78, p. 3282, 1997.

[143] C. Brée, M. Hofmann, A. Demircan, U. Morgner, O. Kosareva, A. Savel'ev, A. Husakou, M. Ivanov, and I. Babushkin, "Symmetry breaking and strong persistent plasma currents via resonant destabilization of atoms," *Phys. Rev. Lett.*, vol. 119, p. 243 202, 2017.

[144] E. Lorin, S. Chelkowski, and A. D. Bandrauk, "Attosecond pulse generation from aligned molecules—dynamics and propagation in h2+," *New J. Phys.*, vol. 10, p. 025 033, 2008.

[145] D. G. Lee, J.-H. Kim, K.-H. Hong, and C. H. Nam, "Coherent control of high-order harmonics with chirped femtosecond laser pulses," *Phys. Rev. Lett.*, vol. 87, p. 243 902, 2001.

[146] V. Cardin, B. E. Schmidt, N. Thiré, S. Beaulieu, V. Wanie, M. Negro, C. Vozzi, V. Tosa, and F. Légare, "Self-channelled high harmonic generation of water window soft x-rays," *J. Phys. B*, vol. 51, p. 174 004, 2018.

[147] B. Boashash, *Time-Frequency Signal Analysis and Processing: A Comprehensive Reference*, 2nd ed. Elsevier Science, 2015, ISBN: 0123984998.

[148] K.-H. Hong, J.-H. Kim, Y. H. Kang, and C. H. Nam, "Time–frequency analysis of chirped femtosecond pulses using wigner distribution function," *Appl. Phys. B: Lasers Opt.*, vol. 74, s231, 2002.

[149] V. S. Yakovlev and A. Scrinzi, "High harmonic imaging of few-cycle laser pulses," *Phys. Rev. Lett.*, vol. 91, p. 153 901, 2003.

[150] A. D. Bandrauk and H. Lu, "Exponential propagators (integrators) for the time-dependent schrödinger equation," *J. Theor. Comput. Chem.*, vol. 12, p. 1 340 001, 2013.

[151] E. Lorin, S. Chelkowski, and A. D. Bandrauk, "Mathematical modeling of boundary conditions for laser-molecule time-dependent schrödinger equations and some aspects of their numerical computation—one-dimensional case," *Numer. Methods Partial Differential Eq.*, vol. 25, p. 110, 2009.

[152] E. Hairer, S. P. Nørsett, and G Wanner, *Solving Ordinary Differential Equations I.* Springer-Verlag Berlin Heidelberg, 1993.

[153] S. Majorosi, M. G. Benedict, and A. Czirják, "Improved one-dimensional model potentials for strong-field simulations," *Phys. Rev. A*, vol. 98, p. 023 401, 2018.

[154] D. Richards, "The dynamics of high harmonic generation," *J. Phys. B*, vol. 29, p. 2925, 1996.

[155] F. Mauger, C. Chandre, and T. Uzer, "Dynamics of recollisions for the double ionization of atoms in intense laser fields," *Phys. Rev. A*, vol. 81, p. 063 425, 2010.

[156] J. G. Leopold and D. Richards, "Harmonic generation by one-dimensional systems," *J. Phys. B*, vol. 26, p. 1519, 1993.

[157] M. Protopapas, D. G. Lappas, C. H. Keitel, and P. L. Knight, "Recollisions, bremsstrahlung, and attosecond pulses from intense laser fields," *Phys. Rev. A*, vol. 53, R2933, 1996.

[158] M. C. Kohler, C. Ott, P. Raith, R. Heck, I. Schlegel, C. H. Keitel, and T. Pfeifer, "High harmonic generation via continuum wave-packet interference," *Phys. Rev. Lett.*, vol. 105, p. 203 902, 2010.

[159] C. Zagoya, C.-M. n Goletz, F. Grossmann, and J.-M. Rost, "An analytical approach to high harmonic generation," *New J. Phys.*, vol. 14, p. 093 050, 2012.

[160] A. Bahl, V. P. Majety, A. Scrinzi, and M. Kolesik, "Nonlinear optical response in molecular nitrogen: From ab-initio calculations to optical pulse simulations," *Opt. Lett.*, vol. 42, p. 2295, 2017.

[161] J. K. Wahlstrand, Y.-H. Cheng, Y.-H. Chen, and H. M. Milchberg, "Optical nonlinearity in ar and n2 near the ionization threshold," *Phys. Rev. Lett.*, vol. 107, p. 103 901, 2011.

[162] I. Babushkin, C. Brée, C. M. Dietrich, A. Demircan, U. Morgner, and A. Husakou, "Terahertz and higher-order brunel harmonics: From tunnel to multiphoton ionization regime in tailored fields," *J. Mod. Opt.*, vol. 64, p. 1078, 2017.

[163] S. Beaulieu, S. Camp, D. Descamps, A. Comby, V. Wanie, S. Petit, F. Légaré, K. J. Schafer, M. B. Gaarde, F. Catoire, *et al.*, "Role of excited states in high-order harmonic generation," *Phys. Rev. Lett.*, vol. 117, p. 203 001, 2016.

[164] C. M. Heyl, J. Güdde, U. Höfer, and A. L'Huillier, "Spectrally resolved maker fringes in high-order harmonic generation," *Phys. Rev. Lett.*, vol. 107, p. 033 903, 2011.

[165] M. Kreß, T. Löffler, M. D. Thomson, R. Dörner, H. Gimpel, K. Zrost, T. Ergler, R. Moshammer, U. Morgner, J. Ullrich, *et al.*, "Determination of the carrier-envelope phase of few-cycle laser pulses with terahertz-emission spectroscopy," *Nat. Phys.*, vol. 2, p. 327, 2006.

[166] C. Chandre, G. Ciraolo, R. Lima, and M. Vittot, "Local control of hamiltonian chaos," *J. Phys.: Conf. Ser.*, vol. 7, p. 48, 2005.

[167] R. Bachelard, A. Antoniazzi, C. Chandre, D. Fanelli, X. Leoncini, and M. Vittot, "Stabilizing the intensity of a wave amplified by a beam of particles," *Eur. Phys. J. D*, vol. 42, no. 1, pp. 125–132, 2007.

[168] R. Bachelard, C. Chandre, D. Fanelli, X. Leoncini, and M. Vittot, "Stabilizing the intensity for a hamiltonian model of the fel," *Nucl. Instrum. Methods Phys. Res., Sect. A*, vol. 593, p. 94, 2008.